MPD-ITS Technical Design Report - v1.0

2022
February

Contents

1 Introduction

1.1 Nuclear matter physics at NICA (by P. Senger)

1.1.1 High-density QCD matter in the cosmos and in the laboratory

Recent astronomical observations, such as the discovery of massive neutron stars, the determination of radii and masses of neutron stars, and the detection of gravitational waves emitted from mergers of compact stars, opened new opportunities for the exploration of the fundamental properties of dense nuclear matter, including the equation-of-state (EOS), and the elementary degrees-of-freedom, which are expected to emerge at those high densities. Complementary information is obtained from laboratory experiments with energetic heavy-ion collisions, which also offer the possibility explore the high-density EOS and to investigate new phases of strongly interacting matter, which may feature characteristic structures such as a first-order phase transition with a region of phase coexistence and a critical endpoint. The experimental discovery of these prominent landmarks of the QCD phase diagram would be a major breakthrough in our understanding of the fundamental properties of strongly interacting matter, with consequences for our knowledge on the structure of neutron stars and the dynamics of neutron star collisions. Equally important is quantitative experimental information on the properties of hadrons in dense matter, which may shed light on chiral symmetry restoration and the origin of hadron masses. Worldwide, substantial efforts at the major heavy-ion accelerators are devoted to the clarification of these fundamental questions, and new dedicated experiments are under construction at future facilities like FAIR in Darmstadt and NICA in Dubna.

1.1.1.1 Dense QCD matter in compact stellar objects

From astronomical observations of masses and radii of massive neutron stars together detection of gravitational waves emitted from neutron star mergers, constraints on the EOS of neutron matter have been extracted up to densities of 4 ρ_0 [1]. These observations provide information on the thermodynamic properties of dense QCD matter, but not on its microscopic degrees-of-freedom. Various microscopic model calculations based on different assumptions are able to produce a stiff EOS at high densities, which is required to stabilize neutron stars with 2 solar masses. Calculation based on chiral effective field theory, which assume nucleonic degree-of-freedoms up to about 4 ρ_0, introduce repulsive 2-body ΛN and 3-body ΛNN interactions in order to increase the Λ chemical potential, and to prevent the decay of neutrons into Λ hyperons. These interactions avoid the appearance of Λ hyperons and provide a stiff EOS at high densities, which is a prerequisite for the existence of massive neutron stars [2].

Model calculations based on the concept of quark-hadron continuity predict a gradual appearance of quark degrees-of-freedom with increasing density and partial restoration of chiral symmetry according to a smooth crossover [3]. For densities below 2 ρ_0, the dominant interactions occur via a few meson or quark exchanges and the matter can be described in terms of interacting nucleons. For densities in the range from 2 ρ_0 to about 5 ρ_0, many-quark exchanges dominate, and the system gradually changes from hadronic to quark matter. For densities beyond about 5 ρ_0, nucleons percolate, start to melt and to dissolve into their constituents, which do not longer belong to particular nucleons. Calculations based on a non-local 3-flavor Nambu Jona-Lasinio model predict a first order phase transition with a mixed phase, where nucleons, hyperons and quarks coexist in the core of a 2 solar mass neutron star above densities of 4 - 5 ρ_0 [4]. In this model, repulsive vector interactions among the quarks are introduced to prevent a softening of the EOS, which otherwise would happen due to the appearance of quarks and hyperons. Pure quark matter is predicted above densities of 8 ρ_0.

Densities up to 4 ρ_0 are also expected to be reached also in neutron star mergers as illustrated in Figure 1.1, which depicts a snapshot of the equatorial plane illustrating the evolution of a neutron star merger with a total mass of 2.8 solar masses calculated with a Chiral Mean Field model [5]. The left part of the plot displays the temperature T, while the right part presents the quark fraction Y_{quark}. The green lines represent contours of constant baryon density in units of the nuclear saturation density ρ_0. The calculation predicts a phase transition to pure quark matter at a density of 4 ρ_0 and at a temperature of about 50 MeV. This phase transition occurs shortly before the high-mass neutron star collapses into a black hole.

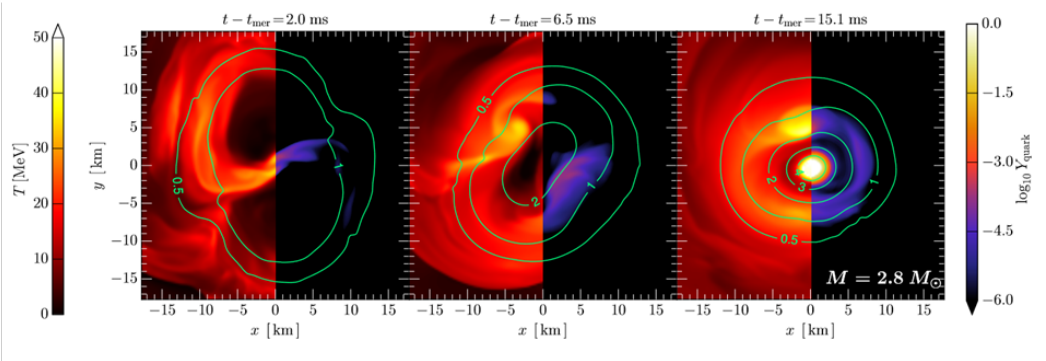

Figure 1.1: Three snapshots of the evolution of two merging neutron stars with a total mass of 2.8 solar masses. The scales at the left and at the right indicate the temperature and the $\log_{10}$ of the quark fraction Y_{quark}, respectively. The green lines represent contours of constant net-baryon density in units of ρ_0 [5].

In conclusion, very different models can provide a stiff EOS at high density, which is required to stabilize massive neutron stars, although they are based on very different assumptions on the forces and the microscopic degrees-of-freedom in dense matter: pure nucleons, a smooth crossover or a 1^{st} order phase transition from hadronic to quark matter. Future laboratory experiments with heavy-ion beams at FAIR and NICA will substantially contribute to further constrain the EOS and to unravel the fundamental degrees-of-freedom at neutron star core densities.

1.1.1.2 Laboratory experiments exploring dense QCD matter

Heavy-ion collision experiments play a crucial role in the investigation of both the EOS of nuclear matter and the QCD phase diagram. The present status of these experiments is briefly reviewed below.

1.1.1.2.1 The nuclear matter equation-of-state

Pioneering experiments at the Bevalac in Berkeley in the 1980s discovered the collective flow of protons. It indicated that a new form of equilibrated and dense matter is created in heavy-ion collisions at beam energies around 1A GeV [6]. Moreover, the multiplicity of pions emitted from this fireball was used to extract the EOS of nuclear matter [7]. More quantitative information on the EOS was obtained by the next generation of experiments in the same beam energy range, which have been performed in the 1990s at GSI. The FOPI collaboration measured the elliptic flow of protons, deuterons, tritons and 3He in Au+Au collisions at energies from 0.4A to 1.5A GeV [8]. IQMD transport calculations could reproduce the experimental results using a soft EOS and momentum-dependent interactions. The flow data are sensitive to the EOS because the collective flow of nucleons is driven by the pressure gradient in the collision zone. Another EOS-sensitive observable was found to be subthreshold strangeness production. According to microscopic transport calculations, for example K^+ mesons are produced in secondary collisions of pions and nucleons in heavy-ion collisions, if the kinetic beam energy is below the K^+ production threshold in nucleon-nucleon collisions, which is 1.6 GeV. These multi-step processes are enhanced at high density and, therefore, are sensitive to the EOS. The KaoS collaboration measured subthreshold K^+ production in a very heavy and light collision system at different beam energies [9]. The kaon data could only be reproduced by RQMD model calculations when assuming a soft EOS and taking into account in-medium effects [10]. The data of both the FOPI and the KaoS experiment support values of the nuclear incompressibility of the order of 200 MeV, corresponding to a soft EOS for nuclear matter densities around twice saturation density. The FOPI and ASY-EOS collaborations at GSI have also studied the symmetry energy at baryon densities above saturation density in Au+Au collisions 400A MeV by measuring the elliptic flow of neutrons and protons. By comparing the FOPI data to the results of UrQMD transport calculations, a value of about $E_{sym} = 60 \pm 10$ MeV was found for 2 ρ_0 [11]. From the ASY-EOS data a value of about $E_{sym} = 55 \pm 5$ MeV at 2 ρ_0 was extracted [12].

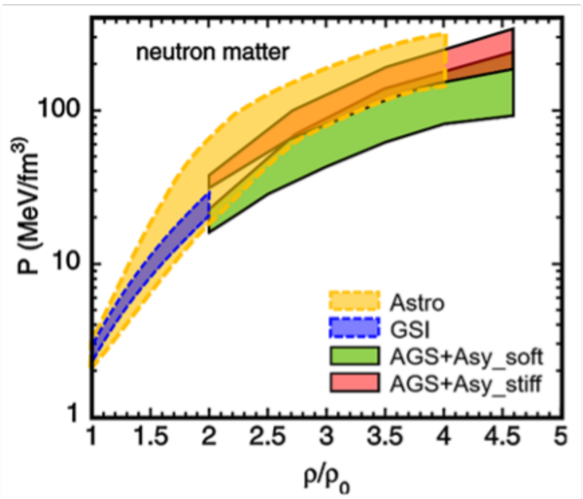

Figure 1.2: EOS for cold neutron matter plotted as pressure versus density. Orange area: Analysis of masses and radii of neutron stars measured by NICER, including mass measurements of the most massive neutron stars, and the tidal deformability estimate from the GW170817 [1]. Blue area: Analysis of the GSI flow and kaon data [8–12]. Pink and green area: analysis of AGS flow data [13, 14] after adding the pressure from asymmetry terms with strong and weak density dependences, respectively

Starting in the 1990s, experiments with gold beams were performed at the AGS in Brookhaven at beam energies between 2A and 11A GeV, i.e. at higher nuclear matter densities. The excitation function of the proton collective flow measured by the EOS collaboration [13] has been analyzed using transport calculations with respect to the high-density EOS [14]. However, the result of this analysis only ruled out very soft or extremely hard EOS. The reason is, that the directed flow data could be explained better by a soft EOS (nuclear incompressibility ($K_{nm} = 210\,\text{MeV}$)), while the data on the elliptic flow pointed towards a stiff EOS ($K_{nm} = 300\,\text{MeV}$).

The present constraints of the equation-of-state for neutron matter, i.e. a combination of information from astronomical observations and from heavy-ion collisions, are illustrated in Figure 1.2. The blue area represents the results of the GSI experiments, which constrain the EOS up to about 2 ρ_0 [8–12]. The green and pink areas correspond to the analysis of the AGS flow data, after adding the symmetry energy with a strong and a weak density dependence, respectively [13, 14]. The orange area reflects the results of astronomical observations, including mass and radii of neutron stars [1], masses of massive neutron stars [15–17], and gravitational waves emitted from neutron star mergers [18].

As illustrated in Figure 1.2, the heavy-ion results constrain the EOS up to 2 ρ_0, while at higher densities the measured masses of the most massive neutron stars exclude a soft EOS as represented by the green area. New measurements of radii and masses of neutron stars together with future laboratory experiments at FAIR and NICA are required to further constrain the EOS at neutron star core densities.

1.1.1.2.2 The QCD phase diagram

The currently available information on the QCD phase diagram is depicted in Figure 1.3, which summarizes experimental data, results of lattice Quantum-Chromo-Dynamics (LQCD) calculations, and QCD based model predictions. The left panel of Figure 1.3 depicts the QCD phase diagram as function of temperature T versus baryon chemical potential μ_B [19]. The various colored symbols represent the freeze-out conditions as extracted by statistical hadronization models from particle yields measured at different energies. For LHC collision energies, a freeze-out temperature of $\text{T} = 156.5 \pm 1.5\,\text{MeV}$ and a baryon chemical of $\mu_B = 0.7 \pm 3.8\,\text{MeV}$ was determined from the data [20]. For similar values of T and μ_B, LQCD calculations found a smooth chiral crossover from the Quark-Gluon Plasma (QGP) to hadronic matter, and obtained a pseudocritical temperature. The HotQCD collaboration determined a pseudo-critical temperature of $\text{T}_c = 156.5 \pm 1.5\,\text{MeV}$ at vanishing μ_B, and extrapolated the crossover region up to $\mu_B \approx 300\,\text{MeV}$, as indicated by the orange band [21]. The WB collaboration found a pseudo-critical temperature of $\text{T}_c = 158.0 \pm 0.6\,\text{MeV}$ with a width of $\Delta\text{T} = 15 \pm 1\,\text{MeV}$ at μ_B =0, and extrapolated the crossover region from imaginary to real chemical potentials up to $\mu_B \approx 400\,\text{MeV}$, as illustrated by the green band [22]. Figure 1.3 (left panel) also presents results of Dyson-Schwinger Equations (DSE) and Functional Renormalization Group (FRG), which agree to the LQCD results at $\mu_B = 0$, and predict the location of a 1^{st} order phase transition for larger values of μ_B together with a critical endpoint [19]. The most recent DSE-FRG calculation for 2+1 flavor QCD represented by the blue-dashed line ends up in a critical endpoint at a temperature of $\text{T}_{cep} = 93\,\text{MeV}$ and a baryon-chemical potential of $\mu_{Bcep} = 672\,\text{MeV}$.

The right panel of Figure 1.3 depicts the results of LQCD calculations as function of temperature, baryon chemical potential, and masses of the light quarks u and d. The calculations have been performed at $\mu_B = 0$, where LQCD is applicable. In addition to the pseudo-critical temperature of the smooth chiral crossover at $\text{T}_{pc} \approx 156\,\text{MeV}$, also the upper limit for the temperature of a hypothetical critical point of a chiral phase transition has been determined at $\text{T}_c = 133$+2-6 MeV for a baryon-chemical potential of $\mu_B = 0$ and for zero quark masses [23, 24]. The red and blue lines show the temperature of a tri-critical point T_{tri} at finite μ_B should be lower, and the critical endpoint at finite baryon-chemical potential μ_B and non-zero light quark masses T_{cep} should be even lower, if it exists at all. This LQCD result corroborates the prediction of the DSE-FRG calculations, and restricts the temperature of the critical endpoint of a hypothetical chiral phase transition to values $T_{cep} <\approx 130$ MeV. According to the freeze-out conditions illustrated in the left panel of Figure 1.3, such a temperature confines the location of a possible critical endpoint to baryon chemical potentials of $\mu_B <\approx 550$ MeV, corresponding to heavy-ion collision energies of $\sqrt{S_{NN}} <\approx$ 5 GeV, which are covered by the FAIR and NICA facilities.

The left panel Figure 1.3 also shows that the only experimental data in the QCD phase diagram are the freeze-out temperatures and baryon chemical potentials for various beam energies. These points characterize the situation, where the hadrons in the fireball cease to interact inelastically, which happens below saturation density ρ_0. At vanishing baryon chemical potential, this freeze-out temperature coincides with the pseudocritical temperature of a chiral crossover transition calculated by LQCD. For larger values of μ_B the QCD phase diagram essentially is Terra Incognita, and the exploration of this region is in the focus of heavy-ion experiments worldwide. In the following, some promising diagnostic probes will be discussed, which will be measured by the MPD experiment at NICA with unprecedented precision, and, therefore, provide a unique potential for the discovery of structures in the QCD phase diagram.

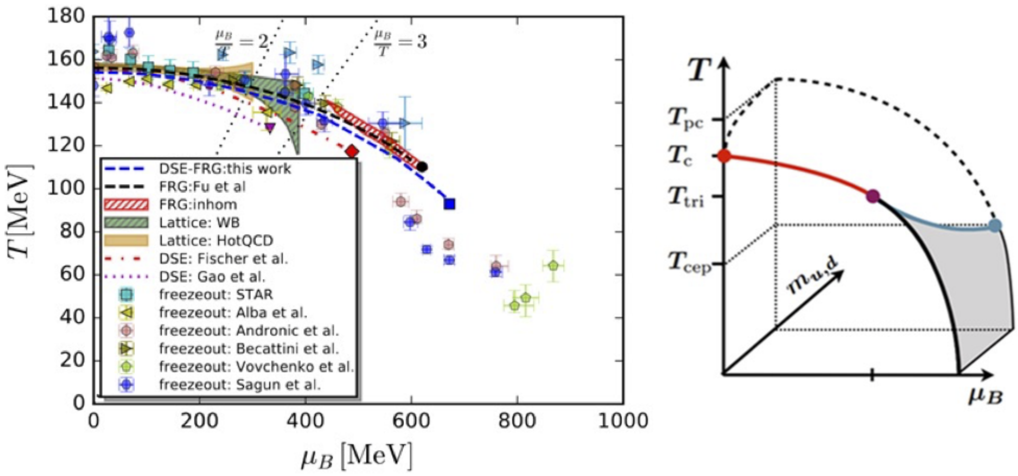

Figure 1.3: Left: Two-dimensional phase diagram for $N_f = 2+1$ flavor QCD in comparison to other theoretical approaches and phenomenological freeze-out data. For details see [19]. The DSE-FRG calculation represented by the blue-dashed line predicts a critical endpoint of a 1^{st} order chiral phase transition at $T_{cep} = 93$ MeV and $\mu_{Bcep} =$ 672 MeV. Right: Three-dimensional phase diagram as function of temperature T, baryon-chemical potential μ_B and mass of the light quarks $m_{u,d} = 0$ as calculated by LQCD. Red dot: upper temperature limit $T_c = 132$+3-6 MeV for the critical endpoint of a first-order chiral phase transition at $\mu_B = 0$ and $m_{u,d} = 0$ [23, 24]. Pink dot: Tri-critical point at $\mu_B = 0$ and $m_{u,d} = 0$. Blue dot: upper limit for the temperature of a critical endpoint for finite μ and physical light quark masses taken from [24].

1.1.2 Conclusions and outlook

The beam energies and luminosities available at NICA perfectly fit the worldwide landscape of heavy-ion accelerators. Situated between FAIR SIS100 and the low RHIC energies, NICA covers the energy range where the highest net-baryon densities can be created in laboratory experiments. This offers the opportunity to produce and to study QCD matter at neutron star core densities and to address fundamental questions related to the high-density EOS, phase structure of strongly interacting matter, to confinement and chiral symmetry.

As a modern heavy-ion experiment, the Multi-Purpose Detector (MPD) at NICA [25] is designed to measure a variety of diagnostic probes as discussed in the previous sections. This feature allows the investigation of different observables, related to the same physics topic. For example, the high density EOS can be studied by (i) the elliptic flow of identified particles, and (ii) the production of multi-strange (anti-)hyperons. A deconfined phase should leave its traces in several observables, including (i) the collective flow, (ii) the high invariant mass slope of dileptons, and (iii) charm production. The order of the phase transition can be determined by the (i) caloric curve determined with dileptons, the (ii) critical point measured with event-by-event fluctuations, and by (iii) the onset of deconfinement extracted from the excitation function of multi-strange hyperons.

The successful execution of these measurements with MDP at NICA will achieve a breakthrough in our understanding of the properties of QCD matter under extreme conditions. This is particularly true if the different results form a consistent picture, for example if the caloric curve obtained from dilepton measurements ends at the same energy, where event-by-event fluctuations exhibit a maximum, indicating the critical endpoint. Such a concordant scenario would tremendously increase the persuasive power of the single observations and could be regarded as the experimental discovery of a first order phase transition in dense baryonic matter. The experiments with MPD at NICA will complement the observations made by the beam-energy scan of STAR and will be complemented towards lower energies by the CBM experiment at FAIR. At even lower energies, the BM@N experiment at NICA will contribute to the progress in the field, although with a reduced set of observables.

The experimental program requires high-statistics measurements of the relevant observable over a large phase space, with particle identification and event characterization capabilities. The core detector of the MPD is a Time-Projection-Chamber (TPC) inside a solenoid magnet providing tracking and particle identification via dE/dx measurements. Particle identification will be improved by a Time-of-Flight (TOP) detector based on Multigap Resistive Plate Chambers (MRPC). These two detector systems, together with an Electromagnetic Calorimeter (ECAL) will also provide electron identification. A Zero Degree Calorimeter (ZDC) will be used to determine the collision centrality and the orientation of the reaction plane.

The TPC will be complemented by an Inner Tracking System (ITS) in order to provide precise tracking, momentum determination and vertex reconstruction. This upgrade will improve the identification of hyperons via the topology of their weak decays ($\Lambda \rightarrow p\ \pi$, $\Xi \rightarrow \Lambda\ \pi$, $\Omega \rightarrow \Lambda\ K$). Due to the short decay lengths of $c\tau = 7.89\,\mathrm{cm}$ (Λ), $c\tau = 4.91\,\mathrm{cm}$ (Ξ^-) and $c\tau = 2.46\,\mathrm{cm}$ (Ω^-) the track measurement should start close to the primary vertex where the track density is high. In particular, the ITS will be required for the identification of D mesons via their hadronic decay into pions and kaons (decay length of $c\tau = 123\,\mu\mathrm{m}$ for D^0, and $c\tau = 312\,\mu\mathrm{m}$ for $D^{\pm}$), and Λ_c^+ hyperons via their decay into $\mathrm{p}K^-\pi^+$ with a decay length of only $60\,\mu\mathrm{m}$. The layout, the technical realization and the performance of the ITS are described in the following.

1.2 The MPD experiment

The MPD experiment is projected to study the hot and dense baryonic matter in collisions of heavy ions over the atomic mass range A = 1–197 at a centre-of-mass energy up to $\sqrt{S_{NN}} =$

11 GeV (for $^{197}_{79}Au^{+}$). The experiment will be setup at the future JINR accelerator complex facility for heavy ions – the Nuclotron-based Ion Collider fAcility (NICA), that is designed to reach the required parameters with an average luminosity of L=10^{27} cm^{-2}s^{-1}.

The MPD apparatus has been designed as a 4π spectrometer capable of detecting of charged hadrons, electrons and photons at high luminosity. To reach this goal, the detector will comprise a precise 3-D tracking system (ITS+TPC) and a high-performance particle identification (PID) system based on the time-of-flight measurements and calorimetry. Since the average transverse momentum of the particles produced in a collision at NICA energies is below 500 MeV/c, the detector design requires a very low material budget. The general layout of the MPD apparatus is shown in Figure 1.4. The whole detector setup includes a Central Detector section (CD) covering ±2 units in pseudorapidity (η).

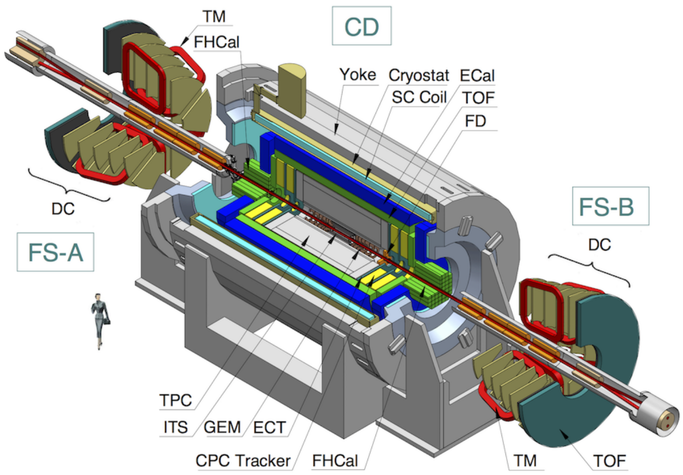

Figure 1.4: 3-D design image of the MPD.

1.2.1 Perspectives for the research program of the MPD experiment

One of the key requirements the future experimental MPD installation must meet is to solve the very challenging task of the high precision registration of strange, multi-strange and charmed particles formed in the relativistic heavy-ion collisions at the energies of NICA collider.

Studies in relativistic heavy-ion collisions of such rare processes as heavy-flavour production, in particular, detection of the short-lived D_0 and D^{+}-mesons, with an average path of ∼120 µm and ∼310 µm respectively, as well as the search for exotic particles decay and hyper-nuclei formation at the MPD require the use of fast, high granularity detectors capable to increase the accuracy of secondary vertices reconstruction. It is also essential to expand into the soft region the p_T range of registration of charged particles required, in particular, to increase the efficiency of charmed mesons detection. Details of physics motivation and model simulations for MPD studies could be found in Chapter 8 of the present Technical Design Report (TDR).

The physics performance requirements are imposing the highest demands on the event-by-event determination of secondary vertexes in case of registration of short-life charmed particles ($c\tau$ ∼100 µm). A resolution accuracy below ∼10 µm will be required here.

It is a well known fact that in order to get the best resolution in accuracy of tracking of charged particle to the primary and secondary vertexes the optimisation of the spatial (geometrical resolution) and of the multiple scattering factors is required. These demands of rare processes registration are making a very challenging tasks for the MPD Inner Tracking System design to implement the best state-of-the-art solutions and technologies available. Therefore, first of all, the application of fast and high granularity pixel sensors surrounding the interaction point (IP) is required. A considerable reduction of the material budget of all Inner Tracking System (ITS) components working in a sensitive region, especially for the innermost layers is also a must to be considered.

More detailed stringent specific requirements to the novel MPD Inner Tracking System with the high accuracy of secondary vertices reconstruction are listed below:

1. The application of the fast, high granularity CMOS pixel sensors with low noise level is needed.

2. The spatial resolution of track coordinate registration by sensors has to be ensured at the level of ∼5–10 µm.

3. The position of the very 1st sensor layer at the closest distance to the IP has to be provided; therefore, the application of the possible smallest diameter beam-pipe is to be considered for the MPD at the 2nd stage of the MPD development.

4. The considerable reduction of the material budget of the ITS has to be achieved by the application in the construction of only low-Z materials.

5. The assembly procedure of the ITS within the limited space inside the main tracking MPD device – the TPC, should be developed with the account of the beam-pipe support, the additional FFD system [26] and also of all cable and cooling ducts services of the ITS and the FFD.

1.3 The ALICE ITS2 first tracker totally based on MAPS technology

The most advanced and well proven ALICE technologies are being used at present as a baseline for the design of the ITS of the MPD at NICA. In this section a brief description is provided about the current state-of-the art Inner Tracking System prepared by the ALICE Collaboration for the Run-3 at the LHC [33].

The goals of the ALICE Collaboration for the upgrade of the installation for high-intensity Run-3 were to develop a fast and efficient tracking system capable to work over an extended transverse momentum range of charged particles, with a special emphasis on very low momenta and very precise reconstruction of secondary vertices from decaying charm and beauty hadrons. In order to meet these challenges a custom-designed chip was developed by the ALICE collaboration [32] basing on the 180 nm CMOS Imaging Sensor process of TowerJazz[1]. This technology of Monolithic Active Pixel Sensors (MAPS) provides the full charge collection efficiency ensured by a continuously active low-power front-end placed into each pixel and giving peaking time of around ∼2 µs and a spatial resolution of around ∼5 µm. Therefore, it opens the possibility to considerably expand the ALICE physics program to the high-precision area of rare processes with heavy flavor production in relativistic nucleus-nucleus collisions.

Results of estimates done by the ALICE collaboration of the expected impact parameter resolution of the upgraded ITS compared to the old ITS used in the period 2008–2018 are shown in Figure 1.5a The track reconstruction efficiency expected for the upgraded ALICE

[1] https://towerjazz.com

ITS is shown in Figure 1.5b. It can be seen the results of the improvements of impact parameter resolution in case of the upgraded ALICE ITS due to the decreasing of multiple scatterings in the soft region of charged particles spectra.

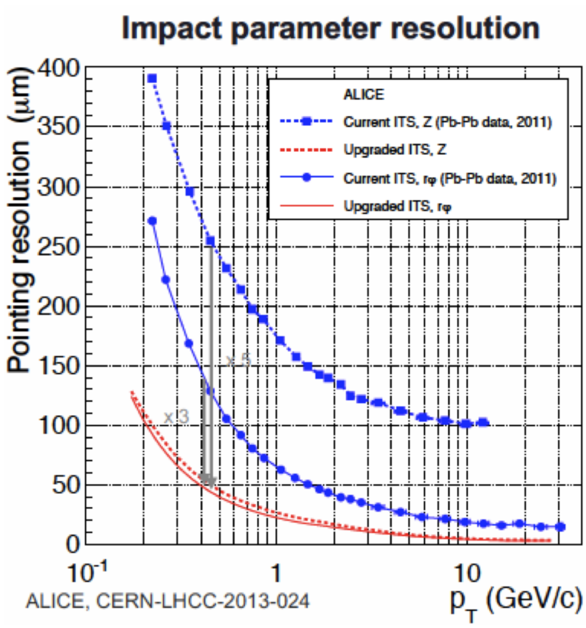

(a) Impact parameter resolution.

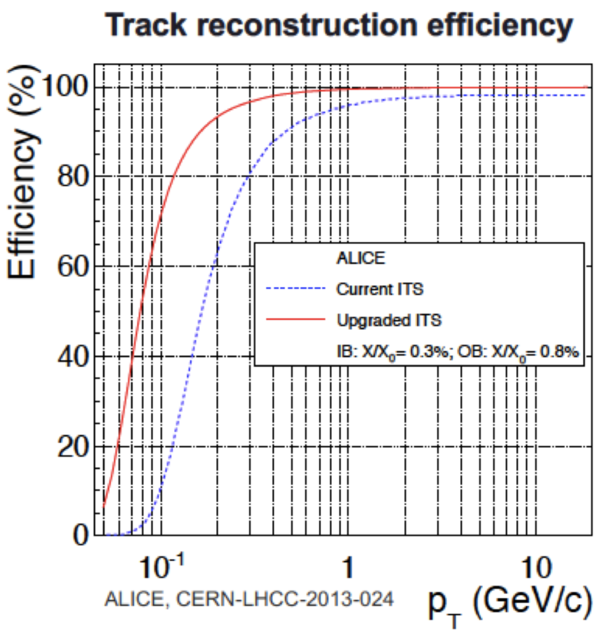

(b) Track reconstruction efficiency.

Figure 1.5: Upgraded ALICE-ITS performance estimates vs precedent ITS [33].

At the moment the present TDR is being written the new ALICE Inner Tracking System has been completed, installed and commisioned at Point 2. The ITS of ALICE is based on seven concentric layers of the MAPS chips. The application of very thin high granularity MAPS chips for its Inner (∼50 µm) and Outer (∼100 µm) barrels, combined with the state-of-the-art extra-lightweight carbon fibre composite structures with integrated cooling, ensures the required precise, thermo- and mechanically- stable positioning, support and efficient cooling of the large arrays of chips. The condition of minimal mass budget in the sensitive tracking region is met by the current design ensuring the overall relative radiation length per layer at the level $X/X_0 \sim 0.3\%$ for the Inner Barrel and $X/X_0 \sim 0.8\%$ for the Outer Barrel of the ITS [33].

These integrated super modules composed of MAPS sensors and the extra-lightweight carbon fiber composite cooling and support structures are called *Staves* and were developed and tested earlier [28–31]. They ensured considerable decrease of the multiple scattering in the soft region of charged particles spectra and allowed the ALICE Collaboration to produce the most transparent for radiation vertex detector used nowadays in the HEP experiments.

The characteristics of the pixel sensors and the solutions for the current Inner Tracking System developed by ALICE are meeting the requirements of the MPD and they could be used for the registration of rare processes in heavy-ion collisions at NICA. Namely, the current ALICE developments [32, 33] will provide the following capabilities which are suitable for consideration by the MPD:

- sensor thickness: 50 µm/100 µm for the Inner/Outer Barrel layers;
- sensor dimensions: 15×30 mm^2;
- spatial resolution: 5 µm;
- readout link bandwidth: up to 1.2 Gb/s;
- power density: 40 nW/cm^2;
- high track reconstruction efficiency for charged particles (see Fig. 1.5b);
- improved impact parameter resolution and extended charged-particle p_T coverage down to 100 MeV/c (see Fig. 1.5a and Fig. 1.5b);
- material overall budget per layer is at the level of $X/X_0 \sim 0.3\%$ for the innermost 3 layers, and at the level of $X/X_0 \sim 0.8\%$ for the outer layers No. 4 and 5.

1.4 MPD tracking system

1.4.1 The TPC

The Time-Projection Chamber (TPC) is the main tracking detector of the MPD central barrel. It is a gas detector for 3-dimensional tracking and particle identification for high multiplicity events [34–36].

The track reconstruction is based on drift time and R-φ coordinate measurement of primary ionization clusters. The track point resolution in X-Y (R-φ) plane is about 600 µm and about 1 mm - in Z. In total up to 52 points are on a track in the pseudorapidity range, $\eta \leq 1.2$.

The TPC performance in heavy ion collisions has studied by means of detailed Monte-Carlo (MC) simulations. These studies were performed within the dedicated software framework MpdRoot, which includes interfaces to several event generators (UrQMD, HSD, LAQGSM, etc.), description of the detector geometry, particle propagation with the GEANT 3 and 4 packages, detailed detector response simulation, as well as event reconstruction and analysis algorithms [37].

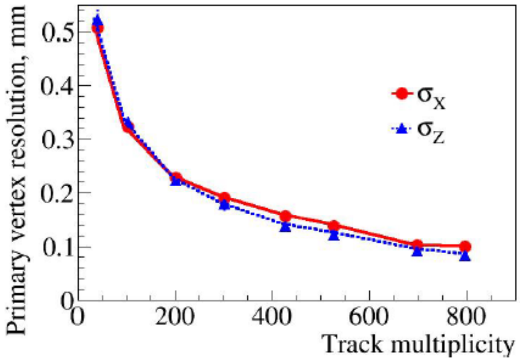

Figure 1.6: The primary vertex position resolution along transverse and longitudinal directions as a function of primary track multiplicity.

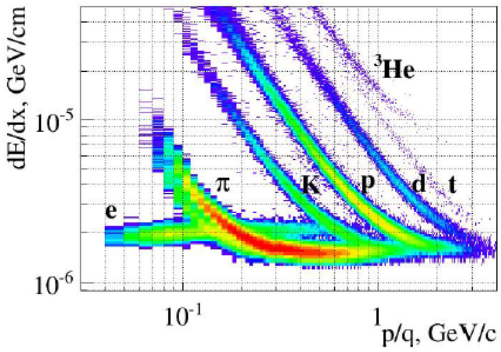

Figure 1.7: Specific energy loss vs magnetic rigidity for electrons, hadrons and light nuclei.

It was found that the transverse momentum resolution $\Delta p_T/p$ as a function of p_T is less than 2 % over the transverse momentum interval $0.2 < p_T < 1$ GeV/c. Although at larger η values the tracking performance degrades sharply for the TPC alone.

The primary vertex position resolution along transverse and longitudinal directions as a function of primary track multiplicity is shown in Fig. 1.6. The primary vertex was found by the extrapolating of all primary tracks reconstructed in the TPC back to the origin and its resolution is defined as the r.m.s. of the distribution of the whole sample of primary track extrapolations at the origin.

To identify charge particle for every track reconstructed in the TPC the specific energy loss dE/dx is calculated as a truncated mean of charges of the TPC hits assigned to the track. The truncation level of 70 % was chosen. As shown in Fig. 1.7 kaons can be discriminated from pions up to momentum of 0.7 GeV/c and protons discriminated from π- and K-mesons up to a momentum of 1.3 GeV/c.

An example of the reconstruction of strange mesons and hyperons in the MPD detector is shown in Fig. 1.8 and Fig. 1.9 [38]. The reconstruction have been done by combining charged tracks reconstructed in the TPC using the secondary vertex finding technique with an optimized set of topological and track quality cuts in order to guarantee that track combinations are associated to real decays. To ensure that the charged tracks are secondary ones, distinct cuts are applied on the minimum value of the impact parameters to the primary vertex. In addition, a pair of tracks is rejected if the distance of closest approach in space between the two opposite charged tracks is larger than a given value. Once the secondary vertex position is defined, only those falling within a fiducial region starting from a given distance from the main vertex are kept. Finally, the invariant mass is calculated under the proper hypothesis.

An accurate determination of the primary events vertex position essentially improves the momentum resolution and the secondary vertices finding efficiency.

1.4.2 The ITS

One of the main Physics goals of the MPD experiment is to study the properties of hot and dense nuclear matter produced in central collisions of heavy nuclei at the energies of NICA collider. By theoretical predictions [39] heavy quarks (c, b) in such reactions are born in the initial hard collisions of nucleons and carry the information about the excited nuclear medium at an early stage of its formation. The interaction between heavy quarks and the nuclear

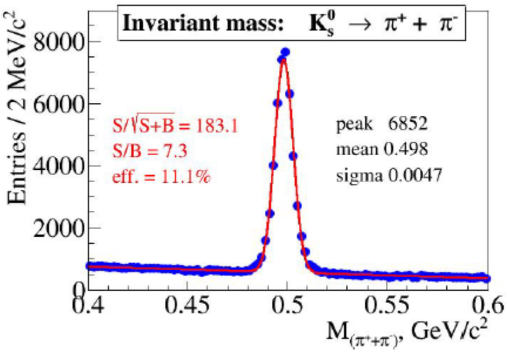

Figure 1.8: Reconstructed invariant mass of π^+ and π^- spectrum.

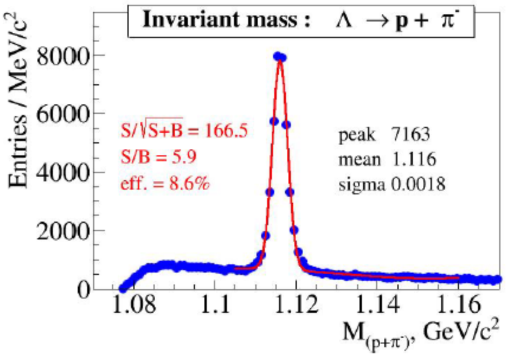

Figure 1.9: reconstructed invariant mass of protons and π^- spectrum.

medium is sensitive to the dynamics of the medium; therefore, heavy quarks are considered perspective probes for studying the properties of strongly interacting QCD matter [40–42].

The yields of particles with heavy flavor which include charmed particles, depend on the phase of excited nuclear matter. This is due to the different properties of the charm carriers at different phases. In the hadron phase D-mesons are carriers of charm, while in the deconfinement phase the carriers are charmed quarks. Producing a D (*anti*-D) pair requires an energy of 1.1 GeV more than producing a quark-antiquark pair c (*anti*-c). Thus, a higher yield of charm is expected in the deconfinement phase than in the hadron phase. Therefore similar to strangeness [43], a change in the dependence of the average number of charmed quarks on the energy of colliding nuclei can be a signal of the beginning of deconfinement phase.

To clarify the formation of heavy quarks mechanisms in relativistic nucleus – nucleus models, it is necessary to know the average number of quark – antiquark pairs generated in the full phase volume. Predictions obtained by various dynamic and statistical models [44–47] differ from each other in almost two orders of magnitude. Thus, obtaining accurate data on the cross sections for the formation of charmed particles will narrow the spectrum of possible theoretical models.

To detect charmed particles whose average ranges λ are several hundred micrometers (for example, $\lambda(D^0) = 123\,\mu\text{m}$, $\lambda(D^+) = 312\,\mu\text{m}$), it is necessary to use vertex detectors with high spatial resolution, located as close to the particle formation point as possible. That is the reason why the TPC, as the main tracker detector of the MPD experiment, will be supplemented by the ITS vertex detector.

The vertex detectors of modern experiments [48–53] are multilayer systems of semiconductor coordinate-sensitive detectors which play a key role in the reconstruction of short-lived particles (multistrange hyperons, charmed mesons, hypernuclei) from the invariant mass of their decay products. Using vertex tracking detector will provide the following advantages:

- improving the accuracy of the the secondary decay vertices coordinates reconstruction of short-lived particles;
- decreasing detection threshold of charged particles with small transverse momentum.

ITS will be built on the basis of modern silicon pixel sensors. The new generation pixel detectors MAPS have the best spatial resolution at a high count rate [48], and the high level of their segmentation into pixels allows this type of detector to be installed at distances of several centimeters from the interaction point without the risk to be overloaded. Therefore the combination of TPC and ITS vertex detectors will allow to detect short-lived products of nucleus-nucleus interactions at the MPD facility with maximum efficiency.

Bibliography

[1] M.C. Miller et al., ApJ. Lett. 887 (2019) L24

[2] W. Weise, PS Conf. Proc. (2019) 011002

[3] G. Baym et al., Rep. Prog. Phys. 81 (2018) 056902

[4] M. Orsaria et al., Phys. Rev. C89 (2014)015806

[5] E. Most E et al., Phys. Rev. Lett. (2019) 122 061101

[6] H.H. Gutbrod, A.M. Poskanzer and H.G, Ritter, Rep. Prog. Phys. 52,10

[7] J. W. Harris et al., Phys. Lett. B 153 (1985) 377-381

[8] A. Le Fevre A et al., (The FOPI Collaboration) Nucl. Phys. A 945 (2016) 112

[9] C. Sturm et al., (The KaoS Collaboration) Phys. Rev. Lett. 86 (2001) 39

[10] C. Fuchs et al., Phys. Rev. Lett. 86 (2001) 1974

[11] Y. Leifels et al., (The FOPI Collaboration) 1993 Phys. Rev. Lett. 71 963

[12] P. Russotto et al., (The ASY-EOS Collaboration) 2016 Phys. Rev. C 94 034608

[13] C. Pinkenburg et al, Phys. Rev. Lett. 83 (1999) 1295

[14] P. Danielewicz, R. Lacey, and W.G. Lynch, W.G. Science 298 (2002) 1592

[15] H. T. Cromartie et al. 2020 Nature Astronomy 4 72

[16] J. Antoniadis et al., Science 340 (2013) 448

[17] Z. Arzoumanian et al., ApJ 859 (2018) 47

[18] LIGO and Virgo Collaborations, ApJ. Lett. 848 (2017) L12

[19] F. Gao and J. M. Pawlowski, Phys. Rev. D 102 (2020) 034027

[20] A. Andronic et al., Nature 2018, 561, 321

[21] A. Bazavov A et al., (HotQCD Collaboration) Phys. Lett. B (2019) 795 15

[22] S. Borsanyi et al., (WB collaboration) Phys. Rev. Lett. 125 (2020) 052001

[23] H. T. Ding et al., (HotQCD Collaboration) Phys. Rev. Lett. 123 (2019) 062002

[24] F. Karsch, arXiv:1905.03936

[25] https://nica.jinr.ru/projects/mpd.php

[26] V. Yurevich, O. I. Batenkov, A. S. Veschikov, A. A. Povtoreyko, "Fast forward detector for MPD/NICA project: Concept, simulation, and prototyping", Physics of Particles and Nuclei Letters 10(3), 2013.

[27] B.Abelev et al., The ALICE Collaboration, Upgrade of the ALICE Inner Tracking System - Technical Design Report,J. Phys. G. 41 (2014) 087002, http://iopscience.iop.org/0954-3899/41/8/087002/ .

[28] S.N.Igolkin,G.A.Feofilov.V.M.Dobulevich, O.I.Stolyarov, "Method for the manufacture of carbon composite products of complex shape and device for its implementation" (valid). St.Petersburg State University, Patent of the Russian Federation, No. 2396168, B29C53 / 56, SPbSU, 2008132278/12, 07/31/2008, 08/10/2010.

[29] S.N.Igolkin,G.A.Feofilov.V.M.Dobulevich, O.I.Stolyarov, "Device for manufacturing carbon composite products of complex shape" (valid). St.Petersburg State University, Patent of the Russian Federation No. 79268, Certificate of the Russian Federation for utility model B29C53 / 56, St. Petersburg State University, 2008132135/22, 08/01/2008, 12/27/2008.

[30] V.I. Zherebchevsky, S.N. Igolkin, E.B Krymov, N.A. Maltsev, N.A. Makarov, G.A. Feofilov, "Extra lightweight mechanical support structures with the integrated cooling system for a new generation of vertex detectors", Instruments and Experimental Techniques, Volume 57, Issue 3, May 2014, Pages 356-360, http://www.maik.ru/ru/journal/pribory/ .

[31] V.I. Zherebchevsky, I.G. Altsybeev, G.A. Feofilov, A. Francescon, C. Gargiulo, S.N. Igolkin, E.B. Krymov, E. Laudi, T.V. Lazareva, N.A. Maltsev, "Experimental investigation of new ultra-lightweight support and cooling structures for the new Inner Tracking System of the ALICE Detector", 2018, JINST, 13, T08003.

[32] M.Mager, On behalf of the ALICE Collaboration, "ALPIDE, the Monolithic Active Pixel Sensor for the ALICE ITS upgrade",NIM Volume 824, 11 July 2016, Pages 434-438. https://doi.org/10.1016/j.nima.2015.09.057.

[33] B.Abelev et al., The ALICE Collaboration, Upgrade of the ALICE Inner Tracking System - Technical Design Report,J. Phys. G. 41 (2014) 087002, http://iopscience.iop.org/0954-3899/41/8/087002/ .

[34] A.Averyanov et al., "Time Projection Chamber for Multi Purpose Detector at NICA, Technical Design Report, rev.07.", Laboratory of High Energy Physics JINR, Dubna, 2019.

[35] Averyanov A. et. al., "Readout system of TPC/MPD NICA project.",Nuclear Physics and Engineering, Physics of Atomic Nuclei, 2015, Vol.78, No.13, pp. 1556-1562.

[36] Sergey Movchan on behalf of the MPD collaboration, "MPD/NICA TPC status (25.02.2020)", International Conference "Instrumentation for Colliding Beam Physics" (INSTR20), Novosibirsk, Russia, 24-28 Feb., 2020.

[37] V. Kireyeu, V. Kolesnikov, V. Vasendina, and A. Zinchenko for the MPD Collaboration, "Towards a realistic Monte Carlo simulation of the MPD detector.", VBLHEP JINR, Dubna, Russia, 2015

[38] M.A.Ilieva et al., "Evaluation of the MPD detector capabilities for study of the strangeness production at the NICA collider.", Physics of elementary particles and atomic nuclei, letters,Vol. 12, No.2(193) 2015, pp.543-559.

[39] Mueller B. Hadronic signals of deconfinement at RHIC // Nucl. Phys. A. 2005. V.750. P. 84-97.

[40] Moore G.D. and Teaney D. How much do heavy quarks thermalize in a heavy ion collision? // Phys. Rev. C. 2005. V.71. P.064904.

[41] Hees H. and Rapp R. Thermalization of heavy quarks in the quark-gluon plasma //Phys. Rev. C. 2005. V. 71. P. 034907.

[42] Uphoff J., Fochler O., Xu, Z., Greiner "C. Heavy-quark production in ultrarelativistic heavy-ion collisions within a partonic transport model", Phys. Rev.C. 2010. V.82. P.044906.

[43] J. Rafelski and B. Muller Phys. Rev. Lett. 48 (1982) 1066. [Erratum: Phys. Rev. Lett.56,2334(1986)].

[44] P.Braun-Munzinger and J.Stachel Phys. Lett. B490 (2000) 196–202, arXiv:nucl-th/0007059[nucl-th].

[45] O. Linnyk, E. L. Bratkovskaya, andW. Cassing Int. J. Mod. Phys. E17 (2008) 1367–1439,arXiv:0808.1504 [nucl-th].

[46] A. P. Kostyuk, M. I. Gorenstein, H. Stoecker, and W. Greiner Phys. Lett. B531 (2002) 195–202, arXiv:hep-ph/0110269 [hep-ph].

[47] P.Levai, T.S. Biro, P.Csizmadia, T.Csorgo, and J. Zimanyi J. Phys. G27 (2001) 703–706, arXiv:nucl-th/0011023 [nucl-th].

[48] B. Abelevet.al., “Technical design report for the upgrade of the ALICE inner tracking system”. Journal of Physics G: Nuclear and Particle Physics. Volume 41, Issue 8, 2014, 08700.

[49] K. Aamodtetal. “The ALICE experiment at the CERN LHC”,JINST3 (2008) 1-245.

[50] https://atlas.cern/discover/detector/inner-detector

[51] http://cms.web.cern.ch/news/silicon-pixels

[52] F.Videbaek. For the STAR collaboration Brookhaven National Lab. https://sss.slideserve.com/shaw/the-star-heavy-flavor-tracker

[53] G.Xie (for the STAR Collaboration). https://arxiv.org/pdf/1704.04353.pdf XXVIth International Conference on Ultrarelativistic Nucleus-Nucleus Collisions, (Quark Matter 2017)

2 The Pixel Chips

The sensors that will be used for the construction of the outer barrel of the MPD-ITS, are based on ALTAI Monolithic Active Pixel Sensors (MAPS). This type of chip is similar to the one originally developed for the construction of the new Inner Tracking System (ALICE-ITS2) of the ALICE experiment at CERN. ALICE is the first experiment at LHC implementing a large silicon tracker ($\sim$10 m^2) with this technology [1]. ALICE-ITS2 has been already completed and is currently undergoing the commissioning phase at CERN.

The sensor was optimized through extensive R&D [2,3] in order to handle collisions rates up to 50 kHz for Pb-Pb and 200 kHz for pp collisions improving the impact parameter resolution the standalone tracking efficiency and p_T resolution. For instance, the impact parameter resolution which should be achieved at 400 MeV/c is 50 µm in both $r\phi$ and z directions [2]. In addition, a power consumption well below 100 mW/cm^2 allows a material budget for the outer barrel of 0.8% X_0 [4].

2.1 The MAPS chips from the ALICE ITS2

The ALTAI chip is based on the 15 mm × 30 mm large MAPS used for the ALICE-ITS2 project implemented in a 180 nm CMOS imaging sensor process by TowerJazz [4]. For the outer barrel layers, 100 µm thick sensors were employed. The novel implementation of deep p-well in the process allows full CMOS circuitry within the pixel matrix (Fig. 2.1) still keeping full charge collection efficiency [1,5]. A very low power consumption of less than 40 mW/cm^2 is achieved by the integration of continuously active low-power front-end into each pixel and in-matrix zero suppression circuit (Priority encoder).

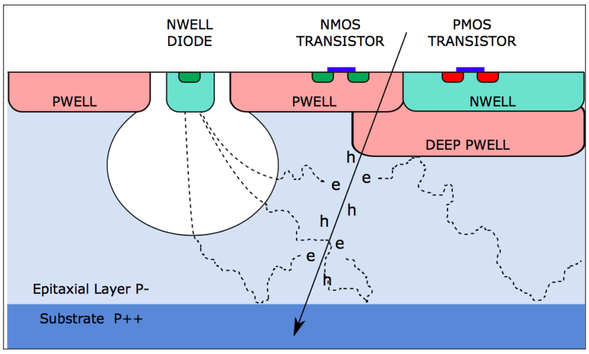

Figure 2.1: Schematic cross section of a MAPS pixel in the TowerJazz 0.18 µm imaging CMOS with the deep p-well feature.

The sensor is segmented in 512×1024 pixels of 29 µm × 27 µm (Fig. 2.2); a periphery circuit region of 1.2 mm × 30 mm implements analog biasing, control, readout and interfacing functionalities (Fig. 2.3). Each pixel contains an n-well sensing diode ($\sim$2 µm diameter), an amplifying and shaping stage, a discriminator and a digital section (Fig. 2.4)with three-hits storage register (Multi-Event Buffer), and two single bit registers for masking and pulsing logic, respectively. The Pulse register allows testing functions: each pixel can be forced to produce a hit using both a test charge injection capacitor (analogue pulsing) or directly setting the pixel state register (digital pulsing).

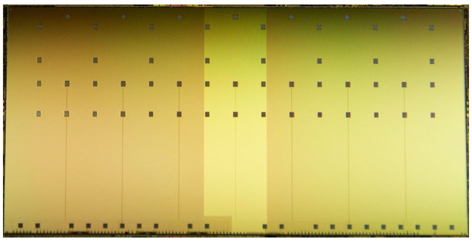

Figure 2.2: ALICE-ITS2 MAPS chip. The interconnection pads size, visible as dark square in the image, is 300 µm; pads in the bottom "digital periphery" are used for clock, control and readout signals, while all others distributed over the sensitive surface are used for digital and analogue power supply, ground and bias connections.

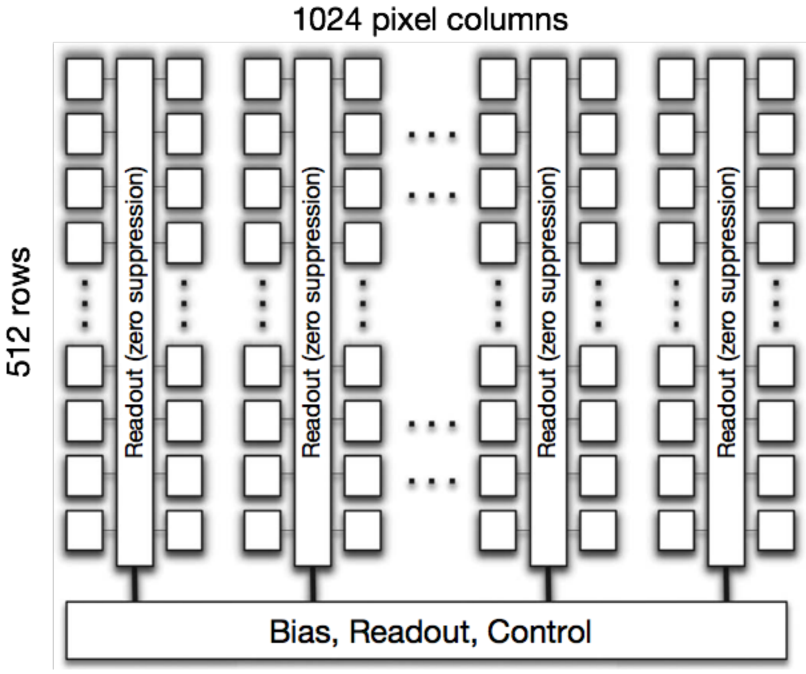

Figure 2.3: Architecture of the ALICE-ITS2 MAPS chip.

There are 512 Priority Encoders, one or every two pixels columns. They implement the buffering of readout and configuration signals to the pixels and provide the periphery with the pixel addresses over threshold which is the only information produced as readout data. The circuits are fabricated on a high resistivity (>1 kΩ cm) P-type epitaxial layer (25 µm thick) on P-type substrate (75 µm thick for the outer barrel). A reverse back-bias voltage V_{bb} of −3 V is applied to the substrate in order to increase the depletion volume and reduce the capacitance which both contribute to increase the S/N ratio.

2.2 Detector technology

The 0.18 µm CMOS technology by TowerJazz, selected for the implementation of the outer barrel layers, has distinguished features that make it suitable and in some respect unique for

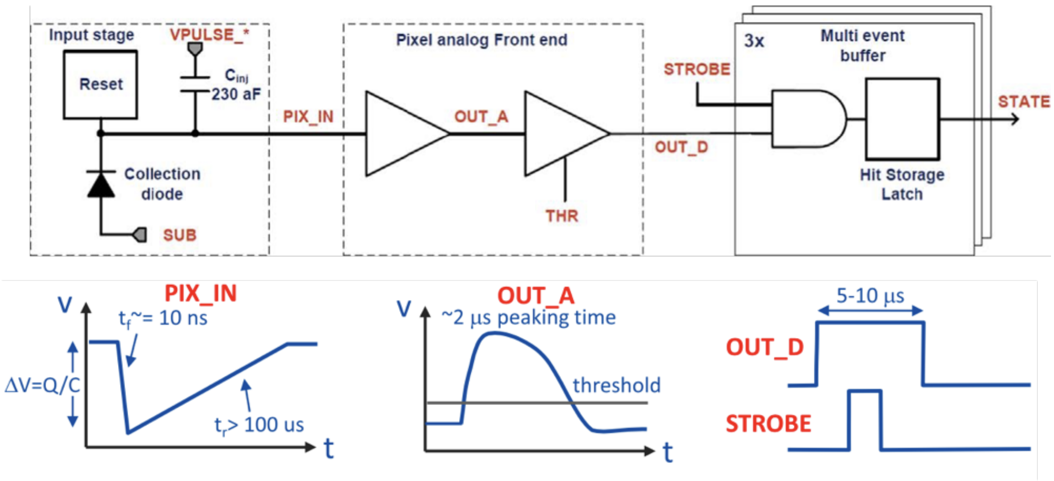

Figure 2.4: Block diagram of the ALICE-ITS2 MAPS chip pixel cell.

the implementation of the MPD-ITS Pixel Chip. As reported in [4]:

- The feature size and the number of metal layers available (up to six) are adequate to implement high density and low power digital circuits. This is essential since a large part of the digital circuitry (e.g. memories) will be located at the periphery of the pixel matrix and its area must be minimized to reduce the insensitive area as much as possible.

- It is possible to produce the chips on wafers with an epitaxial layer of up to 40 µm thickness and with a resistivity between 1 kΩ cm and 6 kΩ cm. With such resistivity, a sizeable part of the epitaxial layer can be depleted. This increases the signal-to-noise ratio and may improve the resistance to non-ionizing irradiation effects.

- The access to stitching technology allows the production of sensors with dimensions exceeding those of a reticle and enables the manufacturing of die sizes up to a single die per 200 mm diameter wafer. As a result, insensitive gaps between neighboring chips disappear and the alignment of sensors on a Stave is facilitated.

- The availability of a deep p-well option allows the production of pixel structures with significantly enhanced functionality.

The last point is a unique feature of this process and can be key to enable low-power readout architectures. In standard implementations, the sensing diode is an n-well diode, normally used as the substrate for PMOS transistors. As a consequence, only NMOS transistors can be used in the pixel area. In fact, any PMOS transistor requires an additional nwell that competes with the sensing diode in collecting the signal charge. The front-end electronics located in the pixel must fully rely on NMOS devices, so only simple, low-gain amplifiers or source followers can be implemented. Hit discrimination, which requires more sophisticated signal processing, cannot be performed at the pixel level and the full matrix must be scanned during the read-out phase. A few alternatives have been proposed to allow the use of PMOS in the pixel, like the use of deep n-well and of high voltage CMOS technologies. However, both options lead to a significant increase in the capacitance of the sensing electrode. Therefore, the power consumption in the front-end must be increased accordingly to preserve an adequate signal-to-noise ratio. This problem is circumvented due to the use of a deep p-well in the region where the front-end electronics is foreseen.

The n-wells that accommodate the PMOS transistors are fabricated on top of the deep p-well. The signal electrons are reflected by the electric potential at the junction between the epitaxial layer and the deep p-well and can be collected only by the sensing diode. Its size can then be tailored to optimize the charge collection efficiency and the signal-to-noise ratio, while full CMOS front-end electronics can be put in the pixel. The effectiveness of the deep p-well approach has already been demonstrated and circuits with complex front ends similar to those used for hybrid sensors read-out have already been produced.

2.3 Principle of operation

2.3.1 Particle detection

As indicated in Figure 2.1, when a charged particle traverses the silicon sensor's active volume, it liberates charge carriers (electrons and holes) in the semiconductor material.

The released charge is then collected by electrodes that reveal not only the presence of a particle but also — due to a fine segmentation — its impinging point onto the sensor. The nature and quantitative behavior of the charge collection mechanism are functions of the material properties (resistivity or doping level/profile) and geometry (thickness of sensitive material, pixel pitch, electrode shape) as well as the electric field configuration (electrode potential and geometry) of the sensor. The amount of deposited charge depends on the particle species and its momentum (Bethe-Bloch). Minimum ionizing particles (MIPs, e.g. 0.5 GeV/c pions) which define the requirement on the minimal detectable charge, typically release some 60 electrons per 1 µm path length in thin silicon layers [6].

A charged particle crossing the sensor liberates free charge carriers in the material by ionization. The electrons released in the epitaxial layer can diffuse laterally while they remain vertically confined by potential barriers at the interfaces with the overlying p-wells and the underlying p-type substrate. The signal sensing elements are n-well diodes (∼2 µm diameter) with an area typically 100 times smaller than the pixel cell area. The electrons that reach the depletion volume of a diode (or carriers that are released directly inside it) induce a current signal at the input of the pixel front-end [1].

2.3.2 Read-out

As described in [7], the sensor pixels are read-out in a binary hit/no-hit fashion. It combines a continuously active, low-power, in-pixel discriminating front-end with a fully asynchronous, hit-driven combinatorial circuit. Figures 2.5 and 2.6 depict schematically the discriminator circuit and the functioning of the ALTAI in-pixel front-end circuitry, respectively.

The in-pixel circuitry consists of a continuously active discriminating amplifier and a multiple-event memory into which data may be strobbed. The rise time of the amplifier is below 2 µs and defines the event time resolution while its shaping time is longer and makes it act as an analogue delay line. This allows data to be discriminated and strobbed with a trigger latency of some 2 µs into the in-pixel buffers in a global shutter mode of operation. Strobbing can also be done with fixed spacing and over longer periods making the circuit record data continuously.

The in-pixel multiple-event memory is read-out asynchronously by means of a priority encoder circuit in each double column. This is both fast and power efficient as the expected occupancies are low and only hit pixels are read-out in a hit-driven fashion [8]. Data is collected at the periphery and shipped off the detector by means of a high-speed serial link. The chip also supports a mode where data of six adjacent chips is collected by one sensor acting as a master [9].

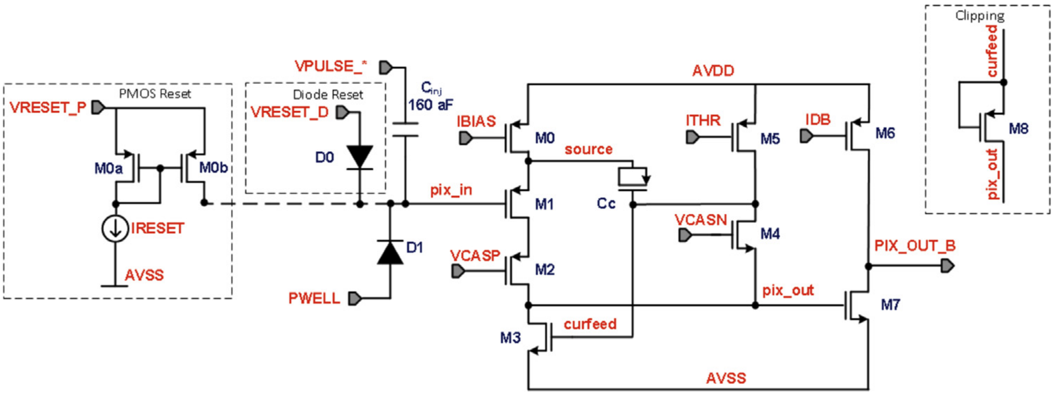

Figure 2.5: Reset, amplification and discrimination circuit of the sensor.

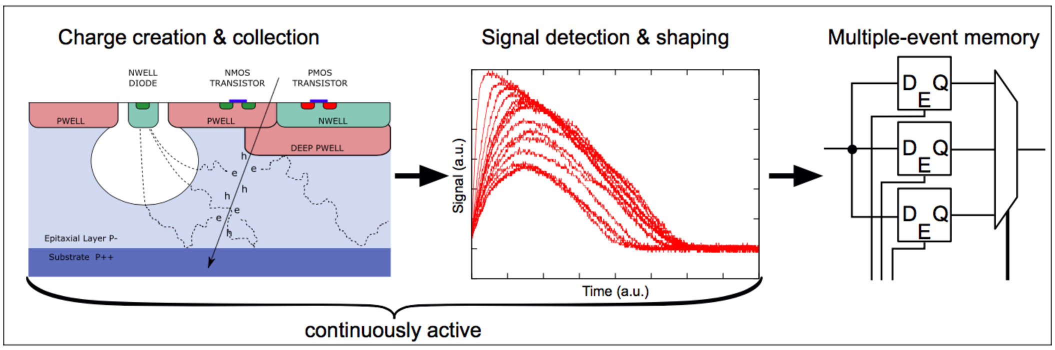

Figure 2.6: Principle of operation of sensor's in-pixel circuitry.

Bibliography

[1] G. Aglieri Rinella,et. al., The ALPIDE pixel sensor chip for the upgrade of the ALICE Inner Tracking System, Nucl. Instr. Methods Phys. Res. A: Accel. Spectromet. Detect. Assoc. Equip. 845 (2017) 583–587

[2] P. Yang, et. al., MAPS development for the ALICE ITS upgrade, Pixel 2014 International Workshop, September 1-5, Niagara Falls, Canada.

[3] Sabyasachi Siddhanta, et.al., The upgrade of the Inner Tracking System of ALICE, Nucl. Phys. A: Nucl. Hadr. Phys. 931 (2014) 1147–1151

[4] B. Abelev, et al., The ALICE Collaboration, Technical design report for the up- grade of the ALICE inner tracking system, J. Phys. G: Nucl. Part. Phys. 41 (2014) 087002

[5] M. Suljic, ALPIDE: the Monolithic Active Pixel Sensor for the ALICE ITS upgrade, J. Instrum. 11 (2016) C11025

[6] H. Bichsel, Straggling in thin silicon detectors, Rev. Mod. Phys. 60, 663–699 (1988)

[7] M. Mager, et. al., ALPIDE, the Monolithic Active Pixel Sensor for the ALICE ITS upgrade, Nucl. Instr. Methods Phys. Res. A: : Accel. Spectromet. Detect. Assoc. Equip. 824 (2016) 434–438

[8] P. Yang, et al., Low-power priority Address-Encoder and Reset-Decoder data-driven readout for Monolithic Active Pixel Sensors for tracker system, Nucl. Instr. Methods Phys. Res. A: Accel. Spectromet. Detect. Assoc. Equip. 785 (2015) 61.

[9] A. Szczepankiewicz, et. al., Readout of the upgraded ALICE-ITS, Nucl. Instr. Methods Phys. Res. A: Accel. Spectromet. Detect. Assoc. Equip. 824 (2016) 465–469.

[10] A. Di Mauro, et. al., The new inner tracking system for the ALICE upgrade at the LHC, Nucl. Instr. Methods Phys. Res. A: Accel. Spectromet. Detect. Assoc. Equip. 936 (2019) 625-629.

[11] ALICE Collaboration, Upgrade of the ALICE Experiment: Letter of Intent, J. Phys. G 41 (8) (2014) 087001.

[12] P. Martinego, et. al., The new Inner Tracking System of the ALICE experiment, Nucl. Instr. Methods Phys. Res. A: Accel. Spectromet. Detect. Assoc. Equip. 967 (2017) 900-903.

3 Detector Layout

The MPD-ITS conceptual layout (Fig. 3.1) repeats the scheme used in ALICE-ITS2 but with a decreased number of MAPS layers from seven (ALICE-ITS2) to five (MPD-ITS). This is due to the significantly smaller internal diameter of the TPC chamber 500 mm of MPD installation. The MPD-ITS will consist of two coaxial cylinders ("barrels"), Inner (IB) and Outer (OB) with layers of different thicknesses and with a completely different design of the supporting structure and cooling system.

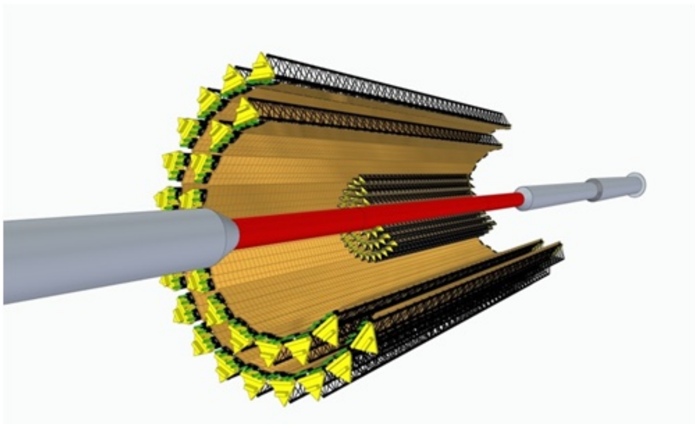

Figure 3.1: MPD-ITS conceptual layout around thin beryllium beam pipe of MPD setup

The Inner Barrel IB contains three layers of detectors and the Outer Barrel OB contains two. Detecting layers are segmented in the azimuthal direction into independent supermodules blocks or "Staves".

The spatial position of the Staves in the layer is determined by the requirement of full coverage of the cylindrical surface. Therefore, taking into account the fact that on the side of the detector plate there is a so-called "dead zone" in which reading and buffering circuits from a position-sensitive matrix are located, the design assumes a certain amount of detectors overlapping in the layer.

The design of the mechanics of the tracker was carried out for two diameter variants of the MPD beam pipe; diameters *project* 40 mm and *initial* 64 mm. This copes with the existing plans for NICA collider to be launched with an "initial" beam pipe diameter 64 mm, which after the adjustment of the machine should be replaced with a "project" beam pipe of a smaller diameter. Appendix .2 exposes the possibilities for the reduction of the beam pipe diameter. It is important to note that with all the provided replacements for the beam pipe, the mechanical structure of the tracker itself remains universal, and the structure and parameters of the Outer Barrel are unchanged. Therefore, the main goal of the first stage of the MPD-ITS project is to design and manufacture the mechanical structure of the tracker and the Outer Barrel of the system. This strategy is explained in details in section 3.1. For this reason, the present chapter is mainly devoted to the aspects related to the assembly, testing and installation of the Outer Barrel of the MPD-ITS. Finally, in section 3.3 the plans for the completion of the Inner Barrel are presented. Three possible variants of the IB are presented here, which include the most-desired design using the novel ALICE-ITS3 ultrathin sensors currently under R&D and two backup variants using the existing ALICE-ITS2 IB sensors depending on the effective diameter of the beam pipe.

3.1 The two stages construction scenario

The existing natural constraints on the minimal diameter of the beam-pipe, coming from the NICA accelerator beam tuning and performance, are to be taken into account for the design of the ITS. At present, two options of the beam-pipe are being considered for the MPD installation with a diameter of 64 mm and 40 mm, respectively. The final choice will be made by the NICA accelerator team after the start of operation. Therefore, two-stages scenario is adopted for the ITS development.

The Stage-1 of the project foresees to start with the development of the so-called Outer Barrel of the ITS based on the ALTAI chip using 180 nm technology from the TowerJazz. Two external layers of CMOS sensors will be built following the existing design of the ALICE ITS [33].

One of the important tasks is the design of the overall assembly procedure of the Inner Tracking System and the long and fragile beam-pipe section. They should be installed inside the limited space of the MPD TPC together with additional FFD [26] detector, the read-out and power supply cables, liquid cooling tubes and air-ducts. These issues are presented in Chapter 4.

At the Stage-2 the innermost layers of the ITS will be constructed for the MPD expecting to have the small diameter beam-pipe. Thus, it is planned to use the most advanced developments of the Inner Barrel by ALICE Collaboration. The ongoing R&D for the future ALICE Inner Barrel of the ITS-3 [1], [2], is based on the 65 nm TowerJazz technology. The 20 µm-thick sensors could be up to 280 mm long and 94 mm wide in Stitching Chip manufacturing and, owing to the flexible nature of silicon at these thickness, they could be bent in case of ALICE ITS3 into half-cylinders of radii of 18 mm, 24 mm and 30 mm respectively to form the new concentric layers of the Inner Barrel [3].

These very thin, ∼20 µm, large area wafers with sensors will be used together with the novel extremely light mechanical and cooling systems for the implementation of the MPD-ITS Inner Barrel. The new detector would reach an unprecedented low material budget below $X/X_0 \sim 0.05\%$ per layer.

On the other hand, taking into account that this 65 nm technology is currently under R&D, a back-up solution for the Stage-2 will be based on the design of the MPD Inner Barrel based on the well proven 180 nm technology.

3.2 Stage-1: The Outer Barrel

The sensors of the Outer Barrel will be arranged on two concentric Layers (layers 4 and 5) with a total of 42 elements called *Staves* (described in section 3.2.1) that follow the existing design from the Outer Barrel of ALICE-ITS at the LHC presented in the Technical Design Report [33].

The cross section of the layout of layers 4 and 5 that conform the Outer Barrel of the MPD-ITS is shown in figures 3.2 and 3.3 (detail), while figure 3.4 shows its side view.

3.2.1 Outer Barrel Staves

This section is dedicated to the description of the Outer Barrel Staves including supporting mechanics, cooling system and assembly process. A large part of the information presented

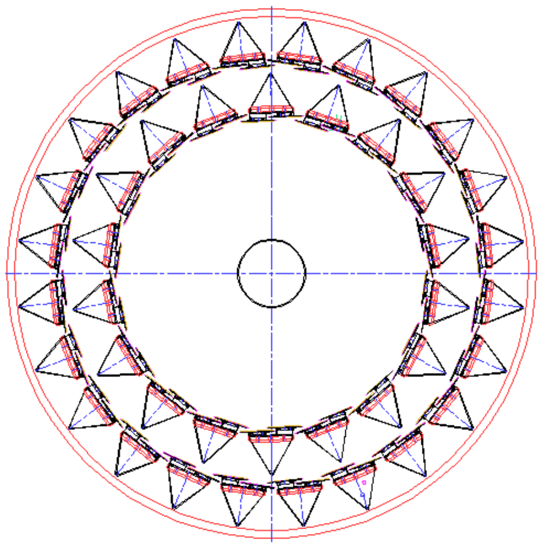

Figure 3.2: Outer Barrel of the MPD Inner Tracking System: cross-section. See parameters of layers 4,5 in the Table 3.7

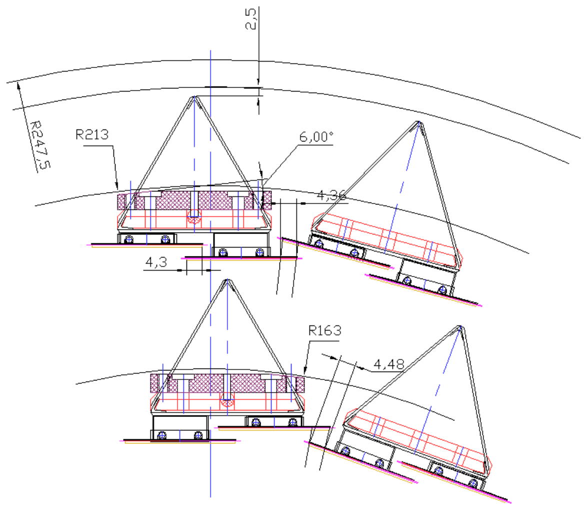

Figure 3.3: Detail of the cross section of the Outer Layers of the MPD Inner Tracking System

here comes from the R&D process carried out by the ALICE Collaboration for the production of the ITS2 detector, as reported in [6].

Each Stave is a segment of a Layer in the azimuthal direction, and it extends over the whole length of the respective layer. The Stave contains all structural and functional components making it the smallest operable part of the detector and the basic detector unit (Fig. 3.5). The Staves are azimuthally split themselves into two Half-Staves which are further fragmented longitudinally in seven HIC (Hybrid Integrated Circuits) modules. Figure 3.6 shows a bottom view of an actual Stave from the ALICE-ITS2 which are geometrically the same as the ones that will be produced for MPD-ITS.

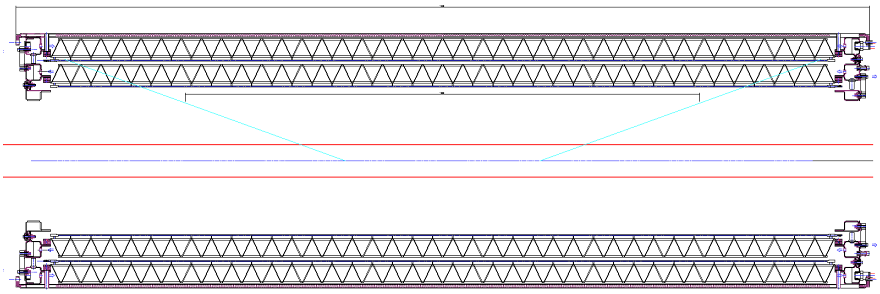

Figure 3.4: Side view of the ITS layers 4 and 5 to be installed at the Stage-1

The detailed composition of the OB Staves is as follows:

- **Space Frame:** lightweight trihedral cross-section structures made of high modulus carbon fibers and an epoxy resin. It provides the mechanical support and the necessary stiffness to the Half-Staves throughout the entire operation period;
- **Ending elements:** structures having precision holes that are fixed at the edges of the Space Frames. They provide high-precision positioning of the Half-Staves during technological transitions of its assembly with detectors blocks and, subsequently, as part of the ITS detection layer;
- **Cold Plate:** a sheet of carbon fiber laminate with high-thermal conductivity values from 800 to 1500 $\mathrm{W\,m^{-1}\,K^{-1}}$ with embedded polyimide cooling pipes. They are in thermal contact with the Pixel Chips to remove the generated heat. The Cold Plates are connected to the Space Frame by U-shaped connectors;
- **Hybrid Integrated Circuit** (HIC): an assembly of a polyimide Flexible Printed Circuit (FPC) on which 14 Pixel Chips are bonded. On each module of the Outer Barrel there are 14 sensors that readout the address of the pixel info hit by a particle. This *modules* can be individually replaced in case of defects during the testing of the assembly;
- **Half-Stave:** the OB Staves are further segmented in azimuth in two halves, called Half-Staves. Each Half-Stave extending over the full length of the Stave consists of a Cold Plate on which a seven HICs are glued.

In order to achieve a nearly full coverage, the two Cold Plates of a Stave overlap in the rφ direction, as shown by the Stave cross section in figure 3.5, and each of them overlaps with the nearest Cold Plate of the neighbouring Staves. The sizes of overlapping dead zones are optimized taking into account the spatial position of the detector Half-Staves in each layer. Actual size of dead zones for the Outer Barrel layers is shown in Figure 3.3.

3.2.2 Supporting mechanics

The Stave mechanical support must fulfil stringent requirements in terms of minimum mass and highest stiffness. Its design is inherently linked to the layout of the cooling system that will be adopted to remove the heat dissipated by the silicon sensors since the cooling system is integrated in the mechanical structure. Each OB Stave is 1524 mm in length with 1474 mm covered by the sensors. The layout of the OB Stave mechanics and cooling consists of a Space Frame and two Cold Plates, one for each Half-Stave. The Cold Plate is made of a

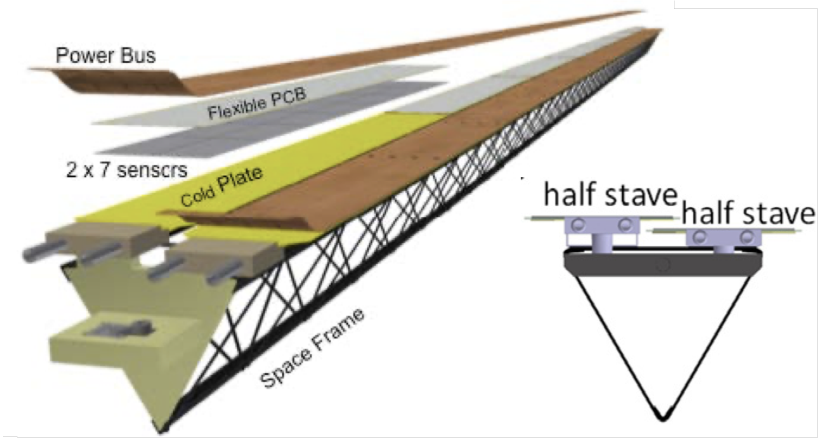

Figure 3.5: Schematic exploded view and cross section of the OB Stave.

Figure 3.6: Bottom-view of an actual Stave from ALICE-ITS2 showing the two Half-Staves structures and the composing HIC modules.

high thermal conductive carbon fibre laminate with embedded cooling pipes on top of which the silicon chips are glued. The heat is conducted into the cooling pipes by the carbon fibre structure and is removed by the coolant flowing in the pipes. For mechanical stability the Cold Plate is stiffened by the Space Frame, a light filament wound carbon structure with a triangular cross section. A mechanical connector at each of the two ends of a Stave provides the precise positioning of the Stave in the Layer configuration.

A general view of the Cold Plate is shown in Figure 3.7. The approved Cold Plate length for layers 4 and 5 is 1502 mm.

The composite structure of the Cold Plate is shown in Figure 3.8. It consists of:

- a substrate made of heat-conducting carbon fiber brand M55J with thermal conductivity along the fiber 155.6 $\mathrm{W\,m^{-1}\,K^{-1}}$ and a thickness of 70 µm, laid perpendicular to the longitudinal axis;
- two polyimide tubes with an inner (outer) diameter of 2.024 mm (2.074 mm);
- thermal graphite foil FGS-003 with thermal conductivity 1500 $\mathrm{W\,m^{-1}\,K^{-1}}$ and a thickness of 30 µm laid on top of the tubes and transferring heat from the Plate to the tubes;

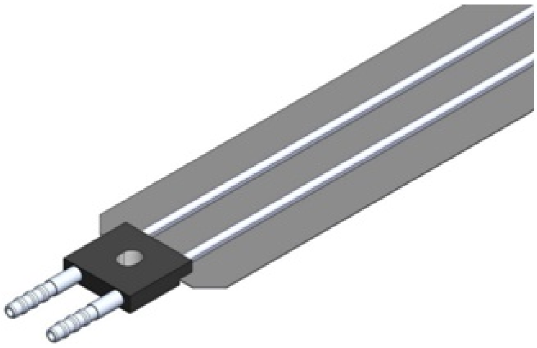

Figure 3.7: Cold Plate of the Outer Barrel Staves of MPD-ITS.

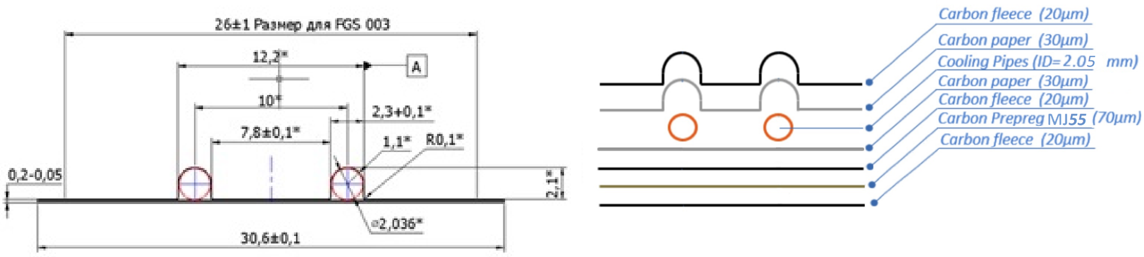

Figure 3.8: Cross section (left) of the Cold Plate and the content of its inner structure (right).

- carbon fleece with a density of $8\,\mathrm{g/m^2}$ and thickness of 20 µm.

To ensure the solidity of the Plate an epoxy compound is used. Complete assembly of the Cold Plate includes edge elements with precision holes that provide solutions to the technological problems of assembly and positioning of the Plates when setting on Half-Staves. The edge elements also contain fittings and transitional connections for supplying and coolant diversion.

On the other hand, Outer Barrel Staves (layers No. 4 and 5) have a total length of 1556 mm in order to ensure the required acceptance of particles detection. Therefore in order to achieve the required rigidity the cross section of the Space Frame (Fig. 3.9) is such that makes it possible to place two paired Cold Plates with Hybrid Integrated Circuit (HICs). The width of the Plate allows to place Hybrid Integrated Circuit (HICs) stacked along the Half-Staves of the Outer Barrel. The gap between the detector chips does not exceed 100 µm. To place them and close the "dead zone" on the sensors, the Cold Plates are staggered at different heights (see Figs. 3.3 and 3.5). The Plates are fastened to the Space Frame through U-legs of different lengths.

3.2.2.1 Material budget

Table 3.1 reports the estimated contributions of the OB Stave to the material budget. The estimated overall material budget is within reach of the required 0.8% X_0. The detailed description of the azimuthal distribution of the material across the Outer Layer Stave is shown in figure 3.10. The neighbouring Half-Staves are partially superimposed to ensure the detector hermeticity, thus giving rise to the peaks around 1.25% X_0. The highest peaks are

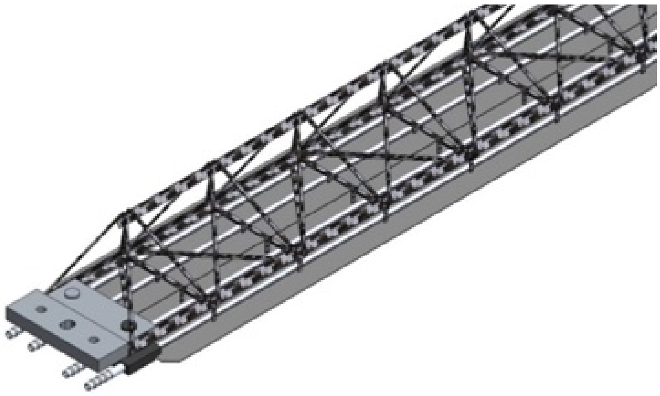

Figure 3.9: Outer Barrel Space Frame with Cold Plates. To complete the first stage of the MPD-ITS a total of 42 Staves plus spares are needed.

due to the polyimide cooling pipes embedded in the Cold Plate assuming they are fully filled with water.

Table 3.1: Estimated contributions of the Outer Layer Stave to the material budget.

Stave element	**Component**	**Material**	**Thickness (µm)**	X_0 **(cm)**	X_0 **(%)**
Module	FPC Metal layers	Aluminium	50	8.896	0.056
	FPC Insulating layers	Polyimide	100	28.41	0.035
	Module plate	Carbon fibre	120	26.08	0.046
	Pixel Chip	Silicon	50	9.369	0.053
	Glue	Eccobond 45	100	44.37	0.023
Power Bus	Metal layers	Aluminium	200	8.896	0.225
	Insulating layers	Polyimide	200	28.41	0.070
	Glue	Eccobond 45	100	44.37	0.023
Cold Plate		Carbon fleece	40	106.80	0.004
		Carbon paper	30	26.56	0.011
	Cooling tube wall	Polyimide	64	28.41	0.013
	Cooling fluid	Water		35.76	0.105
	Carbon plate	Carbon fibre	120	26.08	0.046
	Glue	Eccobond 45	100	44.37	0.023
Space Frame		Carbon rowing		0.080	
Total					**0.813**

3.2.3 Cooling system

The cooling system of the ITS includes water- and gas-cooling sub-systems. Its main goal is to provide precise temperature control of the detectors, electronics and mechanical components of the detector. In particular, the system should:

- remove all heat generated inside the detector by chips and service elements;
- maintain chips at appropriate temperatures for various operating conditions;
- avoid leakage of coolant and condensation inside and outside the detector;
- avoid heat exchange with surrounding detectors;
- be compatible with the equipment planned for installation;

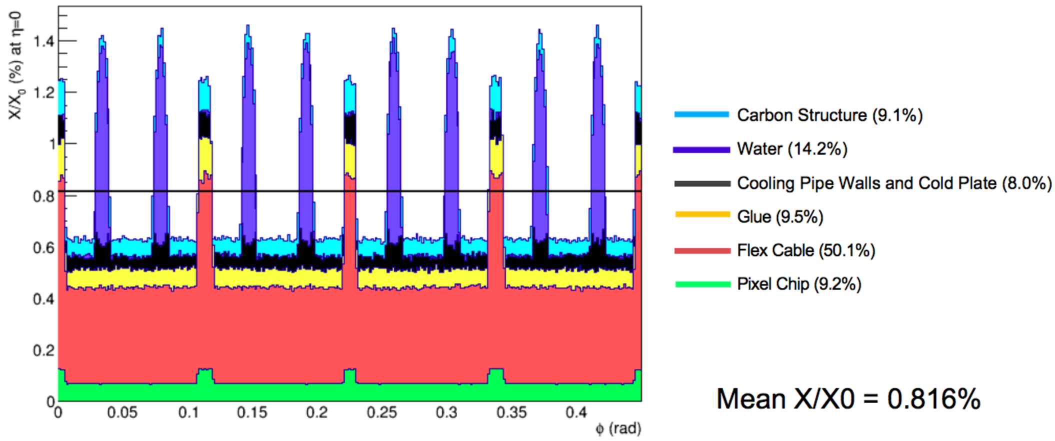

Figure 3.10: The azimuthal distribution of the Outer Layer Stave material traversed by the particles at $\eta = 0$. The highest peaks correspond to the polyimide cooling pipes embedded in the Cold Plate fully filled of water and the others to the Half-Stave overlaps to ensure the detector hermiticity.

- interface with the Detector Control System (DCS) and locking system;
- comply with the safety rules of JINR.

Table 3.2 shows the requirements for the detector and service electronics stable functioning.

Table 3.2: Detector and service electronics requirements

Requirement		Detector	Sevice electronics
T_{max} Pixel chip working		30 °C	40 °C
ΔT_{max} (uneven)		≤5 °C	
Settings	Magnetic field	500 mT*	400 mT**
	Temperature	T=20 °C RH=35% $T_{Dew\ point}$=4 °C	T_{ux25}=24 °C RH_{ux25}=45% $T_{Dew\ point}$=12 °C
Stability		Temporary (it will not be possible to calibrate) detector positioning ≤5 µm	
Installation/ Removal		Ability to move non-functioning boards (3 months)	Ability to move non-functioning boards (3 months)
System access		Detector installation and maintenance available on both sides	Detector installation and maintenance available on both sides

(*)Simulation parameters.
(**)Magnet is ON.

3.2.3.1 Integrated leakless water cooling system

The power density of the pixel chips is about 28 mW/cm^2 for all five layers of the ITS. An additional heat load, about 30 % of the chip load, coming from the power regulators should be considered for each Stave.

For each OB Half-Stave the chips cover a total area of $14 \times 7 \times 1.5 \times 3.0\,\mathrm{cm}^2 = 441\,\mathrm{cm}^2$, with a total heat release of 28 mW/cm^2 + 50 % (14 mW), this amounts to $441 \times 0.042 = 18.5$ W or 4.4 cal/s for a single Half Stave of the OB. To remove this heat at a water ΔT of 2 °C, 4.4 : 2 = 2.2 g/s of water flow or 7.9 l/h will be required.

Table 3.3 shows the cooling requirements for the Staves and the related electronics.

Table 3.3: Technical requirements for Staves and electronics

Technical specifications	Detector Staves	RU Electronics
Power load	OB: 84 pcs (Half Staves) From the detector 1555 W* Bus 63 W Power Cable 22 W	7.5 kW
Stave pressure difference and water consumption	OB: ΔP=0.2 Kg/cm^2 Q=6.3 l/h Σ530 l/h	OB: 0.3 Kg/cm^2 Stave Q=11 l/h
Chip / valid temperature Range	20 °C to 30 °C	20 °C to 40 °C
Chip / working temperature	22 °C±1 °C	30 °C±5 °C

(*)Calculation based on Alpide 4; OB = 28 mW/cm^2 + 50%.

To remove the bulk of the heat, a leakless liquid cooling system using demineralized water is used (Fig. 3.11).

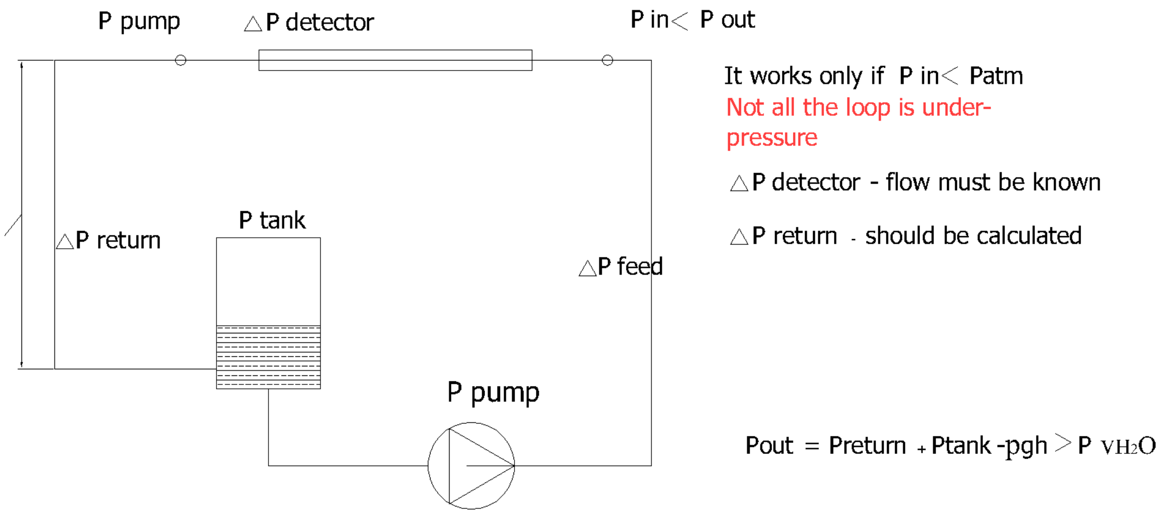

Figure 3.11: Schematic of the leakless water cooling system.

The layout of the Stave mechanics and cooling for the OB consists of a Space Frame and two Cold Plates. The Cold Plate is made of a high thermal conductive carbon fiber laminate, with embedded cooling pipes, on top of which the silicon chips are glued. The heat is conducted into the cooling pipes by the carbon fiber structure and is removed by the coolant flowing in the pipes that are joint at one end. For mechanical stability the Cold Plate is stiffened by the Space Frame, a light filament wound carbon structure with a triangular cross section. A mechanical connector at each of the two ends of a Stave provides the precise positioning of the Stave in the Layer configuration.

This design has been inherited from the ALICE-ITS2 project. The Staves are connected to the cooling system by blocks. The modularity of the connection allows reducing the number of supply and draining pipes. The breakdown schemes of the cooling system into modules are shown in figure 3.12.

The connection of the panels in the modules and the bore sections of the tubes are shown in figure 3.13.

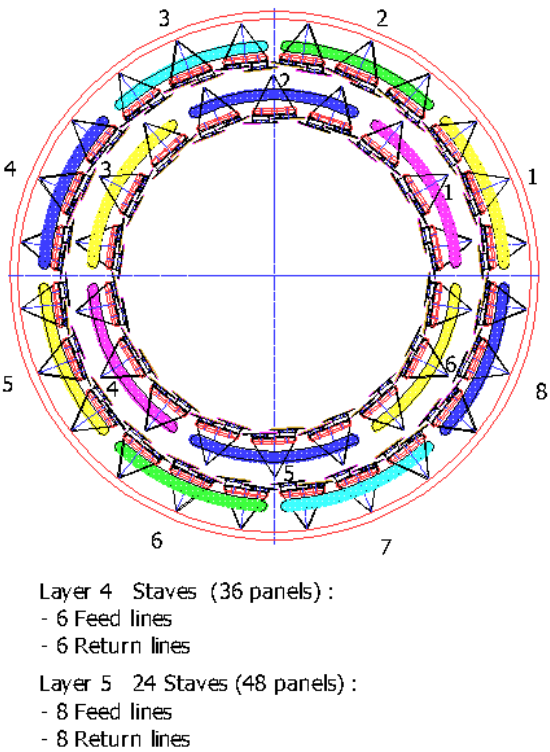

Figure 3.12: Schematic of the water cooling system for the OB Saves.

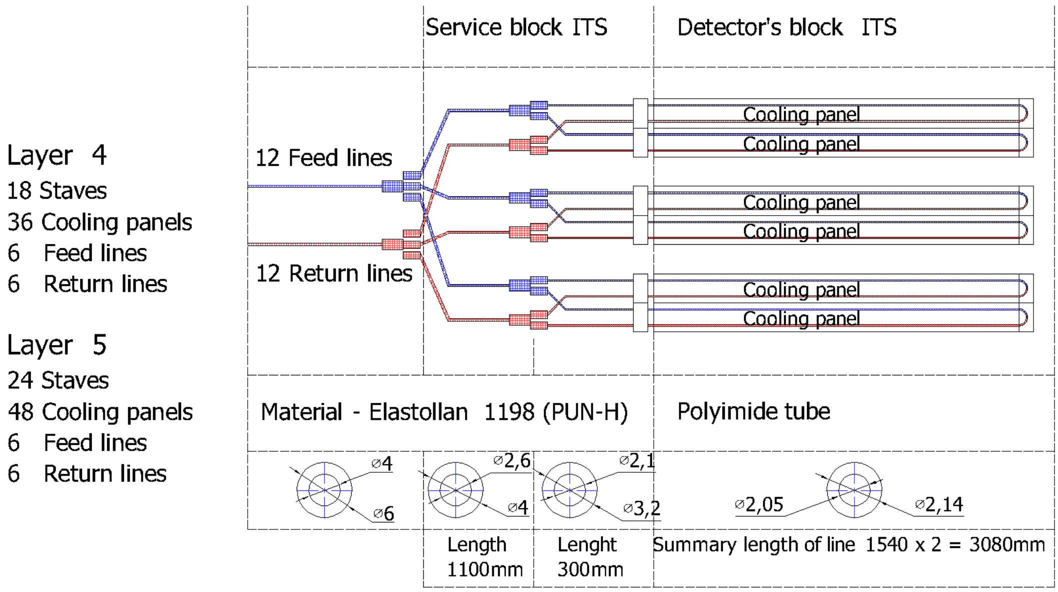

Figure 3.13: Modularity specification of the ITS OB Layers.

3.2.3.2 Integrated gas cooling system

The ITS gas-flow system eliminates the temperature gradient along the vertical axis of the housing and additionally provides humidity control inside the system. An air-flow system is integrated into the support system of the detector Staves with the characteristics shown in table 3.4.

Table 3.4: ITS air cooling sysms basic characteristics.

Parameter	Air circulation
Air flow	Q=30 m^3/h±6 m^3/h OB airflow: 20 m^3/h Service unit: 7 m^3/h
Temperature	T_{in}=20 °C
Humidity	RH_{out}=10 % to 35 % (RH to be set in this range)
Flow direction in the layers*	Layer 5 from A to C Layer 4 from C to A
Flow rate	<2 m/s (Detector housing)

(*)See figures 3.14 and 3.15.

The hollow support end-wheels of the Staves are used as collectors of the distribution system. To do this, cooled and drained air is supplied to the volume of half of the end-wheel from one side of the Stave, through the 5 mm-diameter nozzles on the fittings (Fig. 3.16) from which air flows into the ITS volume directly to the Stave. The extraction of heated air is carried-out in the opposite end-wheel acting as a manifold for sucking in the heated air and discharging it through a pipe system.

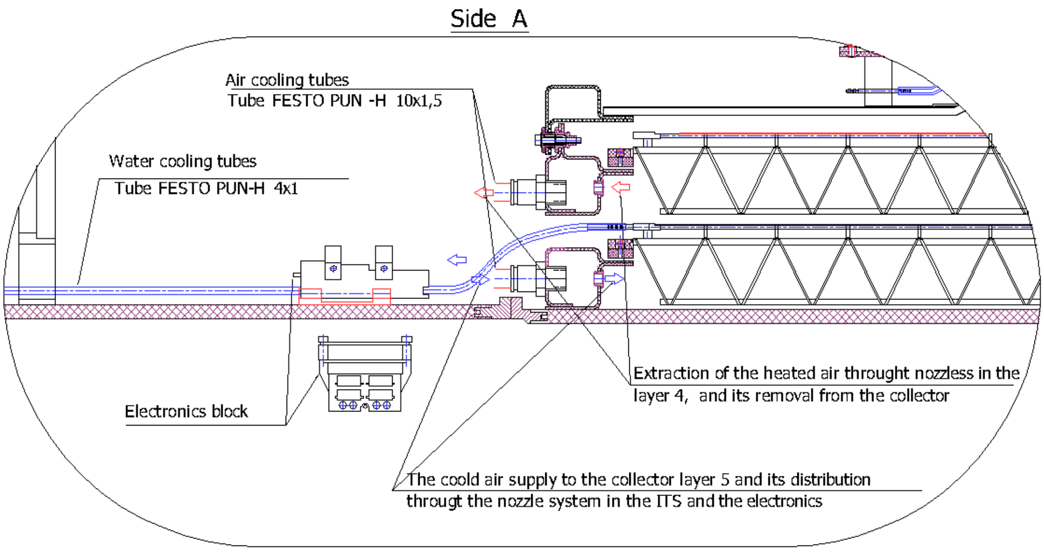

Figure 3.14: Air flow direction in layers 4 and 5 from side A.

The amount of air supplied is regulated by the outlet temperature control system. The estimated air velocity is about 2 m/s. Total air flow in the body volume Q=30 m^3/ hour.

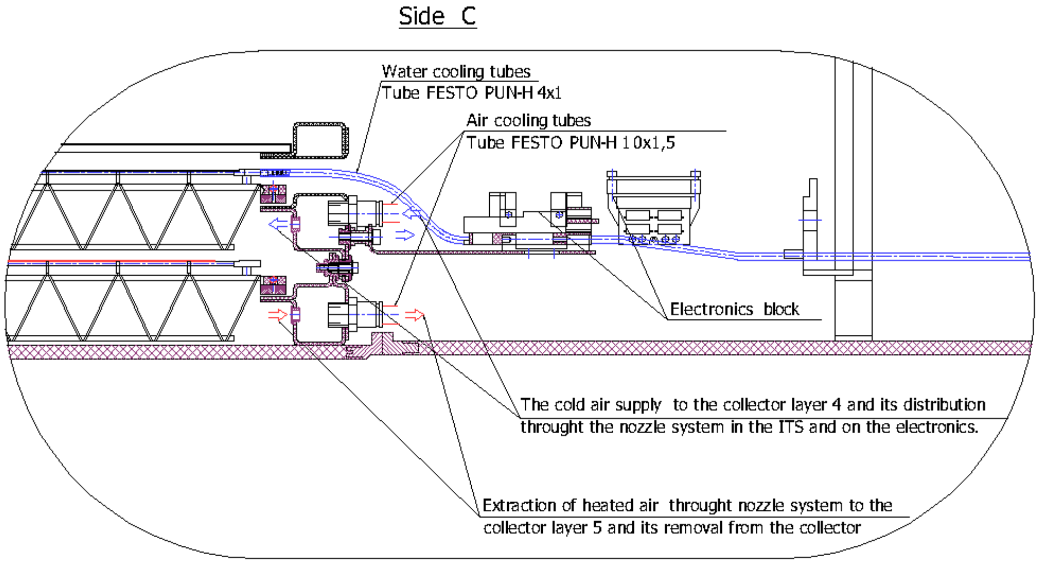

Figure 3.15: Air flow direction in layers 4 and 5 from side C.

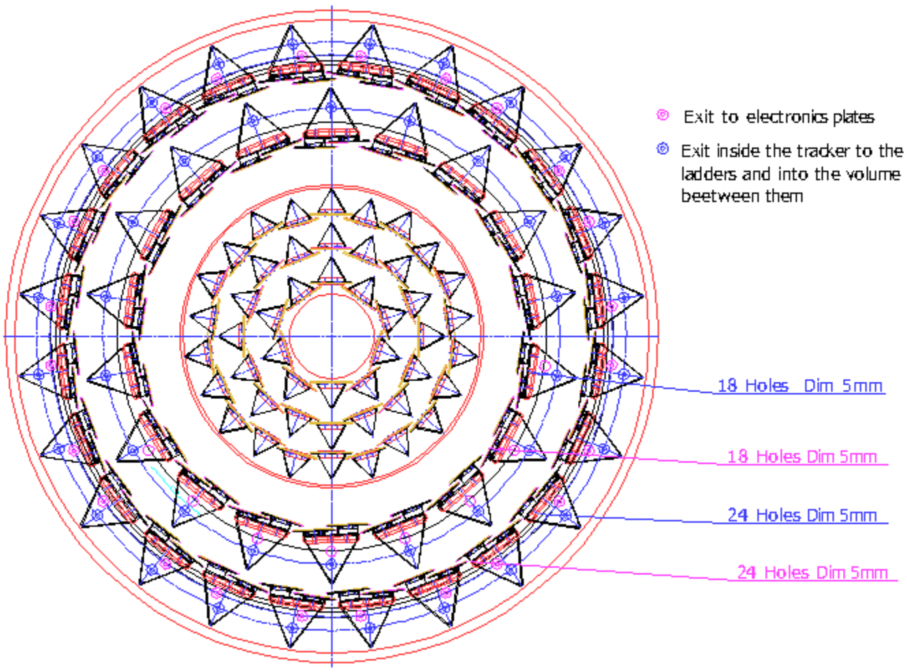

Figure 3.16: Location of nozzles on manifolds Side A.

853 ### 3.2.4 Outer barrel FPC

854 The FPC of the OB Module interconnects 14 Pixel Chips arranged in two rows. Each row of
855 seven chips is treated as an independent array in terms of power distribution and is driven
856 by a master chip located at the end for the bi-directional data exchange.

857 These chips will be connected to the FPC in order to provide:

- The connection to power and ground;
- The connection to the external control and readout electronics;
- The connection between master and slave chips within the OB-Module;
- The connection to other chip structures (substrate and p-well).

All the lines consist of 100 µm wide strips; the distance between strips of the differential pairs is 200 µm (pitch). The nominal differential impedance of the differential lines is 10 Ω.

Finally the flexible circuit includes a line for biasing the substrate and p-well of the chips. Digital and analog power planes are hosted on the top layer, while the ground planes are accommodated on the bottom layer of the FPC circuit.

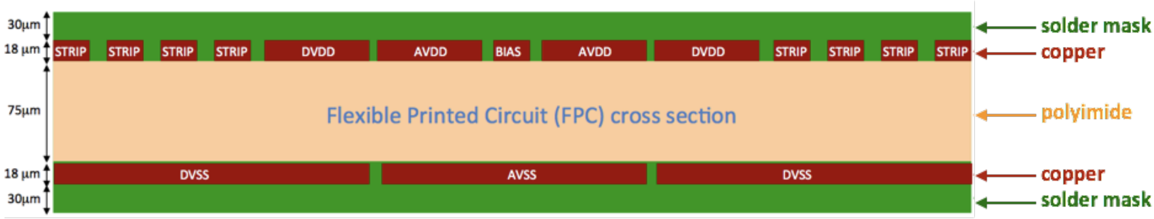

Figure 3.17: Schematic view of a cross section of the central part of the FPC circuit.

All master chips on one Half-Stave long row, i.e. four or seven depending on the Layer, receive the clock and configuration signals from the end of the Stave on a common differential pair and, after regeneration inside the chips themselves, distribute them to the remaining six chips in a Module row. The seven chips of a Module row are connected in daisy-chain mode, which refers to the respective master chip. The master chips send data on two independent differential pairs to the first chip of the adjacent Module and to the first chip of the following Module, thus allowing skipping a Module in case of failure. The serialized data of a Half-Stave-long row are transmitted to a readout link located at the end of Stave by the outermost master chip; each Half-Stave is served by two readout links. The proposed scheme, which provides a reasonable level of redundancy against single chip failures or of an entire Module, has been implemented in the FPC layout shown in Fig. 3.17. An image of an FPC mock-up is shown in Figure 3.18.

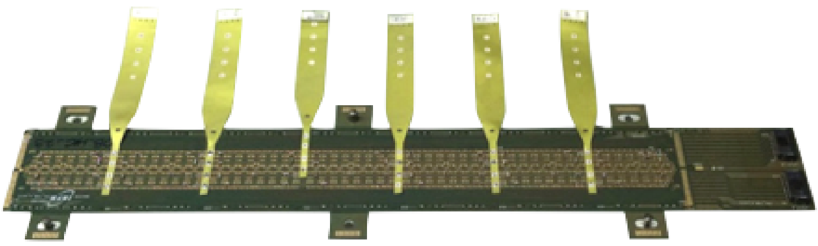

Figure 3.18: Flexible Printed Circuit mock-up. It includes the cross cables for power supply.

3.2.5 Pixel Chip to FPC connection

The electrical interconnection between the chips and the FPC is based on the standard wire bonding through the FPC vias (Fig. 3.26) [10](Ref. from Chapter 2). In order to account

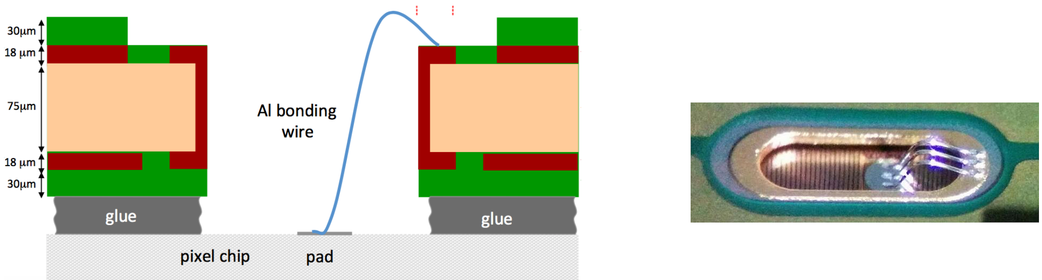

Figure 3.19: Cross section (left) and picture (right) of a FPC via with three bonding wires connected to the underlying chip pad.

for the clearance necessary for the wedge-bonding tool, the FPC vias have oblong shape (1.2 mm × 0.4 mm); in addition, 300 µm interconnection pads are implemented on the top surface. Finally the wire bonding is performed using 25 µm aluminum wire (three wires per connection); a typical force of 11 g with a σ of 0.8 g is measured per wire.

3.2.6 Assembly procedures

3.2.6.1 Outer barrel HIC assembly

The outer barrel Hybrid Integrated Circuit (HIC) consists of an assembly of 14 Pixel Chips arranged in two rows interconnected to an FPC. A custom made automatic Module Assembly Machine (MAM[1]) implementing dimension measurement, integrity inspection and alignment for assembly is used to achieve a reproducible accuracy and the required production speed in the various HIC assembly sites (Fig. 3.20). Using a screen-printing technique, very precise spots of Araldite 2011 (0.6 mm diameter) are applied on the FPC clamped on a gripper jig.

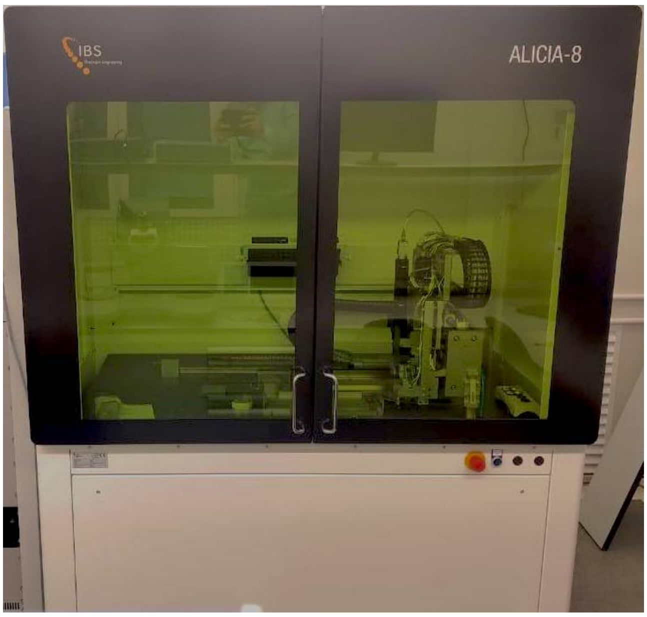

Figure 3.20: Module Assembly Machine at the STS department of LHEP at JINR.

[1] IBS Precision Engineering, http://www.ibspe.com

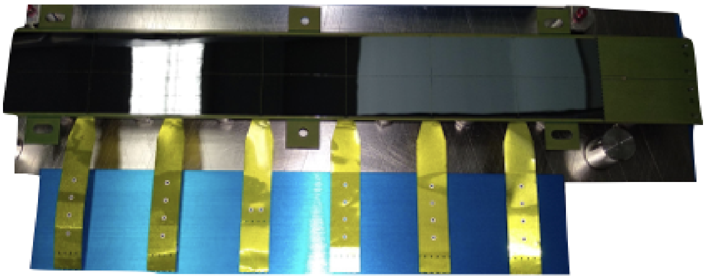

Figure 3.21: Outer Barrel Hybrid Integrated Circuit mock-up. The image shows the 14 chips already glued to the FPC after the alignment.

The stencil is manufactured by laser drilling the holes pattern in an adhesive film (90 µm thick). After chips have been aligned by the MAM onto the assembly table (AT) vacuum chuck with a position accuracy below 5 µm and a spacing of 150 µm, the FPC is overlapped precisely on top using a dedicated jig equipped with 3 mm ruby spheres which are engaged into alignment holes of the AT. Shims of 50 µm are used to compensate gap variations related to tolerances of tooling (planarity: ± 10 µm) and components (FPC thickness: ± 10 µm; chip thickness: 5 µm). The procedure has been validated by mechanical tests where on average a pull strength of 4.5 kg/chip and a peel strength of 300 g have been measured. Figure 3.21 shows a mock-up of an already finished HIC module.

The HIC assembly steps may be summarized as follows:

1. The QR code of a selected chip tray (holding up to 23 chips) is scanned and after autommatically reading the test data previously recorded on the database, each chip is categorized on-the-fly as "SILVER" or "BRONZE" according to cuts applied to 47 parameters (Dead pixels, Fake Hit Rate, etc). This create a "chip map" that is automatically uploaded to the MAM.

2. The tray is physically loaded into the MAM and the alignment of 14 chips starts.

3. The Araldite glue is mixed on a dedicated mixer and spread on the FPC with the help of a gluing mask.

4. The FPC is placed (glued) on top of the already aligned chips with the help of dedicated jigs with a vacumm-holding system and ruby spheres-based alignment system.

5. After the glue has polimerized, the FPC and the chips are wire-bonded. Afterwards, the new HIC may be electrically tested.

The whole assembly process is tracked and document to the dedicated database by means of a customized HIC assembly interface.

3.2.6.1.1 HIC Test and characterization

During the whole assembly procedure, a detailed test protocol will be set in place to verify the electrical functionality and the mechanical integrity of each individual detector element before it is handed over to the following step.

In addition to the electrical and functional tests which ensure that the chips are operating correctly and are well connected to the FPC a visual and metrological inspection will be carried out. The visual inspection ensures that no mechanical damage has been inflicted during the assembly.

The testing of the assembled HICs is performed by means of an automated test system. Readout and control is performed through a dedicated readout card which connects to the HIC through a connector located on a tab of the flex printed circuit. The test system is capable of powering the HICs by means of a power board which connects through spring-loaded adaptors to the cross-cables of the HIC. The power board allows controlling all voltages and reading back currents and voltages through the test software. The test program is divided into a set of individual scans which are executed sequentially. The final classification of the HIC is determined from:

- The number of working chips: chips that fail an initial basic communication test are excluded from the test program.
- The result of the worst scan: scans are classified in *gold*, *silver*, *bronze* or *Not working*. The classification of a HIC is determined by the worst scan result, e.g. to be classified as *silver* a HIC has to pass all scans either *silver* or *gold*. Note that scans with back bias are not considered for this criterion but for the next (see below).

The total classification of the HIC is determined according to table 3.5.

Table 3.5: HIC classification scheme. Any HIC resulting in a 'CAT B' classification is considered as not detector-grade

Worst Scan Result	Working Chips	Back Bias Working	HIC Classification
Gold	14	Yes	Gold
Silver	14	Yes	Silver
Bronze	14	Yes	Bronze
Gold, Silver or Bronze	13	Yes	Partially working
Gold, Silver or Bronze	<13	Yes	Partially working CAT B

Specifically, the HIC tests to be performed are:

- **Impedance Test:** aimed to identify any shorts that may occur between the voltage supplies of the HIC (DVDD, AVDD & BIAS). Testing time around 1 minute and is performed on each HIC individually.
- **Qualification Test:** it performs a series of scans and applies cuts to different parameters for each scan in order to classify the HIC into one of the defined categories. Testing time is around 1 hour and is performed on 1 HIC at a time.
- **Endurance Test:** it performs a series of power cycle scans on the HIC in order to stress the electronics and classify the HIC accordingly. Testing time ca. 3 days. The testing hardware may hold up to 10 HICs in parallel.

All the tests are performed using custom-developed software (scripts and GUIs) that automatically read and write the data to the dedicated Construction Management Information System (CMIS).

Figures 3.22 to 3.24 show the custom hardware for each test, courtesy of the ALICE-ITS collaboration. For this purpose the HIC carrier plates and the test equipment have been designed in such a way that the HICs are tested while inside their own carrier plates. These same equipment (hardware and software) will be also acquired for the MPD-ITS project.

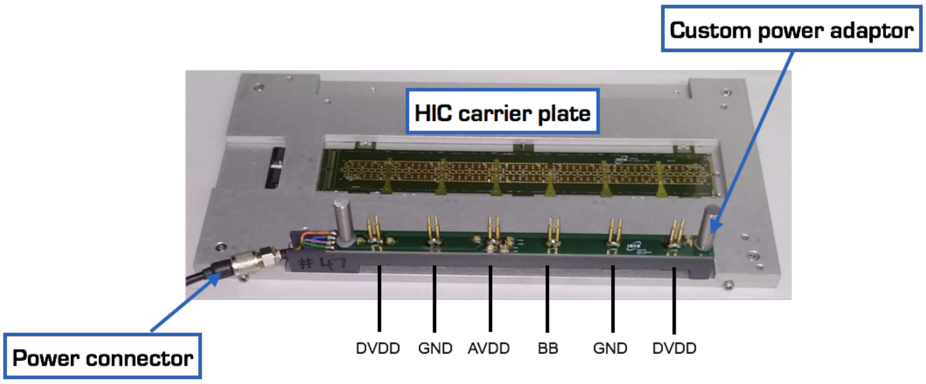

Figure 3.22: Impedance test setup.

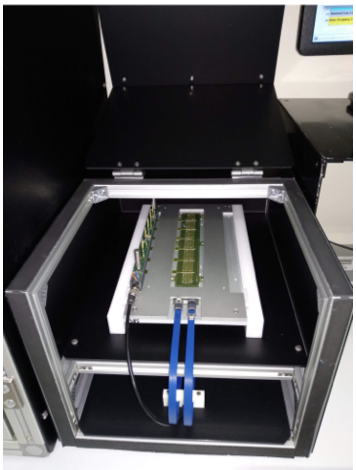

Figure 3.23: Qualification test box holding one HIC inside its carrier plate.

Figure 3.24: Endurance test box holding 10 HICs inside their carrier plates.

3.2.6.2 Outer Barrel Stave assembly

The assembly of the Outer Barrel Staves will be done following the technological and know-how transfer from ALICE-ITS2, including the optimized assembly procedures described in detailed in the *Outer Layer Stave assembly operational manual* compiled by the ALICE-ITS collaboration.

The assembly is performed by means of Coordinate Measuring Machines (CMM) from

Mitutoyo (Fig. 3.25) equipped with custom developed tools and jigs. This allows for the surveying of the assembly steps, with a HIC positioning precision within 10 µm–20 µm. One of such machines has already been bought and delivered to JINR's LHEP. The rest of the customized jigs and tools will be also acquired for the production of the Staves.

(a) (b) (c)

Figure 3.25: Coordinate Measuring Machine general view (a), Camera probe (b) and Touch probe (c).

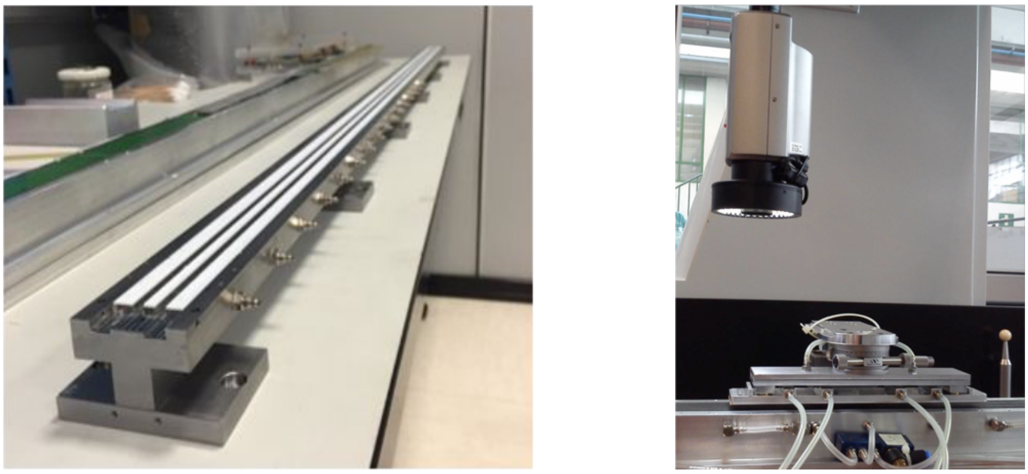

(a) (b)

Figure 3.26: Half-Stave base (a) and Module-alignment station (b).

During the Stave production each Half-Stave (HS) will be assembled and tested separately and afterwards they will be sequentially attached to the Space Frame (SF). Each Half-Stave will be composed by seven HIC modules, which are first aligned on a dedicated jig (Fig. 3.26a), using a customized Module-alignment station (Fig. 3.26b). This jig contains a reference system at the two edges which is based on ruby spheres placed above the plane of the connectors at the ends of the Stave. All elements of the assembly tooling, as for instance the Module support base and the rails for the alignment, are built and mounted referring to this reference system. The same reference system is used to align and position every element of the Half-Stave, and afterwards the Stave itself.

The steps to be followed during the assembly procedure of the Outer Layers Staves may be summarized as follows:

1. Definition of a reference system for a correct positioning of the Modules on the Cold Plate (CP) and aligning of the HS under the SF.
2. Verification of the CP planarity.
3. Electrical tests of the Modules before the alignment/gluing procedure to ensure their correct functioning.
4. Glue deposition for gluing the Modules to the CP.
5. Alignment of the Modules with respect to the CP before permanently gluing them to it.
6. Electrical tests of the Modules after the alignment/gluing procedure to ensure their correct functioning.
7. Soldering of the Power Bus and the Back-Bias bus using the cross-cables already soldered on the FPCs. This procedure has to be done on a different working table with dedicated mechanical supports.
8. Testing of the correct functioning of the HS to ensure the correct functioning of the entire system.
9. Alignment of the HS under the SF.
10. Gluing of the HS on the SF.

Figures 3.27 to 3.31 show the Stave assembly at different stages, courtesy of the ALICE-ITS collaboration.

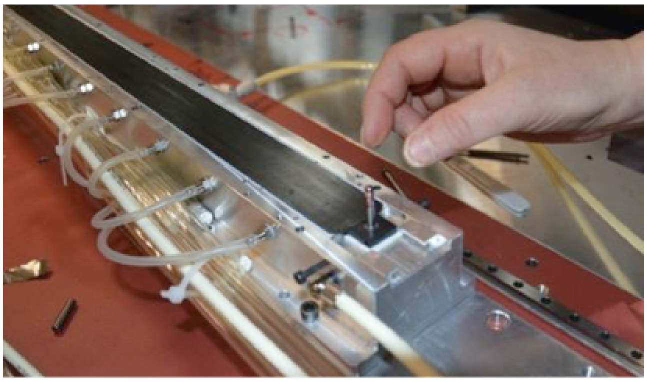

Figure 3.27: Cold Plate positioning.

3.2.6.2.1 Stave Test and characterization

Similar to the one for the HICs, a well defined protocol for the Staves test and characterization will be followed in order to ensure the quality of detector-grade Staves which also allows to sort them on the Layers according to their performance. Ultimately, this protocol aims to minimize as much as possible the necessity of a future intervention for the replacement of a Layer component, which is both a delicate and time consuming tasks that involve other components of the MPD.

Different from the HIC testing where most of the tests are performed at the end of the assembly, the Stave testing process will be performed after specific assembly steps of each Half-Stave before moving to the next step. It will consist of electrical tests to ensure the correct functioning of either the Stave's individual components or the entire Stave as a whole;

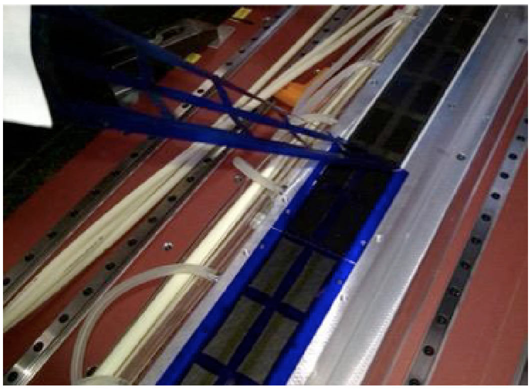

Figure 3.28: Cold Plate glue deposition.

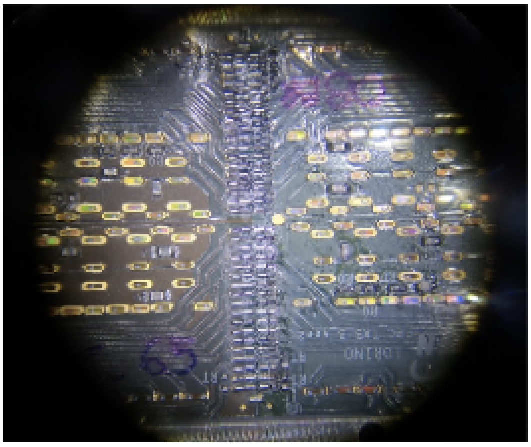

Figure 3.29: HIC to HIC alignment.

Figure 3.30: Space Frame gluing to the Cold Plate.

but also on metrology measurements to guarantee that the geometrical dimensions and the flatness of the HIC and of the Staves are in agreement with the requirements for mounting on the Space Frame.

The test protocol will include:

- **HIC reception test:** To confirm a HIC is detector-grade just before start its assembly on a Half-Stave.

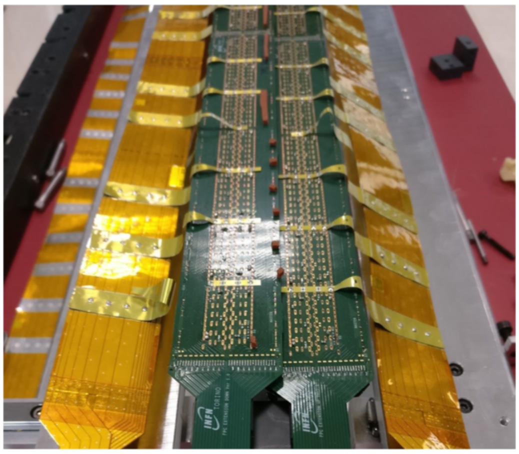

Figure 3.31: Full Stave with the two Half-Staves and the Power Buses.

- **OB-HIC (fast) power test:** Fast power test after tab cut.
- **HS test:** For the classification/characterization of the Half-Stave.
- **Stave assembly – Final metrology:** Stave metrology with CMM.
- **HS test with PB not folded:** For testing each Half-Stave just before folding the PB, which geometrically closes the Stave.
- **HS test with PB folded:** For testing the correct functioning of each HS once the Power Buses have been folded.
- **Stave reception:** For testing incoming Staves before assembly them on a Layer.

3.2.7 The necessity for CMIS

The ITS may be arguably considered the most ambitious and technologically complex of all sub-detectors composing the MPD. The construction of its 2-layers Outer Barrel will benefit from a novel technology developed by the ALICE experiment at CERN for the upgrade of its own Inner Tracking System (ITS2) based on concentric cylindrical layers of 100 µm-thick Monolithic Active Pixel Sensors produced with the 180 nm technology from TowerJazz. It will consists of 42 Staves holding 588 HICs for a total of 8232 MAPS chips (∼4.3 GigaPixels) aligned with a precision <5 µm, plus spares.

The detector will be built as a joint effort of various institutions from Russia and China with the production split among JINR and at least 3 other production sites in China. This includes the shipping of detector components between the production sites, from individual chips to fully functional Staves and the precise testing and characterization of each part at different assembly stages, aiming for a detector-grade yield of 75 % for the Stave production and 85 % for the HIC production.

It is then mandatory to have in place a system that will allow for a fine-grained control and continuous feedback of the whole detector production process. For this purpose a Construction Management Information System (CMIS) will be setup which is an adaptation of the same system used for the production of the ALICE-ITS2.

CMIS is an Oracle-based all-around project management database system, that allows the organization and follow-up of every aspect of the project. This includes (but is not limited to) the human resources, the project organization and planning, as well as the current status and test results history of every component of the detector allowing for the direct interfacing of the assembly and testing hardware/software to the construction database, so that information ranging from the current location of a component in-transit to/from an assembly site down to the final position of a single chip inside the detector along with the threshold and noise values of each of its 512×1024 pixels will be available on the database.

The system is produced and maintained by KYBERNETIKA s.r.o from Košice, Slovak Republic and it is composed by a web-based user interface so that clients may access the application server by means of standard web browsers (Fig. 3.32). It also includes an API functions collection used for the automatic interfacing of the database with the production and testing hardware. This system, which is actually a highly-modular framework that may accommodate several projects in parallel, will be hosted at JINR's LIT and it might be accessed either from inside JINR or from anywhere around the world as it is schematically represented in Figure 3.33 for the context of the MPD-ITS project.

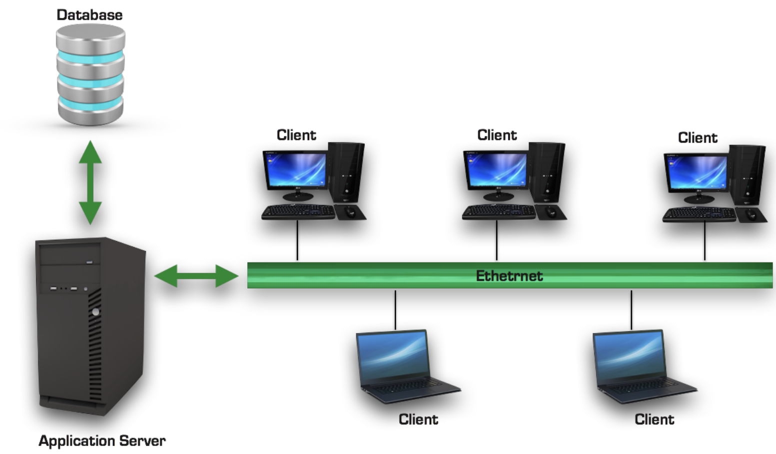

Figure 3.32: Web-based access to CMIS.

3.3 The MPD-ITS finalization after NICA LS1 (Stage-2: the Inner Barrel)

At the Stage-2 the innermost layers of the ITS for the MPD installation at NICA will be constructed using the most advanced developments that are being performed nowadays by ALICE Collaboration for the future ITS-3 [1], [2]. The Letter of Intent for an ALICE ITS Upgrade in LS3 (LoI) is available [7]. The aim is to build a nearly massless Inner Barrel detector consisting of truly cylindrical layers based on curved wafer-scale ultra-thin silicon sensors with MAPS technology. The new developments for the ITS3 for ALICE are based, in particular, on the 65 nm TowerJazz technology for very thin ∼20 µm bent large area sensors. The pixel size of the order of ∼10 µm will be used. The dramatically reduced material budget, the optimized geometry of close proximity to the interaction point and high intrinsic resolution will provide for ALICE at the LHC a significant advancement in the measurement of short-lived particles and low-mass di-electrons which are amongst the main physics goals of ALICE [3].

The conceptual design is shown in Figure 3.34 [7].

An intensive R&D is needed on the Stitching manufacturing of large area 65 nm-Chip

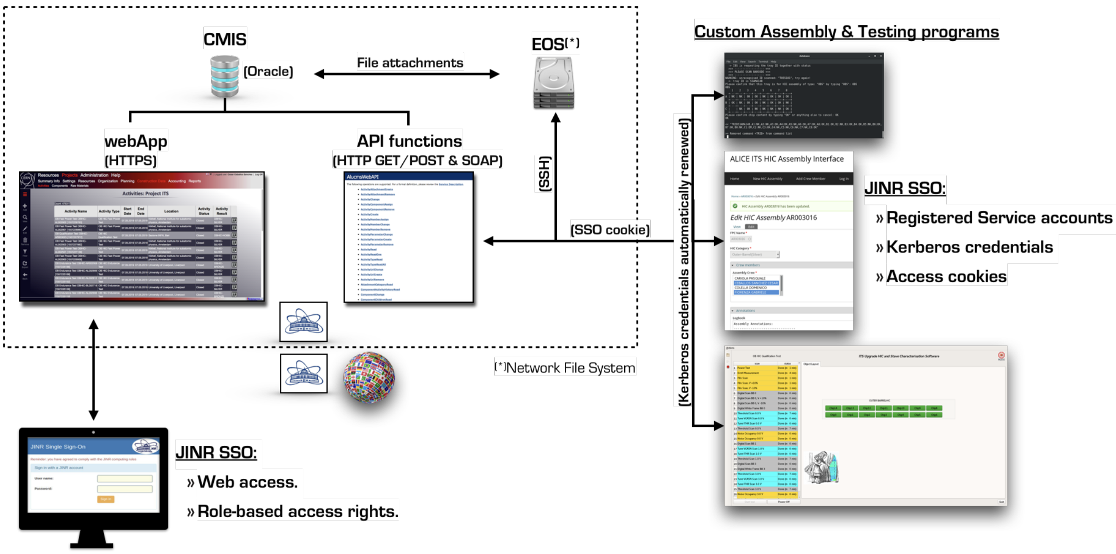

Figure 3.33: CMIS general composition and differentiated users/software access schema in the context of MPD-ITS project.

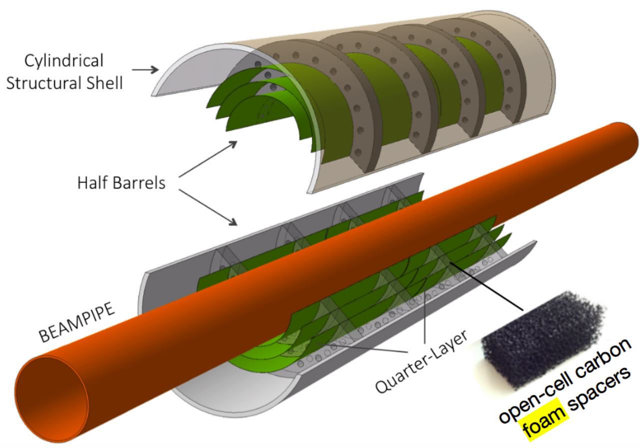

Figure 3.34: Layout of ALICE ITS3 based on thin large area bent sensors.

and on the new MPD beam pipe with a small wall thickness (∼500 µm) and small diameter (below 40 mm). This will allow to place the innermost MAPS layer as close as ∼20 mm away from the nominal beam position, while also reducing the material budget associated with the beam pipe itself. The MPD-ITS may also benefit from the dedicated R&D currently carried out by the ALICE collaboration on the new and extremely lightweight carbon fiber support structures for the thin (∼20 µm) large area bent sensors (up to 280 mm length) [3]. The development of novel efficient gaseous cooling system of thin large area sensors is also required in order to drain the heat from these novel sensors of 20 mW/cm^2 (140 mW/cm^2 from the sensor's digital periphery).

The expected pointing resolution of the new ALICE ITS3 based on these new sensors is shown in Figure 3.35, [7].

A similar performance may be expected for the MPD with a small (40 mm) beam-pipe diameter, considering that its ultra lightweight Inner Barrel Vertex Detector will also consist of thin (∼20 µm) bent large area sensors, arranged in perfectly cylindrical layers, featuring an unprecedented low material budget of $X/X_0 \sim 0.05\%$ per layer. Although in the case of

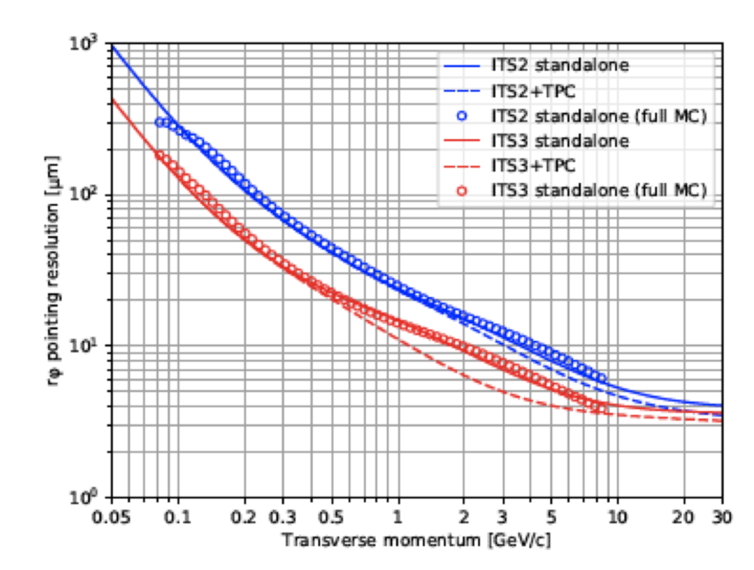

Figure 3.35: Projected pointing resolution of the ITS3 with the bent thin large area sensors (see text). The Figure is from [7].

the Inner Barrel of the MPD, the final choice of the radii for the IB Layers will be done after the final value of the beam-pipe diameter would be decided.

In the context of the MPD-ITS, design and development of the extra-lightweight, state-of-the-art support structures capable to ensure the high level of thermo- and mechanical-stability of these large arrays of ultra-thin silicon sensors are among the challenges to be met. In particular, the length of the MPD Inner Barrel (750 mm) is supposed to be more than twice larger than the one for ALICE-ITS3 (280 mm) (Fig. 3.34). Therefore, a new conceptual design for the MPD Inner Barrel layout is considered. The new IB extra-lightweight support structures (ultra-light-weight CF space frames) will be developed with the account of mechanical properties of the novel arrays of bent ultra-thin silicon sensors. Another challenge is the efficient, very low speed, gas cooling system that will provide the required functionality in terms of lack of vibrations of these thin large area sensors.

The implementation of the advanced thin 65 nm CMOS detectors and of the updated carbon fibre composite technologies to the MPD-ITS Inner Barrel will expand considerably the heavy-flavour research physics programs of the MPD experiment at NICA, JINR, as it is presented in Chapter 7.

3.3.1 Possible variants for mechanics based on ALICE ITS3 modules developed at CERN

The ALICE ITS project has recently begun the commissioning of its upgraded version (ITS2) which includes a new IB consisting of three layers of 30 mm × 15 mm large and 50 µm-thick silicon MAPS chips. However, a project for a further modernization of this Inner Barrel has already started under the name of ITS3 with the goal of replacing the current IB with a more performant one by 2024 – 2025. In doing so it is planned to:

- install a new ALICE beam pipe of a smaller internal radius $R_{min} = 16$ mm and beryllium wall thickness of $\Delta R = 0.5$ mm;

- create an Inner Barrel consisting of three cylindrical sensor layers based on ultra-long

(280 mm) and ultra-thin (20 µm) self-bent MAPS sensors made by the stitching method [8];

- ensure a high transparency of the detector with a material budget of $X/X_0 \approx 0.05\,\%$ by taking the readout and data-aggregation electronics out to the module's tip located outside of the particle registration zone;

- reduce the energy consumption of the sensors to a maximum of $20\,\mathrm{mW/cm^2}$ which will allow to drop the use of water cooling by transferring the cooling system completely to gas;

- ensure full mechanical compatibility of the Inner Barrel constructions ITS2 and ITS3 which guarantees the necessary installation accuracy.

The listed features of the new detector are primarily oriented to place the sensors as close as possible to the interaction point and to reduce the amount of material in the path of secondary particles and their decay products. This will significantly increase the detection efficiency of rare reaction products while allowing to extend the measurements to the region of small transverse momentum of the particles.

In the context of the MPD-ITS project, this same basic concept for the construction of its own Inner Barrel may be applied, although the length of the barrel should be doubled with minimum deterioration of the above listed properties for the new detector. A possible structural solution to this problem is conceptually described in the following.

It should be noticed that in parallel to the ALICE-ITS3 project there is an ongoing R&D inside the MPD-ITS project for the developmemt and produciton in China of large-are MAPS. This R&D of MAPS for Inner Barrel is based on a 55 nm stitching CIS technology. It is a large-area, low-material, low-power, high-speed pixel sensor chip that occupies the entire wafer. It integrates charged particle detection, analog signal processing, A/D conversion and digital signal processing on a single-chip. The first MPW had been submitted on June 25, 2021. The wafers will be delivered in June 2022. The die size is 6 mm x 5 mm, including 10 chips: readout architecture verification chip, diode and pixel test chip, PLL, Serilizer, DAC, LDO, ADC, etc. Due to the delayed delivery of the first MPW, an alternative MPW based on a 180 nm process will be submitted in March 2022 to accelerate the design.

3.3.2 Mechanics and cooling system of the Inner Barrel

The mechanical design of the MPD-ITS IB may consist of an external power case of complex shape with an ultra light central part (Fig. 3.36). The right and left conical parts differ only in the shells due to the conditions for the fixation of the power case to the fourth layer of the MPD-ITS (Outer Barrel). Cables, electronics boards and gas cooling distribution system are located in the conical elements. The main characteristics of the design are:

- the length of the structure at the edges of the base sleeves is 1626 mm;

- the length of the central thin part is 600 mm;

- the diameter of the conical part is 267 mm;

- the diameter of the central thin part is 77 mm;

- the total assembly weight is 2 kg.

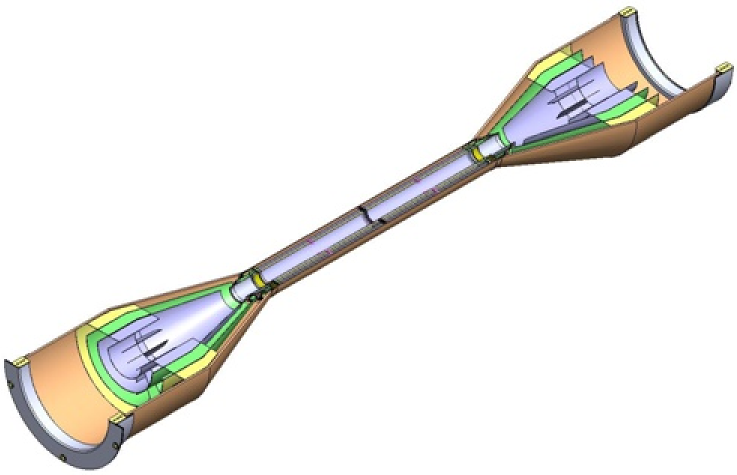

Figure 3.36: General view of the proposed IB.

The central ultra-light part is a semi-cylindrical sandwich made out of a carbon composite where the outer and inner shells are carbon fiber with a thickness of 100 µm and the inner part is AIREX foam with a density of 70 kg/m^3, along the edges of which precision elements of the detectors layers support assemblies are glued.

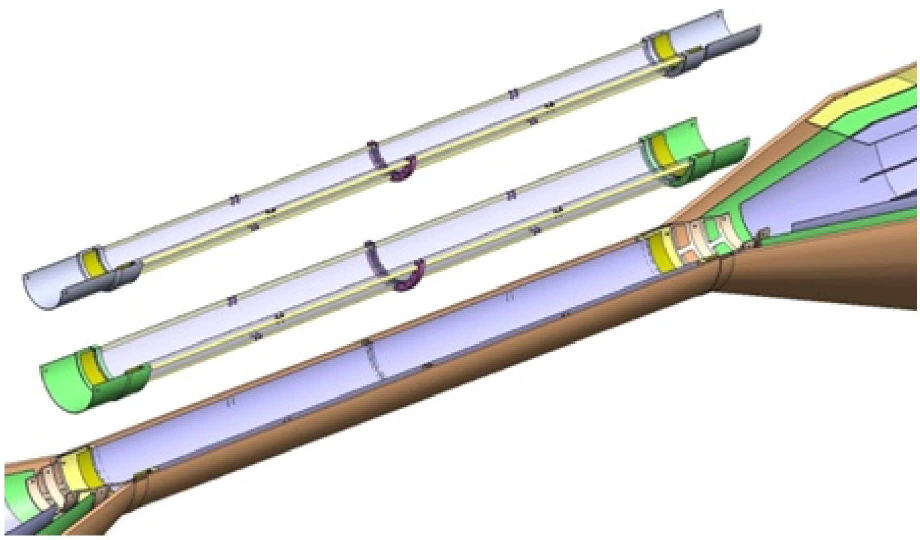

Figure 3.37: Break down of the IB layers to illustrate the IB assembly sequence

In order to optimize the structural elements it will be necessary to carry out R&D related to the rigidity calculations and the determination of the materials to be used for the tracker manufacturing. It is necessary to develop an assembly scenario and auxiliary devices for it which will provide assembly operations and control of the individual sensor layers.

The complexity of developing the design of the detector assembly is to kept the sensor bent along the radius in the same position and its precise fixation. An additional complication is that the detection layer consists of two sensors placed oppositely along the axis of the beam pipe. The linear size of the sensor is determined by the possibility of modern technology for the manufacture of Si wafers with a diameter of more than 300 mm. This allows for the production of sensors with a length of 280 mm. A solution to the problem of building the Inner Barrel is the use of an ultra-light chassis made out of carbon composite materials for each half-layer of the barrel.

One possible design of such a chassis is shown in Figure 3.38. It consists of two supporting half-cylinders (left and right) connected by carbon pipes made by weaving a high-modulus carbon thread. The resulting chassis has three radial bearing surfaces: two at the edges and one in the center. In addition a local supporting element may be put on each tube between the extreme and central supports for holding the bent sensor in the correct position.

It is assumed that the minimum wall thickness of the pipes will be between 0.1 mm and 0.15 mm. The mass of such a pipe 546 mm long with a diameter of 3 mm will be 1.6 g.

Figure 3.38: Possible design of the Inner Barrel chassis

An alternative to this elements could be the use of three-sided space frames manufactured using the well-known technology implemented for building the IB Staves of the ALICE ITS2 project. The design of such a miniature frame is shown in Figure 3.39. If a length of 270 mm is considered, the weight of the frame is only 1 g. For the entire construction it is necessary to use 2 frames which means an estimated 2 g mass of the supporting frames.

3.3.3 Cooling system features of the MPD-ITS Inner Barrel

With the planned heat dissipation of the detectors of the order of 20 mW/cm^2 as well as the placement of the electronics for data readout at the outer edges of the sensors, it is possible to use only an air-based cooling system and completely renounce of using water for cooling the sensors in the particle registration zone. The MPD-ITS project already foresees a cross-cutting gas blowing through the laminar flow of the 4$^{\mathrm{th}}$ and 5$^{\mathrm{th}}$ layers of the tracker so the gas supply for the Inner Barrel will not be very difficult. For this purpose, additional holes can be provided on each of the longitudinal supports of the carbon pipes (see Figure 3.40).

It should be noted that additional R&D is required in order to optimize the design

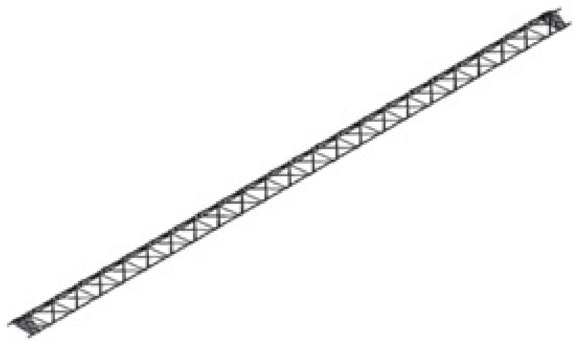

Figure 3.39: Three-sided Space Frame

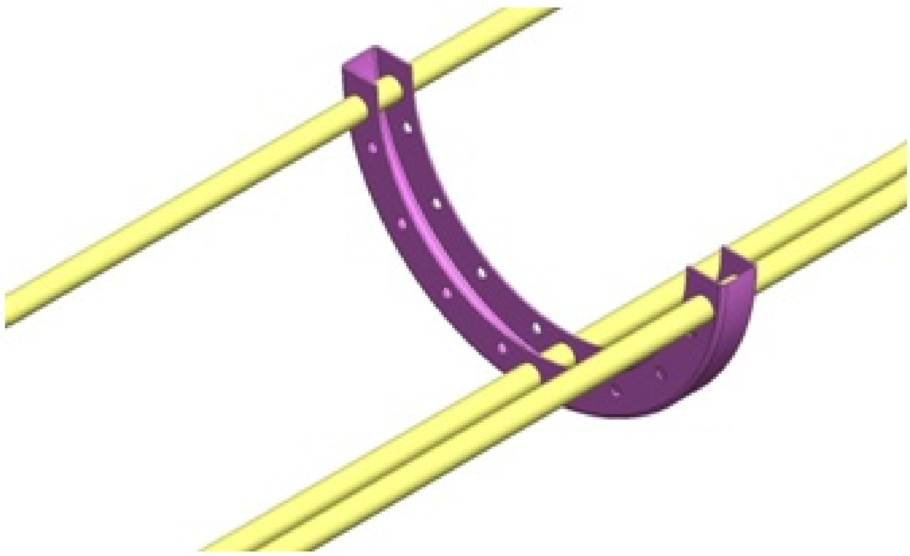

Figure 3.40: Miniature tube carriers adapter with holes for the cooling gas

parameters, especially for its central part. Furthermore, it is assumed that in case of using space frames as connecting structures, only two of them will be used instead of three tubes which will reduce the mass of the substance in the core.

The proposed configuration is feasible for manufacturing and allows to obtain a detachable design suitable for repair and replacement of detector assemblies of any layer. In addition, it could be considered to replace the material of the supporting elements with carbon foam which will further reduce the mass of the material used in the vicinity of the interaction diamond. On other hand, this will require additional research regarding the processing and operation of finished parts from carbon foam due to the possibility of constant formation of carbon dust.

3.3.4 Back-up scenario for Stage-2 of the ITS construction

The MPD-ITS project decided to seize the opportunity of benefit from the future ALICE-ITS IB Staves (ITS3) currently under development, due to its potentialities of enhancing the physics program foreseen with development of NICA by 2025. Anyhow, a back-up solution for the Stage-2 is planned to be provided by the MPD Inner Barrel based on the well proven 180 nm MAPS technology developed by the ALICE collaboration.

In this case the design of the mechanics of the tracker was carried out for two diameter variants of the MPD beam pipe; diameters named *project* (40 mm) and *initial* (64 mm). This accounts for the plans of launching the NICA collider with an "initial" beam pipe diameter of 64 mm which after the adjustment of the machine will be replaced with a "project" beam pipe of a smaller diameter. It is important to note that with all the provided replacements for the beam pipe the mechanical structure of the tracker itself remains universal, and the structure and parameters of the Outer Barrel are unchanged.

The spatial position of the Staves in the layer is determined by the requirement of full coverage of the cylindrical surface. Therefore, taking into account the fact that on the part of the detector plate there is a so-called "dead zone" in which reading and buffering circuits from a position-sensitive matrix are located, the design assumes a certain amount of detectors overlapping in the layer. Specifically for this type of pixel detector the overlapping is 4.3 mm. Figure 3.41 shows the ITS cross section for the Inner and Outer layers. The first three layers of detector Staves IB, intended to ensure overlapping of the dead zones, are installed in a staggered order in height for the *initial* and in the fan-shaped for the *project* version of ITS. The Outer Barrel detectors (OB) have two detector panels installed at different heights.

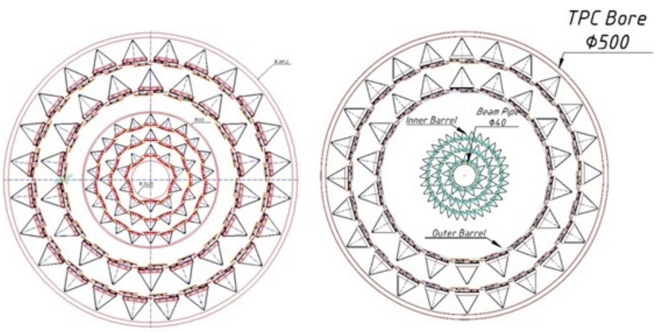

Figure 3.41: Schematic view of the ITS cross section in the *initial* version for beam pipe diameter of 64 mm (left) and in the *project* version for beam pipe with a diameter of 40 mm (right).

Figure 3.42 shows schematic view of the tracker profile in the *project* version. The geometric parameters of the position of detectors are given for the first 3 layers of both versions of the tracker in Table 3.6 (*initial*) and Table 3.7(*project*). In both tables are reported the radius from the center of the beampipe to the middle of the sensor (R_{min}), and to the edge of the sensor (R_{max}). In the case of the *initial* version it can be see from Figure 3.42 (left) that on each Inner Barrel layer half of the sensors are place at a lower level and the other half at a higher level, alternatively. That is why in Table 3.6 for each layer two pairs of R_{min} and R_{max} values are provided, with the layers themselves named as i-1 and i-2 ($1 \leq i \leq 3$) corresponding to the sensors at level 1 or 2 respectively. On all staves ALTAI sensors with an overall size of $15{\times}30\,\mathrm{mm}^2$ are used. The dead zone of the detectors with a width of 2 mm is located on the larger side of the sensor (30 mm) directed along the axis of the beam.

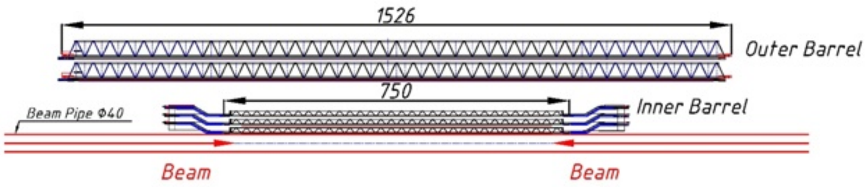

Figure 3.42: Schematic view of the tracker profile in the *project* version

Table 3.6: Geometrical parameters of the Inner Layers for the tracker *initial* variant.

Layer number	**Number of Staves (pcs)**	**R_{min} (mm)**	**R_{max} (mm)**	**Length (mm)**
1-1	5	35.45	38.50	902.9
1-2	5	40.45	43.16	902.9
2-1	8	62.50	64.28	902.0
2-2	8	66.45	68.13	902.9
3-1	11	88.40	89.72	902.9
3-2	11	92.33	93.55	902.9

Table 3.7: Geometrical parameters of all Layers for the tracker *project* variant.

Layer number	**Number of Staves (pcs)**	**R_{min} (mm)**	**R_{max} (mm)**	**Lentgh (mm)**	**Effective thickness** (µm)	η
1	12	22.4	26.7	750	50	±3.3
2	22	40.7	45.9	750	50	±2.8
3	32	59.8	65.1	750	50	±2.45
4$^{(*)}$	18	144.5	147.9	1526	700	±2.3
5	24	194.4	197.6	1526	700	±2.0

$^{(*)}$ In the case of the Outer Barrel (layers 4&5) each Stave is composed by two Half Staves eachone with the same amount of sensors.

Bibliography

[1] D. Adamová et al.,A next-generation LHC heavy-ion experiment, arXiv:1902.01211v2[physics.ins-det], 2 May 2019.

[2] G. Feofilov, I. Altsybeev, E. Andronov, S. Belokurova, A. Erokhin, S. Igolkin, V. Kovalenko, T. Lazareva, N. Maltsev, K. Nametysheva, D. Nesterov, N. Prokofiev, D. Prokhorova, A. Merzlaya, A. Zarochentsev, A. Puchkov, V. Sandul, A. Rahmatullina, A. Seryakov, F. Valiev, V. Vechernin, V.Zherebchevsky, Contribution from the Laboratory of Ultra-High Energy Physics of Saint-Petersburg State University (Russia) for the 2020 update of the European Strategy for Particle Physics, "Heavy-flavour production in relativistic heavy-ion collisions and development of novel generation of extra-low-material-budget Vertex Detectors for future experiments at CERN and JINR", https://indico.cern.ch/event/765096/contributions/3295619/

[3] M. Mager, on behalf of the ALICE collaboration, Upgrade of the ALICE ITS in LS3, PoS (Vertex2019) 040.

[4] G.Trubnikov et al., Status of NICA Project at JINR. Proc. of International Particle Accelerator Conf. (IPAC 2014), Dresden, Germany, 2014, p. 1003-1005.

[5] Technical Project of the NICA Complex. Dubna, 2015.

[6] B. Abelev et. a.l and The ALICE Collaboration, Technical Design Report for the Upgrade of the ALICE Inner Tracking System, J. Phys. G: Nucl. Part. Phys. 41 (2014) 087002

[7] ALICE Collaboration, Letter of Intent for an ALICE ITS Upgrade in LS3, 2019,CERN-LHCC-2019-018, LHCC-I-034

[8] ALICE Collaboration, "ALICE ITS 3: the first truly cylindrical inner tracker", arXiv:2111.09689 [physics.ins-det]

4 Support Structure and System Integration

4.1 Services

4.1.1 Cooling system for the MPD-ITS

4.1.1.1 General description

The main objectives of the cooling system are effective heat removal, as well as a high operating safety level. To reach these functionalities system should be carefully designed and suit these tasks. The fundamental feature of this system will be no leaks (leakless). Part of the system that will be inside the MPD solenoid should be operating below atmospheric pressure. Moreover, the system should be able to detect the leak and safely remove water from the damaged loop signaling the "power-off" command to the DCS. Cooling systems used in a similar experiment, as example ALICE experiment, have the same operating principles. The system that will be used in MPD experiments will inherit the design of the ALICE ITS cooling plants. However, it should be updated to suit standards nowadays. The main field of the upgrade will be electronic and control systems. In the next part of this chapter, there is a description of ALICE's cooling plants.

4.1.1.2 ALICE cooling plant

The ALICE cooling plant has been designed to provide the proper working condition for the ALICE-ITS detector, as well as for all associated systems. The cooling is realized by demineralized water in the temperature range of 18 °C to 23 °C. The temperature is controlled via a PLC (Programmable Logic Controller) PID (Proportional-Integral-Derivative) loop and 3-way electric control valve installed on the primary cooling network side. The inverter, which controls the pump, ensures constant outlet pressure, despite the number of open loops. The system is responsible for cooling the following elements: the inner barrel, outer barrel mid-layer, outer barrel outer layer, and patch panel crates. The cooling system's design allows evacuating 14kW from the ITS detector's electronics and the detector itself.

4.1.1.3 Concept of leakless cooling

The concept of a liquid cooling system follows a leakless cooling scenario suggested [1] and successfully used [2] at CERN. The principle of under-pressure cooling is depicted in Fig. 4.1. The cooling-liquid circuit is a closed circuit, which allows to operate all or part of the cooling lines below atmospheric pressure, especially inside the solenoid. The cooling-liquid tank is kept at under pressure, which by the proper choice of length and diameter of the return pipes and of the circulation-pump output pressure, ensures that the water pressure inside the detector is below atmospheric pressure. This has the obvious advantage of an active protection against the occurrence of leaks. In the MPD inside-magnet detectors case, the space constraints due to the extremely dense front-end readout does not allow space-consuming high-pressure certified fittings. Therefore, simple silicon hoses without any special lock mechanism to couple to the cooling arteries are used. Though the connection

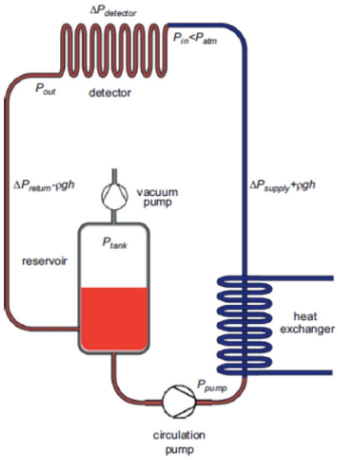

Figure 4.1: Principle of under-pressure operation [2].

between the silicon hoses and the cooling tubes is usually tested to hold overpressure of 2.5 bar over an extended period (24h), they are mechanically fragile, e.g., against tears or cuts. These considerations that led CERN LHC detectors to develop the sub-atmospheric 'leakless' technology for cooling circuits inside the volume of the momentum analysing magnet is more detailed in [3].

An apparent disadvantage of the sub-atmospheric 'leakless' technology is the limited range of operation P $<$ 1 bar. This implies that the allowed pressure ΔP loss, in the detector is rather limited. The situation is further aggravated, in cases of TPC and ECAL, due to a difference in height of about 8 m between the highest inlet and the cooling plant located on the floor of the experimental hall. While the input pressure at each inlet can be adjusted independently via balancing valves, initially this has not been foreseen for the return lines such large-size detectors as TPC and ECAL since all detectors 'see' a combination of the reservoir pressure, the hydrostatic pressure and the pressure loss in the return pipes. This can result in very low pressure values in some of the return lines, which might cause a cavitation phenomena that has to be avoided. Luckily for the ITS, its height spans is only half a meter, which seems to simplify the task for tuning its leakless cooling system (LCS).

4.1.1.4 The MPD ITS objects for cooling and the description of the cooling lines

The MPD ITS objects for cooling are the 42 supermodules called "Staves" each one carrying two cold plates to which the position sensitive modules called HICs are glued onto (Fig. 4.2). These structures will be cooled by means of circulating demineralized water. The cooling lines of 6 staves (12 cold plates) are grouped into a single "loop" with the help of manifolds located in the Service Barrel of the ITS. The total number of cooling loops the ITS OB is 7 as shown on Fig. 4.3.

The relevant information about the he material and diameter of the liquid cooling inlet and outlet arteries used by ALICE ITS2 in the region of detector and outside is provided on figures 4.4 and 4.5. Figure 4.6 shows the working principle of the control sensors of a loop while Appendix .1 provides the exact schematics of the most recent cooling plant built by the Engineering Department of CERN for the ALICE ITS2 project (Courtesy of the ALICE Collaboration).

Figure 4.2: One of 42 OB MPD ITS staves cooling sections.

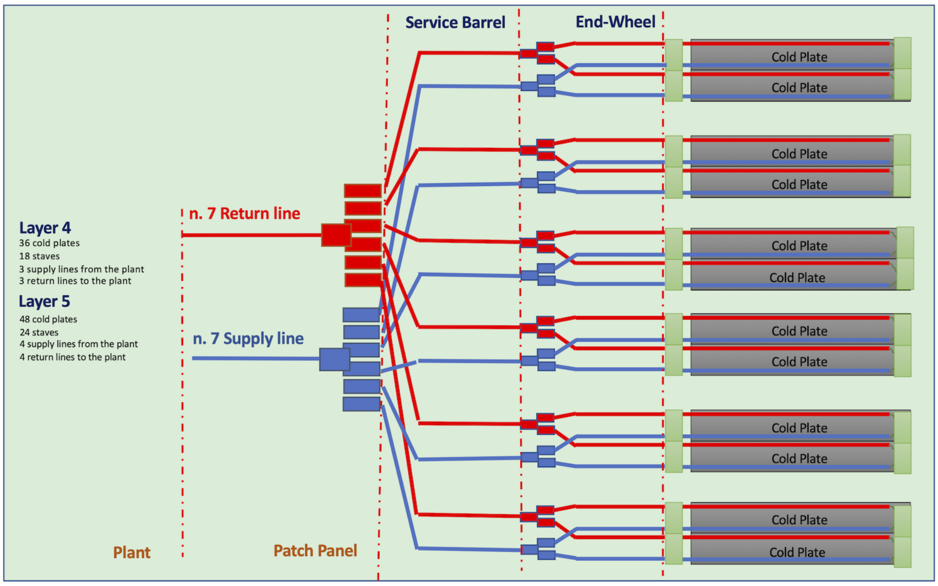

Figure 4.3: Cooling loops of the MPD ITS OB (Courtesy of the ALICE Collaboration).

4.1.1.4.1 Leakless operation

To maintain the leakless operation, the vacuum pump keeps the reservoir pressure below the atmospheric pressure. The pressure drop is minimized inside the detector and return lines, contributing to maintaining the reservoir pressure level below atmospheric. In case of any leak, the air infiltrates into the plant and accumulates on top of the reservoir. The build-up pressure is measured, then PLC decides whether to stop the cooling or continue the operation. The operation can continue if the leakage is below the threshold value. All of those operations prevent the water from leaking. The leak may also occur in part in between the pump and the detector inlet. This section is above the atmospheric pressure. In such a case, the reservoir's level transmitter detects the loss and stops the circulator pump. Stoppage of the circulator pump prevents the leakage of water by bringing the installation to a sub-atmospheric pressure. Another possibility is shutting the loop where the leak occurs. The system is designed in such a way that this operation can be done remotely.

4.1.1.4.2 Operational modes

The system and its components can operate in different modes, which are listed below.

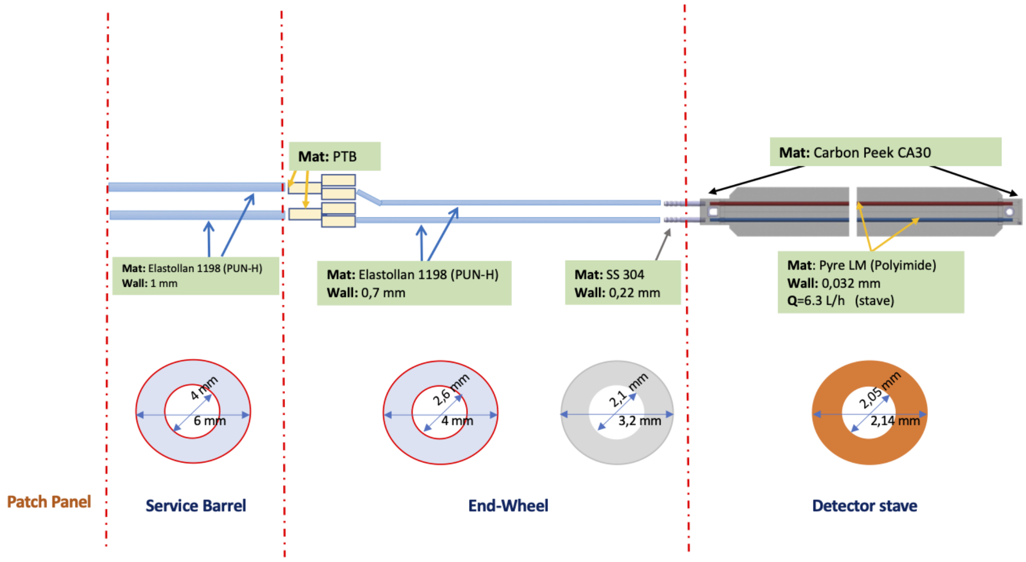

Figure 4.4: Specification of cooling arteries inside the Service Barrel (Courtesy of the ALICE Collaboration).

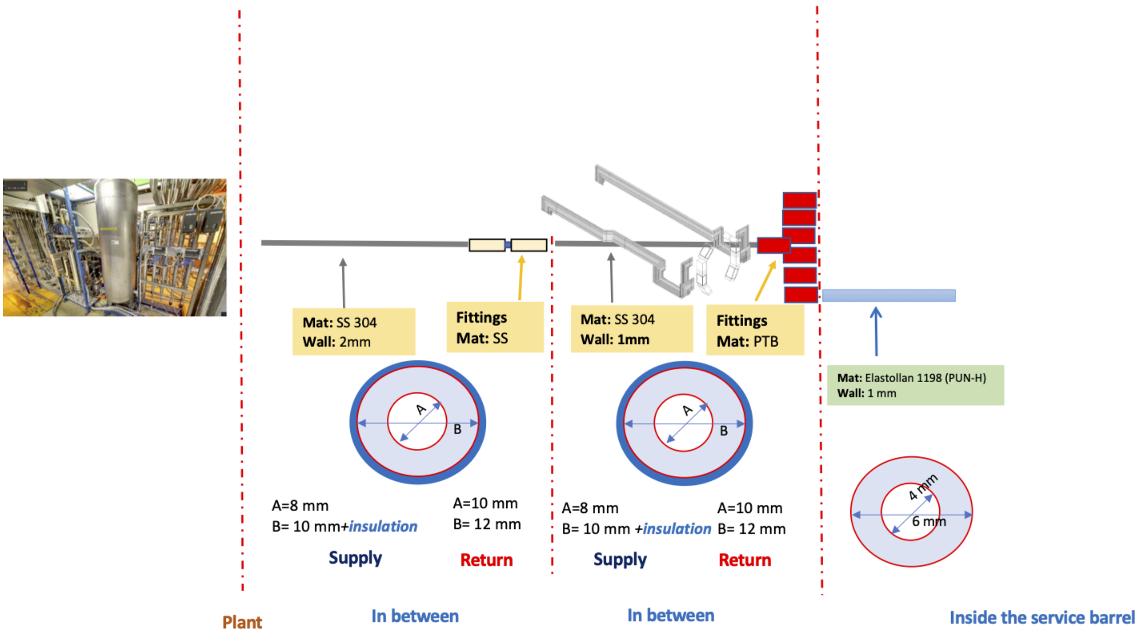

Figure 4.5: Specification of cooling arteries outside the Service Barrel (Courtesy of the ALICE Collaboration).

1. Mode request

- **Stop mode** – each component is without power, in a safe fail mode, no regulations, nothing is running.
- **Stand-by** – circulation is off, tank pressure is controlled, its level state is monitored. In this mode, the whole system (plant + piping + detector) is below atmospheric pressure. To be used for short cooling interruption or looking for leaks.

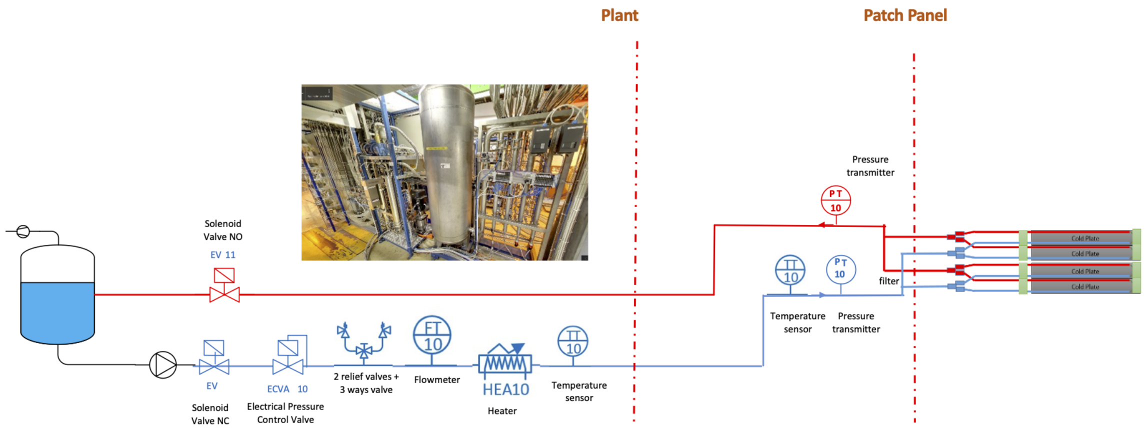

Figure 4.6: Working principle of the control sensors of a loop (Courtesy of the ALICE Collaboration).

- **Run** – Water circulation with pressure and temperature control. It is possible to control the temperature and pressure of the cooling plant. In this mode, only the return pipes and part of the detector is in negative pressure. Any water leakage should happen only in this mode.

2. Loop Control
Each loop is controlled independently. The three predefined states of the loops are:

- **Off** – the loop is closed, the injection valve is closed, and the return valves are open. The circuit is connected to the tank pressure and keeps the leakless protection. Pressure and temperature regulation are off.
- **On** – the loop is open, injection and return valve are open. The water circulates. Pressure regulation is on. PID loop responsible for the pressure and regulating the pneumatic is on.
- **Locked** – the loop is closed, injection and return valve are closed. The circuit is not connected to the tank pressure. Pressure and temperature regulation are off. This mode is used to isolate the leaking loop. In this mode, there is the risk of overpressure and liquid leakage. The safety valve acts as the last overpressure protection

3. Temperature regulation
Each manifold has a heater and a temperature sensor. In normal mode, PLC regulates the temperature in the range of 18 °C to 23 °C. The cooling plant's temperature is 0.5 °C below the lowest temperature setting out of the cooling manifolds
4. Pressure regulation
Each manifold, has a pneumatic regulation valve and the pressure sensor. In normal mode, PLC regulates the pressure to the user setpoint in the range of 0.5 bar and 1.5 bar. The cooling plant operates on one fixed pressure regulated via a PID loop that acts on the pump speed.
5. Tank Pressure regulation
The water tank has a pressure sensor and a vacuum pump. In standby and run operation, the PLC regulates pressure to a specific value. Usually, the value is between 0.6 to 0.96 bar. In case of any failure, the safety valve limits the pressure up to 1.5 bar.

4.1.1.4.3 Alarms

The PLC controls all measured values. Therefore, it is responsible for sending alarm signals further that trigger an interlock or an alarm. Interlocks and alarms are divided into three types:

- **Minor** – particular value is not in the normal range. There is no risk for the equipment nor humans. The system does not need to be interrupted. However, it requires investigation.
- **Potentially dangerous for the material** – a particular value is not in the normal range. There is a risk for the installation, but not for the humans. The plant has to be switched to "standby" mode, and all loops have to be turned off.
- **Potentially dangerous for humans** - a particular value is not in the normal range. There is a risk for the humans in the nearest vicinity of the installation. The plant has to be switched to "stop" mode, and all loops have to be turned off.

4.2 The beam pipe

One of the most critical elements of the NICA MPD project is the nine meters long thin-wall UHV-compatible beam pipe. Figure 4.7 shows a preliminary sketch drawing of it. The manufacturing of the beam pipe is a very complex and risky task for the MPD, which could turn out to be a stopper of the whole project since RF industry had never produced similar objects before.

The LHC experiments gained enough experience in the design and production of similar unique pipes, with rare ends made out of Aluminum while the central part is made out of Beryllium. The typical minimum wall thickness reached so far is 800 um for both, Beryllium and Aluminum parts.

So far, USA-based company “Materion” is the only one able to produce such a unique component. Unfortunately, under the policy of the sanctions impossed to Russia, NICA is not allowed to make a contract with “Materion” and is currently developing the technology for producing the beam pipe somewhere else. Russian industry is capable of producing the Beryllium part of the beam pipe but meets technological challenges for the production of the Aluminum parts with the required thickness and, especially, for assembling all parts together UHV-tight. German industry is heavily involved in the EXFEL project at DESY and has already built thin wall aluminum beam pipes of relatively small dimensions. We are proposing our German partners to further developing this technology jointly and to build the beam pipe for the MPD in Germany. To that end, a specific item is included in the list of the GSI-NICA in-kind cooperation plan.

4.3 Installation and removal

A description of the mechanics and service environment for ITS detectors is given in this section along with the installation and removal procedure of the entire ITS structure. A general overview is shown in Figure 4.8. The mechanical structures supporting the Staves, the water and air-cooling systems, the cable duct systems, the cooling system pipes and vacuum pipe support systems are highly integrated and they will be considered sequentially. To facilitate the construction and utilization of its structure, the ITS has a connector on the horizontal plane.

4.3.1 Basic system requirements

The placement of mechanical elements of the ITS structure observes the following criteria:

- minimization of materials bulk in the measurement zone;
- guaranteeing high accuracy and log-term stability for the detector positioning;
- providing high accuracy on the detector positioning relative to both, the TPC and beam pipe;
- placement of the ITS inner-most layer at a minimum distance from the wall of the beam pipe;
- guaranteeing its thermomechanical stability during its entire lifetime;
- simplicity and accessibility to control the ITS elements;
- ease of assembly and disassembly of the detector layers and detector Staves.

The main body of each half of the ITS is composed by two cylinder-shaped carbon shells (external and internal) with 1.2 mm and 5 mm of Rocacell foam in between and aluminum-alloy flanges glued at the edges.

To support the detector Staves, hollow clamps are fixed to the edges of the body and flat supports equipped with ruby balls are glued in pairs with high accuracy to the wings of the clamps. Such a design allows the installation of detector arrays with high accuracy and also guarantees a stable position for disassemble or replacement of the arrays (Fig. 4.9).

To ensure a high accuracy on the aggregation and positioning of the Staves, their supports have a round hole at one end (for positioning in two directions) and an elongated one at the other end, allowing some movement in the axial direction. Staves from layer 4 are assembled on clamps of similar design with ruby supports, but they do not have a rigid body and are assembled on a special assembly stand. The rigidity of the structure is ensured by the assembly itself.

Layers No. 1, 2 and 3 are assembled in a similar way. The Staves of layer No. 3 are installed in a casing, and the Staves of layers 2 and 1 are assembled according to a frameless scheme. The detector layers are connected to each other by means of precision clamps. The complete ITS enclosure assembly also includes left and right service enclosures and connector

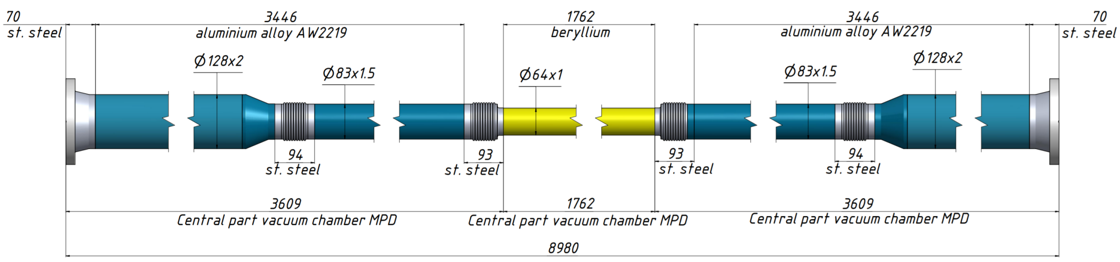

Figure 4.7: A tentative design of the MPD beam pipe. There is no indication of the vacuum equipment at the rare ends of the beam pipe. According to the integration scenario the beam pipe is baked at the vacuum stand and filled-in with dry Neon and only then is shipped to the assembly stand c/o the MPD ITS team.

block housings. The total assembly length is 4220 mm. A general view of this element is shown in Figure 4.10.

The service housings contain pipe supports, FFD detector supports, cable fasteners, pipes for water- and air-cooling systems and electronics unit supports. All supporting elements have windows on the periphery for fixing cables and pipes from the cooling systems. The blocks of connectors are used to accommodate power connectors, connectors signal circuits, as well as pipes of water and air-cooling systems. The cables of the FFD detector block are output through the central hole of the connector block.

4.3.2 Assembly operations sequence

ITS assembly is performed in a clean room according to the following sequence:

- the housing units of the lower and upper cases are assembled;
- in service buildings, elements for fixing electronics blocks are attached to the walls;
- air- and water-cooling pipes are attached and fastened;
- power-supply cables and signal cables are placed with the connectors attached in the housing of the connector block;
- the Staves of layer No. 5 are installed and connected to the corresponding cables and pipes of the cooling systems;
- a block Staves of layer 4 is assembled on a separate assembly stand. Layer 4 is installed in the assembly housing and cables and pipes routing is performed;
- assembly of layers 1, 2 and 3 is performed as a separate block and then installed to the block as well;
- FFD lower detector blocks are mounted in the lower case block;
- the beam pipe is installed;
- FFD upper detector blocks are installed;
- half-cases are assembled together using guide pins and rigidly fastened with screws on the planes of the clamps and the planes of the connector block.

To install the ITS beam pipe setup, additional technological housings are attached to the connector blocks of the detector assembly. Technological housings are equipped with additional support elements for holding the beam pipe. A general view of such an assembly is shown in Figure 4.11

When fully assembled, the setup is a round container that allows to install the ITS into the NICA facility by means of rail guides with trolleys. With this configuration, no support for the beam pipe is required. A schematic diagram of the installation process is shown in Figure 4.12.

After fixing the container in the required position, the housing supports are set on the right and left, rigidly fixing the position of the detector assembly to the TPC frame on one side, and by a sliding fit on the other side. After fixing, the container is sequentially disassembled, so:

- top technological housings are removed;
- the pipe is hung out and fixed on previously prepared supports;

- the lower technological housings are removed;
- rail guides are dismantled;
- the beam pipe is connected to the vacuum system.

4.3.3 MPD Inner Tracking System installation procedure

Due to the limited space available, the mounting of the Inner Tracking System in the working position inside the TPC at the MPD is a challenging task. The clam-shell design of the ITS for the MPD, similar to that of ALICE ITS, simplifies the general assembly of two half-cylinder modules of the ITS around the beam-pipe. However, the task is more complicated further by the demand to keep the central positioning of this low diameter, thin wall thickness, very long and rather fragile central section of the MPD beam-pipe. Besides, the existing space inside the TPC does not allow to use rails for the ITS sliding in/out.

Therefore, a different approach is proposed here. The MPD installation scenario, presented below for the ITS, ensures the robust mounting and dismounting of specific, rather complex, central barrel composed of the Inner Tracking System, the beam-pipe central section of 1.7 m in length, the Fast Forward Detector (FFD) and services including power and data cables, cooling and air-ducts.

The approach is based on the modular design of the so-called insertion container. It is designed to meet the requirements of

(i) assembly of the detectors (ITS and FFD),

(ii) services inside the insertion container,

(iii) fixation of the beam-pipe central section, and

(iv) positioning all systems inside the TPC.

All modules of the insertion container are designed in a clam-shell shape, a general view of one of the MPD-ITS service barrels in a clam-shell design is shown in the Figure 4.13. The insertion container is composed of several barrels with specific functionality. For example, the service barrels at both ends of the ITS detector barrel, are designed for mounting loops of signal and power cables, power converters, distribution manifolds, liquid and air cooling tubes, etc (see Fig. 4.14). Components for fixation of detector systems, services and beam-pipe are shown in yellow.

The design of theinside the volume of the insertion container provides the opportunity to change the modules of the MPD detector systems and/or of the beam-pipe. In all cases the procedure of mounting/dismounting of detectors inside the inner part of the TPC is similar.

The positioning inside the TPC of the insertion container with the integrated detector systems and services and containing the beam-pipe central section, requires additional tooling to provide the movement of the whole assembly in (or out) the TPC. This tooling assumes external supporting rails mounted outside the MPD on both sides during the operation with the insertion container (see Fig.4.15).

Schematics of the final assembly of the ITS inside the TPC is shown in the Figure 4.16

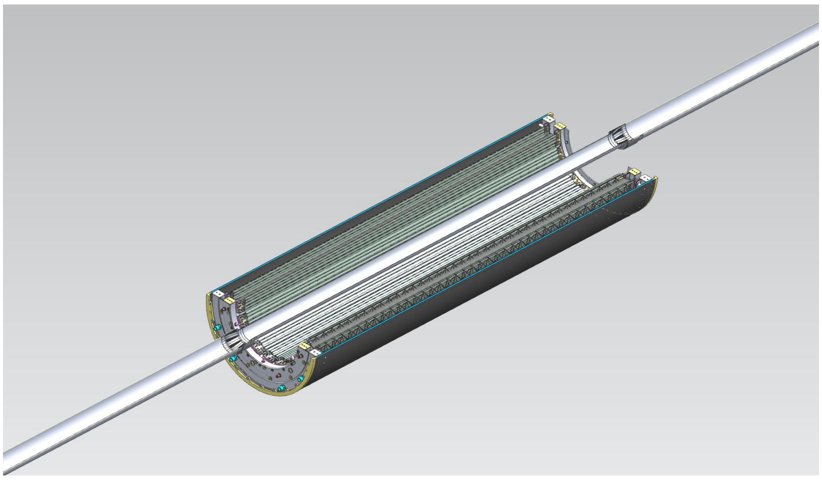

Figure 4.8: General overview of the mechanics for installing the ITS layers (internal supports are not depicted).

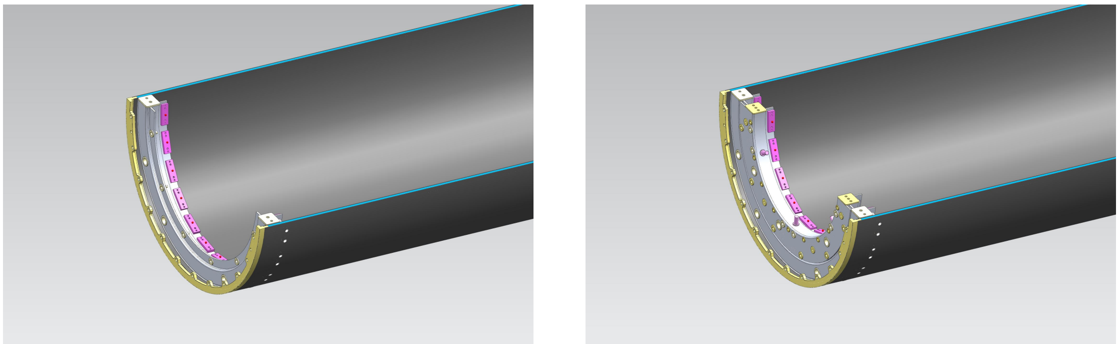

(a) **(b)**

Figure 4.9: ITS outer case element for layer 5 (a) and 4 (b).

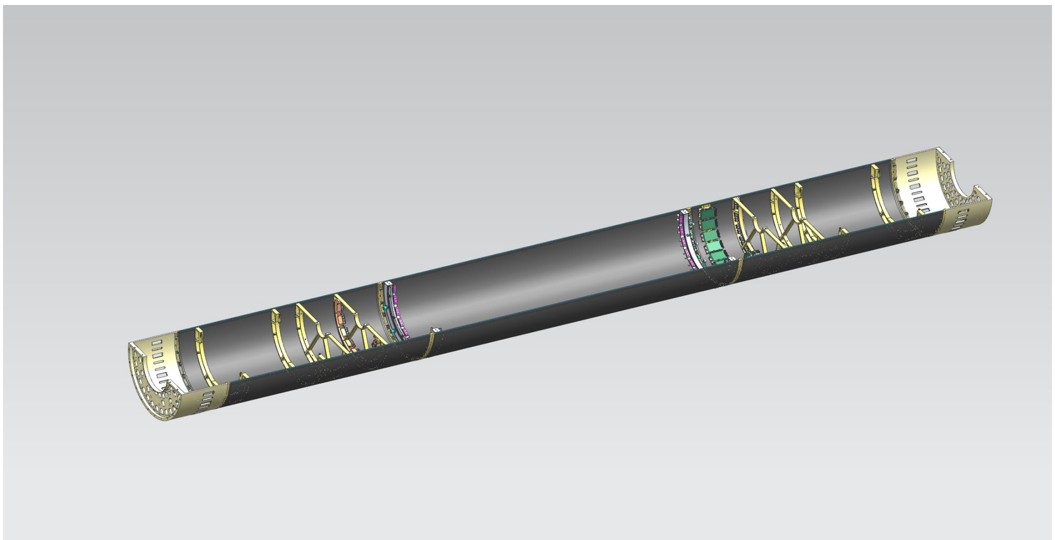

Figure 4.10: General view of the ITS case assembly.

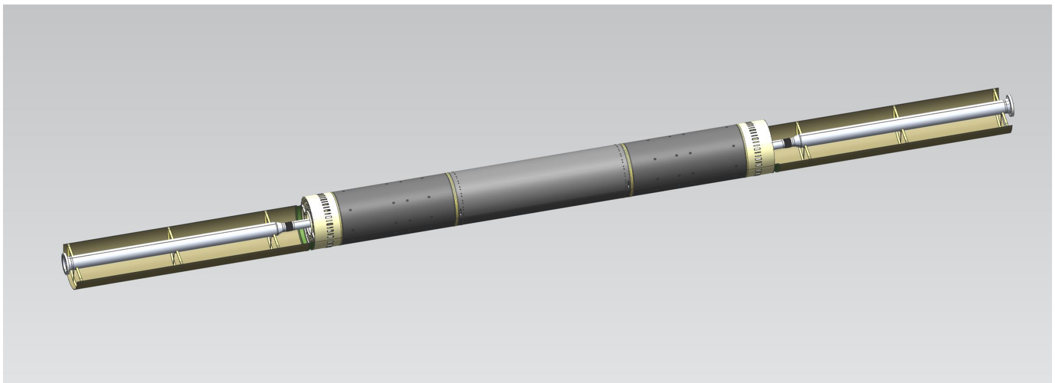

Figure 4.11: General view of the insertion conrainer. For convenience, the upper parts of the technological barrels are not shown.

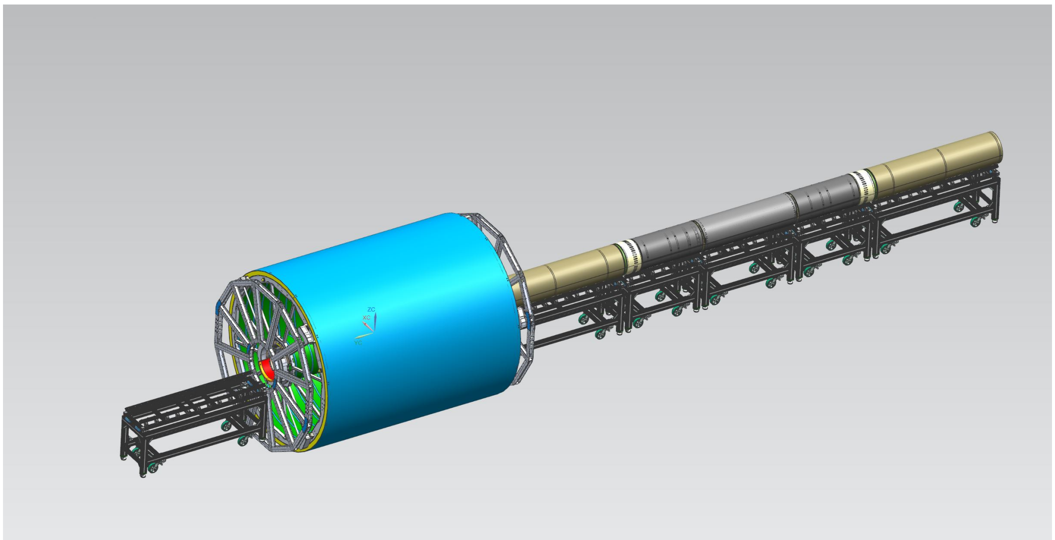

Figure 4.12: Installation of the insertion container of the MPD-ITS into the TPC bore.

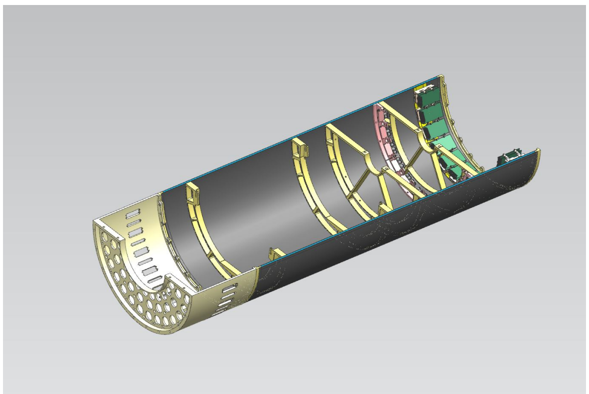

Figure 4.13: General view of one half of the MPD-ITS service barrel cases in a clam-shell design.

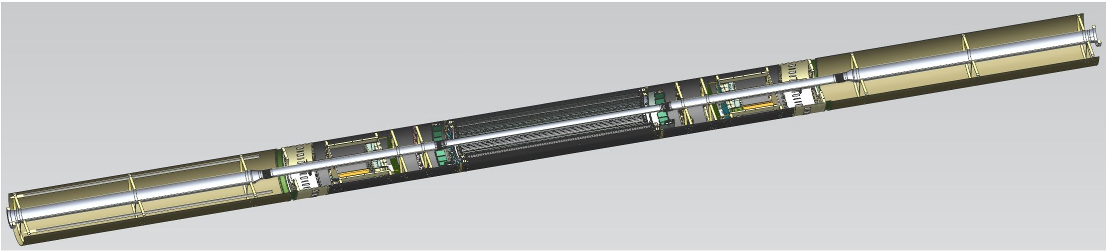

Figure 4.14: General view on half of the MPD-ITS insertion container with ITS and FFD detector systems mounted.

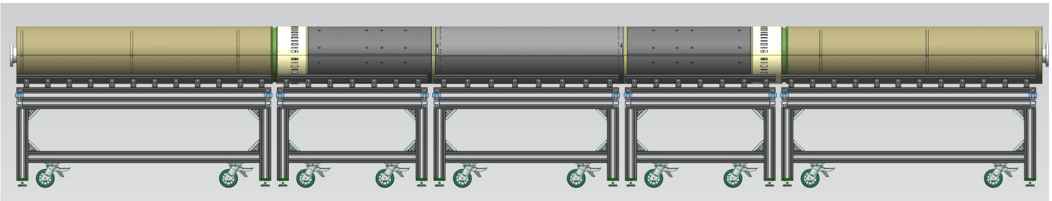

Figure 4.15: MPD-ITS insertion container on the supporting rails.

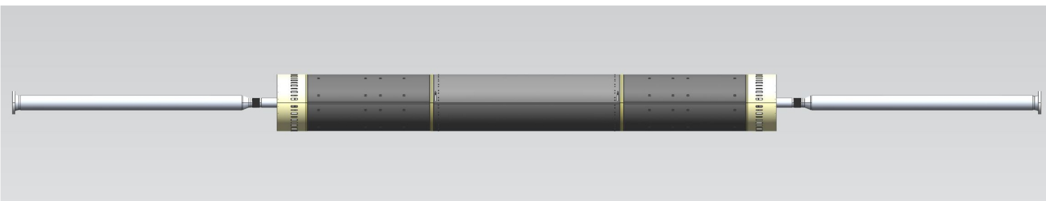

Figure 4.16: Final geometry of the ITS insetion container inside the TPC.

Bibliography

[1] P.Bonneau, M.Bosteels, "Liquid cooling systems (LCS2) for LHC detectors.", https://cds.cern.ch/record/434520

[2] J. Alme, Y.Andres, H.Appelshauser et al., "The ALICE TPC, a large 3-dimensional tracking device with fast readout for ultra-high multiplicity events.", Nucl. Instr. And Meth. in Phys. Res. A622(2010)316–367

[3] M.Pimenta dos Santos., "ALICE TPC Readout Chambers Cooling System.", CERN-ST/CV-2003-490540, 2003.

5 The DAQ System

5.1 Radiation environment

The evaluation of the radiation environment of the MPD-ITS was done using the FLUKA code version 2-11.2x-8. For this purpose a simplified geometry of the ITS consisting of five concentric cylindrical layers was defined inside the geometry of the MPD. The *Total particle fluence (1-MeV n equivalent in Si)* and *Dose rate* were calculated along the radius of the setup for two main zones of interest, the full MPD and the ITS regions. For the ITS region the Dose and Fluences were estimated in 5 layers defined in Table 5.1.

Table 5.1: ITS layers as defined for the FLUKA simulations

Layer	Radius (cm)	Lenght (cm)
1	2.2	75.0
2	4.1	75.0
3	6.0	75.0
4	14.5	152.6
5	19.4	152.6

The conditions of the simulations are described below.

Geometry set-up

The simulated geometry is shown in a 2D projection in Figure 5.1 where the following regions were defined:

1. Solenoid based on the MPDroot geometry.
2. Pipe:
    - middle section(150 cm in length centered at the MPD IP) was defined as a Be tube with an inner and outer radii of 1.9 cm and 2 cm, respectively;
    - outer sections were defined as Al tubes with an inner and outer radii of 3.9 cm and 4 cm, respectively.
3. Simplified TPC detector based on the MPDroot geometry version v7.
4. Simplified FFD detector.
5. FHCal calorimeters with 44 modules each (each module was implemented as a single homogeneous material.)
6. ECal was implemented as a single homogeneous material.

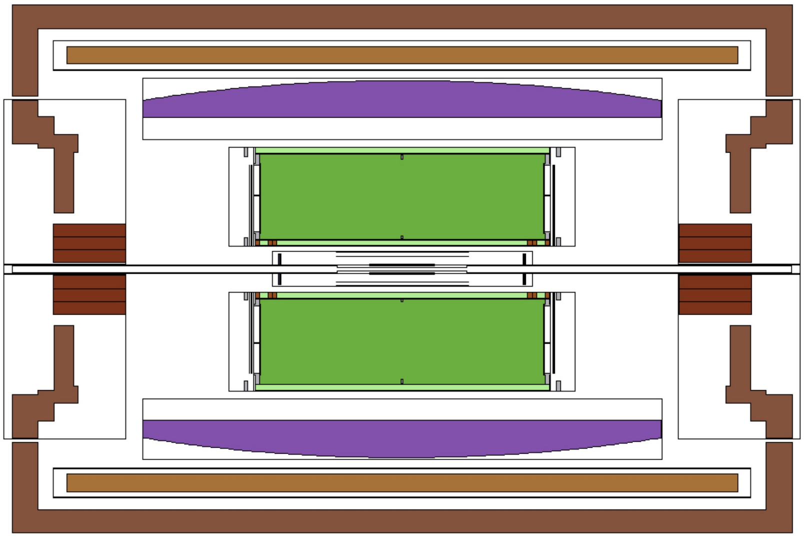

Figure 5.1: Implemented MPD geometry for FLUKA simulations.

Primary events

A file from DCM-QGSM event generator for minimum-bias Au-Au collision at $\sqrt{S_{NN}}$=11 GeV/n was converted to be read by FLUKA as a source of primary events. A total of 10^4 primary events were used in the simulation. The beam was specified to have the Gaussian profile defined by standard deviation σ=60 cm in the beam-line direction Z (Fig.5.2-left panel) with beam particles uniformly distributed over a 2 mm-radius circle in the X-Y plane at the MPD IP (Fig.5.2-right panel).

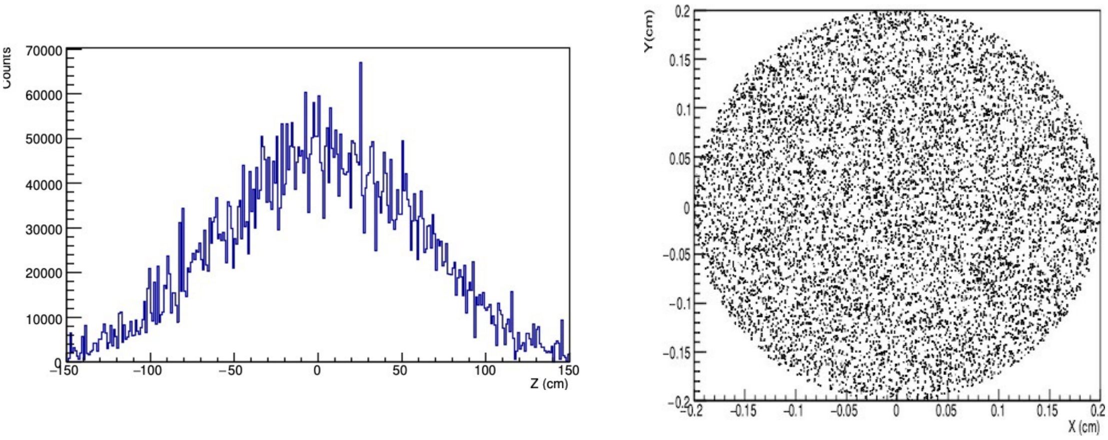

Figure 5.2: Left: Beam Gaussian profile along the beam-pipe. Right: Beam cross section.

5.1.1 Radiation levels in the detector regions

The results of the simulations are shown in figures 5.3 to 5.5 for the 5 layers of the ITS and in figures 5.6 to 5.8 for the whole MPD setup. As it can be seen from figure 5.5 the TID rate for the two OB layers is of the order of 5×10^{-5} Rad/s. Assuming a yearly running time for the MPD of 50%, it is around 10 kRad over 10 years which represents a complete non radiation-hard environment. As so, figure 5.8 shows a very low dose rate of about 10^{-9} Rad/month in the area just above the MPD yoke where the ITS readout electronic will be placed.

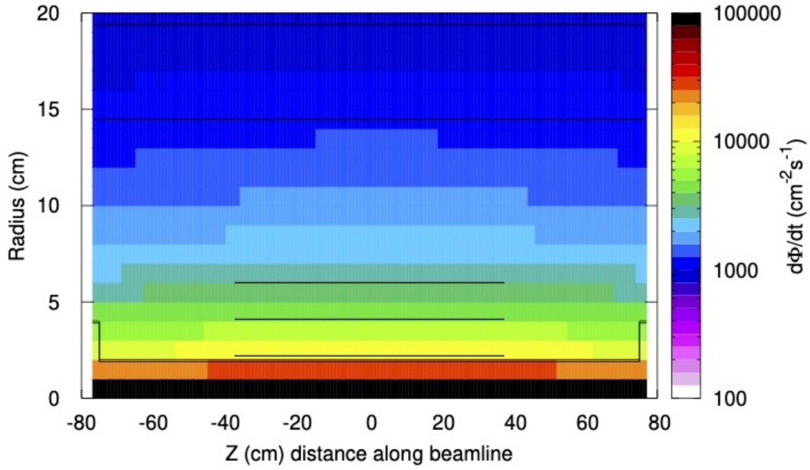

Figure 5.3: Total particle fluence on the ITS regions.

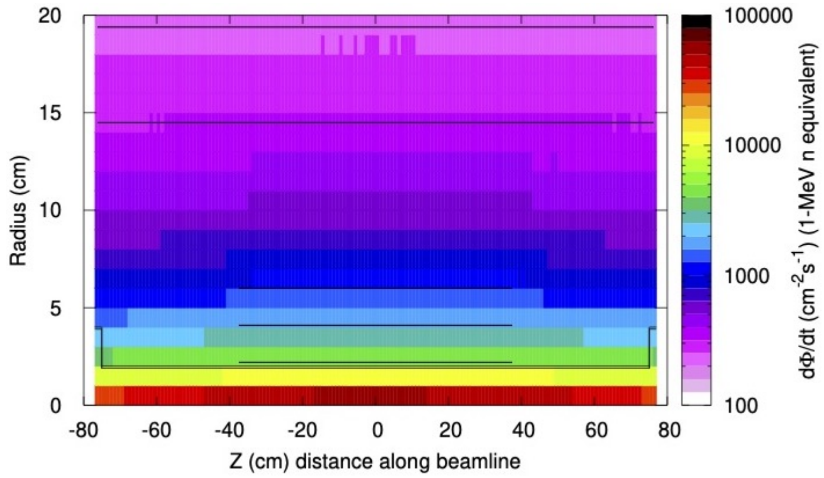

Figure 5.4: Total particle fluence on the ITS regions (1-MeV n equivalent in Si).

5.2 Sensors layout and interconnections

The MPD-ITS is divided into two main regions, Inner (3 layers) and Outer (2 layers), each characterized by a different mechanical arrangement of the sensors around the beam axis. From the readout electronic point of view, what what is important is that the different operating mode of the sensors in such regions and the different speed of the data streams, which depends on the physics implementation of the data bus.

5.2.1 Inner Layers

All references, in this section, to the Inner layers refer to the back-up solution for the Stage-2 is planned to be provided by the MPD Inner Barrel based on the well proven 180nm MAPS technology developed by the ALICE collaboration.

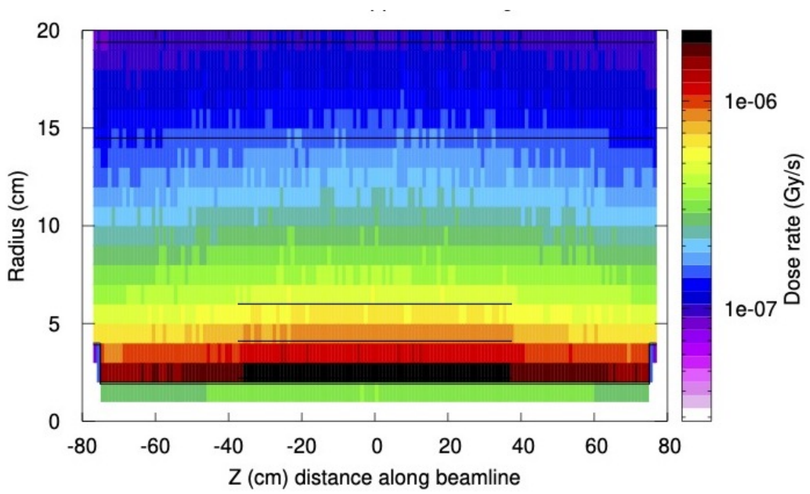

Figure 5.5: Dose rates on the ITS regions.

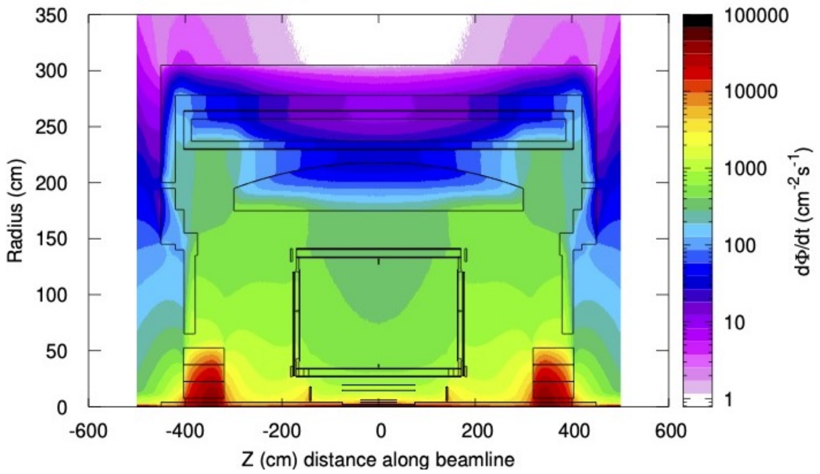

Figure 5.6: Total particle fluence on the MPD.

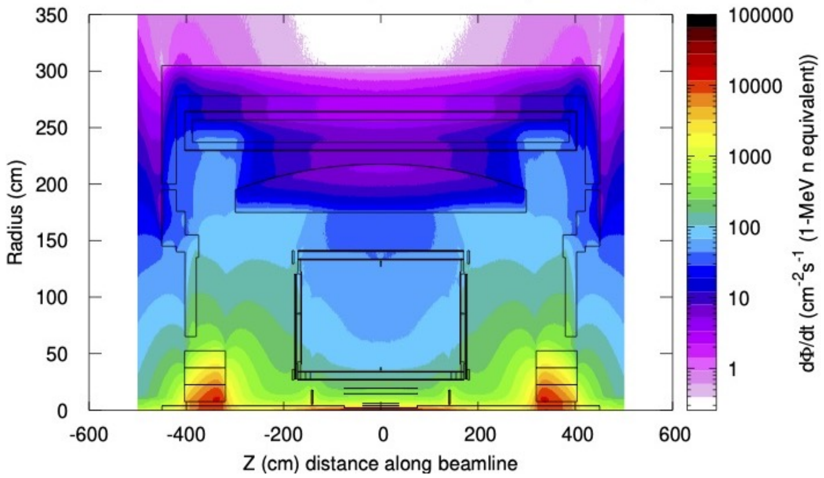

Figure 5.7: Total particle fluence on the MPD (1-MeV n equivalent in Si).

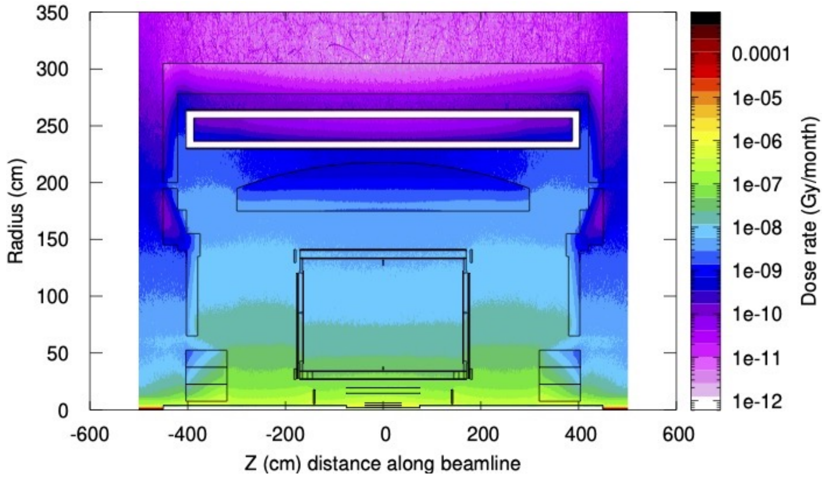

Figure 5.8: Dose rates on the MPD.

The three innermost layers are composed by a different number of identical staves, each one supporting nine chips. Each chip has dedicated bus lines to receive and send data from/to the Readout Electronics.

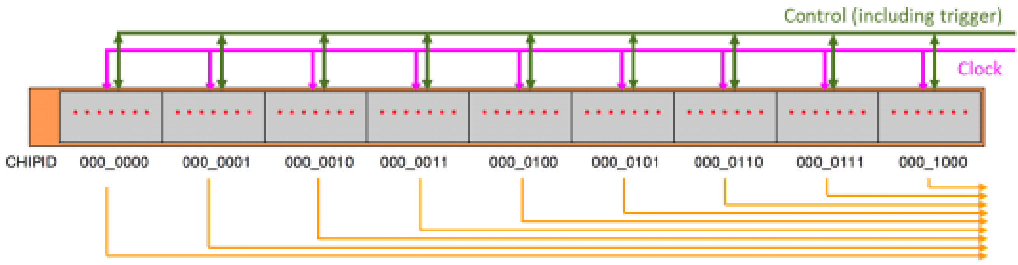

Figure 5.9: Inner Layers stave sensors and connections schematic.

Figure 5.9 illustrates all the links connecting the sensors with the readout electronics. The clock link (purple) is a mono-directional multi-drop differential connection running at 40 MHz. The control link (green) is a bi-directional multi-drop differential connection mastered by the Readout Electronics which can run up to 40 Mb/s. The control link will also carry the trigger, as a special, high priority packet. During acquisition time the control line will just carry the trigger and some slow control commands; while the detector is not running it mainly be used for reading back sensors status and parameters for setup and control purposes.

Orange lines in Figure 5.9 represent the high-speed data lines, which are point-to-point, one way differential links connecting each sensor directly to the Readout Electronic.

5.2.2 Outer Layers

A module is composed by two rows of seven sensors, and each row has a master sensor which communicate with the outside world, while the other six chips share a bus to send and receive data to/from the master. The master chip will have a digital interface identical to the Inner Layers chips, therefore the control lines will be identical. With reference to Figure 5.10, the clock link (purple) is a mono-directional multi-drop differential connection running at 40 MHz. The control link (green) is a bi-directional multi-drop differential connection mastered by the Readout Electronics which can run up to 40 Mb/s. The control link will also carry the trigger, as a special, high priority packet. During acquisition time the control line will just carry the trigger and some slow control commands, while it will be used for reading back sensors status and parameters for setup and control purposes.

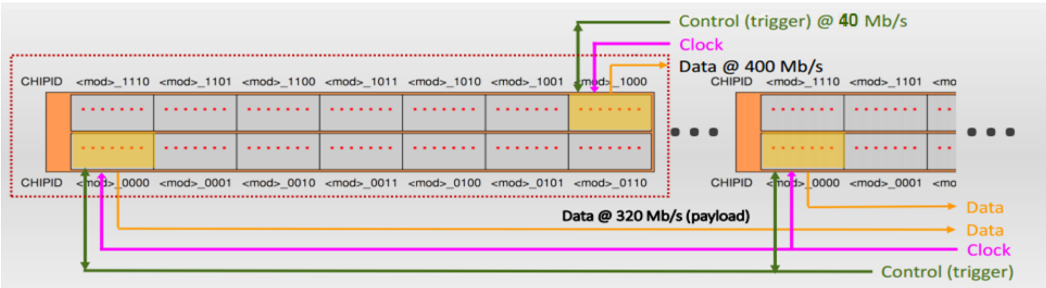

Figure 5.10: Outer Layers stave sensors and connections schematic.

Data lines will be again a point-to-point differential link connected directly to the Readout Electronics. The slave sensors communicate with the master by a dedicated, 4-bit single ended bus connecting the master and the six slaves. The Outer Modules by staves carrying two rows of seven modules each (Figure 5.10).

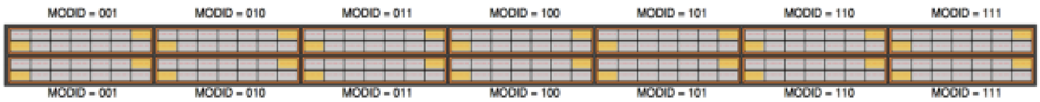

Figure 5.11: Outer Layers stave modules arrangement (master sensors in orange).

5.2.3 Links and connections

The topologies illustrated in the previous section requires the signal to and from the sensor to travel through a bus for the full length of the stave at which end a copper link will connect it to the Readout Electronic. Simulations (communication line models) and early prototyping did show how the main limit for high-speed communication comes from the bus, while the copper links (about 8-meter-long for all the layers) play a lesser role (but not negligible for the faster inner layers link).

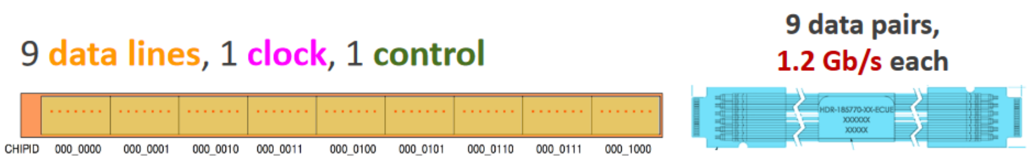

Figure 5.12: Inner layer links

The important thing for this general system overview is that the bandwidth available to transmit the data is limited to 1.2 Gb/s for the Inner Layers link, and to 400 Mb/s for the Outer Layers link, where the much longer bus is the bottleneck.

Table 5.2 summarizes the foreseen links per each layer and the total data bandwidth. The rated values are all maximal system design values, not actual average values, which should stay sensibly lower to ensure smooth operations.

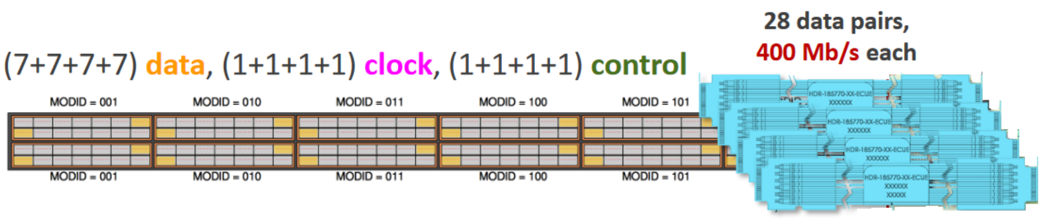

Figure 5.13: Outer layer links

Table 5.2: Copper links count and capacity summary (max design values).

Layer	Staves	Links per stave	Links bandwidth [Gb/s]	Links payload [Gb/s]	Bandwidth per stave [Gb/s]	Payload per stave [Gb/s]	Bandwidth per layer [Gb/s]	Payload per layer [Gb/s]
0	5	9	1.2	0.96	10.8	8.64	54	43.2
1	8	9	1.2	0.96	10.8	8.64	86.4	69.12
2	11	9	1.2	0.96	10.8	8.64	118.8	95.04
3	18	28	0.4	0.32	11.2	8.96	201.6	161.28
4	24	28	0.4	0.32	11.2	8.96	268.8	215.04
Total							729.6	583.64

5.3 Readout Electronics

5.3.1 Overview

The Readout Electronics (RE) interfaces the sensors on the staves of the different layers to the readout, control and trigger systems of the MPD. On the detector side, it collects the high-speed data streams from the sensors and re-organize them to optimize the data transmission through the e-links used by the Common Readout Unit (CRU). It also manages the control lines which distribute the trigger, the clock and the slow control commands. The Readout Electronic also performs auxiliary functions like the power supply lines monitoring to quickly detect and interrupt latch-up states. On the experiment side, the RE feeds the CRU with the MPD-ITS data and collects slow control commands and trigger signals.

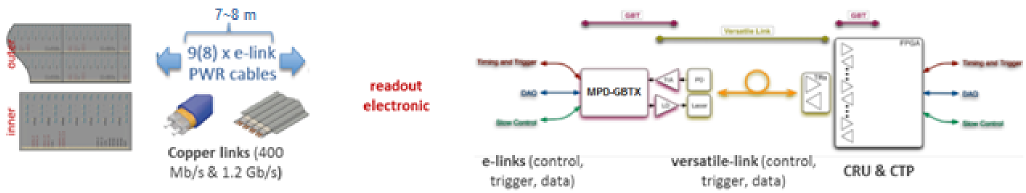

Figure 5.14: Readout electronic main components.

Other than signals management and flow control, the Readout Electronics is responsible for managing the following tasks:

- Trigger filtering, i.e. managing triggers too close in time to be successfully accepted by the sensor.
- Busy signal dealing with sensor/modules not able to handle a trigger.
- Data labelling to associate data from the sensor with received trigger before sending them to the CRU.
- Monitoring the sensor status by recognizing a specific code-word in the data stream.
- Generating the necessary clock/trigger patterns for the sensor, depending which operation mode is selected (continuous/triggered).
- Perform power monitoring to deal with latch-up states of the sensors.

Figure 5.15 synthetizes the main functions the Readout Electronic will implement and the data flow to/from the detector and the CRU.

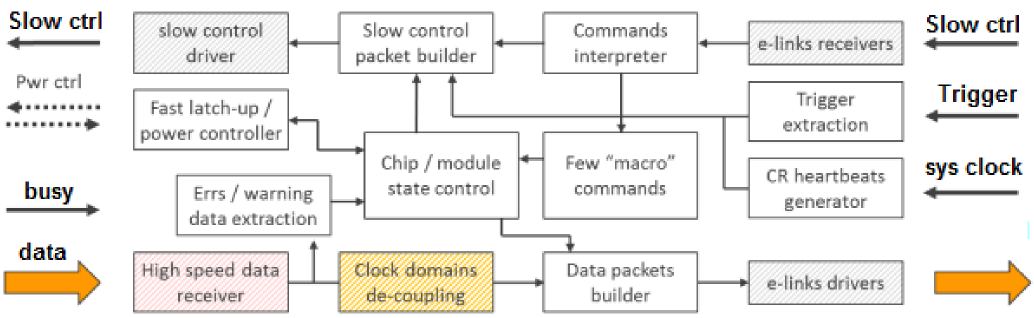

Figure 5.15: Readout Electronics main functions.

The MPD-ITS will be readout and controlled by a cluster of Readout Units (RUs) which will control, trigger and read each single sensor in the detector. The RUs receives control commands and delivers data directly from/to the CRU via the MPD implementation of the CERN Versatile Link. To maximize modularity, a single RU design will serve the whole detector; the only difference between RUs attached to different layers being firmware parameters. The current baseline architecture for the RU is sketched in Figure 5.16 where only the most important connections are reported.

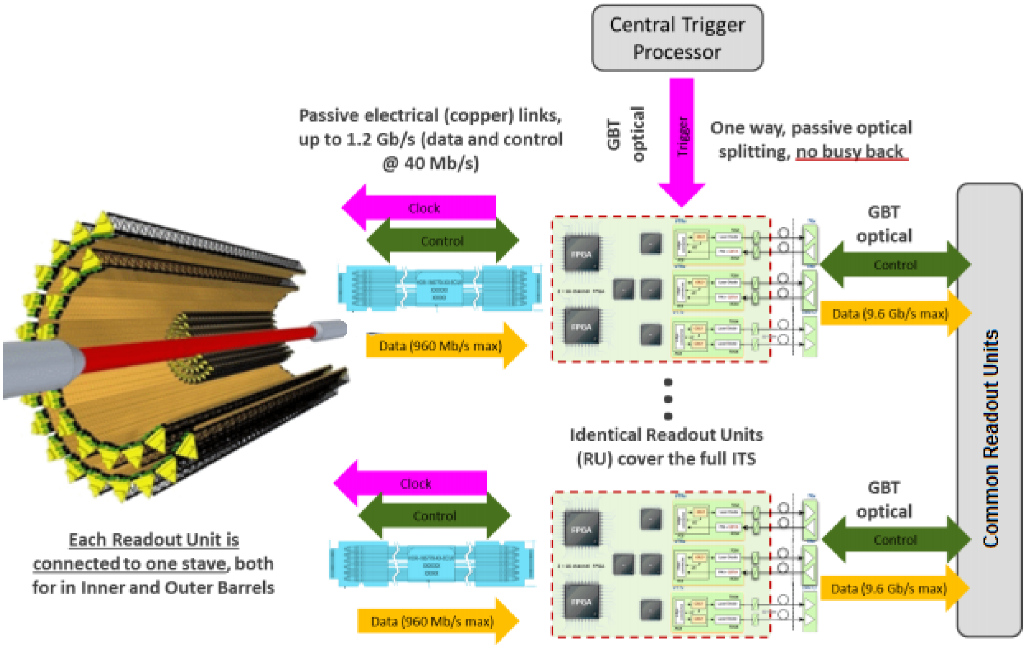

Figure 5.16: Readout Unit (RU) modular implementation.

5.3.2 NICA-MPD ITS Readout Unit

5.3.2.1 Structure of NICA-MPD ITS Outer Layer readout electronics

The function of NICA-MPD-ITS RU is to implement the control and readout of the Monolithic Active silicon Pixel Sensor (MAPS) of the ITS Outer Layers and to send the data to the data acquisition system via high-speed serial interfaces.

Since ITS is not involved in triggering, the RU only needs to passively receive the trigger signal from the trigger system, and then generate the corresponding control signal to send to the detector's ALTAI chip after receiving a valid trigger signal to start the data readout process.

The structure of the readout system is shown in the diagram below. The core component of the system is the RU module, which is connected to the detector module via a cable and sends control signals to the ALTAI chip on the one hand and receives data from the ALTAI chip on the other. Then the processed data will be delivered to CRU via the GBT interface. The diagram is shown in Figure 5.17.

The effective data rate of the GBT interface is set at 3.2 Gbps with an effective rate of 320 Mbps (after 8b/10b) per channel of serial data stream, so that up to 10 ALTAI serial interfaces can be connected to each GBT interface. Given the data transfer and the need for trigger communication, three GBT fiber optic interfaces are designed on each RU module

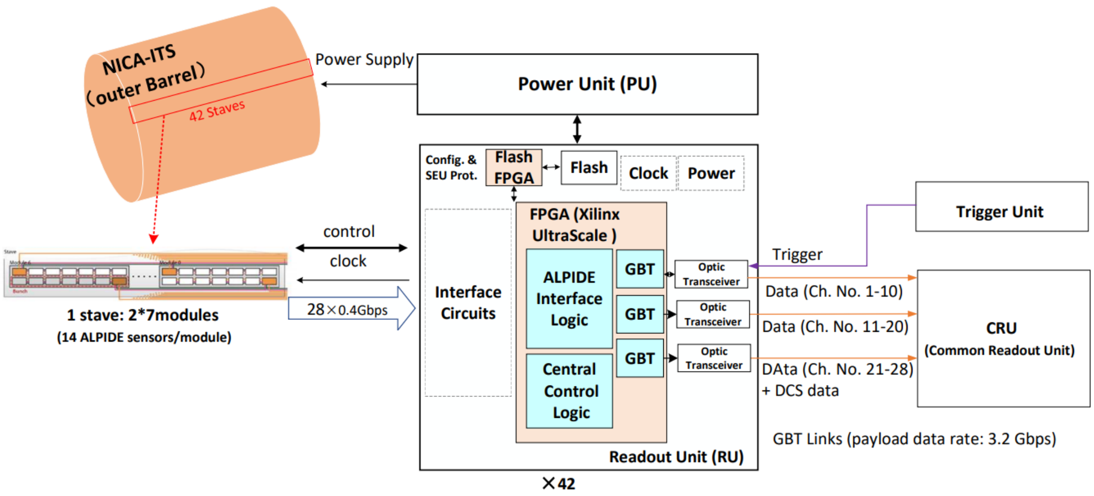

Figure 5.17: Structure of the readout system.

which are used to send ALTAI data to the CRU and to receive trigger and clock signals from the trigger unit.

Besides, the RU module needs to communicate with the Detector Control System (DCS) via the interface of the CRU. To simplify the system design, this function will be implemented using one of the GBT interfaces for communication. The downlink fiber channel of the GBT interface is used for the transmission of the DCS data; the uplink channel, which is responsible for only 8 ALTAIs serial data, has a margin of data bandwidth (640 Mbps) and is used for the transmission of uplink DCS information.

5.3.2.2 RU module design

5.3.2.2.1 Technical approach

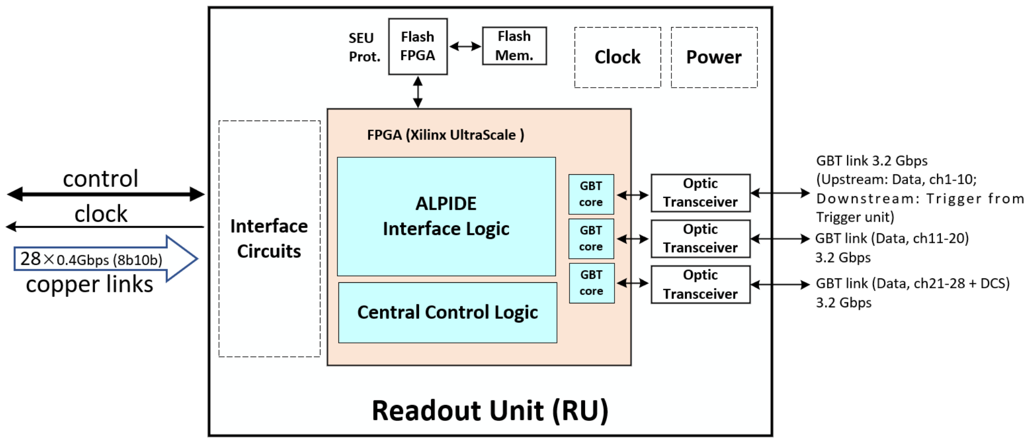

Figure 5.18: FPGA-based RU design solution.

As mentioned above, the function of RU is ALTAI readout and packetized data transfer. In this project, we considered two approaches to implement RU. The first technical approach

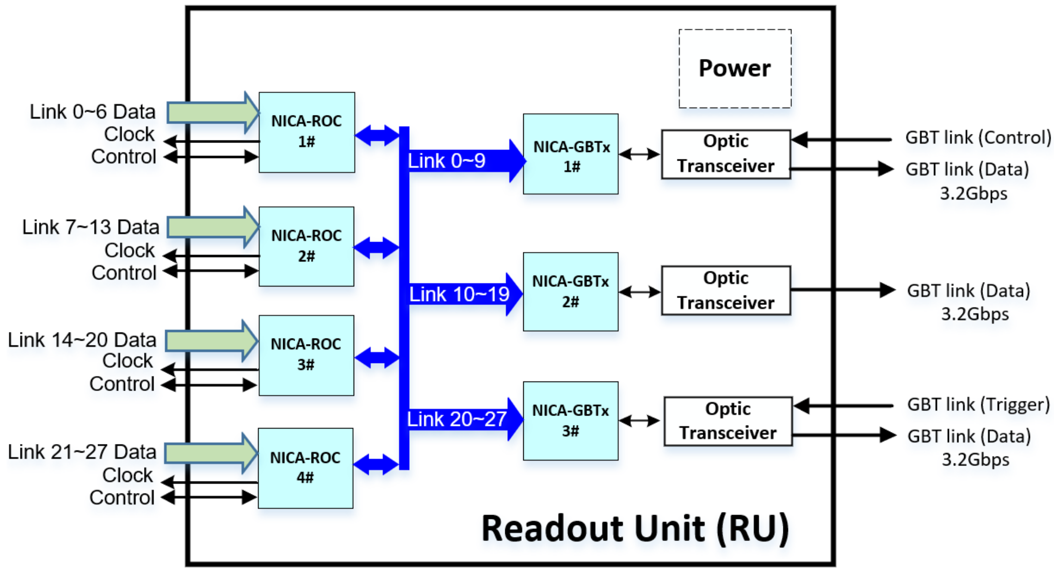

Figure 5.19: ASIC-based RU design solution.

is based on FPGA implementation using FPGAs to complete data receiving, assembly, and sending out. The other technical approach is based on ASIC implementation where NICA ASICs are expected to be used to implement the main functions of the RU. The design schemes of the two technical routes are shown in Figures 5.18 and 5.19.

5.3.2.2.2 ALTAI data readout

ALTAI is one of the MAPS chips originally designed for the upgrade of the CERN LHC experiment ALICE-ITS using the Tower Semiconductor LTD. Towerjazz 0.18 µm CMOS process.

The structure of the final version of ALTAI, is shown in Figure 5.20 [1]. The single-chip includes a total of 512 rows × 1024 columns of pixels, with a pixel size of approximately 29.24 µm × 26.88 µm, and its sensitive area is 30 mm × 13.8 mm. Together with the width of the peripheral circuitry at the bottom of 1.2 mm, the ALTAI's total width is 15 mm.

The ALTAI chips use a global shutter readout, i.e. all pixels in the whole chip are shaped and over-threshold screened at the same time and hit data latching is done under the control of a trigger signal. When hit data is latched in the cache cell of any pixel, the front-end readout circuity automatically reads it out immediately under the control of the memory selector signal. The front-end readout circuitry, which includes Priority Encoder and zero compression, is shared between every two rows of pixels and transmits the latched data to the periphery readout circuitry at the bottom of the chip after encoding with a high-speed serial bus bandwidth of up to 1.2 Gbps and an effective trigger rate of up to 100 kHz - 200 kHz.

ALTAI's data readout interface is divided into two groups. One is an 8-bit parallel readout interface used in Single Data Rate (SDR) mode in which 8 bits are used, or in Double Data Rate (DDR) mode in which only the lower 4 bits are used. The other set of interface outputs 8b/10b encoded high-speed serial data via a LVDS differential pair.

In this project, 28 pairs of high-speed serial data will be transferred to RU separately. After packing through the internal GBT logic of FPGA, the data will be sent out to CRU from the high-speed transceiver.

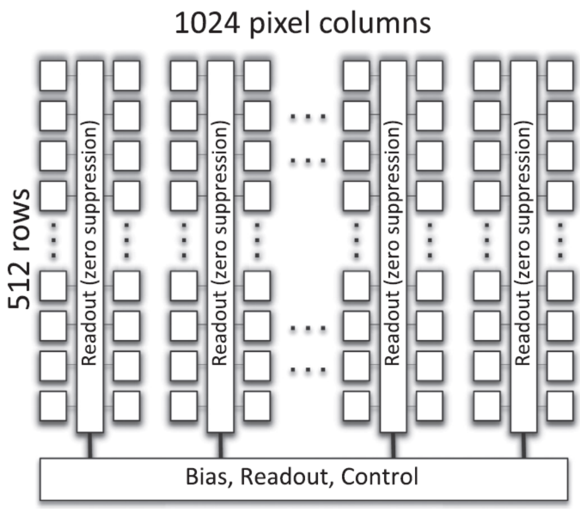

Figure 5.20: ALTAI chip structure.

5.3.2.2.3 ALTAI control

The next sections (1.3.2.2.3-1.3.2.2.5) elaborate the FPGA-based RU scheme, while the ASIC-based readout scheme is specifically presented in "1.3.4.1 NICA_ROC". Due to the complex structure of ALTAI, the number of pixels, and its register configuration parameters up to 500,000, it is a significant task to achieve online configuration of ALTAI working parameters. The configuration parameters will be generated by the DCS system and the configuration data will be sent to the CRU via GBT interface, then to the FPGA on the RU via the GBT downlink and finally distributed to the individual ALTAI chips.

In this project, the control signals of ALTAI are transferred from the CRU to the high-speed data transceiver of FPGA in RU, then processed by the FPGA logic, and finally fed to each Stave. Since the control and clock signals at the ALTAI are MLVDS, a chip is used to convert the LVCMOS signals to MLVDS signals. Besides, an uplink and downlink fiber optic interface is reserved for busy signal. The block diagram is shown in Figure 5.21.

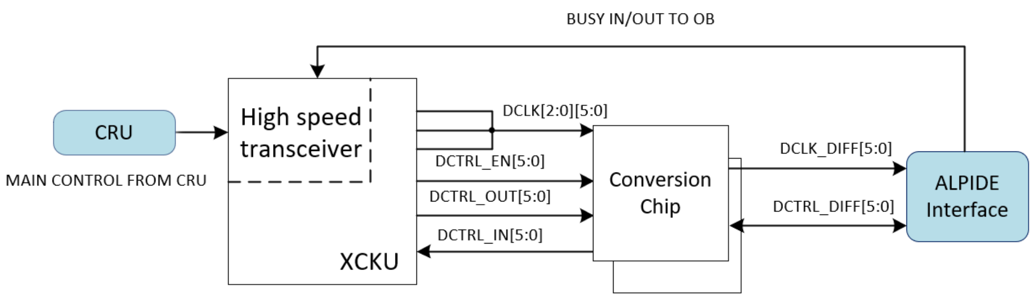

Figure 5.21: ALTAI control.

5.3.2.2.4 Configuration and Scrubbing of FPGA

First, for RU design, the radiation dose where RU resides is very low, so it is not necessary to consider the TID caused by electrons, but we still implement anti Single-Event Upset (SEU) design to enhance the reliability of the electronics. In this regard, on the one hand, TMR (triple-mode redundancy) and even automatic error correction design are adopted for critical configuration registers, critical global control signals, and critical data memories; on the other hand, error detection (or error correction) design is adopted for important data streams.

Second, the SRAM-type Xilinx's UltraScale series FPGA is used as the main FPGA (i.e. the XCKU FPGA in Figure 5.22) in RU for implementing large-scale, high-performance digital logic. However, to prevent it from SEU, a flash-type FPGA (immune to SEU) is added outside the main FPGA, as shown in the figure below. The scrub control signals are used for the scrubbing operation, while the 8-bit select map signal is used to indicate which region of the main FPGA will be scrubbed, and the GPIOs & DP IOs are the ports for the bit stream transfer between the main FPGA and the flash FPGA. Switches are also reserved to ensure the customized and fast transfer of configuration information. The configuration of the FPGA is stored in the flash memory, and the flash FPGA periodically reads back configuration information from the master FPGA and verifies it. Once an SEU error is found, that part of logic will be reconfigured, while the logic function of the FPGA remains unchanged during this process. The block diagram is shown in Figure 5.22.

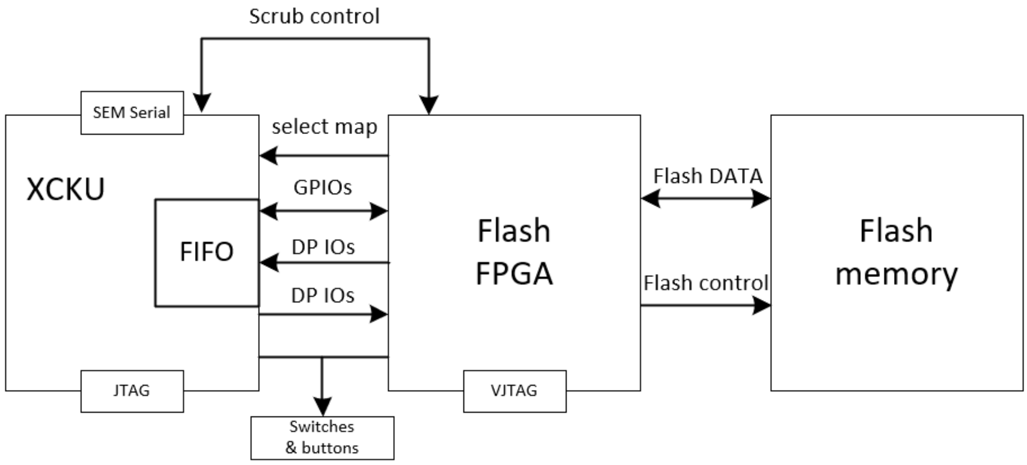

Figure 5.22: Configuration and Scrubbing.

Finally, as shown in Figure 5.22, because Xilinx FPGA has an automatic error correction function Soft Error Mitigation (SEM), a serial port is reserved for connecting with a PC to achieve the effect of supervision and scrubbing as described in its official manual.

5.3.2.2.5 High-speed data interface

In this project, the high-speed data interface between the RU module and the back-end data acquisition system is proposed to be implemented using the GBT link proposed by CERN. The background of GBT generation is that the strong radiation environment brought by the high-energy particle collision after the LHC upgrade has put forward the demand for irradiation tolerance performance for the front-end electronics, and the long-distance transmission between the front-end electronics and the back-end electronics is prone to bit error. For this reason, CERN conducted development of GBT, to ensure the reliability of the data transmission in high radiation environments. The outcome includes an radiation tolerant GBT chipset, the GBT frame, a data format that enables data error detection, and the GBT-FPGA core, a code containing the functions of the GBT chip which can be implemented in FPGAs.

The data transfer process between the front-end electronics and the back-end data acquisition system based on the GBT protocol is shown in Figure 5.14. The left side is the front-end electronics of the detector, which consists of an radiation tolerant electronics chipset (e.g. CERN's GBTx chip, or other ASIC chips conforming to the GBT protocol), or FPGAs containing the similar functionality; the right side is the CRU and CTP, which consists of commercial devices. The long-distance bidirectional data transmission between the CRU & CTP and the front-end electronics is accomplished through a Versatile Link with a data rate of 4.8 Gbps and a user data rate of 3.2 Gbps.

Besides, the RU have a serial interface to the Power Unit (PU) which is described in the following sub-section. And one RU controls two PUs, with RU as the master to initiate read and write process.

5.3.3 NICA-MPD ITS Power Unit

5.3.3.1 Structure of the power system in ITS Outer Layer of NICA

Power Board (PB) is designed for powering the ALTAI staves. Each PB consists of two PUs including a Power Unit Right (PUR) and a Power Unit Left (PUL). The structure of the power system for the ITS Outer Layer is shown in Figure 5.23. A CAEN power supply system powers the PUs that in turn supply power to the staves and monitor them. PUs are controlled and monitored by RUs through a serial interface, as mentioned above.

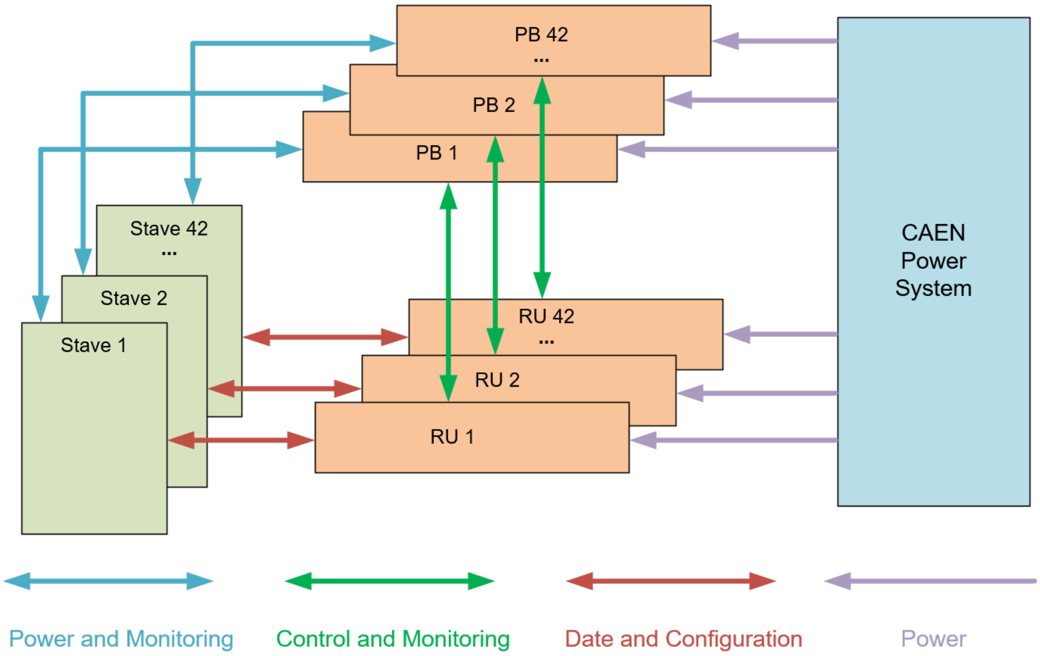

Figure 5.23: The structure of the power system in NICA.

5.3.3.2 Functionality of the PU

PU supplies 1.8 V positive power, as well as negative power used as bias for the staves. The Low Dropout Regulator (LDO) used in PU should have low noise. Besides, high current capability should be taken into consideration during positive LDO selection.

In addition to supplying power to the staves, PU is also controlled by RU through the serial interface to implement the following functions:

- Separate enabling of power channels and bias channels;
- Adjusting the power supply voltage separately;
- Adjusting the bias voltage in one PU;
- Over current protection with adjustable threshold on each power channel;
- Overheat protection on each PU;
- Monitoring of voltage, current and temperature.

In NICA, we consider taking use of VersaModule Eurocard (VME) crates (VME 6023-913) to integrate PBs and RUs. There are 3 slots for 6U/160mm VME64 cards and 17 slots for 9U/400mm VME64 cards in one crate. A total of 9 VME crates are needed for the ITS Outer Layer. The arrangement of RUs and PBs is shown in Table 5.3 and Figure 5.24.

Table 5.3: Arrangement of RUs and PBs.

	Number of Staves Number of RUs	**Number of PB**	**Location of (RU+PB) in four frames of crates**
L3	18	18	**(5+5) (5+5) (5+5) (3+3)**
L4	24	24	**(5+5) (5+5) (5+5) (5+5) (4+4)**

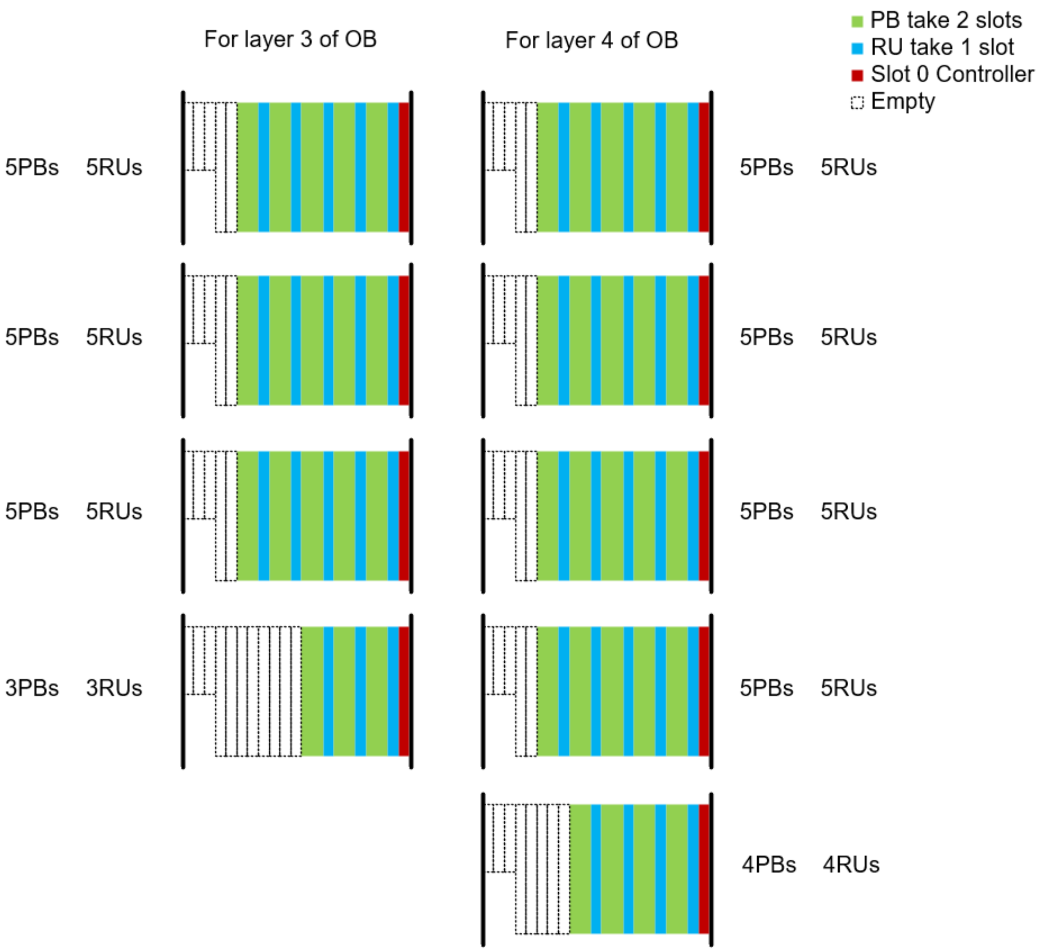

Figure 5.24: Arrangement of RUs and PBs.

5.3.3.3 PB module design

In reference of the structure of the PB in ALICE, one PB consists of two functionally identical and operationally indistinguishable Power Units (PUR and PUL) referenced to the same ground. The circuitry on each PU is distributed mainly to three power domains: two positive voltage domains and one negative voltage domain. Each PU generates 16 nominally 1.8 V power supply voltages with high current strength and 4 additional negative voltage outputs with low current strength that are used as bias for the staves. The PUR receives input power from the external CAEN power supply, and the PUL receives input power from the PUR. The block diagram of PB is shown in Figure 5.25. When the PU supplies power to the Outer Layers, a PU provides 7-way positive voltage analog power supplies, 7-way positive voltage digital power supplies and 3-way negative voltage bias outputs.

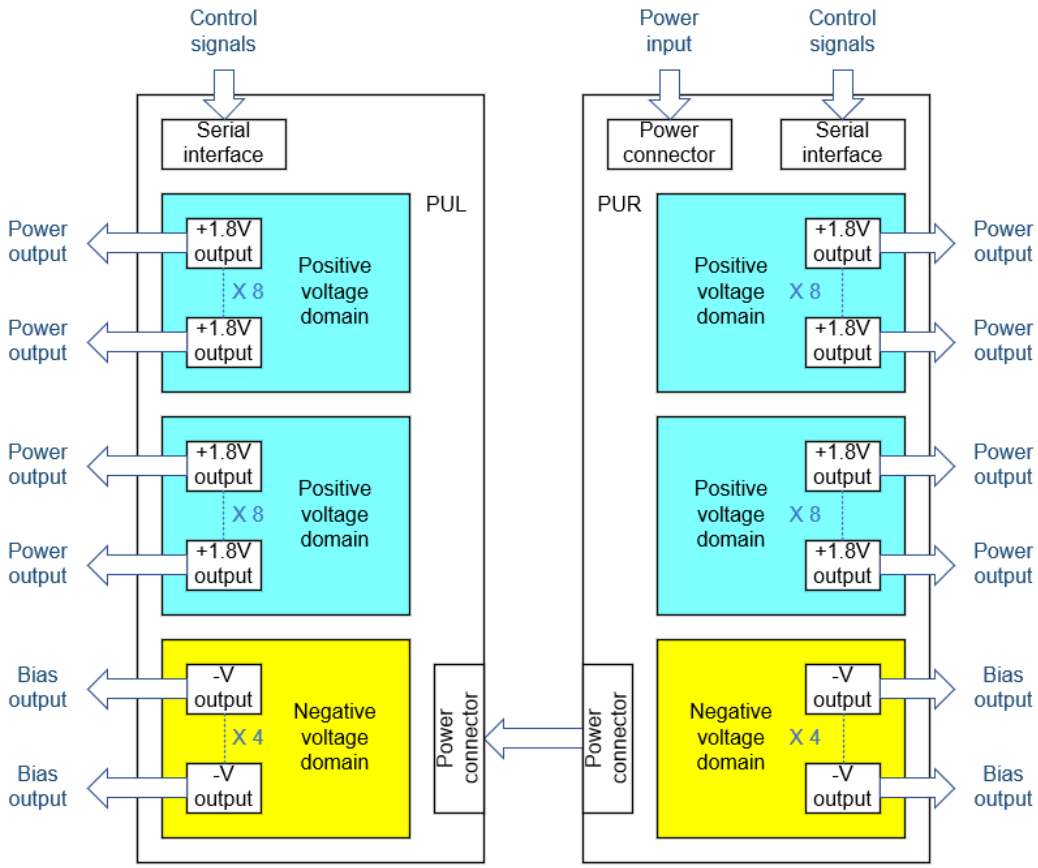

Figure 5.25: The scheme of PB.

CAEN power system provides PUs with positive voltage power and negative voltage power. The positive voltage power is directly supplied by CAEN A3009PS. The first negative voltage power in the same VME crate is supplied by CAEN A2519, and the rest is supplied by the daisy chain. The power input connection is shown in Figure 5.26.

In order to achieve heat dissipation during normal operation, heat exchanger is equipped. The temperature of each PU can also be monitored by an on-board temperature sensor. Each PU is equipped with multiple LEDs on the front panel to indicate the status of each part, which helps to identify possible problems.

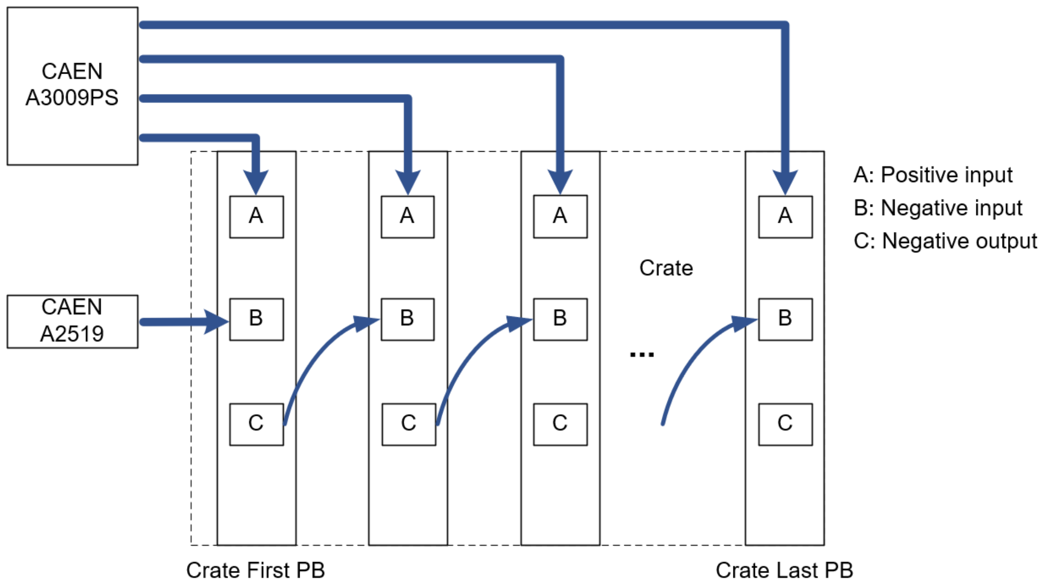

Figure 5.26: Power input connection.

5.3.4 NICA ASICs

As a second approach to implement the readout electronics for the outer barrel of ITS, a series of ASICs (NICA_ROC, NICA_GBTx, NICA_LD and NICA_TIA) is also planned to be developed as shown in Figure 5.27. All these ASICs would be located on the RU board.

NICA_ROC is being designed to concentrate the output data of front-end ALTAI chips and transfer the packaged data to the following NICA_GBTx ASIC. It also receives control commands, clocks, and trigger signals from the backend and distributes them to ALTAI chips.

NICA_GBTx is a high-speed bidirectional data interface ASIC for optical links. It receives multichannel data from the front-end (NICA_ROC), performs scrambling, encoding, frame building and serializing as the main function for the up-link direction. And it also receives high-speed serial data from the back-end, performs CDR (Clock and Data Recovery), deserializing, decoding and distributing to the front-end as the main fuction for the down-link direction.

NICA_LD (Laser Driver) and NICA_TIA (Transiempedance Amplifier) are two analog ASICs that would be integrated together with the laser and PD (Pin Diode) in the customized optical transceiver module. NICA_LD receives the high-speed up-link serial data from NICA_GBTx and amplifies the signal to drive the laser. NICA_TIA receives the down-link serial signal from the pin diode, and amplifies the signal to NICA_GBTx, so that the data can be furthered processed in NICA_GBTx. These four ASICs will be introduced in the following sections.

5.3.4.1 NICA_ROC

As depicted in Figure 5.28, the NICA_ROC will aggregate data from up to 8 ALTAIs. Each ALTAI data connection is a 400 MHz serial link in the outer barrel mode with the data being 8b/10b encoded. The input data from each channel needs to be recovered, decoded, preprocessed and buffered. For flexibility, the crossbar routes the 8 input channel data to different sDACT captures for packaging and reformatting. And the connection between NICA_ROC and NICA_GBTx is based on the HSSI (High-Speed Serial Interface) protocol (such as the E-LINK interface).

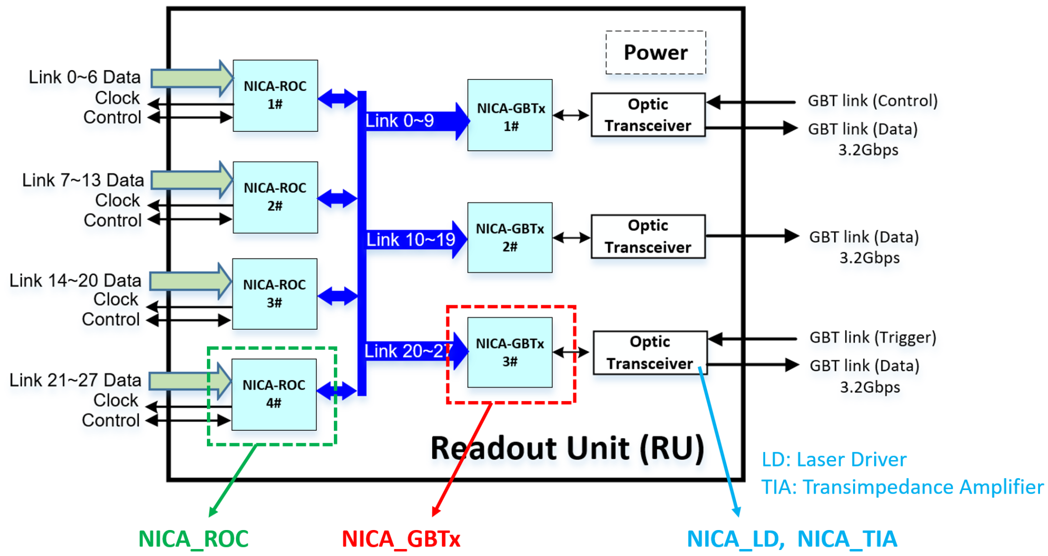

Figure 5.27: ASICs in the readout electronics system.

For the TTC (Timing, Trigger and Control) data flow path, the NICA_ROC receives TTC information from the Common Readout Unit (CRU) and the trigger system and forwards them to the ALTAI chips. The PLL in NICA_ROC receives a synchronous clock signal from the back-end system via GBTx and fans out the clock to ALTAIs and data transfer blocks after in-chip phase modulation.

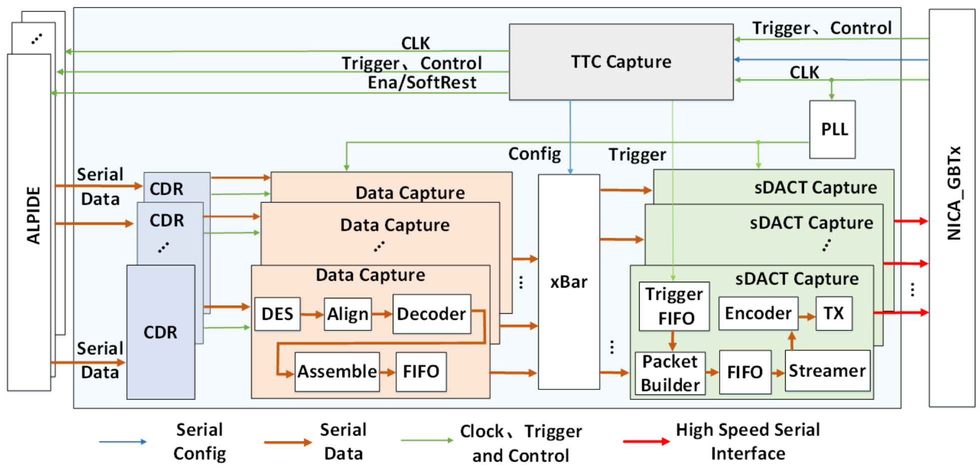

Figure 5.28: Block diagram of NICA_ROC structure.

5.3.4.1.1 Data Capture block

The Deserializer (DES) in the Data Capture block converts the serial data to 10-bit parallel data and the Comma Align block monitors the presence of the comma character K28.5 in the DES output stream. Once this character is identified, the proper boundary can be settled, and the synchronization is achieved between ALTAI and NICA_ROC.

The aligned data is decoded by an 8b/10b decode circuit with 10-bit input and 8-bit output, and the 8-bit words from decoder are further assembled into 32-bit words in the

Assembler block. With 4-bit additional message added, finally, 36-bit words are sent to the FIFO.

The FIFO stores the 36-bit words and implements the clock domain crossing between 400 MHz and 40 MHz. The diagram is shown in Figure 5.29

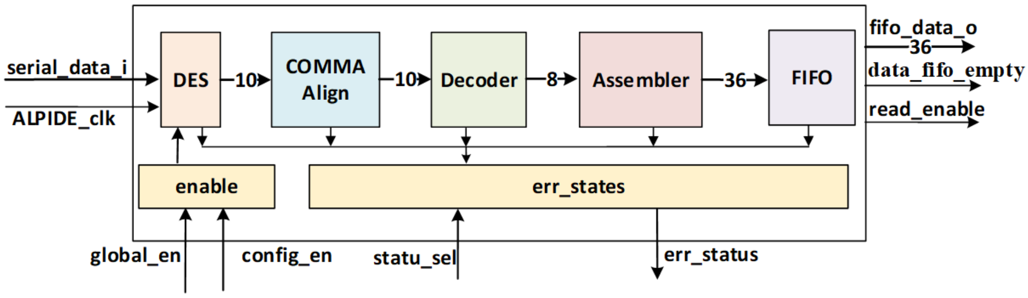

Figure 5.29: Block diagram of Data Capture.

5.3.4.1.2 xBar block

The xBar block is a fully combinational logic circuit that routes 8 Data Capture modules to 8 sDACT capture block in a full-mesh network. The connection between the Data Capture block and the sDACT capture block can be configured according to the application requirement. The xBar block consists of 8 DMUXes on Data Capture side and 8 MUXes on sDACT side. Figure 5.30 shows a simplified structure.

Each sDACT receives 8 configuration bits corresponding to the destination Data Capture blocks. For example, if the sDACT 0 is connected to Data Capture 0, Data Capture 5 and Data Capture 7, the configuration bits received by sDACT 0 will be 1010_0001. Because at a certain moment, each sDACT can connect only one Data Capture, another 3 configuration bits are sent to each sDACT representing the current connection.

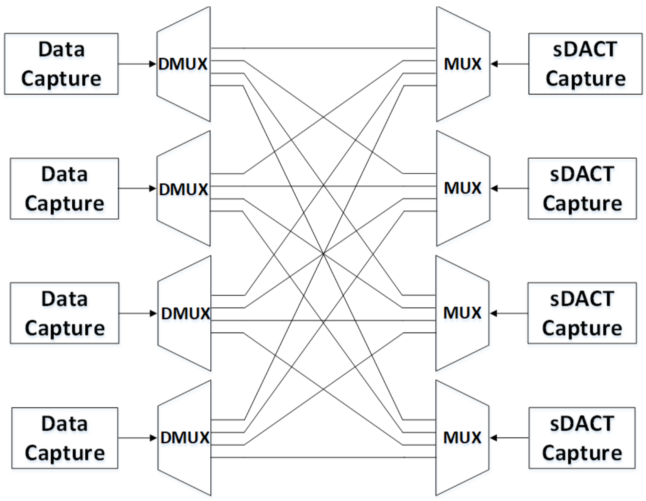

Figure 5.30: Simplified block diagram of the xBar structure.

5.3.4.1.3 sDACT Capture block

sDACT Capture block receives data from data capture block through xBar, forms data packets based on the trigger signal received by TTC Capture block. After receiving the trigger signal, the data packaging process starts. The sDACT capture reads data from the connected data capture FIFO in a circular manner, and the trigger ID, packet header (SOP) and packet trailer (EOP) are added to the data packet. Besides, the busy_on and busy_off flags also inserted in the data stream according to the busy status of ALTAI and NICA_ROC.

After 8b/10b encoding, the output data is sent out of the chip by a parallel-to-serial conversion block. The final output port uses E-LINK protocol to match with the back-end GBT ASIC.

The diagram is shown in Figure 5.31

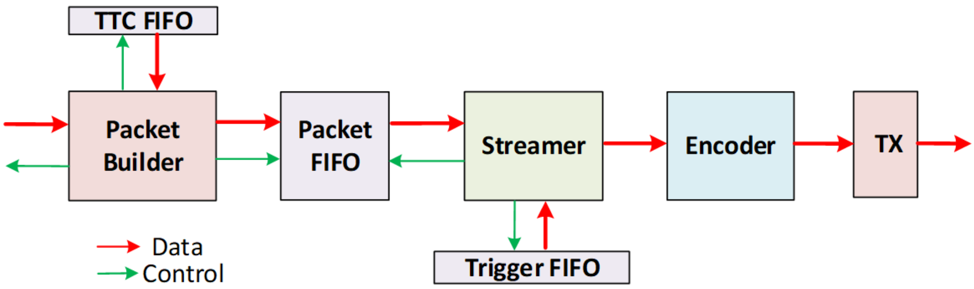

Figure 5.31: Structure of the sDACT block.

5.3.4.1.4 TTC Capture block

The TTC Capture receives clock, trigger and control signals and forwards to ALTAI chips and other blocks in the NICA_ROC. For control data path, the serial input is DDR on the 40 MHz clock, resulting in an 80 Mbps data stream. The TTC Capure extracts ALTAI configuration words and NICA_ROC configuration words from the control data stream respectively, and also transmits back the status of ALTAI and NICA_ROC to CRU. For trigger data path, once the trigger signal is received, the corresponding trigger ID will be stored in the Tigger FIFO, which will be used to mark data packets. When the busy signal in NICA_ROC is valid, the trigger signal will be masked.

5.3.4.2 NICA_GBTx and NICA_LD/TIA

The NICA_GBTx and NICA_LD/TIA are chipsets that constitutes the complete electrical functions of a high-speed bidirectional optical data transmission system. The NICA_GBTx serves as the data interface chip mainly performing the encoding/decoding, serializing/deserializing tasks. The NICA_LD/TIA are two analog AISCs that would be respectively integrated with the laser and pin diode in the optical transceiver module. Figure 5.32 depicts the bidirectional optical data transmission system with these three ASICs.

5.3.4.2.1 NICA_GBTx

The NICA_GBTx receives multi-channel data from the front-end (NICA_ROC), processes the parallel data to the encoded high-speed serial data for the uplink transmission. And for the downlink direction, it receives the data stream from back-end, decodes the data and distributes to the front-end.

Currently the NICA_GBT is planned to be compatible with the GBTx to some extent. An internal block structure of the NICA_GBTx is shown in Figure 5.33 revealing the main functions of the AISC. It is mainly composed of the D-Link interface, data phase control,

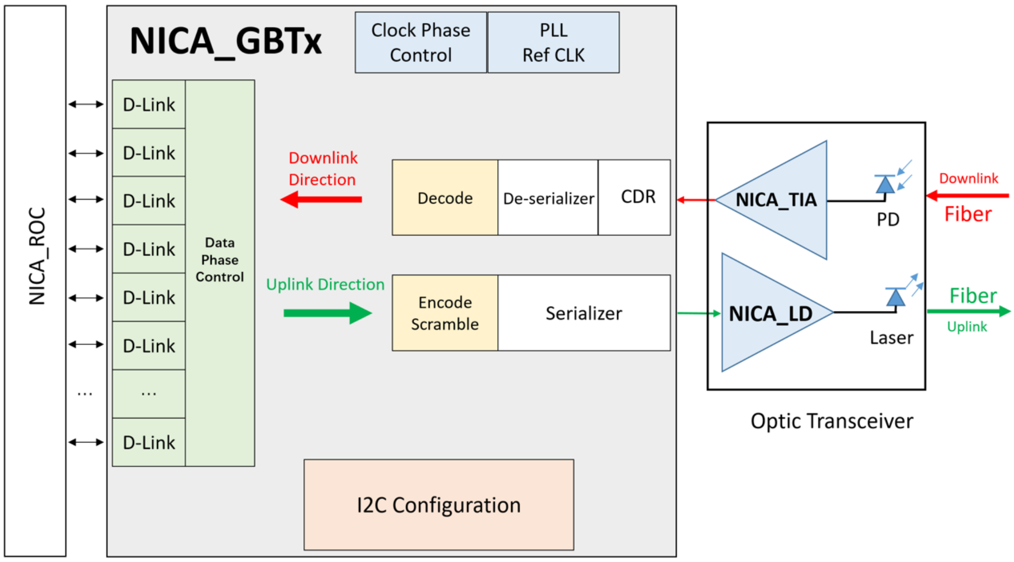

Figure 5.32: Bidirectional optical transmission system with NICA_GBTx, NICA_LD/TIA.

phase lock loop (PLL), clock phase control, encoder/decoder, serializer/deserializer and clock data recovery (CDR) sub-modules.

The D-Link is a universal Tx/Rx interface to/from the front-end. To be compatible with the GBTx chip, each D-Link will consist of three signal lines (differential pairs): differential clock, differential downlink data output (to NICA_ROC and front-end), differential uplink data input (from NICA_ROC). The Data phase control module together with each D-link is used to adjust/align the phase of the input data (uplink) for reliable sampling within the NICA_GBTx. The encode/decode modules perform the digital function of the ASIC, the data protocol is currently planned to follow the GBTx data frame that is adopted in the ALICE readout system.

The serializer submodule receives parallel data from the encode module, and transforms to the high speed serial signal as the final output of the NICA_GBTx in the uplink direction. The deserializer submodule receives serial downlink data, transforms the serial data back to the parallel data for the decode submodule. The downlink data will finally be recovered after decoding and then send to the front-end via D-Link. The CDR circuit will also be integrated within the deserializer to recover the clock from the downlink data. Besides, an independent PLL submodule would also be included within the NICA_GBTx. It will generate internal clock through the external reference clock, and the generated clock can also be distributed to the front-end via D-Link for the clock synchronization consideration.

More specifications and details for each submodule need to be decided and added here after further joint discussion from the system level.

5.3.4.2.2 NICA_LD

NICA_LD is a laser driver ASIC located at the uplink direction as shown in Figure 5.32. It receives high speed serial data from NICA_GBTx, amplifies and transfers it to the current signal to driver laser in the optical transceiver module. Figure 5.34 demonstrates the block diagram of the NICA_LD prototype under design. In the current prototype design, NICA_LD is a four channel array laser driver that would work with a four channel laser array (VCSEL Array). In this case, one optical transceiver module can provide four independent

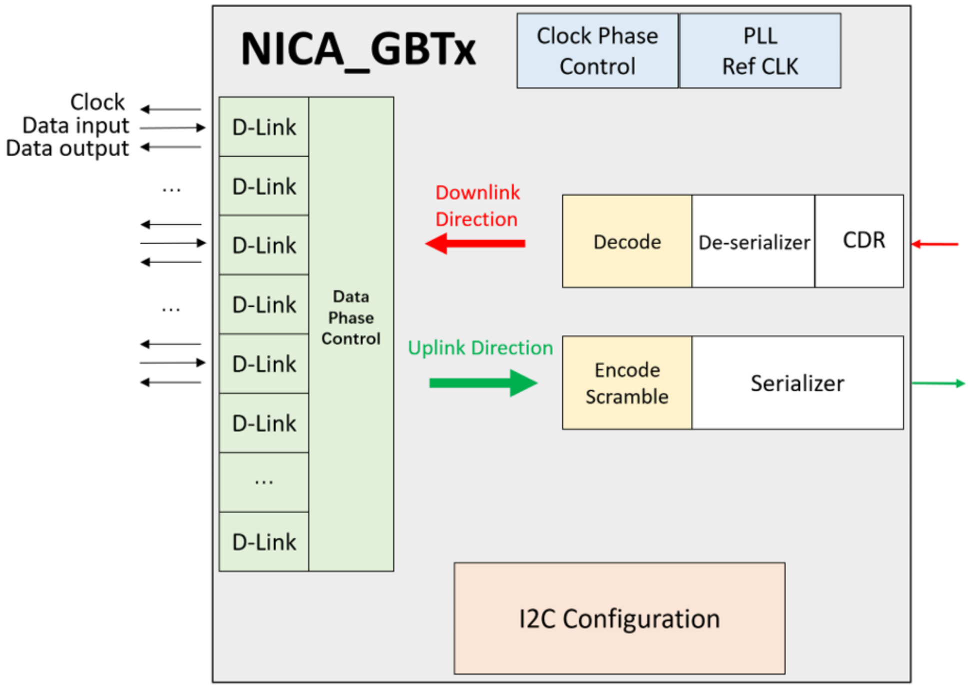

Figure 5.33: Block diagram of NICA_GBTx.

optical transmit channels. However, the final form and channel number of the NICA_LD will be decided and updated here after further discussion from the system level.

It mainly consists of the pre-driver stage and the output driver stage. The pre-driver stage, working as a limiting amplifier (LA), receives the high speed differential signals (CML signals normally) and amplifies them to suffice magnitude with high enough bandwidth. The output driver stage would transfer the differential voltage signals to the single-end current signal for driving the laser outside the chip.

The vdd12 and vdd25 power supplies shown in Figure 5.34 are currently compatible with the GBLD laser driver from CERN. It may change according to the power supply conditions at the system level.

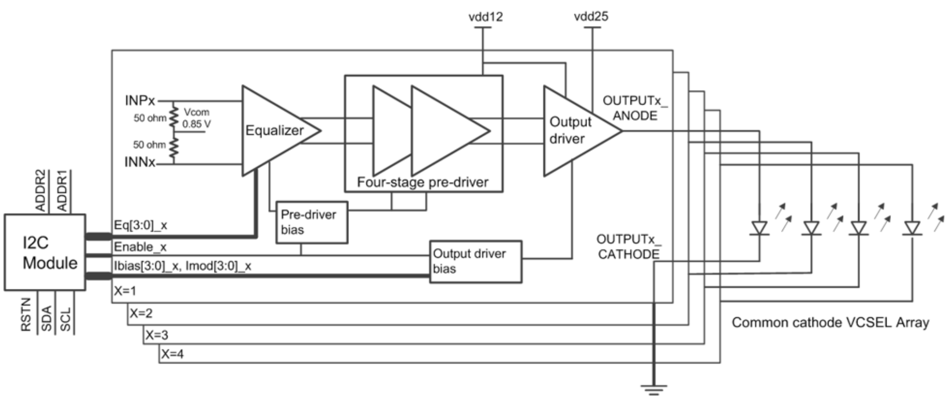

Figure 5.34: Current block diagram of NICA_LD prototype.

5.3.4.2.3 NICA_TIA

NICA_TIA is an analog transimpedance amplifier ASIC located at the downlink direction as shown in Figure 5.32. It receives high speed serial data (small current signal) from PD in the optical module, amplifies and transfers it to the differential voltage signals (CML signals). Figure 5.35 illustrates the block diagram of the NICA_TIA prototype under design. Similar to the current NICA_LD prototype, NICA_TIA adopts also the four channel array form, which will work with a four channel PD array. The final form and channel number of the NICA_TIA will also be decided by further discussion.

The main submodules of the NICA_TIA are TIA core and limiting amplifier as shown in Figure 5.35. The TIA core directly receives the small current signal from PD and performs the transimpedance amplify to obtain the voltage signal at the first step. The following limiting amplifier would further amplify the signal using the differential stages. The final output driver stage is a CML driver to deliver the standard CML logic output.

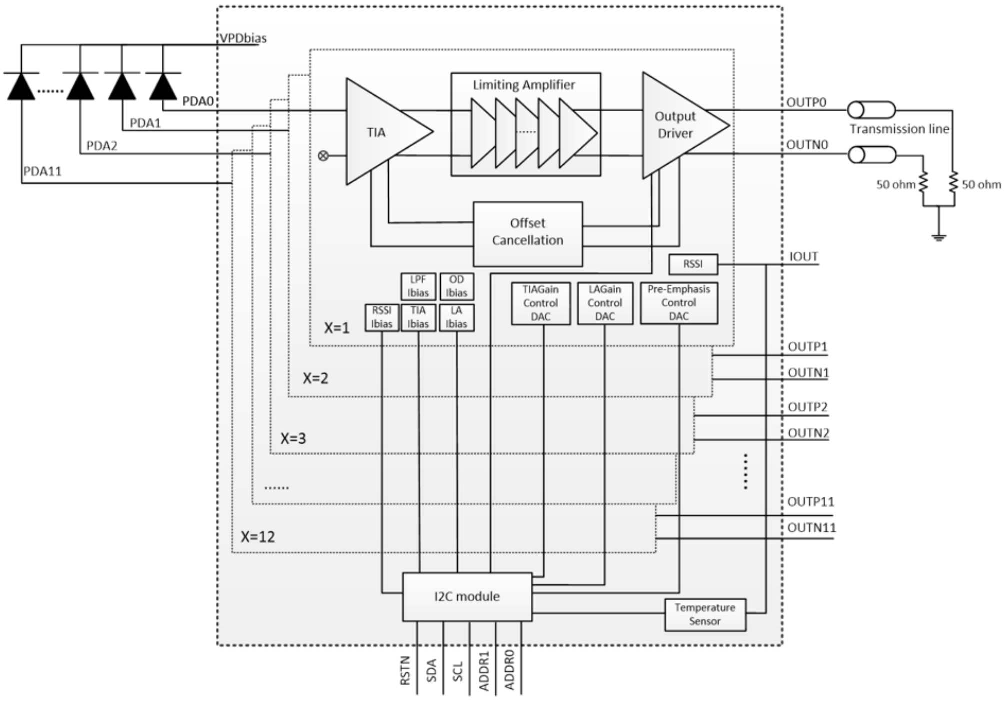

Figure 5.35: Current block diagram of NICA_TIA prototype.

Bibliography

[1] ALICE collaboration, ALPIDE: the Monolithic Active Pixel Sensor for the ALICE ITS upgrade, Nuovo Cimento C 41 (2018) 91. 3 p.

6 The detector control system of ITS

6.1 Tasks of the ITS management and control system

The MPD is a modern experimental setup with complex sub-detectors, one of which is the Inner Tracking System (ITS). During the collection of experimental data, it is necessary to monitor the state of the working systems of the ITS in an automated mode. It is also essential to control and monitor the configurations of the data acquisition system in express-offline mode, including storage, management and visualization of the settings of the components of the readout electronics and trigger (voltage thresholds, time delays, etc.). The status of the ITS systems and the configuration of the data acquisition system directly affect the quality of the recorded data, which also needs to be monitored.

One of the main components that ensure a failure-free operation of the detection subsystems is the so-called "slow" control system, which performs the functions of controlling and monitoring the nodes of a physical installation. The reliability and correct operation of the MPD and its electronic components depend on the control and management systems for the main parameters of the equipment: supply voltage, current consumption of modules and their individual functional units, temperature of microcircuits, environmental humidity and a number of other parameters. Monitoring and control of all the indicated parameters is performed by the Detector Control System (DCS), which allows to control the detector as a whole, as well as its subsystems, and to respond to errors that may occur, avoiding critical states of devices.

The DCS should provide:

- continuous and safe sub-detector control;
- uniform interface to all sub-detectors and elements of technical infrastructure;
- turning the sub-detectors on and off;
- changeable configuration of electronics;
- synchronization of all control and monitoring processes;
- control of installation parameters, generation of alarm and warning messages;
- archiving of the controlled and monitored MPD parameters;
- safe operation of the MPD.

The processing system must meet the most stringent requirements for control systems and research automation and be certified for a high level of security, which simplifies the overall certification of the control system.

The Supervisory Control And Data Acquisition (SCADA) system for processing, visualizing and storing data should be suitable for use in large and complex applications with high demands on scalability, reliability and security, and should provide implementation of special user functions.

The ALICE experimental setup at CERN is used as a prototype for design of the MPD. In particular, many systems of the MPD ITS are either copies or modified versions of the ones of the ALICE ITS. The structure and solutions used in DCS of MPD ITS closely follow the DCS of ALICE ITS.

The ITS DCS will be a part of the general MPD DCS. It is based on WinCC OA software platform developed by ETM company, owned by Siemens AG [1], and uses the JCOP [2] and UNICOS [3] software framework containing common tools and components of control systems developed by collaboration of CERN experiments.

6.2 Architecture of the ITS management and control system

The ITS DCS will control the operation of the power supply system, the cooling system and the front-end electronics. It is a subsystem of the general MPD DCS, but it should be able to work autonomously for maintenance and troubleshooting operations. For that it should store locally all necessary configuration data, and its local operator's GUI should have the relevant design. A finite state machine (FSM), describing the ITS, should be included in the ITS DCS.

The MPD detector control system assumes a three-level hierarchical structure. The two upper levels of the control system are based on SCADA. These levels contain one system per sub-detector and one root control node. To ensure convenience in working with the nodes of the control system, several User Interfaces (UI) are used, connected to each node and running on separate computers. Thus, each of these additional control computers has the ability to execute window panels of several distributed subsystems.

The lower level of the hierarchy of the control system consists of server computers that provide exchange with sub-detector equipment in order to offload the upper-level computing power from the equipment polling procedures performed on a low-level communication protocol that require significant computer time. SCADA should only receive filtered result information containing only relevant data.

The general scheme of ITS DCS control is depicted in Figure 6.1.

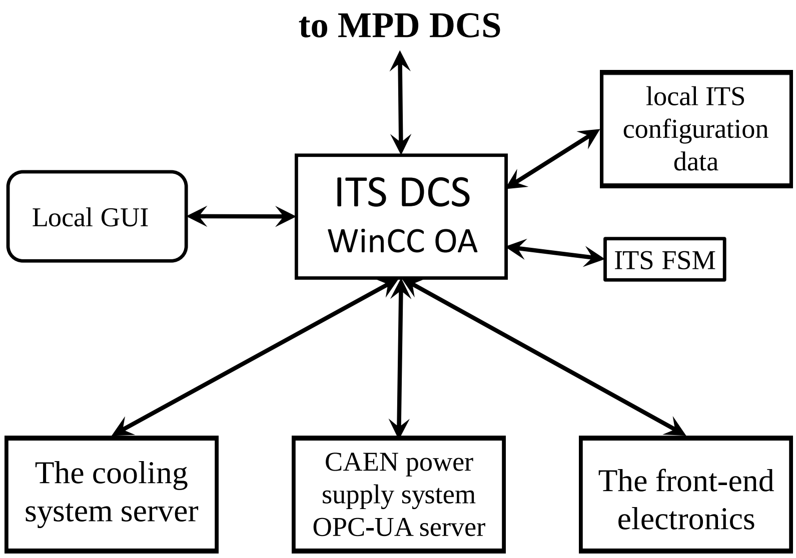

Figure 6.1: Scheme of the ITS DCS.

6.3 Main components of the ITS DCS

6.3.1 Low Level Interfaces (DIM, OPC)

The developed communication interfaces (communication servers) must correspond to an increased data transfer rate, since the transmitted data volume will be quite large.

Communication interfaces should be able to be flexibly configured when replacing and disconnecting electronics modules.

The lower level of the hierarchy of the control system consists of server PCs that provide exchange with sub-detector equipment. The server should be able to debug and test the system at a low level and should allow to see the flow of information in the I/O system. If the communication protocol with the equipment is complex, it is necessary to develop a hardware emulator that will simplify the diagnosis of the problem and troubleshooting.

The Object Linking and Embedding (OLE) Process Control protocol is based on Component Object Model/Distributed Component Object Model (COM/DCOM) technology. The Distributed Information Manager protocol (DIM) was developed at CERN. The DIM software package includes the WinCC OA API managers for both the DIM client and server. The DIM addresses variables by their name. The sub-detector must have its own domain to provide internal exchange between servers and clients.

Programs that provide exchange with hardware should be compiled executable modules that are "hardware servers".

6.3.2 Control of the ITS Power Supply System

CAEN low voltage power supply system provides power for the MPD ITS. A scheme of the power supply control chain is depicted in Figure 6.2. The ITS DCS communicates with the JCOP OPC-UA server running on a LINUX PC via OPC-UA protocol.

The server communicates with the CAEN software running on A4548 CPU installed in SY4527 mainframe crate of the power supply system. A proprietary communication protocol built on top of the IP is used, with Ethernet being the physical link. The server is, actually, an interface between the OPC-UA and CAEN protocols.

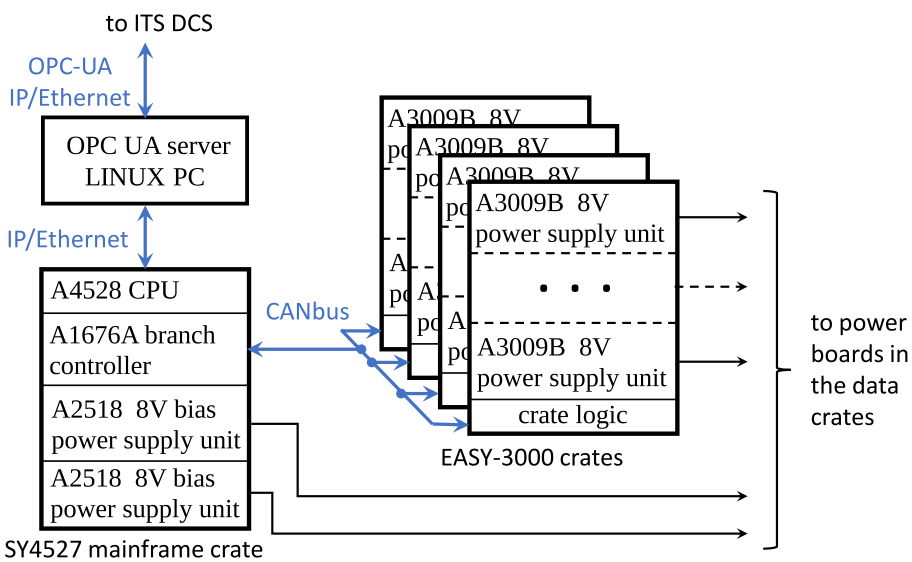

Figure 6.2: The ITS power supply control.

A4548 CPU controls the A2518 power supply units, installed directly in the mainframe crate, via the local bus. The units supply bias voltages for the sensors.

16 units of multichannel A3009B power supply will be used to provide power for analog and digital circuits of the ITS outer barrel pixel sensors. They will be installed in 4 CAEN EASY-3000 crates close to the MPD, in environment with magnetic field and radiation. The

crates are connected via CANbus to A1676A branch controller in the mainframe crate, and are visible to its A4528 CPU via the mainframe local bus.

6.3.3 Control of the ITS Frontend Electronics

The frontend control subsystem of the ITS DCS controls the ITS power boards and the pixel detector chips.

The power boards (PB) are powered from the CAEN power supply units. The PBs convert and split the voltages to several power channels and feed the power supply lines that go to the ITS staves. The DCS allows to monitor and adjust the voltages, and turn the power lines on and off. The control data are transmitted via I2C interface connecting the PB to the readout unit (RU), which, in turn, relays the control data further to the ITS DCS.

The frontend control subsystem also controls about 9000 pixel detector chips, and that is why it is the most complex part of the ITS DCS. The chips are sophisticated devices with complex internal structure and require elaborated configuration and control operations. Each single chip should be individually configured depending on the ITS operation mode.

The chip control data are transmitted over a serial line using half-duplex protocol. Several chips may be connected to the same line forming a serial bus. Two types of serial lines are used: a local line, connecting several chips to each other within a flexible printed circuit (FPC) on which they are installed, and a "global" line that connects chips to the readout unit located outside of the MPD volume The global line is implemented as copper differential line with length of several meters and a bandwidth of 80 Mbits/sec. The RU of the ITS outer barrel drives 4 differential control lines connected to a single stave.

The ITS outer barrel chips are connected hierarchically. Only one of each seven chips (the master) is connected to the global line. The other six ones (the slaves) are connected to the master via a "local" serial line. The master relays the control data with a relevant address between the global line and the slave.

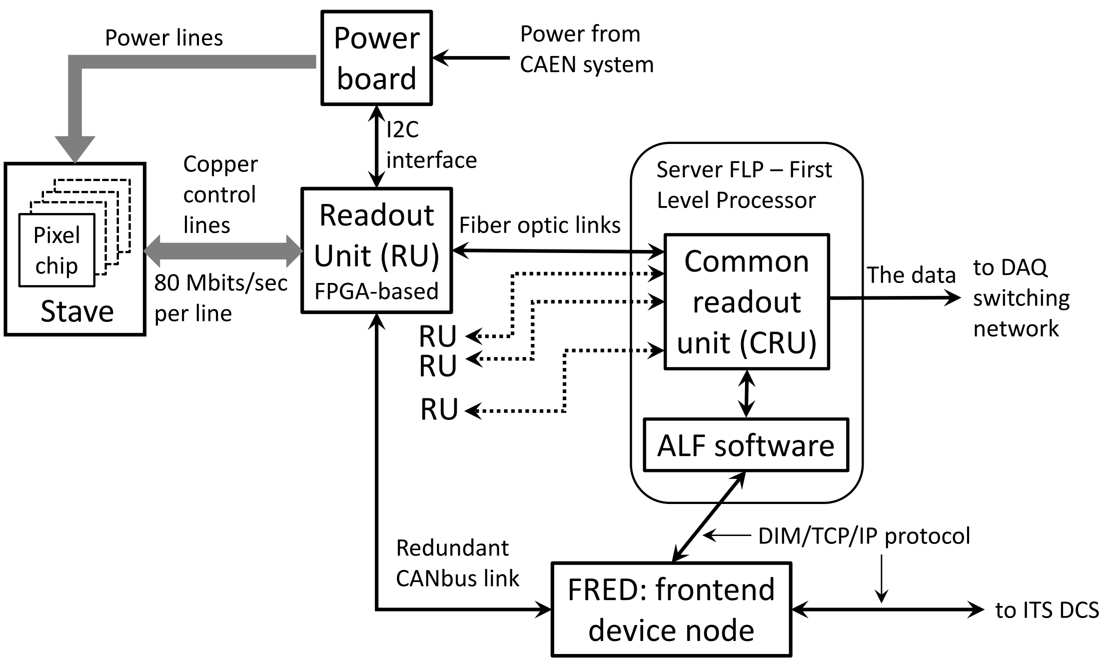

Figure 6.3: The single stave control scheme.

The control chain of an ITS stave is depicted in Figure 6.3. The stave control serial lines are connected to circuits of the RU which provides two uplink data paths.

The first path is used at normal ITS operation. The control data are transmitted together with the detector raw data via the optical link between the RU and the common readout unit (CRU). The data multiplexing is performed by the RU firmware at one end of the link, and, at another end, by the CRU firmware and software running in the CRU board server – the First Level Processor (FLP). Then, the control data are relayed via DIM protocol further to the ITS DCS frontend node FRED.

The second control data path is redundant. It is implemented with a CANbus link that connects the RUs with the corresponding FRED node in bypass of FLP. The CANbus bandwidth is by orders of magnitude less than the one of RU-CRU fiber-optics link. However, it allows to perform basic control operations when FLPs are down and enhances the safety of ITS operation.

The FRED is a software entity that serves as an interface between WinCC OA and the ITS frontend electronics. The ITS DCS sees FRED as a WinCC OA device server. The DCS may command FRED to set the frontend electronics parameters like voltages, thresholds, timing etc. and may retrieve the frontend status data like temperature, currents, errors. FRED converts the DCS commands into low level command sequences that are transmitted via the serial control data links to the frontend electronics. The conversion between the DCS high level commands and the low level frontend commands is a CPU-intensive procedure. Hence, FRED takes the computational load of the WinCC OA.

6.3.4 Control of the ITS Cooling System

For a temperature system, which is an autonomous part and programmed using Programmable Logic Controller (PLC), the Data Integration Protocol (DIP) is used as low-level communication interface.

6.3.5 Alert System

The ITS DCS should continuously monitor all required parameters, compare them to threshold values and issue warning signals on the central alarm screen if a safety threshold is exceeded and programmatically processes these signals. Warnings from both, the lower and upper sides of the monitored value may be of three levels, depending on the degree of deviation from the norm: Warning (Warning), Error (Error), Fatal (Alarm). Certain operator actions should be provided for each level, as it is shown in Figure 6.4.

The warning system consists of settable threshold values for sensors, warning classes, and warning messages displayed on the central alarm screen. The threshold values of the sensors may change over time, therefore, a software interface is required that allows to easily and quickly change the threshold values in all recipes, not only to system experts, but also to those on duty for the sub-detector.

To prevent emergency conditions and failure of nodes, it is planned to develop special software that will automatically turn off the high-voltage and low-voltage power supply systems of the sub-detector upon receipt of a certain number of warning messages of the "Alarm" level.

The threshold values of all monitored sensors and alarm messages should be clearly documented, which includes a description of each alarm and the required actions of the person on duty for this alarm.

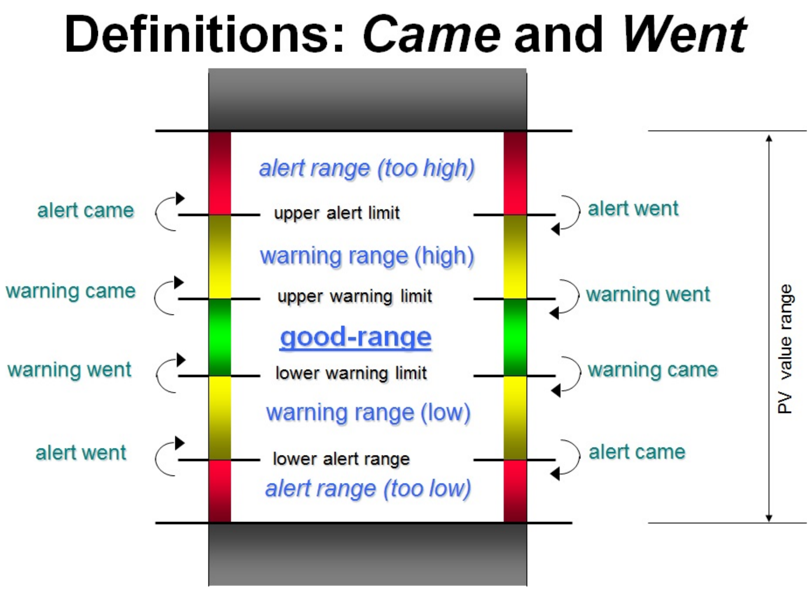

Figure 6.4: Schema of the ITS DCS alarm system.

6.3.6 ITS monitoring system

Monitoring software should provide:

- view trends of any controlled parameter;
- convenient graphical menu, providing:
  - any time interval for viewing a trend;
  - any scaling and graph view;
  - the ability to save the graphs in a format convenient for physical processing;
  - the ability to determine the physical location of the monitored sensor.

6.3.7 Databases (Condition DB, Configuration DB)

Databases should provide:

- authorized connection to databases (Condition DB, Configuration DB);
- archiving of all monitored parameters;
- the set of the ITS configurations may be modified by the configuration editor;
- the ability to save the sub-detector configuration;
- the ability to store and quickly load sets of HV and LV values when changing the operating mode;
- the selection of parameters from the configuration database is performed by the client executing the request in accordance with the selected data set mode.

6.3.8 System Access (remote and local) and access control.

User access to computers of the control and monitoring system should be carried out both locally and remotely. Access control must be protected. Login with a password or a list of experts allows a certain level of management. Logging in without a password allows only for visual observation without intervention in management.

Each user with administrator rights has the ability to change login rights and passwords. The following features will be provided for this: *Log Out*, *Log In*, *Tools*, *Change Password*, *Administration*, and *Help*.

1. *Log Out* - exit the current user mode.
2. *Log In* - logging in a new user. In this case, the current user mode will be closed.
3. *Tools* - allows you to find a specific user or see the current users of subsystems.
4. *Change Password* - change the password of the current user.
5. *Administration* - provides access to administration / management functions on the basis of levels "Users", "Groups", "Domains".
6. *Help* - help on the component Framework Access Control.

The *Domains* level allows you to create and modify system domains. A domain named ITS will be created specifically for users of the ITS project, and will include the following user groups:

- ITS_developer - users with full access to all system components. Such users can modify the existing code as desired, add and remove detector subsystems, start FSM, and change the state of system components.
- ITS_expert - users who have the right to change the states of system components, if the developer gave them the opportunity to do so.
- ITS_operator - has the same rights as ITS_expert.
- ITS_observer - an observer who has the right only to monitor the current state of the system, but is not allowed to change its state in any way.

By default, all members of the ITS collaboration have *observer* status for all ITS subsystems.

Bibliography

[1] ETM website: https://www.winccoa.com

[2] CERN JCOP Project: https://jcop.web.cern.ch

[3] CERN UNICOS Project: https://unicos.web.cern.ch

7 Detector Performance

7.1 The MPD TPC in a nutshell

The Time-Projection Chamber (TPC) is the main tracking detector of the MPD central barrel and its basic design parameters are summarized in Table 7.1.

Table 7.1: Basic parameters of the TPC.

Parameter	Value
Length of the TPC	340 cm
Vessel outer radius	140 cm
Vessel inner radius	27 cm
Drift volume outer radius	133 cm
Drift volume inner radius	34 cm
Drift volume length	163 cm (each half)
HV electrode	Membrane at the center of the TPC
Electric field strength	140 V/cm
Magnetic field strength	0.5 T
Drift gas	90% Ar+10% Methane
Gas amplification factor	104
Drift velocity	5.45 cm/µs
Drift time	<30 µs
Temperature stability	<0.5 °C
Number of readout chambers	24 (12 per each End-plate)
Segmentation in φ	30 °C
Pad size	$5\times12\,\mathrm{mm}^2$ and $5\times18\,\mathrm{mm}^2$
Number of pads	95232
Pad raw numbers	53
Zero suppression	up to 90%
Maximal event rate	<7 kHz (Lum. 10^{27})
Electronics shaping time	180−190 ns
Signal-to-noise ratio	30:1
Signal dynamical range	10 bits
Sampling rate	10 MHz
Sampling depth	310 time buckets
Resolution of two tracks	1 cm

It is the detector for 3-dimensional precise tracking of charge particles and will provide:

- an overall acceptance of η <1.2;
- a momentum resolution for charge particles under 3% in the transverse momentum range $0.1 < p_T < 1$ GeV/c;
- a resolution of two tracks of about 1 cm;

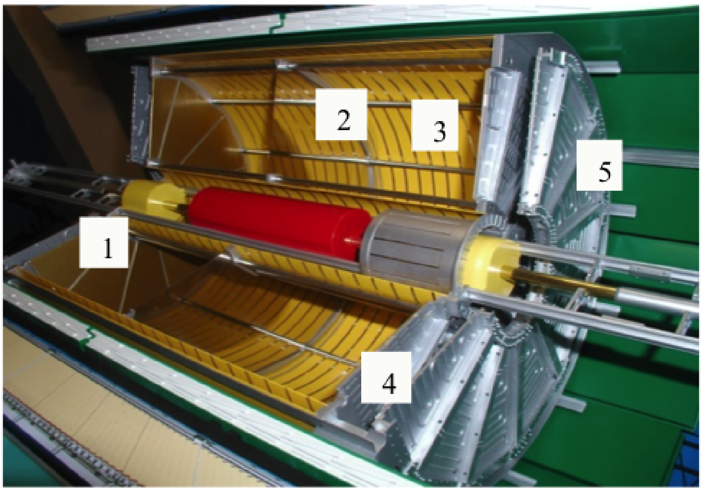

Figure 7.1: MPD-TPC mock up. 1-MWPC; 2-HV electrode; 3-Field cage; 4–Flange with MWPCs and FEE electronics; 5-End cap thermal screen. .

- Hadron and Lepton identification by dE/dx measurements with a resolution better than 8%.

These requirements must be satisfied at the NICA design luminosity with event rate about 7 kHz and maximum charged particle multiplicity up to 1000 tracks in central Au-Au collisions.

Track reconstruction is based on drift time and rφ coordinate measurement of primary ionization clusters created by charge particle. In order to minimize the error in the absolute track point position measurement by TPC, it is necessary to take into account both, static and time-dependent distortions in the drift path of the ionization cloud. The static distortions are the result of non-uniformities in the magnetic ($\vec{B}$) and electric ($\vec{E}$) fields. The time-dependent distortions may result from the changes in gas performance, environmental variables (temperature or atmospheric pressure), or from spontaneous failures.

The TPC consists of four cylinders (C1-C4) manufactured by the Russian industry from composite materials (Fig. 7.1). This approach results in cylinders with small radiation length ($0.4\,\mathrm{g/cm^2}$) and enough strength along the axial direction (in the worst case, the deformation in the middle of the cylinder at a load of 80 kg is less than 100 µm. Two aluminum flanges interconnect all four cylinders. Nitrogen gas (N_2) is blown through the gap between C1–C2 and C3–C4 as a protection against high-voltage discharges and prevention from H_2O and O_2 diffusion into the drift volume of the TPC.

The central high-voltage electrode membrane divides the drift volume into two parts and creates the necessary electric field strength for the drift of the generated electron-ion clusters to the TPC end-caps (Fig. 7.1, pos. 2). The membrane is produced with the 110 µm Mylar film. The non-uniformity of the magnetic field must be not worse than $\vec{B}r/\vec{B}z \sim 10^{-4}$. The Field cage (Fig. 7.1, pos. 3) is symmetrical with respect to the high-voltage electrode consisting of 112 pairs of 13 mm-wide mylar strips (outer and inner structures) stretched on special rods with the same pitch and an accuracy of 50 µm. The high-voltage electrode is connected to the nearest mylar strip by a resistor, and each subsequent strip is connected to the next one by a resistor. This chain forms a HV divider from -24 kV (high voltage electrode) to zero (TPC end-caps).

The main subsystems of TPC include:

- Readout Chambers (ROC);

- Gas System;
- Laser Calibration System;
- Cooling System;
- FEE, Readout and DAQ;
- DCS;
- HV and LV systems.

7.2 Simulations of the TPC-ITS tracking system

This section presents the results of modeling the functionality of the MPD tracking system including the TPC and the ITS, as well as the basic algorithms for the track reconstruction.

7.2.1 ITS Pointing resolution for different beam pipe diameters

The spatial resolution of the design of the MPD-ITS was evaluated in the framework of the simplified code developed by the ALICE collaboration which allows the tracking of charged particles through cylindrical silicon layers with a specified radiation length. At each step of the tracking in a layer with a given radius, a covariance noise matrix is calculated which takes into account multiple scattering that degrade the angular resolution when moving to the next layer.

The characteristics of the MPD-ITS silicon layers with an average radius r for the configuration used in the calculations are presented in Table 7.2.

Table 7.2: Modelling parameters for a 5-layer ITS with a 40 mm beryllium beam pipe (MPD-ITS).

Layer number	r (mm)	σ(rφ) (µm)	X/X_0 (%)
beam pipe	20.0	-	0.22
1	24.6	4.0	0.30
2	43.3	4.0	0.30
3	62.5	4.0	0.30
4	146.2	4.0	0.30
5	196.0	4.0	0.30

The dependence of the spatial resolution of the MPD-ITS on the transverse momentum of pions, protons, and kaons, the main charged decay products of strange and charmed particles, is shown in Figure 7.2

The deterioration of the spatial resolution in the region of small transverse momenta is due to an increase in the Moliere angle defined by the equation [2]:

$$\theta = \sqrt{2}\frac{13.6\,\mathrm{MeV}}{\beta cp} Z \sqrt{\frac{X}{X_0}}[1 + 0.038\ln(\frac{X}{X_0})], \tag{7.1}$$

where p is the particle momentum, $c\beta$ is its velocity, Z is the charge, X is the thickness of the substance and X_0 is the radiation length.

As it can be seen from Figure 7.2, the spatial resolution of the 5-layer ITS for pions with a transverse momentum of 300 MeV/s is 60 µm, and for kaons and protons with the same transverse momentum, the spatial resulotion is 100 µm and 160 µm, respectively. Such a

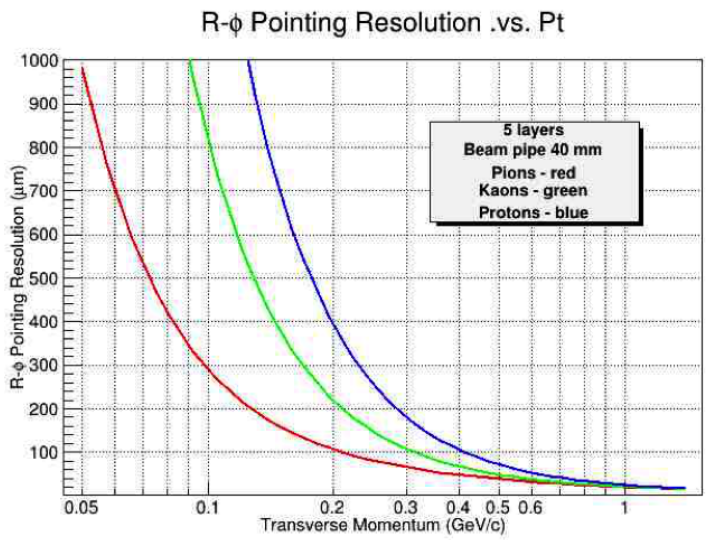

Figure 7.2: Dependence of the spatial resolution of MPD-ITS on the transverse momentum of pions (**red line**), kaons (**green line**) and protons (**blue line**).

resolution would allow for reconstructing the decay vertex of charmed D_0 mesons through the channel $D_0 \to K^- + \pi^+$ (average path length $\lambda = 123\,\mu m$) with small transverse momenta up to 500 MeV/s. Two other configurations were evaluated for the same five layers of MAPS but assuming a beam pipe diameter of 50 mm (configuration ITS5-50) and 60 mm (configuration ITS5-60), respectively.

The geometrical parameters of the IT5-50 and IT5-60 models are shown in Table 7.3, and a comparison of the dependence of the spatial resolution on the transverse momentum of the pions for all three models with 5 layers is shown in Figure 7.3. As it can be seen, the use of a beam pipe diameter with a 40 mm would significantly improve the spatial resolution of particles with a small transverse momentum which is especially important for the reconstruction of the decay vertices of short-lived charmed particles.

Table 7.3: Geometrical parameters of two 5-layer models IT5-50 and IT5-60 (50 mm and 60 mm beam pipe diameter, respectively).

Layer number	IT5-50 r (mm)	IT5-60 r (mm)	IT5-50 & IT5-60 $\sigma(r\varphi)$ (μm)	IT5-50 & IT5-60 $X/X_0(\%)$
beam pipe	25.0	30.0	-	0.22
1	35.0	40.0	4.0	0.30
2	67.4	69.4	4.0	0.30
3	91.3	104.3	4.0	0.30
4	146.2	146.2	4.0	0.30
5	196.0	196.0	4.0	0.30

7.2.2 ITS momentum resolution

The dependency of the momentum resolution on the transverse momentum of protons, pions and kaons, of the 5-layers ITS for a beam pipe with a diameter of 40 mm is shown in Figure 7.4. The simulation was performed using the same code as for the spatial resolution. The input parameters of the ITS model used in the calculations are shown in Table 7.2. The

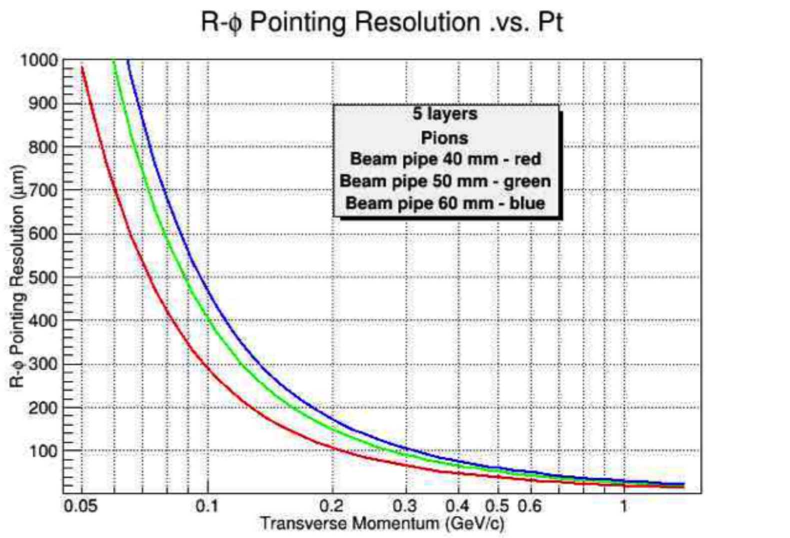

Figure 7.3: Pion track pointing resolution for of a 5-layer ITS and a beam pipe with a diameter of 40 mm (**red line**), 50 mm (**green line**) and 60 mm (**blue line**).

particles were tracked in a magnetic field of 0.5 T.

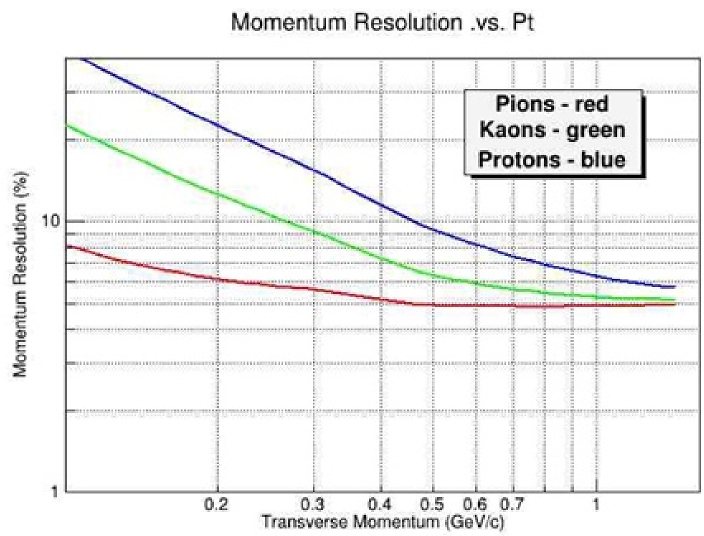

Figure 7.4: Dependence of the momentum resolution of the IT5-40 on the transverse momentum of pions (red line), kaons (green line) and protons (blue line).

As it can be seen from Figure 7.4, the momentum resolution of pions remains almost constant value of 5 % over a wide range of p_T. On the other hand, for heavier particles (kaons and protons) the resolution deteriorates at low p_T values and reaches a level of 5 % only at $p_T > 1\,\mathrm{GeV/c}$.

7.2.3 ITS+TPC simulation tools

The simulation of the MPD ITS+TPC tracking system was carried out using the MpdRoot software [3] the main interfaces and components of which are shown in Figure 7.5. The

GEANT software package integrated into the MpdRoot provides the Monte Carlo (MC) transport of particles delivered by a suitable event generator. At the transport step an output file is generated with information on the coordinates of all particle tracks falling into the sensitive volume of the detectors. At the reconstruction step the detector responses are formed and charged particle tracks are searched using the Kalman filter method [4] .

The generation of the signal from the pixel detectors required for the track reconstruction was performed using a hit-producer software module specially developed for this purpose. This module converts MC transport data into the digitized response of the detector providing a connection between the MC points of the tracks falling into the detector and the information read out from the detector by electronic circuits. In the case of pixel sensors, this information is the column and row numbers for the corresponding pixel in the pixel matrix on which the charge is released due to the passage of a charged particle through the detector.

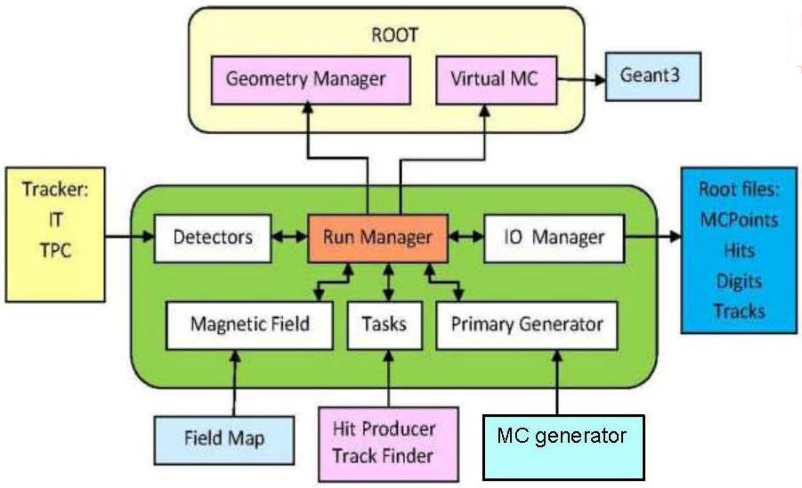

Figure 7.5: The software environment of MpdRoot.

The track reconstruction procedure includes two stages: track search [4] and track fitting [5]. The track search is based on the Kalman filter algorithm which begins by selecting a cluster in the initial layer of detectors and then attaches the cluster in the next layer, and so on layer by layer. The tracks found in the TPC by a large number of clusters (~ 40) are then extended to the ITS. After the candidate tracks that match all possible combinations of different clusters in the same layers are selected, they are fitted to choose the best track with the minimum value of χ^2.

7.2.4 ITS+TPC track reconstruction efficiency

The tracking efficiency of the MPD tracking system including the TPC and the project configuration (ITS5-40), was estimated with MpdRoot using the QGSM [1] central event sample of 10^5 Au+Au collisions at $\sqrt{S_{NN}}$=9 GeV. The efficiency of the track reconstruction of charged primary particles as a functions of their transverse momentum p_T is shown in Figure 7.6. As it can be seen the reconstruction efficiency of proton and pion tracks is close to 100 %, starting from $p_T > 200$ MeV/c, while the Kaon track reconstruction efficiency reaches 90 % at $p_T > 400$ MeV/c.

The track reconstruction efficiency of secondary particles was estimated on the example of pions and protons formed as a result of the decay of Λ -hyperons in the channel $\Lambda \to \pi^- + p$. For this purpose 5×10^3 events of central Au + Au collisions at $\sqrt{S_{NN}}$= 9 GeV

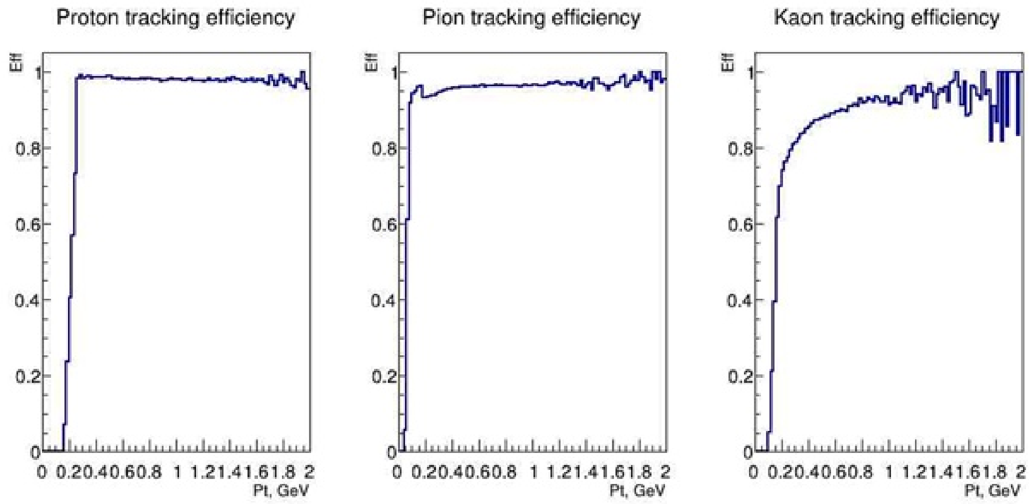

Figure 7.6: Track reconstruction efficiency of primary tracks for protons, pions and kaons generated in 10^5 events of central Au+Au collisions at $\sqrt{S_{NN}}$= 9 GeV as a function of their transverse momentum.

were processed with the formation of about 20 Λ in every event. Figures 7.7 and 7.8 show the transverse momentum distribution of the generated and reconstructed decay products of Λ-hyperons, as well as the dependency of their tracks reconstruction efficiency on the particle transverse momentum. It can be seen that the tracking algorithm used provides reliable track reconstruction of the secondary pions and protons reaching an efficiency level of 90 % at p_T above 150 MeV/c and 400 MeV/c respectively.

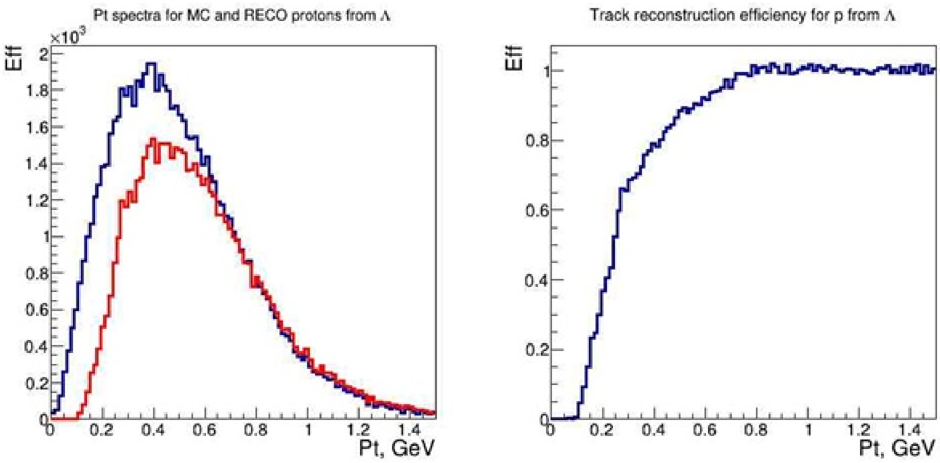

Figure 7.7: p_T distribution of the generated (blue) and reconstructed (red) protons from the Λ decay (left) and the reconstruction efficiency of their tracks depending on p_T(right)

7.2.5 Phase space coverage for protons and pions

The reconstructed tracks of protons and pions formed in 10^4 events of central Au + Au collisions at $\sqrt{S_{NN}}$= 9 GeV and simulated using the QGSM generator were considered in order to estimate the phase space covered by the ITS + TPC tracking system. Along with the tracks

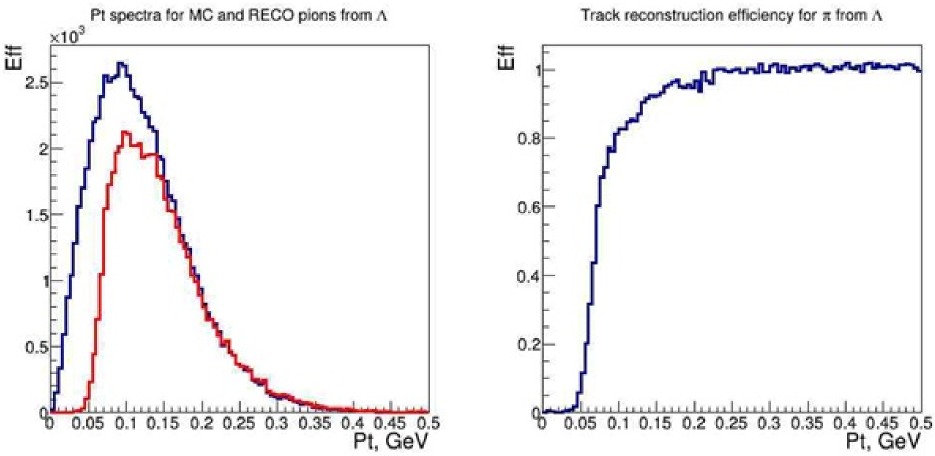

Figure 7.8: p_T distribution of the generated (blue) and reconstructed (red) pions from the Λ decay (left) and the reconstruction efficiency of their tracks depending on p_T(right)

of particles coming from the vertex of the nuclei interactions the tracks of secondary pions and protons, the decay products of Λ-hyperons, were analyzed. 2-dimensional distributions on the rapidity–transverse momentum plane are shown in Figure 7.9 for primary particles and in Figure 7.10 for secondary particles. As it can be seen the proposed TPC+ITS setup has a sufficient coverage to study both the longitudinal and transverse distributions of primary and secondary particles.

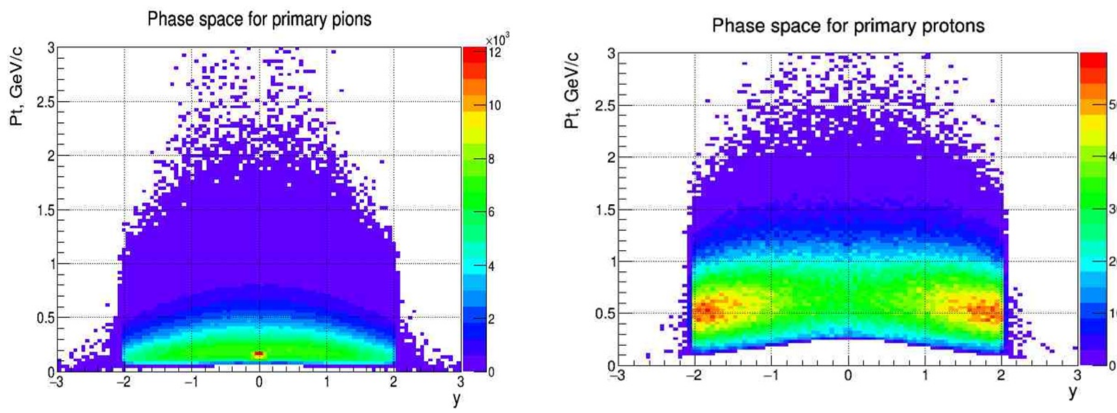

(a) (b)

Figure 7.9: y-p_T phase space of primary pions (a) and protons (b) covered by TPC+ITS setup.

7.2.6 Vector finder algorithm for TPC+ITS track reconstruction

The current MPD track reconstruction method is based on the Kalman filter in the TPC. Its simple extension to the ITS is not adequate to fully exploit the potential of the MAPS-based detector, therefore such a method can not be considered as a good tool to study the ITS performance. That is why another Vector Finder algorithm, based on the cellular automaton approach [7] was developed. The main idea of the method is to run a combinatorial search of hit pairs belonging to the same track using a priori constraints to reduce the combinatorics. Presumably, such a method should produce good results for tracks with relatively small

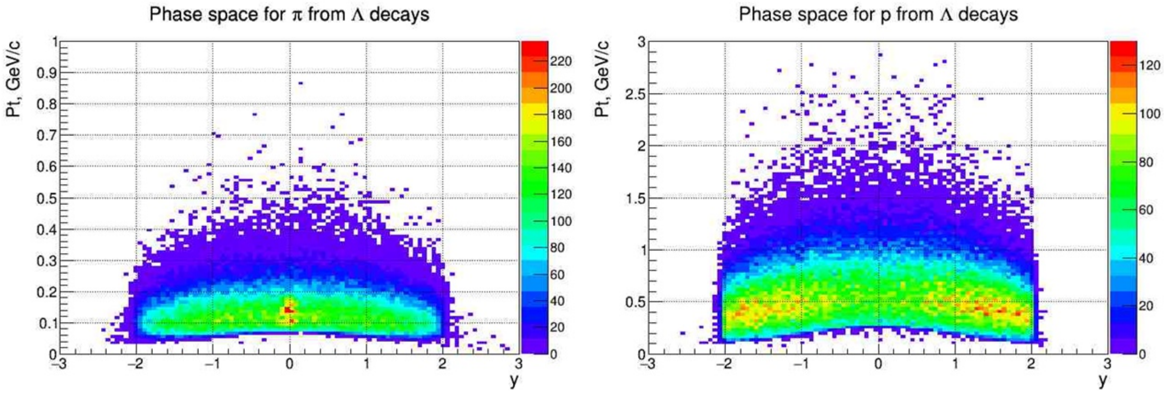

(a) **(b)**

Figure 7.10: y-p_T phase space of secondary pions (left) and protons (right) from Λ decays coved by TPC+ITS setup.

number of hits per track as is the case for the stand-alone ITS tracking.

The "Vector Finder" algorithm [8] is an optimized combinatorial search that uses information about the angular positions of hits in the transverse (ϕ) and longitudinal (θ) projections relative to the beam axis to construct track candidates.

In the longitudinal plane the magnetic field directed along Z does not affect the track trajectory and the track is close to a straight line. Therefore in order to extend the candidates for the tracks for each next layer of the detector, an "angular window" *epsphi* of constant size is used, as shown in Figure 7.11. In the transverse projection, the candidate for the tracks should be close to the arc of a circle, the radius of which is determined by the transverse momentum of the particle creating the track. The size of the angular window *epsphi* is inversely proportional to the current estimated transverse momentum of the particle, as shown in Figure 7.12.

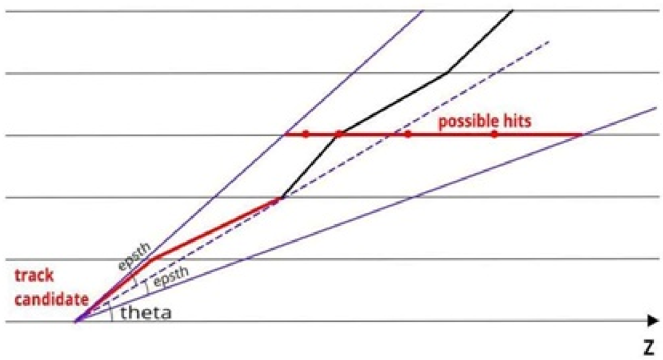

Figure 7.11: Choosing of angular window for tracks in longitude plane

For analysis of particles momentum, a minimum of 3 hits is needed. The 1st hit for the primary track is the interaction point (see Figure 7.13). The illustrations for the schematic projections of the tracks presented in Figures 7.11 and 7.13 are made for the version of the algorithm that constructs the candidate for the tracks starting from the interaction point. Currently it is used the algorithm version which starts to build candidates for tracks from the last layer of the detector.

The track reconstruction algorithm for the 5-layer ITS is as follows:

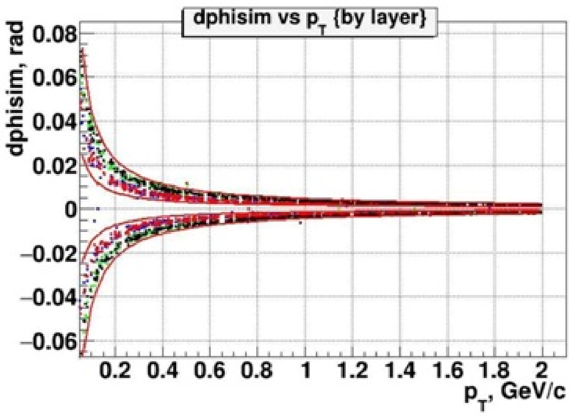

Figure 7.12: Choosing of angular window for the track in the transverse plane

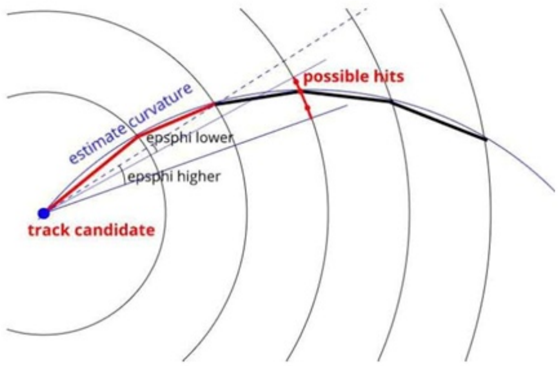

Figure 7.13: Projection of the track on the transverse plane for the particle momentum analysis

1. The initial candidates for the tracks are built backwards starting from their hits in the last layer of the detector.

2. For the remaining layers of the detector (1 - 4) the hits are organized into multimap structures, where they are sorted by transverse and longitudinal angles (for each layer there are two multimaps for transverse and longitudinal angles, respectively).

3. For each track candidate:

    - the transverse momentum is estimated for layers 1-3 (at least 3 hits are needed, including the interaction point to estimate the track curvature). For layer number 4 the angular windows are taken in a very large size in order to guarantee the inclusion of all possible candidates for the tracks;
    - the dimensions of the angular window in the transverse and longitudinal projections are calculated and the corresponding hits are extracted from the related multimap, resulting in two sets of hits; those that went into the angular window for the transverse projection and those for the longitudinal projection;
    - the two sets (angular and longitudinal) are intersected and for each hit in the resulting intersection set a new track candidate is created for the next detector layer.

The tracking algorithm was implemented as part of MpdRoot framework for the 5-layer geometry of the ITS detector. The algorithm was tested using UrQMD event generator for central Au + Au collisions at $\sqrt{S_{NN}}$=9 GeV.

The quality of the tracking is shown on Figure 7.14.

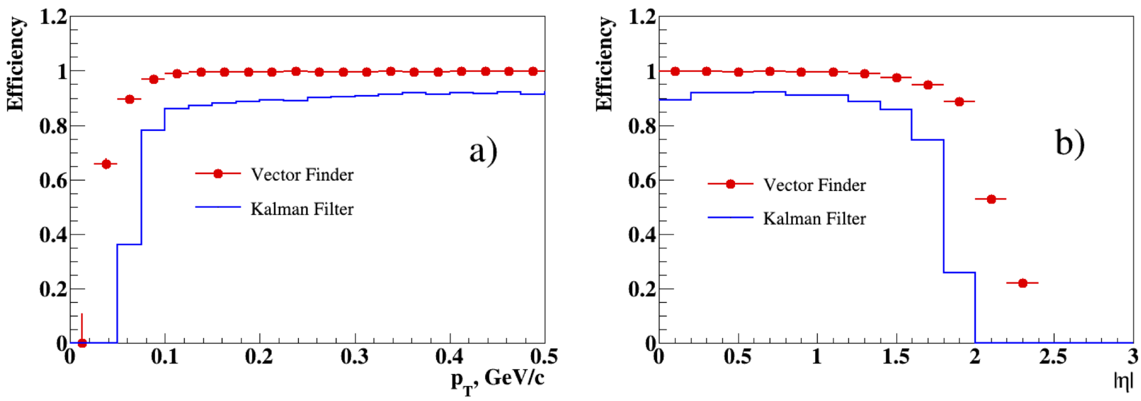

(a) (b)

Figure 7.14: Vector Finder vs Kalman Filter track reconstruction efficiency comparison: efficiency vs p_T at $|\eta| < 1.2$ (a) and efficiency vs $|\eta|$ at Pt > 0.1 GeV/c (b) .

Matching procedure for ITS and TPC tracks

After reconstructing the tracks in the ITS it is necessary to match them with those from the TPC. The following special match-up procedure was developed for this:

1. Extrapolate TPC and ITS tracks to a cylinder around the beam line such that the ITS detector is located inside the cylinder and the TPC detector is left outside (i.e., the cylinder lies in between the two detectors).

2. Update z (longitudinal projection) and *rphi* (transverse projection) coordinates of the tracks using the extrapolations from point 1.

3. For each track from ITS find the set of TPC tracks with coordinates z and *rphi* within the given window from the parameters of the ITS track (see Figure 7.15)

4. Extend the TPC track with hits from the corresponding ITS track if they match each other sufficiently (χ^2 metric is used to verify compliance)

5. If no TPC tracks were found within the specified parameter window, the ITS track is added by default. If several matches were found for one TPC track, it is necessary to choose the best match using the special quality function:

$$quality = N_{hits} + (100.0 - min(\chi^2, 100.0))/101.0 \tag{7.2}$$

   where N_{hits} is the number of hits in the track.

The matching procedure was tested on events received using the UrQMD generator. The resulting dependencies of the efficiency on p_T and on η are shown in Figure 7.16.

The key differences in the reconstruction of secondary tracks are the following:

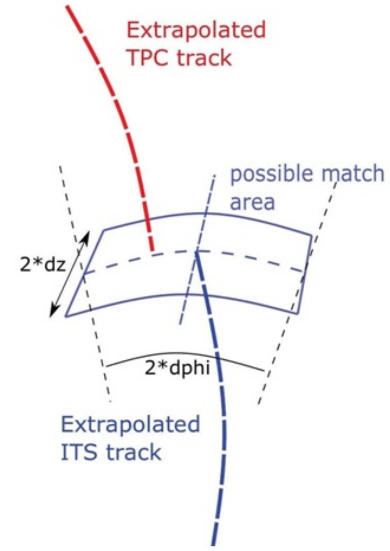

Figure 7.15: Scheme of ITS and TPC tracks matching

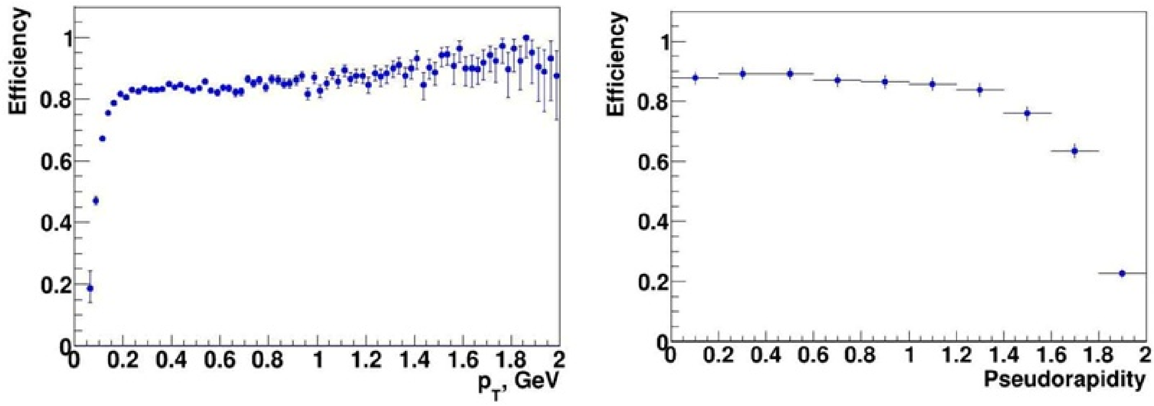

(a) (b)

Figure 7.16: Dependency of matching efficiency for primary tracks on p_T at $|\eta| < 1.2$ (a) and on $|\eta|$ at $p_T > 0.1\,\mathrm{GeV/c}$ (b) .

1. It is impossible to use the interaction point as a “dummy hit” for estimating the momentum of a particle. Thus, in order to evaluate the momentum and determine the size of the angle cuts, it is necessary to look through at least 3 layers of the detector.

2. The angular coordinates of the hits in the longitudinal section of the detector are not useful to restore tracks in this case. Therefore instead of *theta* coordinates, the coordinates of the hits along the z axis are used. Since the track still remains close to the straight line in the longitudinal projection, the difference in the z coordinate between the hits of the track at adjacent levels should be proportional to the distance between the layers of the detector within some possible error margin which is fixed on both sides of the calculated hit location.

The results of restoring secondary tracks for a set of 100 events generated by the UrQMD generator with the parameters indicated above are shown in Figure 7.17.

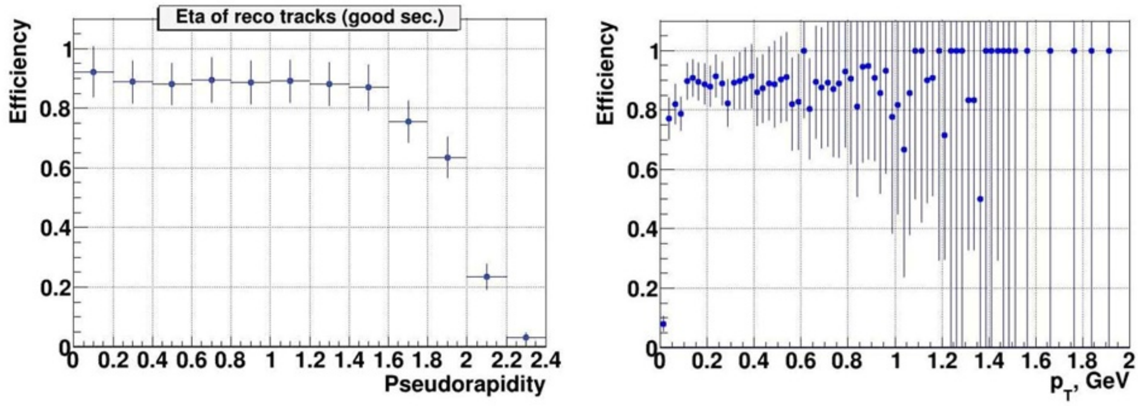

(a) (b)

Figure 7.17: Dependency of secondary tracks reconstruction efficiency on p_T (left) and pseudo-rapidity (right) .

7.3 Conclusions

The main functional capabilities of MPD ITS+TPC tracking system resulting from the computer simulations may be summarized as follows:

- The estimated spatial resolution of the ITS *project* version consisting of 5 coaxial cylindrical layers of pixel sensors around a beam pipe with a diameter of 40 mm shows that it is similar to that of the upgraded inner tracker system of the ALICE facility. Such resolution provides the possibility of reconstructing the decay vertices of the short-lived charmed D^+ and D^0 mesons having a decay length of 312 µm and 123 µm, respectively.

- The momentum resolution of the ITS *project* version for pions, protons and kaons which are the main decay products of strange and charmed particles remains not worse than 10 % in a wide range of transverse momentum p_T down to 400 MeV/c, and for pions it reaches the level of 5 % at $p_T > 400$ MeV/c.

- Estimation of the reconstruction efficiency of charged hadron tracks in the MPD tracking system including TPC and the *project* version of ITS, reaches a 95 % level for primary protons and pions starting from $p_T >$200 MeV/c. For secondary pions and protons a level of 90 % efficiency is achieved at $p_T > 150$ MeV/c and $p_T > 400$ MeV/c, respectively.

- The analysis of the phase space covered by the MPD tracking system for primary protons and pions indicates their reliable registration in the pseudo-rapidity range $|\eta| < 2$, defined by the acceptance of the MPD tracking system.

Bibliography

[1] A. Mastroserio et al., "Simulation tools for the its upgrade", ALICE Internal Note at ‘http://aliceinfo.cern.ch/ITSUpgrade/sites/aliceinfo.cern.ch.ITSUpgrade/ files/documentsUpgrade_IN.pdf’, 2012.

[2] G.R.Lynch and O.I.Dahl. “Approximations to multiple Coulomb scattering”, Nucl. Instr. Meth. B 58 (1991) 6.

[3] MpdRoot Software. http://git.jinr.ru/nica/mpdroot

[4] Fruehwirth R., "Application of Kalman filtering to track and vertex fitting", Nucl. Inst. Meth. A., 2662, 1987, V. 262. p.444-450.

[5] Billoir P. Track fitting with multiple scattering: a new method, Nucl. Inst. Meth. A., 2668, 1984. V.225 (2). p.352-366.

[6] Gudima KK, Mashnik SG, Sierk A. J . User Manual for the Code LAQGSM, Los Alamos National Laboratory Report. LA-UR-01-6804. Los Alamos. 2001.

[7] V. Akishina and I. Kisel, J. Phys. Conf. Ser.599, 012024 (2015)

[8] D.A. Zinchenko, A. I. Zinchenko, E. G. Nikonov. "Vector Finder — a toolkit for track finding in the MPD experiment", Particles and Nuclei, Letters. T 18. No 1(233) C. 134. 2021.

8 Physics Performance

This chapter presents the results of studying the identification capability of the MPD tracking system composed by the TPC and the ITS for the reconstruction of the decay of strange and charmed particles produced in $\sqrt{S_{NN}} = 9\,\mathrm{GeV}$.

The simulations were carried out for various ITS configurations differing in the number of detector layers used and the beam pipe diameter. Section 8.2 presents the results of the hyperons reconstruction with an ITS version consisting of only two outer layers of MAPS (Outer Barrel) and a beam pipe diameter of 64 mm. The reconstruction of both strange and charmed particles with the 5-layers ITS including the Outer and Inner Barrels and a beam pipe whith a diameter of 40 mm and 64 mm is considered in section 8.3.

8.1 Simulation methods

Reliable identification of short-lived charmed particles can be performed by determining the invariant mass of their decay products. So, for an efficient reconstruction of decay vertices close to the interaction point an inner tracking system with high pointing resolution is needed. The identification of specific decay pattern is difficult due to the presence of a large combinatorial background related to all charged particles emerging from the primary collision vertex. This background is especially large (S/B$\sim$1:10^3) in heavy ion collisions. Therefore, the measurement of the yields of charmed mesons and baryons should be based on a highly efficient reconstruction of the secondary decay vertex of short-lived particles.

The identification ability of the MPD ITS during the reconstruction of strange and enchanted particles was assessed in the MpdROOT framework

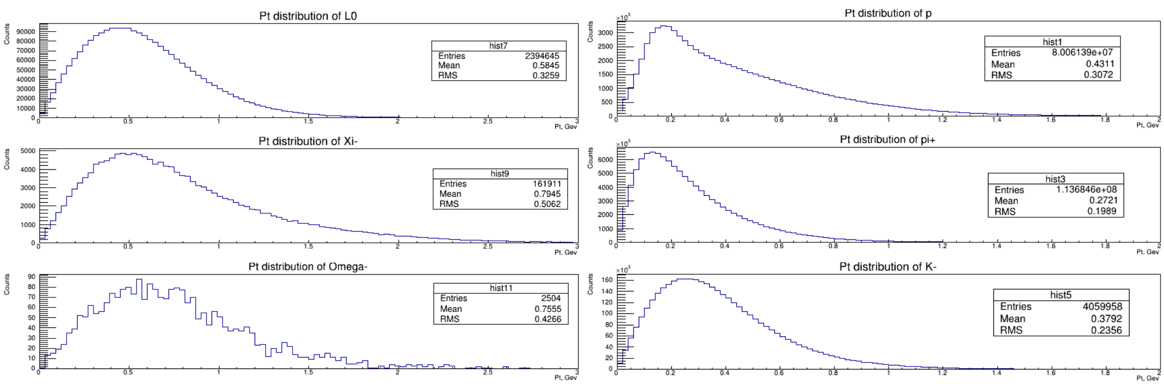

(a) (b)

Figure 8.1: Transverse momentum spectra of Λ, Ξ^- and Ω^- hyperons and charged particles p, π and K, generated by QGSM in 10^5 central Au + Au collisions at $\sqrt{S_{NN}} = 9\,\mathrm{GeV}$.

The QGSM event generator, based on the quark-gluon string model [1], was used to generate nucleus-nucleus collisions events at the energies of the NICA collider ($\sqrt{S_{NN}}$=4÷11 GeV). Figure 8.1 shows the transverse momentum distributions of strange particles generated in 10^5 central (b < 4 fm) collisions at $\sqrt{S_{NN}} = 9\,\mathrm{GeV}$, as well as the transverse momentum spectra of charged particles conforming the combinatorial background during the reconstruction of hyperons in the decay channels indicated in Table 8.1.

Pure signal events corresponding to decays of multi-strange and charmed particles (see Table 8.1) were generated by tuning the thermal generator [2] to the energy of NICA collider.

Table 8.1: The decay channels of strange and charmed particles used for their reconstruction in the MPD tracking system.

Hadron	Mass (MeV/cm^2)	Average path length $c\tau$(mm)	Decay channel	BR (%)
Λ	1115.68 ± 0.01	78.9	$\pi^- + \mathrm{p}$	63.9
Ξ^-	1321.71 ± 0.07	49.1	$\pi^- + \Lambda^0$	99.9
Ω^-	1672.45 ± 0.29	24.6	$K^- + \Lambda^0$	67.8
D^+	1869.62 ± 0.20	0.312	$\pi^+ + \pi^+ + K^-$	9.13
D^0	1864.84 ± 0.17	0.123	$\pi^+ + K^-$	3.89
D_s^+	1968.474 ± 0.032	0.150	$\pi^+ + K^+ + K^-$	5.49

A strict set of criteria for signal selection corresponding to real particle decays is used to suppress a large combinatorial background in Au + Au central collisions. The topology of the decay of short-lived particles into charged hadrons defines the following selection parameters:

- the distance of closest approach between the tracks of decay products and the primary vertex of interaction of colliding nuclei (*dca*);
- the distance between the tracks of daughter particles at the vertex of the decay of the parent particle (*distance*);
- the path length of the parent particle from the point of its formation to the decay point (*path*);
- angle between the vector connecting the primary and secondary vertex, and the vector of the reconstructed momentum of the parent particle (*angle*).

The cut values of the selection parameters were optimized for each type of particle based on the requirement of maximum significance $\frac{S}{\sqrt{S+B}}$, where S and B are the number of signal and background events. The short-lived hadrons were identified by appearance of the peak corresponding to the parent particle in the invariant mass spectrum of its decay products in a certain hadron channel. MC-identification of tracks was used, although in a real experiment it will be based on information about the time of flight from the TOF detectors and the specific energy losses of charged particles in the TPC.

8.2 First stage ITS simulation: Outer Barrel + Beam Pipe ⌀64 mm

This section presents estimations of identification ability of the MPD tracking system which includes TPC plus the ITS Outer Barrel (two layers of MAPS) adopted for a beam pipe with a diameter of 64 mm. Outer Barrel of ITS will be installed during the first debugging phase of the MPD facility operation. Estimates of the reconstruction efficiency of Λ, Ξ and Ω^--hyperons for such configuration of the tracking system are presented below.

8.2.1 Λ-hyperons

The reconstruction of Λ-hyperons was performed for 5×10^4 central Au + Au collisions at $\sqrt{S_{NN}} = 9\,\text{GeV}$ simulated using the QGSM generator. In order to extract the signal from the invariant mass spectrum $M(\pi^-, p)$ of Λ decay products the following criteria were used:

$$dca(p) > 0.45\,\text{cm} \;\&\; dca(\pi^-) > 1.25\,\text{cm} \;\&\; path(\Lambda) > 3.0\,\text{cm} \;\&\; distance(\pi^-, p) < 0.7\,\text{cm} \;\&\; angle(\Lambda) < 0.09\,\text{rad}. \tag{8.1}$$

The spectrum was approximated by the sum of a Gaussian function with a width σ and a polynomial function. The area of the spectrum under the curve of the polynomial function in the interval $\pm 2\sigma$ around the peak determines the level of the background (B), and the integral with respect to the Gaussian distribution in the same interval provides an estimate of the number of reconstructed Λ hyperons. It should be noted that the described algorithm was used to select the signal in the invariant mass spectrum for all reconstructed strange and charmed particles.

The results of reconstruction are shown in Figure 8.2a. As it can be seen the extraction of Λ signal with the given configuration of the Inner Tracking System can be performed with an efficiency of 3.9 % and a signal-to-noise ratio of 3.6.

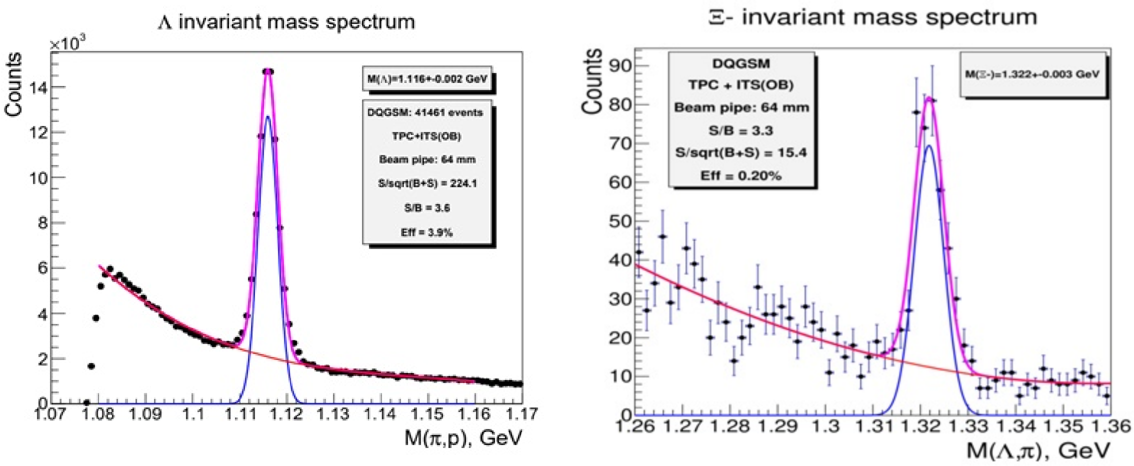

(a) (b)

Figure 8.2: Signals of Λ (a) and Ξ^- (b) in the invariant mass spectrum $M(\pi^-, p)$ extracted from 5×10^4 central Au+Au collisions at $\sqrt{S_{NN}} = 9\,\text{GeV}$ (**purple line** - full spectrum, **blue line** - signal, **red line** - residual combinatorial background).

8.2.2 Ξ^--hyperons

The extraction of the Ξ^- - hyperon signal is a more difficult task compared to the reconstruction of Λ-hyperon, since they are characterized by an order of magnitude smaller multiplicity in central Au+Au collisions at NICA energies. At the same time the cascading nature of their decay leads to a larger number of topological selection criteria ($\Xi^- \to \pi^- + \Lambda \to \pi^- + p$). As a result, the following set of selection criteria was obtained:

$$angle(\Lambda) < 0.08\,\text{rad} \;\&\; distance(p, \pi^-) < 0.35\,\text{cm} \;\&\; distance(\Lambda, \pi^-) < 0.45\,\text{cm} \;\&\; angle(\Xi^-) < 0.045\,\text{rad} \;\&\; dca(\pi^-) > 0.85\,\text{cm} \;\&\; dca(p) > 0.3\,\text{cm}. \tag{8.2}$$

In addition, the cut by the invariant mass of Λ particle was applied to the Λ candidates selected during the Λ particle reconstruction: $\mathrm{M}(\pi \mathrm{p}) = \mathrm{MPDG}(\Lambda) \pm 6\sigma$. The cut values for the given selection parameters (Eq. 8.2) were chosen so that the significance level reached a maximum for each parameter with fixed values for the remaining parameters.

The invariant mass spectrum $M(\pi^-, \Lambda)$ for Ξ candidates obtained after applying all the cuts considered is shown in Figure 8.2b. As it can be seen the Ξ^- reconstruction efficiency is 0.20 % with a signal-to-noise ratio of 3.3.

8.2.3 Ω^--hyperons

The reconstruction of Ω^--hyperons was performed using the mixed events method which assumes that signal and background events are processed separately and then reduced to the same statistics and summed up. This method not only allows to increase statistics during reconstruction of particles with low multiplicity without a significant increase in computational resources, but also makes it easier to find the optimal selection parameters for extracting useful events.

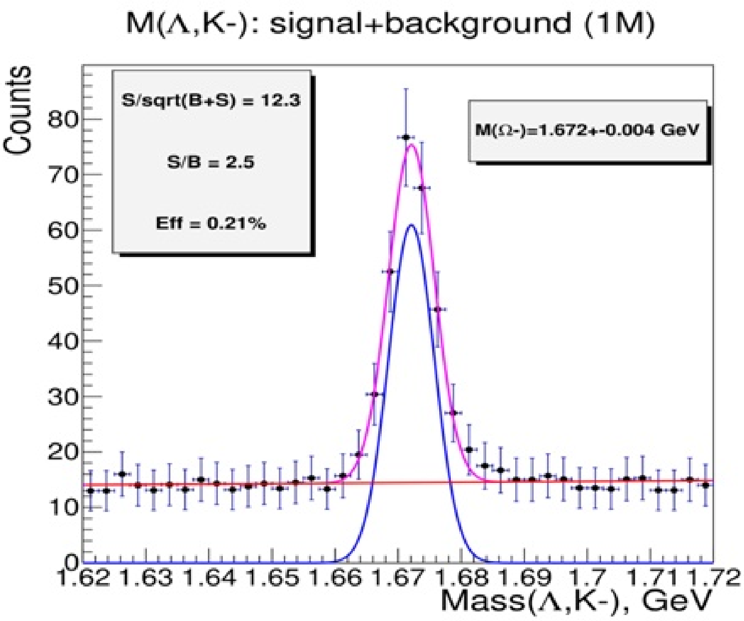

Figure 8.3: Signal of Ω^--hyperons in the invariant mass spectrum extracted in 10^6 central Au + Au collisions = 9 GeV (**purple line** - full spectrum, **blue line** - signal, **red line** - residual combinatorial background).

To estimate efficiency of the Ω^- reconstruction 10^6 signal events corresponding to the decay channel $\Omega^- \to \Lambda^0 + K^-$ were generated with the thermal generator, while for the background 10^5 events of central Au + Au collisions at an energy of $\sqrt{S_{NN}} = 9$ GeV were generated by the QGSM generator.

Taking into account the cascade nature of the Ω^- decay, selection criteria similar to the case of Ξ^--hyperons were chosen to extract their signals. The cuts for the selection parameters were set according to the maximum of the significance function $\mathrm{Sign}(a)$ for each parameter a

$$Sign(a) = \int_0^a \frac{S}{\sqrt{S+B}} da \tag{8.3}$$

resulting the following values:

$$Mass(\Omega) > 1.62\,\text{GeV} \ \&\ Mass(\Omega) < 1.72\,\text{GeV} \ \&\ Mass(\Lambda) > 1.110\,\text{GeV} \ \&$$
$$Mass(\Lambda) < 1.122\,\text{GeV} \ \&\ angle(\Lambda) < 0.1\,\text{rad} \ \&\ angle(\Omega) < 0.12\,\text{rad} \ \&$$
$$distance(\Lambda, K) < 0.34\,\text{cm} \ \&\ distance(p, \pi) < 0.42\,\text{cm} \ \&\ dca(\Omega) < 0.56\,\text{cm} \ \&$$
$$dca(K) > 0.5\,\text{cm} \ \&\ dca(\Lambda) > 0.4\,\text{cm} \ \&\ path(\Lambda) > 6.0\,\text{cm} \ \&\ path(\Omega) > 2.2\,\text{cm}. \quad (8.4)$$

The invariant mass spectrum obtained after applying the cuts from Eq. 8.4 to signal events was reduced taking into account the multiplicity of Ω^- hyperons and the branching ratio of the given decay channel and then it was added to the background spectrum normalized to 10^6 central Au+Au collisions. The multiplicity of Ω^-- in central Au+Au collisions at the NICA collider energies is 10^{-1} hyperon/event according to theoretical estimations [3]. The resulting spectrum is is shown in Figure 8.3 and it can be seen that the Ω^- reconstruction efficiency is 0.21 % at a significance level of 12.3.

8.3 Project ITS simulation: Outer Barrel + Inner Barrel

This section presents the identification capability of the MPD tracking system, including the TPC and the project version of the 5-layer ITS, when reconstructing decays of strange and charmed particles produced in central Au+Au collisions at $\sqrt{S_{NN}} = 9$ GeV. The reconstruction efficiency of hyperons as well as D mesons in the ITS + TPC tracking system with a beam pipe diameter of 40mm is estimated in section 8.3.1. Two methods were used to extract the signals of the charmed particles in the invariant mass spectrum of the decay products: the classical method of topological cuts (TC) and the method of multivariate data analysis (MVA). Section 8.3.3 contains a comparison of the reconstruction results for two configurations of 5-layer ITS adapted for a beam pipe diameter of 40 and 64 mm, respectively.

8.3.1 Strange particle reconstruction with a beam pipe diameter of 40 mm

8.3.1.1 Λ-hyperons

Figure 8.4 shows the invariant mass spectrum $M(\pi^- p)$ of Λ decay products obtained in 10^5 central Au+Au collisions at $\sqrt{S_{NN}} = 9$ GeV which satisfies the following selection criteria:

$$dca(p) > 0.3\,\text{cm} \ \&\ dca(\pi^-) > 0.3\,\text{cm} \ \&\ distance(\pi^-, p) < 0.5\,\text{cm} \ \&\ path(\Lambda^0) > 3.0\,\text{cm} \ \&$$
$$angle(\Lambda^0) < 0.09\,\text{rad} \quad (8.5)$$

As it can be seen, the efficiency of Λ reconstruction with a 5-layer ITS configuration is 8 % with a signal-to-noise ratio of 11.3.

8.3.1.2 Ξ^--hyperons

The efficiency of reconstruction of Ξ^--hyperons was evaluated by extracting the signal in 10^5 central Au + Au collisions at $\sqrt{S_{NN}} = 9$ GeV. The suppression of the combinatorial background was carried out in accordance with the selection criteria dictated by the kinematics of the cascade decay $\Xi^- \to \pi^- + \Lambda^0 \to \pi^- + p^+$

To reduce the combinatorial background the following *dca* values for the decay products of Ξ^- and Λ^0 were selected:

$$dca(\pi^-) > 0.5\,\text{cm}, \ dca(p) > 0.5\,\text{cm} \ for \ \Lambda^0;$$
$$dca(\pi^-) > 0.1\,\text{cm}, \ dca(\Lambda^0) > 0.1\,\text{cm} \ for \ \Xi^-. \quad (8.6)$$

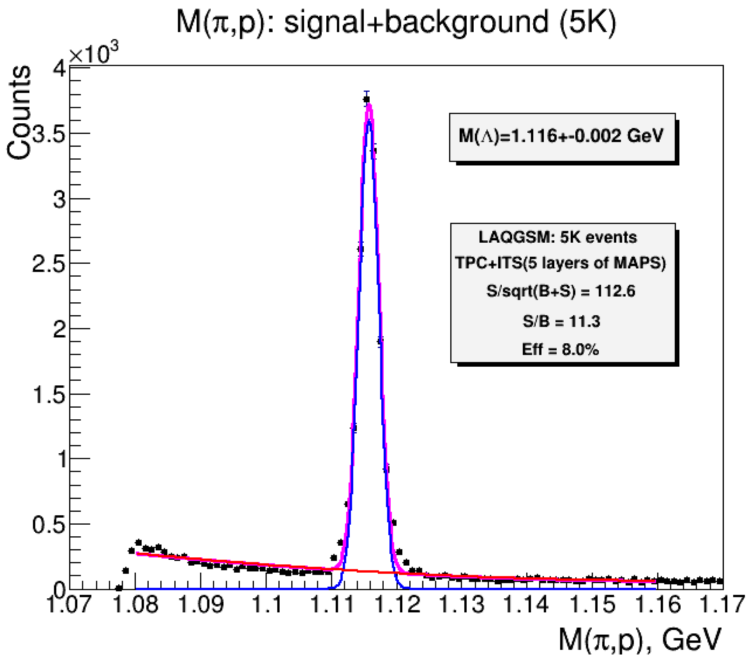

Figure 8.4: Λ^0-hyperons invariant mass $M(\pi^- p)$ spectrum for 10^5 central Au + Au collisions at $\sqrt{S_{NN}} = 9\,\mathrm{GeV}$ (**purple line** - full spectrum, **blue line** - signal, **red line** - residual combinatorial background).

The distributions for the remaining selection parameters for signal and background events and the corresponding significance functions are shown (Figs. 8.5 and 8.6). Based on these plots the following cut values were selected:

$$distance(\pi^-, p) < 0.05\,\mathrm{cm} \;\&\; distance(\Lambda^0, \pi^-) < 0.2\,\mathrm{cm} \;\&\; angle(\Lambda^0) > 0.02\,\mathrm{rad} \;\&\; angle(\Xi^-) < 0.05\,\mathrm{rad} \quad (8.7)$$

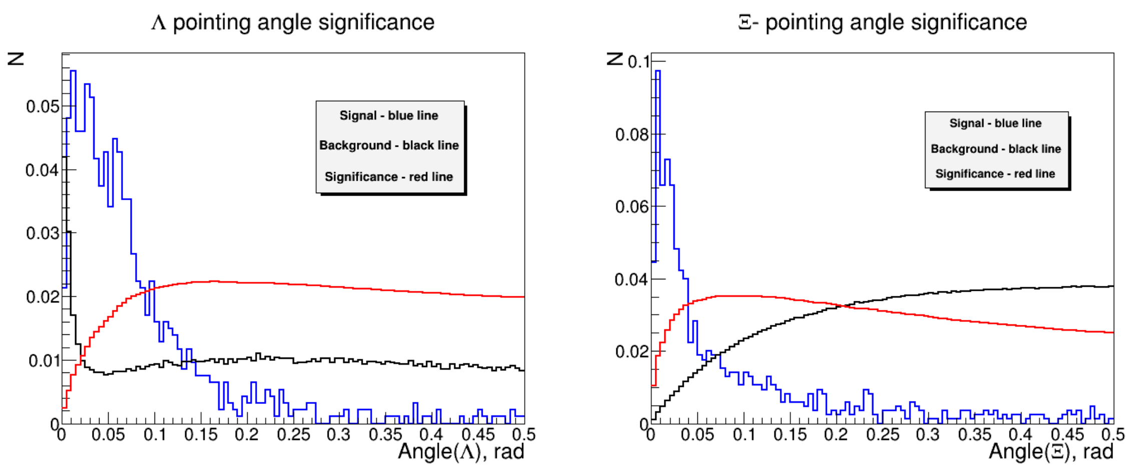

(a) (b)

Figure 8.5: Distribution of parameter $angle(\Lambda^0)$ (a) and $angle(\Xi^-)$ (b) for signal and background events.

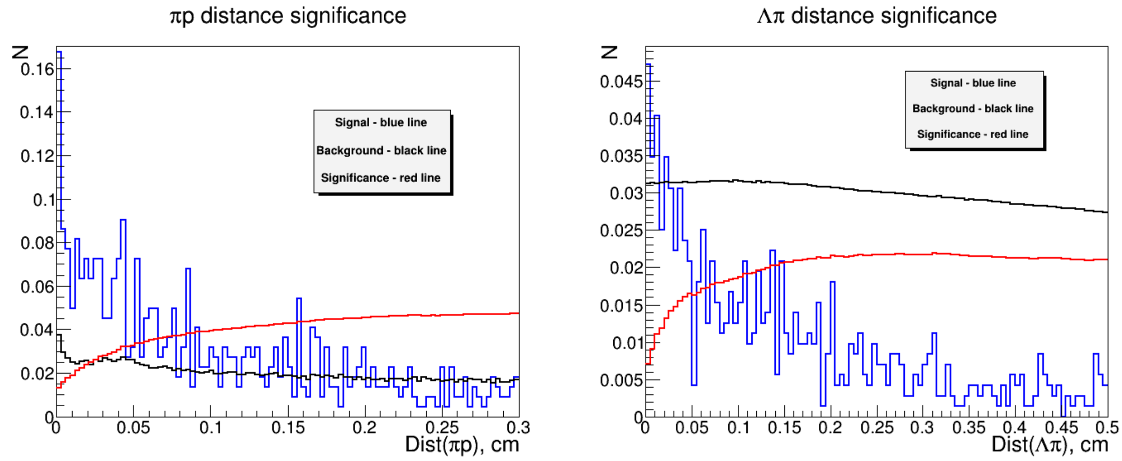

(a) **(b)**

Figure 8.6: Distribution of parameters $distance(\pi, p)$ (a) and $distance(\Lambda, \pi)$ (b) for signal and background events.

The invariant mass spectrum $M(\pi^-\Lambda^0)$ for Ξ^--candidates built after applying all the considered cuts is shown in Figure 8.7. The resulting signal-to-noise ratio of 24.4 makes it possible the reconstruction of Ξ^- with an efficiency of 1.3 %.

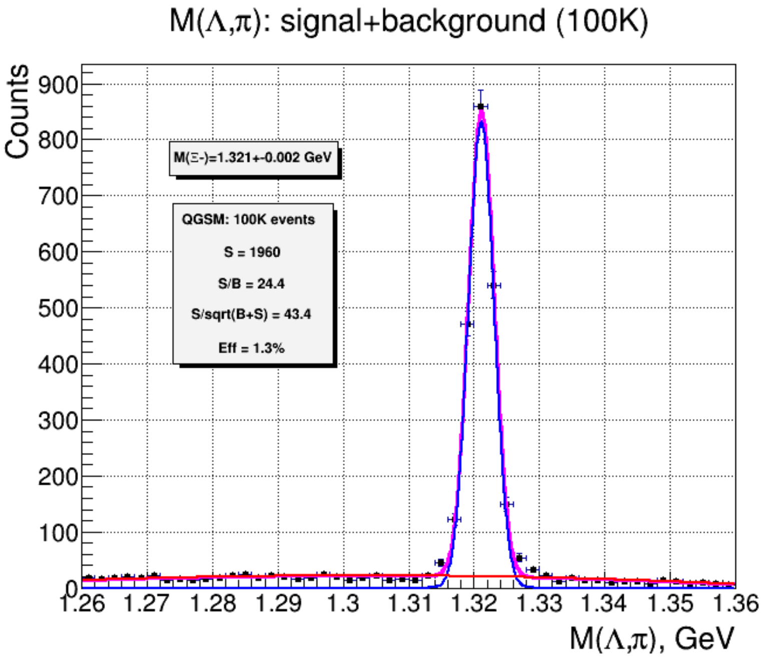

Figure 8.7: Ξ^--hyperons signal on the invariant mass spectrum $M(\pi^-\Lambda)$ for 10^5 central Au + Au collisions at $\sqrt{S_{NN}} = 9\,\text{GeV}$ (**purple line** - full spectrum, **blue line** - signal, **red line** - residual combinatorial background).

8.3.1.2.1 Ω^--hyperons

The reconstruction method considered above for Ξ^- was used to extract Ω^- signals in 10^5 events of central Au + Au collisions at energy $\sqrt{S_{NN}} = 9\,\text{GeV}$. In this case, the combinatorial background was suppressed by choosing the optimal cuts according to the same topological parameters as for Ξ^- (Eq. 8.6–8.7) but replacing the pions by kaons in accordance with the kinematics of cascade decay $\Omega^- \to K^- + \Lambda^0 \to \pi^- + p^+$

Based on the maximum of the significance functions the following cut values were selected:

$$dca(\pi^-)> 0.05\,\text{cm} \,\&\, dca(p)> 0.05\,\text{cm} \,\&\, dca(K^-)> 0.1\,\text{cm} \,\&\, dca(\Lambda^0)> 0.1\,\text{cm} \,\&$$
$$distance(\pi^-, p)< 0.3\,\text{cm} \,\&\, distance(\Lambda^0, K^-)< 0.1\,\text{cm} \,\&\, angle(\Lambda^0)> 0.01\,\text{rad} \,\&$$
$$angle(\Omega^-)< 0.015\,\text{rad} \,\&\, dca(\Omega^-)> 0.005\,\text{cm} \,\&\, path(\Lambda^0)> 5\,\text{cm} \,\&\, path(\Omega^-)< 8\,\text{cm}. \quad (8.8)$$

Figure 8.8a shows mass spectrum $M(K^-, \Lambda^0)$ for Ω^--candidates built after applying the cuts. It can be seen that statistics of 10^5 central Au + Au collisions at $\sqrt{S_{NN}} = 9\,\text{GeV}$ are insufficient for a reliable selection of Ω^- -hyperons. To increase the significance of Ω^- reconstruction 10^6 pure signal events $\Omega^- \to K^- + \Lambda^0$ were processed in addition to the 10^5 background events.

The invariant mass spectrum obtained by mixed events method (see Sec. 8.2.3) and normalized to 10^6 central Au+Au collisions is shown in Figure 8.10. As a result the Ω^- reconstruction efficiency is 1.5 % at a significance level of 30.

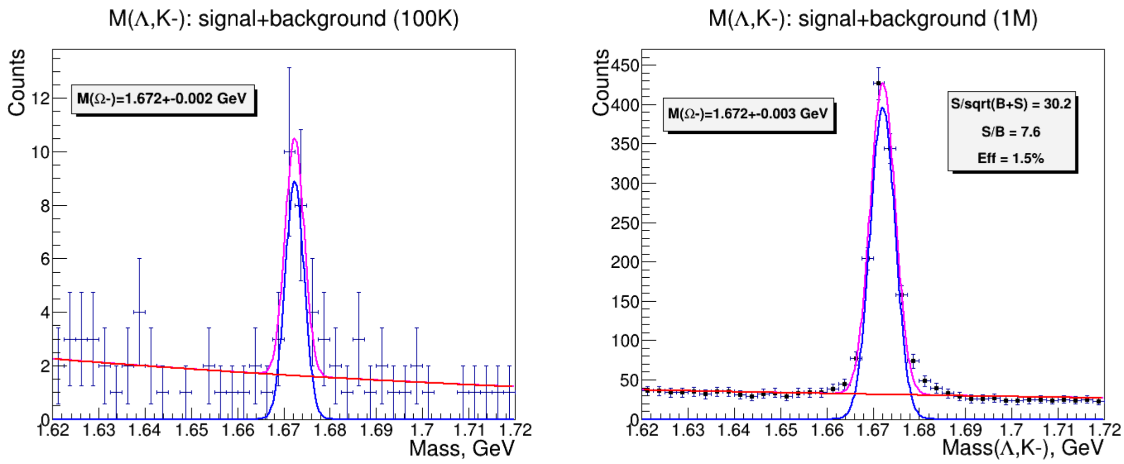

(a) (b)

Figure 8.8: Ω^--hyperons signal on the invariant mass spectrum $M(\pi^-\Lambda)$ for 10^5 (a) and 10^6 (b) central Au + Au collisions at $\sqrt{S_{NN}} = 9\,\text{GeV}$ (**purple line** - full spectrum, **blue line** - signal, **red line** - residual combinatorial background).

8.3.2 Reconstruction of charmed particles.

The identification ability of the MPD track system in the reconstruction of charmed particles was evaluated using D^0 and D^+-mesons as test case. For this purpose 10^6 signal decay-events of $D^0 \to K^- + \pi^+$ and $D^+ \to K^- + \pi^+ + \pi^+$ and 10^5 background events of the central Au+Au collisions at $\sqrt{S_{NN}} = 9\,\text{GeV}$ were processed. The selection of D signals from the invariant mass spectrum of their decay products was carried out in two ways: the classical method of topological cuts (TC) and the method of multivariate data analysis (MVA).

8.3.2.1 Reconstruction of D-mesons by the TC method.

8.3.2.1.1 D^0-mesons.

When reconstructing the decay vertex of the D^0 mesons, only the tracks of their decay products that were reconstructed by hits in all 5 layers of the ITS were selected. In order to reduce the combinatorial background *dca* cuts were set to 2σ from the width of their distributions:

$$dca(K) > 0.012\,\text{cm}\ \&\ dca(\pi) > 0.012\,\text{cm}, \tag{8.9}$$

the reconstructed distributions for $distance(\pi, K)$, $path(D^0)$ and $angle(D^0)$ of signal and background events and the corresponding significance functions are shown in Figures 8.9a – 8.9c.

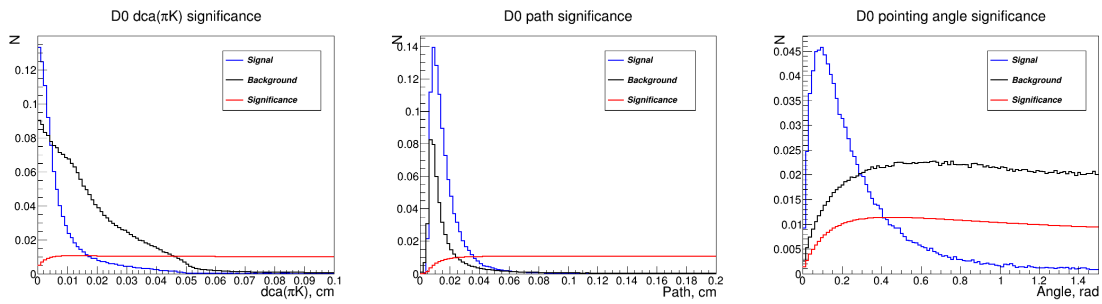

(a) **(b)** **(c)**

Figure 8.9: Distribution of parameters $distance(D^0)$ (a), $path(D^0)$ (b) and $angle(D^0)$ (c) for signal ($D^0 \to K^- + \pi^+$) and background Au+Au events.

Based on the maximum of the significance functions the following cuts were applied to signal and background events:

$$distance(\pi, K) < 0.019\,\text{cm}\ \&\ path(D^0) < 0.044\,\text{cm}\ \&\ angle(D^0) < 0.15\,\text{rad} \tag{8.10}$$

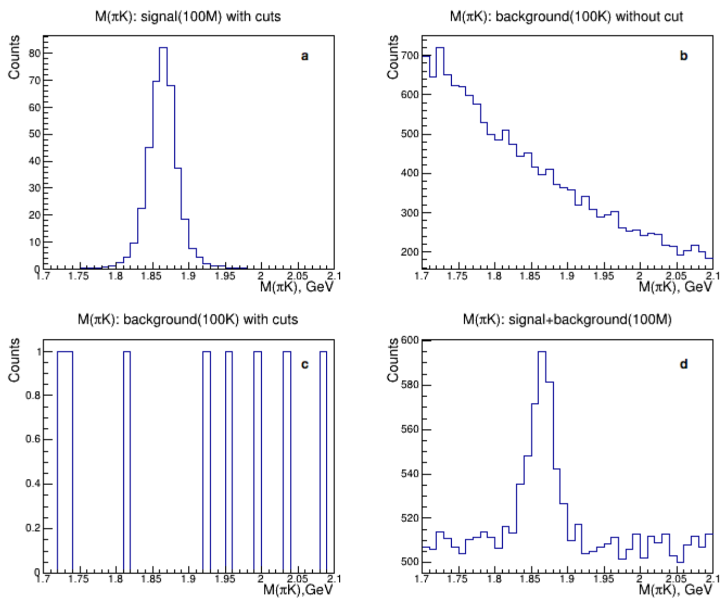

Figure 8.10: Invariant mass $M(K^-\pi^-)$ signal events spectra for 10^8 central Au + Au collisions after applying the cuts (**a**), for background events in 10^5 central Au + Au collisions before (**b**) and after (**c**) applying the cuts, and for the sum of spectra **a** and **c** scaled to the statistics of 10^8 central Au + Au events (**d**).

Figure 8.10(a) shows the invariant mass $M(K^-\pi^+)$ signal spectrum that satisfies the selection criterion from Eq. 8.9 and 8.10 scaled to statistics of 10^8 central Au+Au collisions accounting for the multiplicity of D^0-mesons and the probability of their decay to the channel $D^0 \to K^- + \pi^+$. The multiplicity of D-mesons in central Au + Au collisions was estimated using the dynamic model of the hadron string [4] resulting in 10^{-2} mesons/event at NICA collider energies. The background spectrum in 10^5 events *before* and *after* applying the cuts (Eq. 8.10) is shown in Figures 8.10(b),(c). The residual combinatorial background (Fig. 8.10(c)) was uniformly distributed over the chosen range and then scaled to statistics of 10^8 events with the addition of the statistical fluctuations. Figure 8.10(d) shows the resulting spectrum obtained by adding the signal and background spectra normalized to 10^8 central Au + Au collisions. Figure 8.11 shows the signal selection on a combinatorial background with the same statistics. It can be seen that the reconstruction efficiency for D^0 is 0.8% at a significance level of 5.3. The mass of reconstructed D^0-mesons is in good agreement with its PDG value (see Table 8.1).

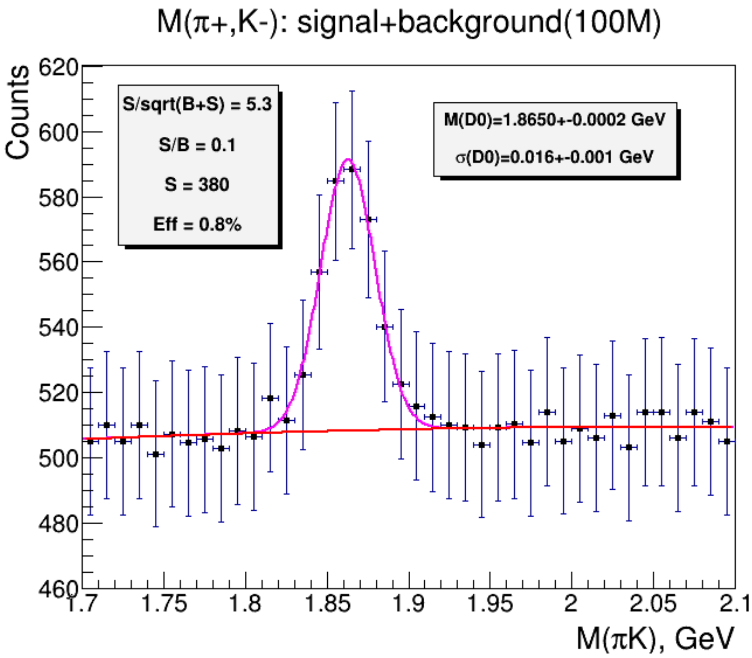

Figure 8.11: D^0-mesons signal on the invariant mass spectrum $M(\pi^+K^-)$ for 10^8 central Au + Au collisions at $\sqrt{S_{NN}} = 9\,\text{GeV}$ (**purple line** - full spectrum, **red line** - residual combinatorial background).

8.3.2.1.2 D^+-mesons.

To reconstruct the D^+, the background was suppressed by applying selection criteria for the topological parameters related to the kinematics of three-particle decay $D^+ \to K^- + \pi^+ + \pi^+$. In this case, the parameter distance was determined as the sum of the shortest distances between each pair of tracks of the daughter particles at the decay point. To build the $\pi^+ + \pi^+ + K^-$ invariant mass spectrum, the cuts for the selection parameters were chosen according to the maximum value of the significance function (see Fig. 8.12) for each parameter:

$$dca(K) > 0.029\,\text{cm} \;\&\; dca(\pi) > 0.029\,\text{cm} \;\&\; distance < 0.06\,\text{cm} \;\&\; path(D^+) < 0.11\,\text{cm} \;\&\; angle(D^+) < 0.15\,\text{rad} \tag{8.11}$$

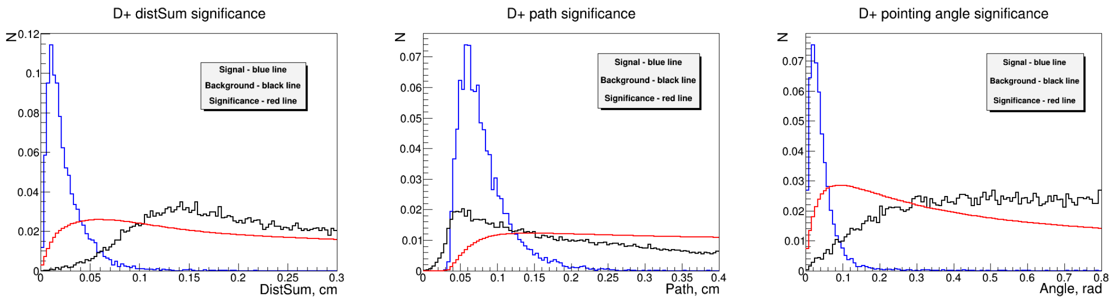

(a) **(b)** **(c)**

Figure 8.12: Distribution of parameters $distance(D^0)$ (a), $path(D^0)$ (b) and $angle(D^0)$ (c) for signal ($D^+ \to K^- + \pi^+ + \pi^+$) and background Au+Au events.

The resulting invariant mass spectrum normalized to 10^8 central Au + Au events and satisfying the cut criteria (8.11) was built following the same procedure as described for D^0-mesons. Figure 8.13 shows the isolation of the D^+ signal extracted from the residual combinatorial background. It can be seen that the D^+ reconstruction efficiency is 0.5 % at a significance level of 7.0, and the mass of reconstructed D^+ mesons is in good agreement with its PDG value (see Table 8.1).

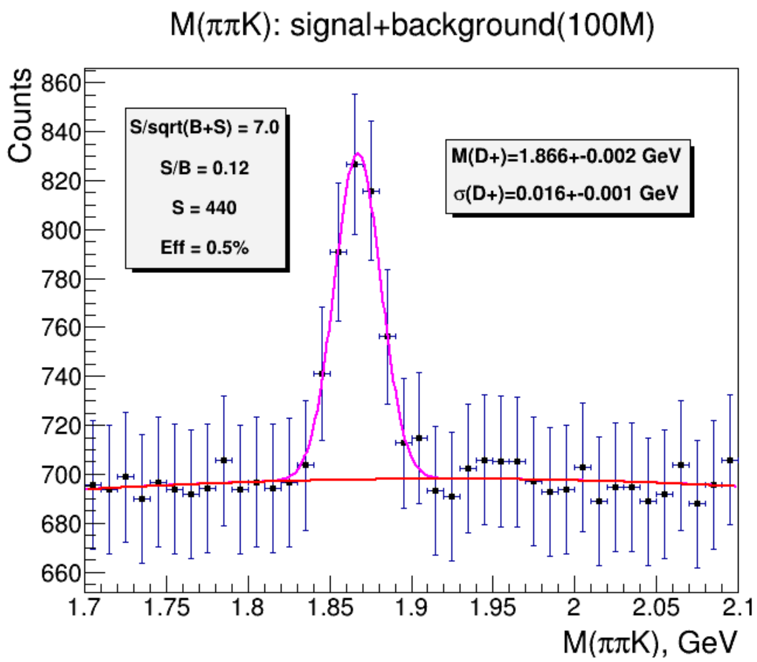

Figure 8.13: D^+-mesons signal on the invariant mass spectrum $M(\pi^+\pi^+K^-)$ for 10^8 central Au + Au collisions at $\sqrt{S_{NN}} = 9\,\text{GeV}$ (**purple line** - full spectrum, **red line** - residual combinatorial background).

8.3.2.2 Reconstruction of *D*-mesons by the MVA method

The package for multivariate data analysis TMVA [5] integrated into the MpdROOT environment provides several classification algorithms designed to solve the problem of separating the signal from the background. A typical TMVA classification analysis consists of two independent steps:

1. Training phases, where multivariate analysis methods are tested and evaluated;
2. Application phases, where the selected methods are applied to the specific classification problem for which the training was conducted.

In the training phase, a relationship is first established between user data sets and MVA methods. Data for training and testing selected methods is presented in a tree format. The *TreeS* tree includes data that is known to correspond to a signal. The *TreeB* tree includes data that does not contain useful information, but corresponds to the background. The classification results for each registered MVA method are recorded in weighted files with N input variables V are mapped to the one-dimensional variable R (response): $V^N \to R$. At the analysis stage, the cut for this variable R is applied to a data set with an unknown composition of the signal and the background.

Multivariate analysis was used to reconstruct D-mesons mesons. The input data was tested and evaluated using the BDT (Boosted Decision Tree) classifier.

8.3.2.2.1 D^0-mesons

The same *path*, *distance* and *angle* variables used as selection parameters for the reconstruction of D^0-mesons by the TC method were taken as the input data for the selected BDT classifier. The distributions of these variables in 10^6 signal and 10^5 background events are shown in Figure 8.14, while Figure 8.15 shows their various transformations: decorrelation (Deco), Gaussian (Gauss) and principal components analysis (PCA). The result of the input variable classification is shown in Figure 8.16.

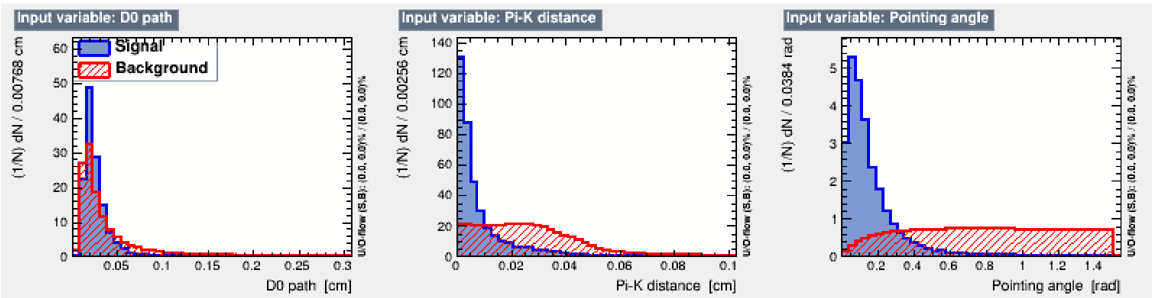

Figure 8.14: Distributions of input variables $path(D^0)$ (left panel), $distance(\pi^+K^-)$ (middle panel) and $angle(D^0)$ (right panel) for signal ($D^0 \to K^- + \pi^+$) and background (Au+Au) events.

To separate the signal from the background the classifier response cut $BDTD\_response$ > 0.3, was applied to signal and background events. After that, the signal and background invariant mass spectra of π^+K^- combinations were concatenated according to the procedure described in Sec. 8.3.2.1. The resulting spectrum normalized to 10^8 central Au+Au is shown in Figure 8.17. It can be seen that the D^0 reconstruction efficiency is 0.85 % at a significance level of 5.5, which is in full agreement with the results obtained by the classical method of topological cuts (see Figure 8.11).

8.3.2.2.2 D^+-mesons

The reconstruction of D^+ by MVA method was carried out in the same way as for D^0 mesons. The results of the classification of input variables $distance(\pi^+\pi^+K^-)$, $path(D^+)$ and $angle(D^+)$ with the application of the BDT method are shown in Figure 8.19, according to which the classifier cut was chosen as $BDTD\_response > 0.25$. The invariant mass spectrum

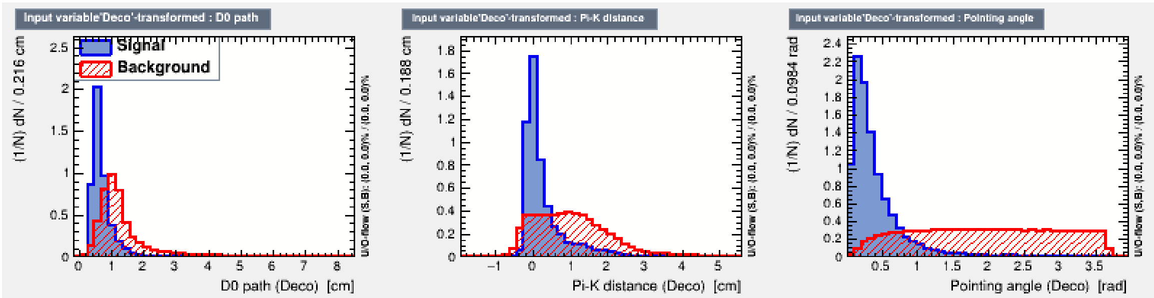

(a)

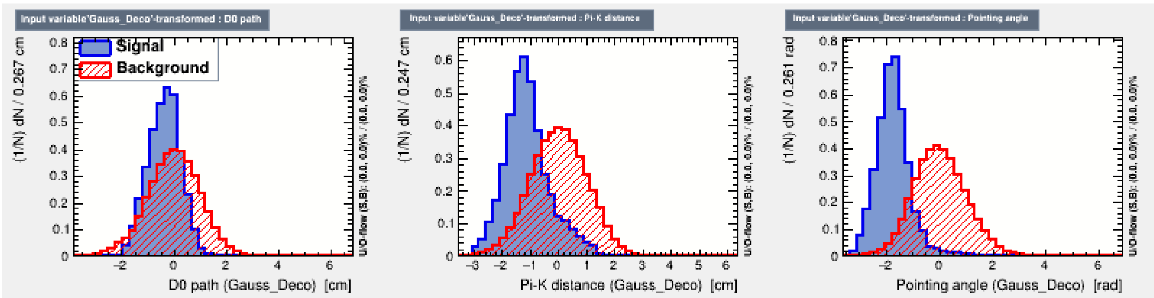

(b)

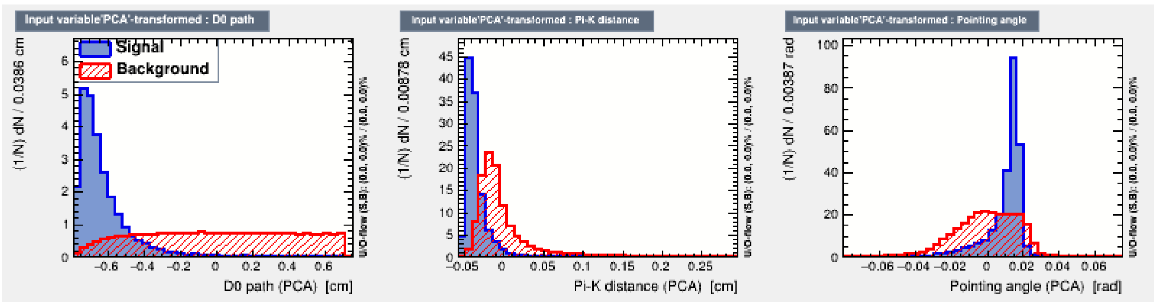

(c)

Figure 8.15: Distributions of input variables for signal ($D^0 \rightarrow K^- + \pi^+$) and background events after *decorrelation* (a), *Gaussian* (b) and *PCA* (c) transformations.

of D^+ decay products normalized to 10^8 central Au+Au collisions is presented in Figure 8.20. It is shown that the efficiency of D^+ reconstruction by MVA method is 1 % at the significance level 10.5. The comparison with the results obtained by TC method (see Figure 8.13) shows that the use of multivariate analysis in the case of D^+ increases the reconstruction efficiency by a factor of 2 at a higher level of significance.

8.3.2.3 Transverse momentum spectra of reconstructed D mesons

The normalized distributions of the transverse momentum p_T of D-mesons generated by thermal generator and reconstructed with ITS+TPC tracking system are shown in Figure 8.21. It can be seen that p_T - spectra of reconstructed and generated D-mesons are in good agreement. The observed shift of the average p_T for the reconstructed D-mesons toward large values indicates that the reconstruction efficiency decreases with a decrease in the transverse momentum of the D meson.

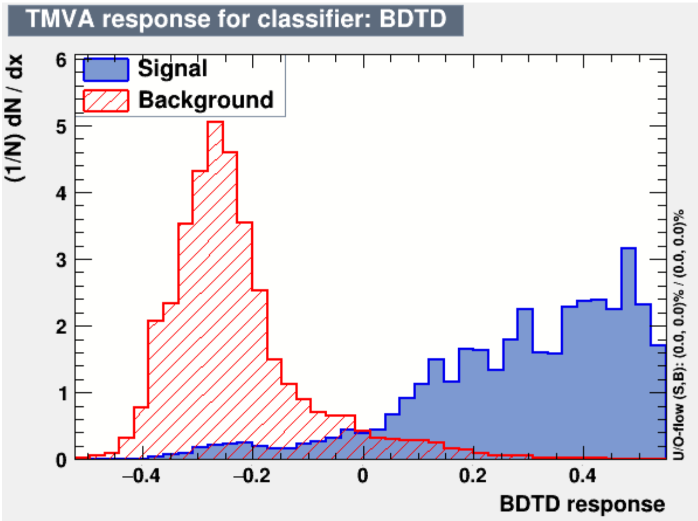

Figure 8.16: Distribution of BDT classifier responses to signal ($D^0 \to K^- + \pi^+$) and background (Au+Au) events.

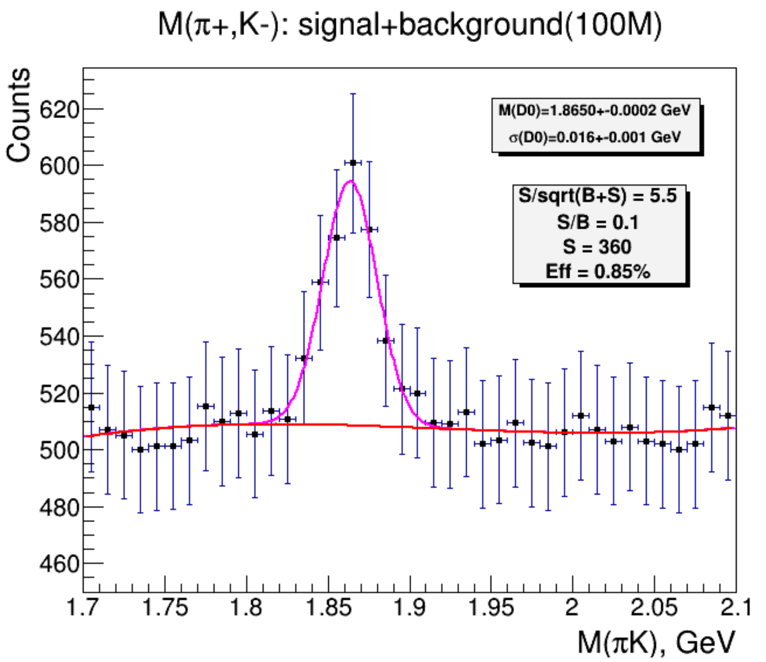

Figure 8.17: D^0-meson signal on the invariant mass spectrum in 10^8 central Au + Au collisions at $\sqrt{S_{NN}} = 9$ GeV extracted by the MVA method (**purple line** - full spectrum, **red line** - residual combinatorial background).

8.3.2.4 Yield of strange and charmed particles

The obtained estimates values of the reconstruction efficiency ε of hyperons and D mesons were used to evaluate their yields in the MPD experiment with the tracking system including the TPC and the *project* version of the ITS.

At the optimal luminosity of the NICA collider the Au+Au interaction rate will be about R $=8 \times 10^3$ events/s [6] and a fraction of central collisions with impact parameter less 4 fm is $\delta = 0.1$. Taking into account the theoretical evaluation of the particle multiplicity M at NICA collider energies [3, 4] and the branching ratio BR of the paticle decay by the given channel

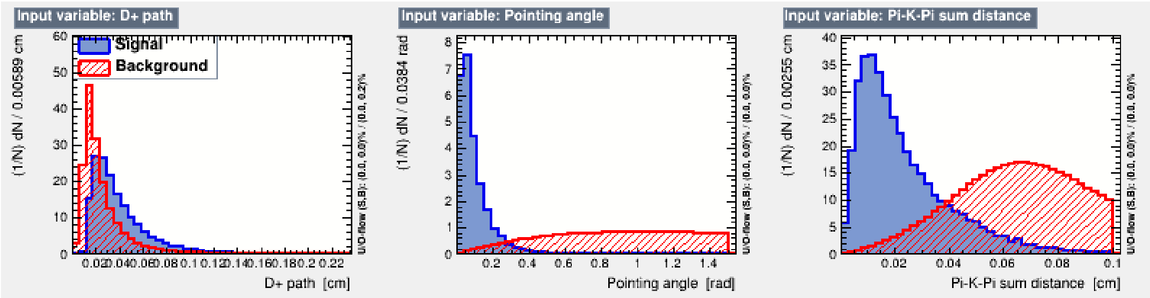

Figure 8.18: Distributions of input variables for signal ($D^+ \to K^- + \pi^+\pi^+$) and background events.

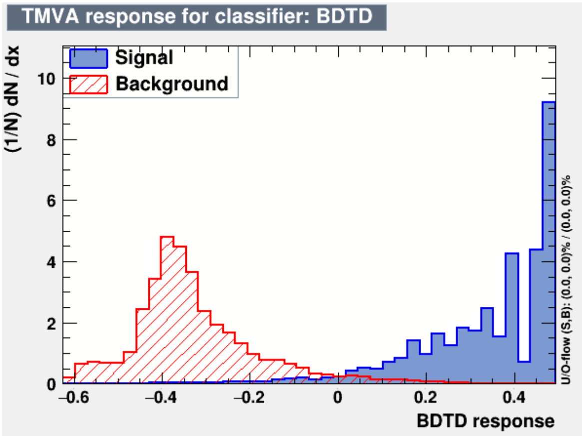

Figure 8.19: Distribution of BDT classifier responses to signal ($D^+ \to K^- + \pi^+\pi^+$) and background events.

(see Table 8.1) it is possible to calculate the particle yield in the MPD experiment during one month (T = 2.6×10^6 s) of the NICA collider continuous operation as $Y = R\cdot\delta\cdot M\cdot T\cdot\varepsilon\cdot BR$. The evaluated yields of strange and charmed particles in central Au+Au collisions at $\sqrt{S_{NN}}$ = 9 GeV as well as the main reconstruction parameters are given in Table 8.2.

Table 8.2: Reconstruction parameters of strange and charmed particles in central Au+Au collisions at $\sqrt{S_{NN}} = 9$ GeV with the *project* ITS.

Particle	Λ	Ξ^-	Ω^-	D^0		D^+	
Reconstruction method	TC*	TC	TC	TC	MVA**	TC	MVA
Multiplicity	20	1.2	10^{-1}	10^{-2}	10^{-2}	10^{-2}	10^{-2}
Number of events	5×10^3	10^5	10^6	10^8	10^8	10^8	10^8
Efficiency [%]	8.0	1.3	1.5	0.80	0.85	0.50	1.0
Significance ($S/\sqrt{S+B}$)	112.6	43.4	30.2	5.3	5.5	7.0	10.5
S/B ratio (2σ)	11.3	24.4	7.6	0.10	0.10	0.12	0.14
Yield [particles/month]	2×10^9	3×10^7	2×10^6	6.5×10^3	7×10^3	10^4	2×10^4

* TC: topological cuts; ** MVA: multivariate analysis

8.3.3 Strange and charmed particle reconstruction for a beam pipe diameter of 64 mm

This section compares the identification capabilities of the ITS+TPC tracking system with a beam pipe diameter of 40 mm and 64 mm when reconstructing strange and charmed particles. The signals of hyperons and D-mesons in the invariant mass spectra of their decay products

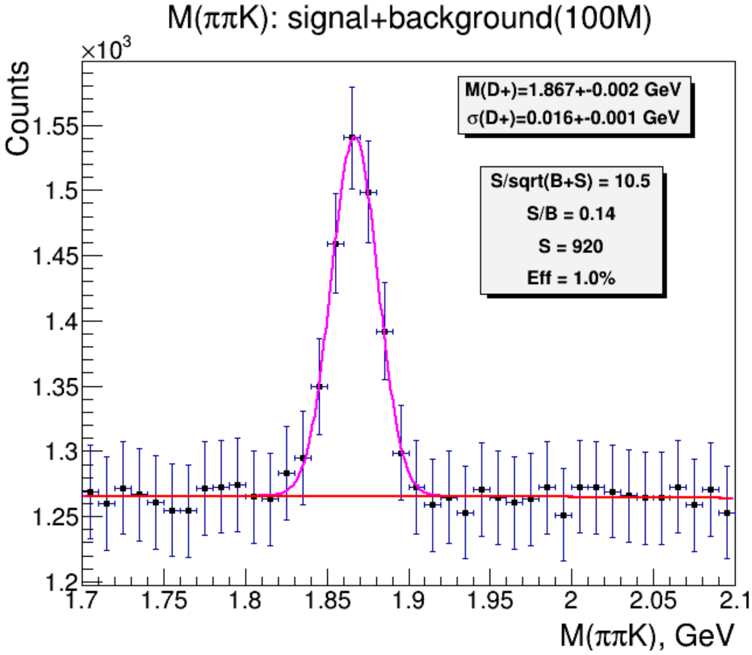

Figure 8.20: D^+-meson signal in the invariant mass spectrum $M(\pi^+\pi^+K^-)$ extracted by the MVA method in 10^8 central Au + Au collisions at $\sqrt{S_{NN}} = 9\,\text{GeV}$ (**purple line** - full spectrum, **red line** - residual combinatorial background).

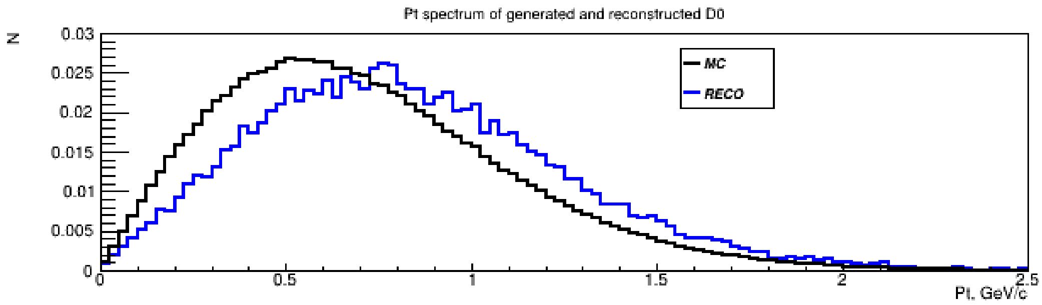

(a)

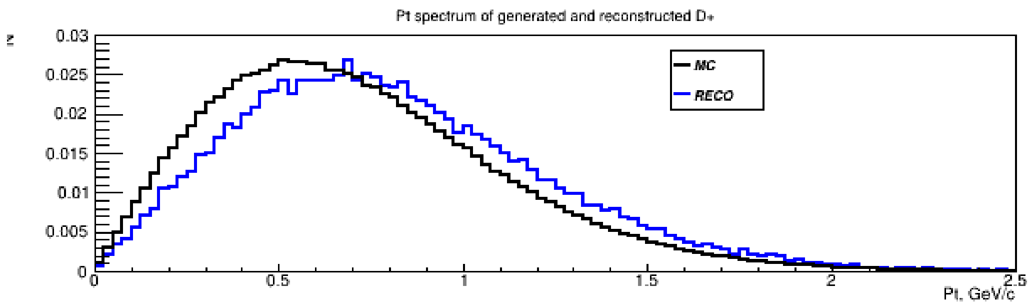

(b)

Figure 8.21: Transverse momentum distribution of generated (MC) and reconstructed (RECO) D^0 (top panel) and D^+ (bottom panel).

with a 5 layer ITS and a beam pipe of ⌀ 64 mm (configuration ITS5-64) were extracted using the same methods and the same statistics of Au+Au events as with the ITS adapted to a beam pipe ⌀ of 40 mm (configuration ITS5-40). The results of the reconstruction of multi-strange hyperons and of D^+ mesons are presented in Table 8.3 and in Figures 8.22 and 8.23. As it can be seen from Table 8.3 the reconstruction quality of multi-strange hyperons slightly deteriorates when increasing in the diameter of the beam pipe from 40 mm to 64 mm, while the reconstruction efficiency of D mesons decreases by an order of magnitude making it almost impossible to extract the signal with ITS5-64. The results obtained indicate that for a reliable reconstruction of charmed particles collected with the required statistics, it is necessary to reduce the diameter of the MPD beam pipe to an optimal value of 40 mm.

Table 8.3: Reconstruction parameters of the ITS + TPC tracking system of the MPD for strange and charmed particles in central Au + Au collisions at $\sqrt{S_{NN}} = 9$ GeV for a beam pipe diameter of 40 mm and 64 mm.

Particle	Ξ^-		Ω^-		D^+		D^+	
Reconstruction method	TC		TC		TC		MVA	
Number of events	10^5		10^5		10^8		10^8	
Beam pipe diameter [mm]	40	64	40	64	40	64	40	64
Efficiency [%]	1.3	1.2	0.7	0.6	0.5	0.04	1.0	0.06
Significance ($S/\sqrt{S+B}$)	43.4	42.5	3.7	3.5	7.0	0.9	10.5	0.9

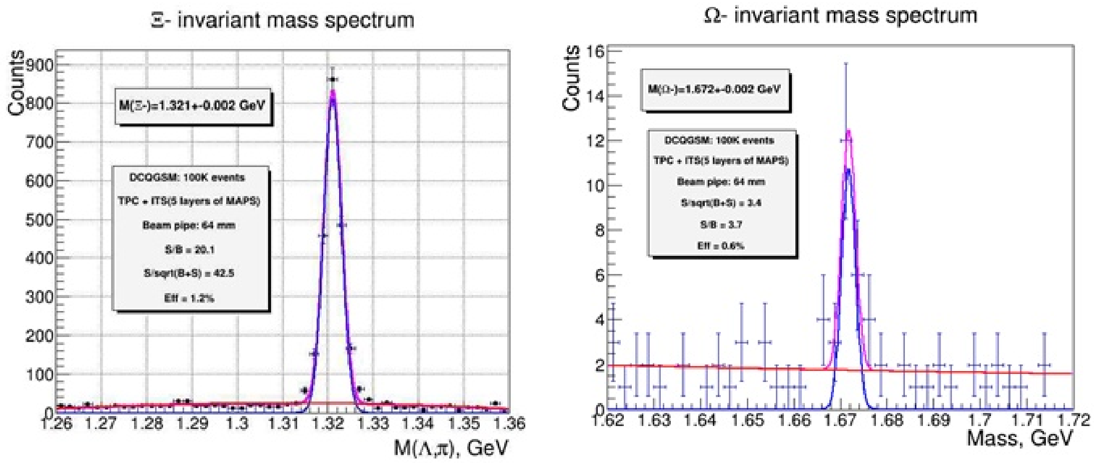

Figure 8.22: Multi-strange hyperon signal on the invariant mass spectrum for 10^5 central Au + Au collisions at $\sqrt{S_{NN}}$= 9 GeV for the ITS + TPC tracking system with a beam pipe diameter of 64 mm (**purple line** - full spectrum, **red line** - residual combinatorial background).

8.3.4 Charmed particle reconstruction using Vector Finder tracking mechanism

This section presents the identification capability of the MPD tracking system, including the TPC and the *project* version of the 5-layer ITS when reconstructing decays of D mesons using the Vector Finder (VF) tracking algorithm (see Section 7.2.6) instead of Kalman Filter (KF) method. The extraction of D signals in the invariant mass spectra was carried out on statistics of 10^8 central Au+Au collisions at $\sqrt{S_{NN}} = 9$ GeV by TC and MVA methods. The reconstruction results are shown in Figure 8.24 and Table 8.4. As it can be seen from Table

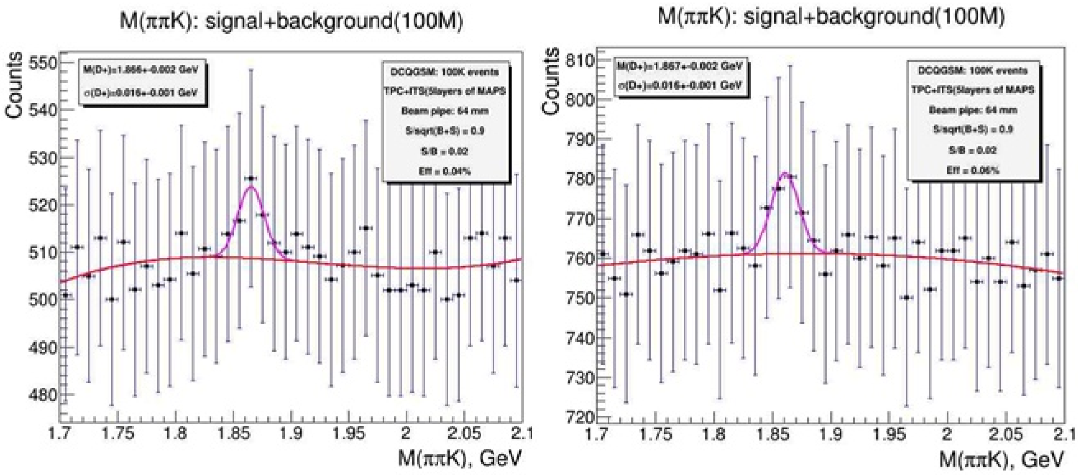

Figure 8.23: D^+ signal in the invariant mass spectrum extracted from 10^8 central Au + Au collisions at $\sqrt{S_{NN}}$= 9 GeV in ITS + TPC tracking system with beam pipe diameter of 64 mm by TC method (left) and MVA method (right) (**purple line** - full spectrum, **red line** - residual combinatorial background).

8.4 the use of VF mechanism allows us to reconstruct D with higher efficiency and at higher level of significance compared to KF technique.

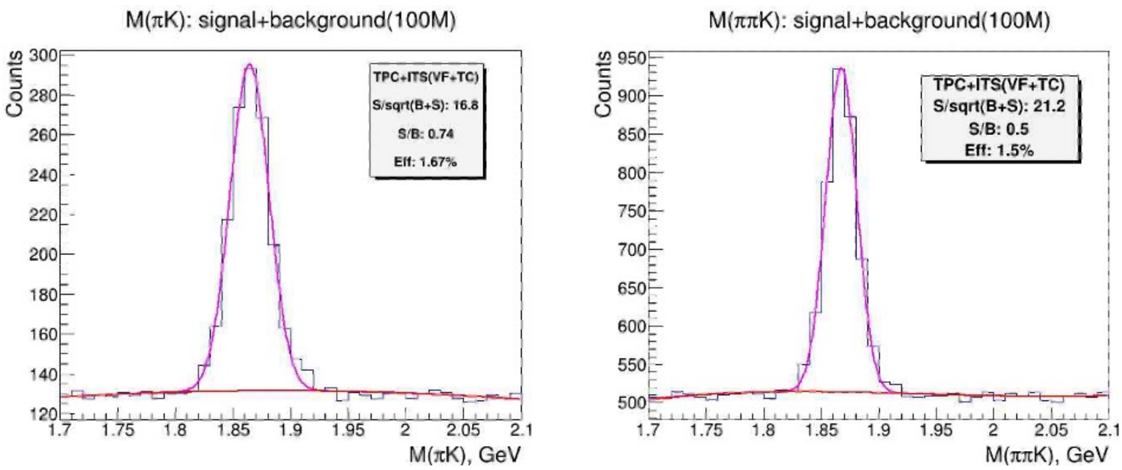

(a) **(b)**

Figure 8.24: Signal of D^0 (a) and D^+ (b) in the invariant mass spectra extracted from 108 central Au+Au collisions at $\sqrt{S_{NN}}$ = 9 GeV by TC method using VF tracking mechanism (**purple line** - full spectrum, **blue line** - signal, **red line** - residual combinatorial background).

8.4 Conclusions

The identification capability of the MPD tracking system, which includes the time-projection chamber (TPC) and the ITS vertex detector based on monolithic active pixel sensors, was studied during reconstruction of strange and charmed particles produced in central Au+Au collisions at $\sqrt{S_{NN}}$= 9 GeV. Three variants of the ITS were considered:

Table 8.4: Reconstruction parameters of the ITS + TPC tracking system of the MPD for strange and charmed particles in central Au + Au collisions at $\sqrt{S_{NN}} = 9\,\text{GeV}$ for a beam pipe with a diameter of 40 mm and 64 mm.

Particle	D^0				D^+			
Tracking method	KF		VF		KF		VF	
Reconstruction method	TC	MVA	TC	MVA	TC	MVA	TC	MVA
S/B ratio	0.10	0.11	0.74	0.75	0.12	0.14	0.50	0.80
Significance	5.3	5.5	16.8	17.0	7.0	10.5	21.2	28.5
Efficiency [%]	0.80	0.85	1.67	1.70	0.5	1.0	1.5	2.0

- the ITS-5-40 configuration consisting of 5 layers of pixel sensors (3 layers of the Inner Barrel + 2 layers of the Outer Barrel) and considering a pipe diameter of 40 mm (*project* variant);
- the ITS-5-64 configuration consisting of 5 layers of pixel sensors (3 layers of the Inner Barrel + 2 layers of the Outer Barrel) and considering a beam pipe diameter of 64 mm (*intitial* variant);
- the ITS-2-64 configuration consisting of 2 layers of pixel sensors of the Outer Barrel and considering a beam pipe diameter of 64 mm (*first stage of the project*).

The *project* and *intitial* variants as well as the *first stage of the project* have been defined in Chapter 3.

Estimates of the extraction efficiency of hyperons Λ, Ξ^- and Ω^- and charmed mesons D^0, D^+ from the invariant mass of charged decay products for the three configurations of vertex detector show that ITS-5-40, having the best spatial resolution, provides reliable detection with an efficiency of about 1 % for both multi-strange and charmed particles when collecting the relevant statistics of Au + Au collisions.

On the other hand, for the configuration ITS-5-64 the efficiency of reconstruction of hyperons decreases by 10 %, while for D-mesons the efficiency of their reconstruction decreases by an order of magnitude which makes it almost impossible to register them at the same level of statistics. Therefore the study of the physics of heavy-flavour in experiments on nucleus-nucleus collisions at the NICA-MPD facility turns out to be promising assuming that the diameter of the MPD beam pipe is reduced to an optimum value of 40 mm.

As for the version ITS-2-64 to be implemented as the first stage of the project, the extraction of multi-strange hyperons with the tracking system, including the TPC and only the Outer Barrel of the Internal Tracker, can be performed with an efficiency of 0.2 % which is sufficient to assess its identification capability at the debugging stage.

Bibliography

[1] Gudima KK, Mashnik SG, Sierk A. J . User Manual for the Code LAQGSM, Los Alamos National Laboratory Report. LA-UR-01-6804. Los Alamos. 2001.

[2] Tawfik AN, Abbas E. Thermal Description of Particle Production in Au-Au Collisions at STAR Energies, Letters to ECHAYA. 2015. T12. No4. (195). s.818-831.

[3] Blume C. Energy dependence of hadronic observables, J. Phys. G: Nucl. Part.Phys, 2005. V.31. P.S57-S68.

[4] Cassing W., Bratkovskaya EL, Sibirtsev A, Open charm production in relativistic nucleus-nucleus collisions, Nucl. Phys. A, 2001, V.691 (3), p.753-778.

[5] Hoecker A., Speckmayer P., Stelzer J., Therhaag J., von Toerne E., Voss H. TMVA4 - Toolkit for Multivariate Data Analysis with ROOT. arXiv:physics/0703039v5 [physics.data-an]. 2009.

[6] Kekelidze V.D., NICA project at JINR: status and prospects, JINST, 2017, V.12, P.C06012.

9 Project Organization and Time Lines

The MPD-ITS construction tasks will be distributed among the participating institutes from JINR and China under the supervision from CERN, as it is shown in Figure 9.1. This organization forsees the use of existing infrastructures in the institutes but also the setting up of new infrastructure for HIC and Stave assembly in both countries. To that purpose it is planned to use the existing Outer Barrel HIC assembly site on CCNU (Wuhan) and to set up another two identical HIC assembly centers in JINR (Russia) and IMP (China). Additionally, three Stave assembly sites will be set up in Russia (JINR) and China (CCNU and IMP), respectively. These centers will receive components either directly from industry or from other Institutes participating in the MPD-ITS Project

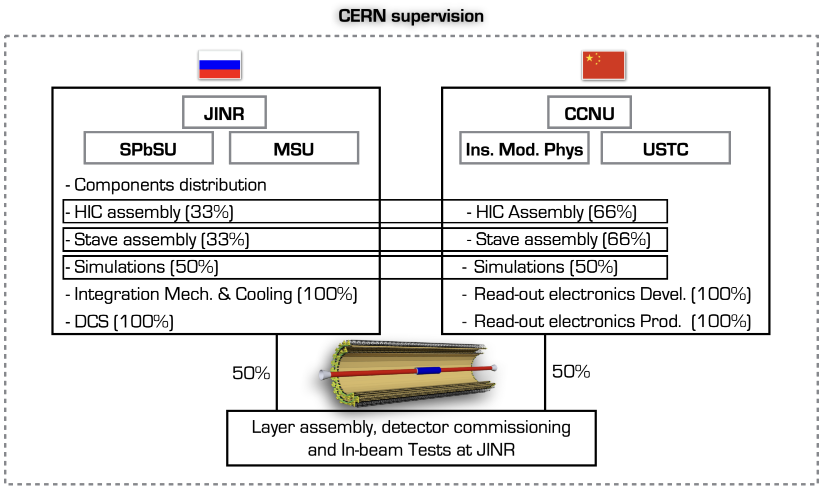

Figure 9.1: Scheme of ITS and TPC tracks matching

All detector elements (e.g. Pixel Chip, FPC, HIC) need a thorough quality control and require numerous acceptance tests. Following there is a short overview of the preliminary distribution of responsibilities for the construction of the MPD-ITS.

Pixel Chip. The Pixel Chip for the outer barrel (ALTAI) is based on the MAPS chips used for the recent upgrade the ALICE ITS Project and manufactured by TowerJazz, which is one of the world's leading companies in the field of CMOS imaging sensors. The characterization of the prototype circuits and of the final engineered full-scale chip is a major enterprise, which involves different groups: JINR, Kurchatov Institue, CCNU, CERN, DISCO, Yonsei. The ALICE ITS Project will provide to TowerJazz the description of the Pixel Chip at the layout level, in the format of standard GDSII data stream, which will be used by the manufacturer to generate the photomask set. A total production of about 415 wafers, which has been estimated assuming a 50 % yield, will be manufactured in 3 tranches.

The Pixel Chip for the Inner Barrel is foreseen to be of the type "Large-area MAPS" which is currently under R&D at CERN and in parallel in China. In case this option would fail, the backup solution would be to use an ALTAI variant of the MAPS chips used for

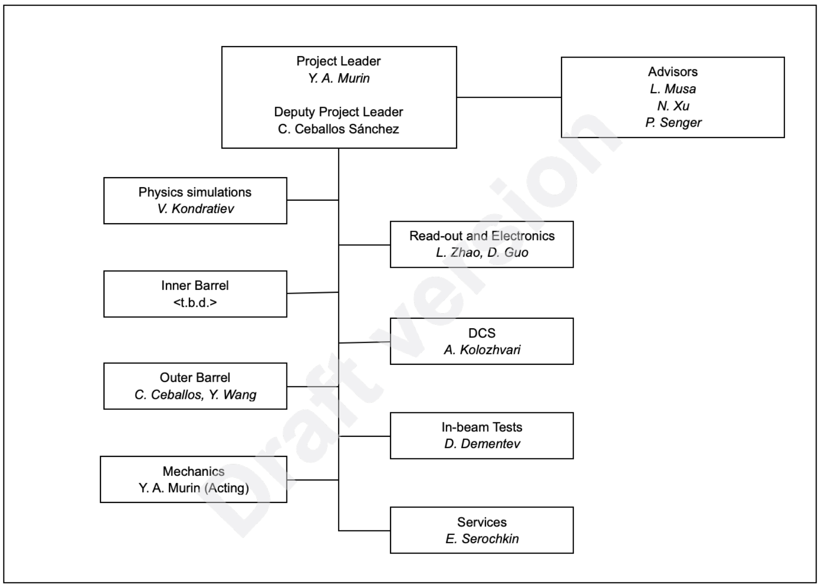

Figure 9.2: Management structure of the MPD-ITS project

upgrade of the Inner Barrel of ALICE ITS.

Flexible Printed Circuit. The FPC for the Outer Barrel (and the Inner Barrel in case of need) will be produced based on the final design used to produce the Outer (Inner) Barrel of the upgraded ALICE ITS and will be manufacture by the SwissPCB company. The metrological tests will be carried-out by the company Modus97 (Bologna, Italy) and the visual inspection and electrical test for the entire production will be done at JINR where the proper equipment and expertise for this purpose already exists.

Hybrid Integrated Circuit. The construction, assembly and final test of the HICs and Staves for the Outer Barrel will be done split between JINR and Chinese institutions. We plan to construct a total of 42 Staves considering an additional 20 % of spares.

Inner Barrel. The production of the Inner Barrel is foreseen to be done in China, based on large-area MAPS.

Layer and Service support mechanics. The development of the Layer and Service Support Mechanics is coordinated by JINR. The Layer Support Mechanics is developed by JINR, including the insertion container and the insertion scenario for the placing and integration of the ITS, the FFD and the beam pipe of the MPD inside the bore of the TPC.

Read-out, power cables and patch panels. The read-out electronics will be developed and produced mainly in China (USTC and CCNU), while the power and data cables and the patch panels will be produced by JINR.

Cooling plant and services. The entire cooling system, including the cooling plant and the distribution of the cooling fluid to the detector circuits, will be developed at JINR.

The management structure of the MPD-ITS project is shown in Figure 9.2 while Table 9.1 reports the estimate cost for each major part of the project and their budgeting sharing between Russia and China. This table does not include neither the cost related to infrastructure nor to logics (import/export of components between Russia and China). It should be notice that regarding READOUT and INNER BARREL (large-area MAPS) the Chinese party will fund the R&D activities upto the prototype production in both cases while the Russian side will fund the series production and tests.

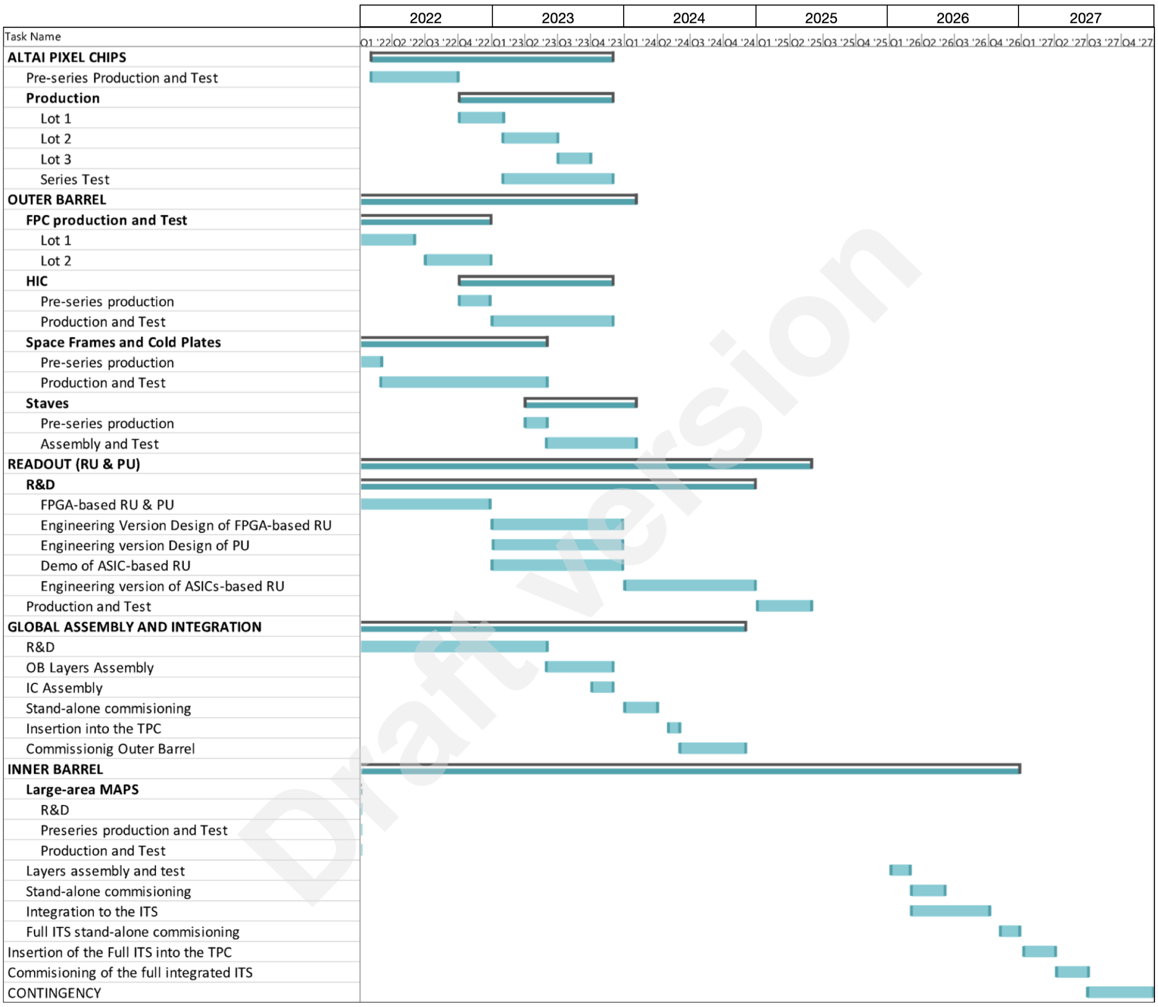

Figure 9.3: MPD-ITS Project timeline.

Table 9.1: Cost estimate and sharing of budgeting between Russia and China.

Item	**Russia (k$)**	**China (k$)**
ALTAI PIXEL CHIPS	1800	-
OUTER BARREL	1210.4	1466
READOUT	3315	1904.8
DCS	392	-
MECHANICS	1000	-
INNER BARREL	2000	2342.7
SERVICES	300	-
TOTAL	**10017.4**	**5995.4**

2793
.1 Appendix A - ALICE ITS2 leakless cooling system

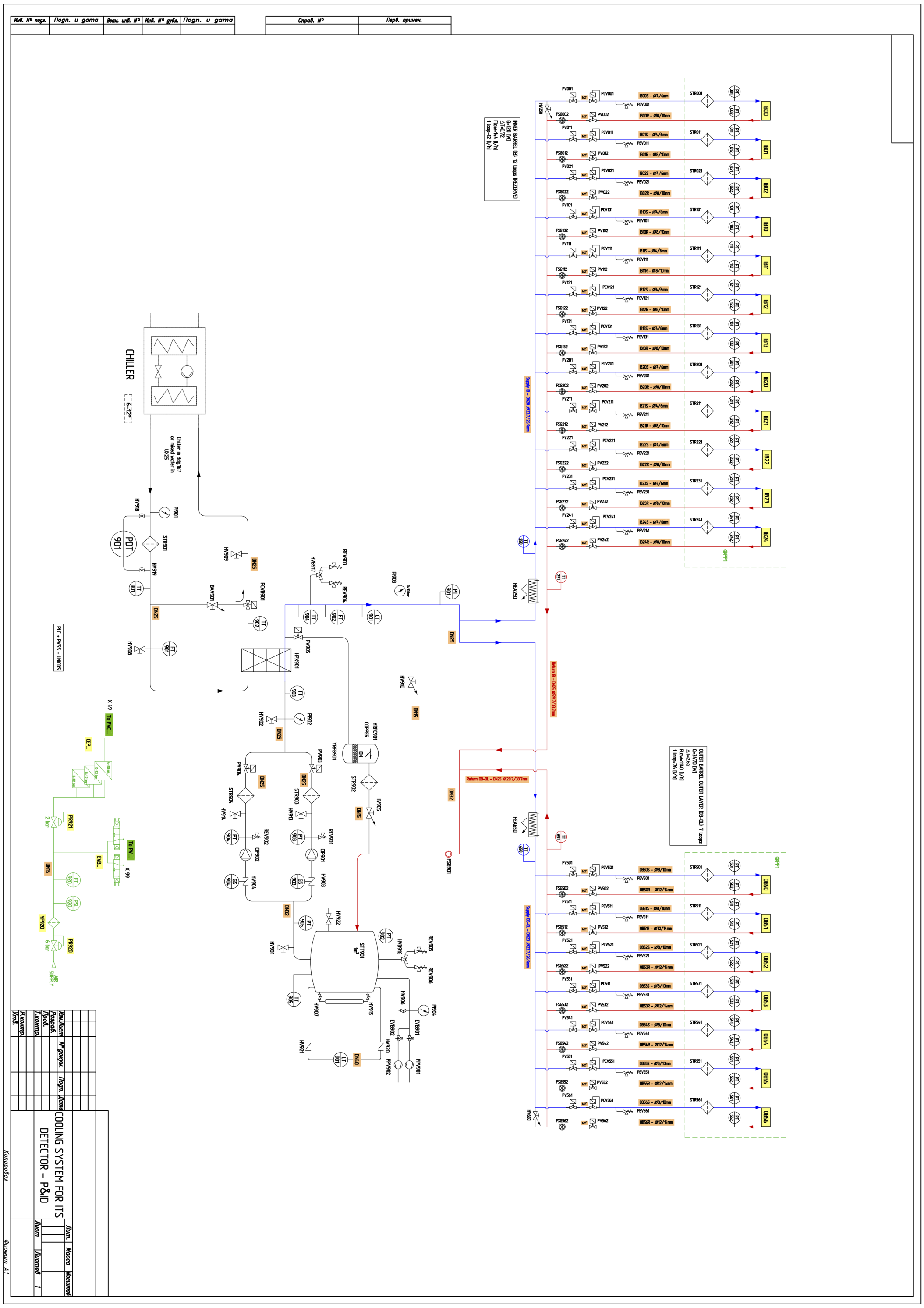

.2 Appendix B - Possibilities for the reduction of the beam pipe diameter

NICA Collider

The Nuclotron-based Ion Collider fAcility (NICA) [4] is a new accelerator complex being constructed at JINR. Two collider rings are designed and optimized to achieve the required luminosity at two interaction points (IP). The first IP is connected with Multipurpose detector (MPD) for the ion-ion ($^{197}_{79}Au^{+}$) collider experiments in the energy range of 1÷4.5 GeV/n. The second IP is aimed for the polarized proton-proton (5÷12.6 Gev) and deuteron-deuteron (2÷5.8 Gev/n) collisions. The collider lattice is based on the technology of super-ferric magnets developed in VBLHEP, JINR. The collider optics is optimized to obtain the required luminosity with the certain effects which set constraints on the lattice parameters: luminosity lifetime limitation by intrabeam scattering in a bunch (IBS), space charge tune shift, threshold of microwave instability, slippage factor optimization for efficient stochastic cooling, maximum required RF voltage amplitude. The first stage considers the $^{197}_{79}Au^{+}$ heavy ion mode of facility operation at center of mass energies of $\sqrt{S_{NN}}$=4÷11 GeV. The developed optical structure of the collider will use two systems of beam cooling (electron and stochastic), and a special scenario of rings operation will provide the required average luminosity of $10^{27}\,cm^{-2}s^{-1}$ in each of the two colliding points.

Optics

The magnetic structure of the Collider [5] (sequence of dipoles, quadrupoles and correction magnets along the reference orbit of the each storage ring) conforms the magnetic optics for each of the circulating beams. The optical structure of the Collider ensures the fulfillment of the following requirements:

- ensure the design peak value of the luminosity of the installation of 10^{26}–$10^{27}\,cm^{-2}s^{-1}$
- ensure that the luminosity lifetime is much longer (≥1 hr) than the beam preparation time (10 min);
- on the other hand, the maximum luminosity suggests a compact perimeter;
- large dynamic acceptance (both transverse and longitudinal);
- a sufficiently small value of the beta function (β) at the IPs;
- a certain ratio of the longitudinal length of the bunch length (σ_s) and β at the IPs;
- the maximum possible number of bunches.

Collider rings are in the form of a racetrack with a perimeter of 503.04 m (2 Nuclotron perimeters) and are located one above the other at a distance of 0.32 m. The basis of the magnetic system is composed of two-aperture dipole and quadrupole magnets of the Nuclotron type, quadrupole magnets of the final (before the meeting points) beam focusing and dipole magnets of the vertical beam separation system. A cell of the FODO type is selected as the basis of magnetic optics in the bending arcs. The phase advance of betatron oscillations in horizontal and vertical positions on one cell is 90°. In the long straight sections of the collider rings are:

- MPD and SPD detectors;

- elements of the injection system (septum and shock magnet) of beams;
- beam dumping systems;
- elements of a high-frequency accelerating system;
- electron beam cooling system; devices for stochastic beam cooling (pick-up stations and kickers);
- feedback system devices;
- halo beam collimation system.

Other equipments placed along the collider rings includes multipole magnetic correctors (dipole, quadrupole, sextupole and octupole) for the correction of imperfections of the magnetic field and beam dynamics, beam position monitors for measuring closed beam orbit distortions, vacuum equipment connection module.

Collider luminosity

For identical colliding beams with a round transverse cross section, the peak luminosity can be written in the form:

$$L = \frac{N_i^2}{4\pi\varepsilon\beta^*} F_{coll} f_{HG}(\sigma_s, \beta^*) \tag{1}$$

where N_i is the number of ions in a bunch, ε is the r.m.s. transverse emittance, β^* is the value of the Twiss amplitude function at the beam interaction point, σ_s is the longitudinal beam length, F_{coll} is the frequency of bunch collisions, and the so-called hour-glass effect (f_{HG}) is calculated by the equation:

$$f_{HG}(\sigma_s, \beta^*) = \frac{1}{\sqrt{\pi}} \int_{-\infty}^{+\infty} \frac{e^{-u^2} du}{1 + (u\sigma_s/\beta^*)^2}. \tag{2}$$

The longitudinal size of the beam is chosen to concentrate the whole luminosity in the central part of the MPD detector. If the beam size σ_s is much less than the value of the beta function at the interaction β^*, the function f_{HG} is close to unity. However, a decrease in the longitudinal beam size leads to an increase in the peak current and, as a consequence, to a larger shift of the betatron frequency and probability of coherent instability. The value σ_s=0.6 m was taken for the collider as a compromise derivative. The maximum allowable number of bunches in each of the collider rings is limited by the requirement for the absence of spurious collisions in the interaction region and is equal to 22.

The collider must maintain the design luminosity for a long time it takes to carry out a physical experiment. This process supposes the formation of a highly intense ion beam with a sufficiently low emittance. At the same time, it is required to provide the necessary lifetime of the beam. The maximum achievable lifetime is limited by the single scattering of ions at large angles by atoms of the residual gas. The design pressure of the residual gas in the beam chamber corresponds to a maximum beam lifetime of about 10 h. Effects of the space charge betatron tunes shift to the region of high order resonances, which can decrease the lifetime of an intense beam in the collider. At low particle energies, the strongest effect is that of the incoherent shift of the betatron frequency (the Laslett tune shift):

$$\Delta Q_{Las} = \frac{Z^2}{A} \cdot \frac{r_p N_i}{\beta^2\gamma^3 4\pi\varepsilon} \cdot F_{SC} F_b, \; F_b = \frac{C_{ring}}{\sigma_s\sqrt{2\pi}}. \tag{3}$$

where Z and A are the ion charge and mass, r_p is the classical proton radius, β and γ are the relativistic Lorentz factors, F_b is the beam bunching factor, C_{ring} is the ring perimeter, σ_s is the rms bunch length, and ε is the geometric transverse emittance. The second effect is the betatron oscillation frequency shift due to particle scattering in the electromagnetic field of the incoming bunch, the linear part of which is described by the so-called beam–beam parameter:

$$\xi = \frac{Z^2}{A} \cdot \frac{r_p N_i (1+\beta^2)}{4\pi\beta^2\gamma\varepsilon}. \tag{4}$$

In practice, beam stability in the collider is estimated using the criterion of maximum allowable total betatron frequency shift

$$\Delta Q_{total} = \Delta Q_{Las} + n_\xi \xi \leq 0.05, \tag{5}$$

where $n_\xi = 2$ is the number of collision points and the limit shift value of 0.05 is chosen with respect to the working point of the collider in the space of betatron frequencies. Here it is assumed that space charge effects have no significant effect on the beam lifetime at a smaller betatron frequency shift. Based on Eq. 1–3, the following dependences of luminosity and frequency shift on the intensity and emittance of the beam may be written as

$$\begin{aligned} L &\propto \frac{N_i^2}{\varepsilon} f_1(E_i) f_{HG}, \\ \Delta Q &\propto \frac{N_i}{\varepsilon} f_2(E_i), \end{aligned} \tag{6}$$

where E_i is the ion energy and f_1, f_2 are functions describing the energy dependences of the parameters. The maximum luminosity of the collider is reached in the case where the intensity and emittance of the beam corresponds to the limit with respect to the space charge. In this operation mode of the collider, an increase in the beam intensity increases the luminosity at a constant frequency shift. The frequency shift is maintained constant by increasing the emittance proportionally to the beam intensity; then the luminosity depends linearly on the number of ions. The maximum luminosity in this mode is reached when the phase volume of the beam equals the ring acceptance at a total frequency shift corresponding to the chosen maximum limit value of 0.05. This option of the collider operation called “space charge domination mode” is described by the following relationships,

$$\begin{aligned} L &\propto \Delta Q_{total}^2 \cdot \varepsilon \cdot f_3(E_i) \cdot f_{HG}, \\ N_i &\propto \Delta Q_{total} \cdot \varepsilon \cdot f_4(E_i). \end{aligned} \tag{7}$$

If the ion energy exceeds 3 GeV/n, the space charge domination mode can be optimized by decreasing the equilibrium emittance and intensity of the beam, N (Fig. 4). In this case, at a fixed peak luminosity, it is possible to work with a frequency shift below the resonance boundary ΔQ_{total}. In this regime, the main total effect capable of limiting the beam lifetime is the intrabeam scattering (IBS). The IBS leads to a diffusion growth of the beam emittance, and suppressing it is what the electron or stochastic cooling is used for. This “IBS domination mode” is characterized by the equilibrium between the beam heating due to the IBS and beam cooling, which corresponds to the equality of characteristic times of these processes: $\tau_{IBS} = \tau_{cool}$. Then, at a fixed luminosity, relationships 6 can be rewritten in the form

$$\begin{aligned} N_i &\propto \sqrt{L \cdot \varepsilon} \cdot f_5(E_i, \beta^*, \sigma_s), \\ \Delta Q_{total} &\propto \sqrt{\frac{L}{\varepsilon}} \cdot f_6(E_i, \beta^*, \sigma_s) < \Delta Q_{max} (= 0.05). \end{aligned} \tag{8}$$

From these proportions it is seen that the minimum value of ΔQ_{total} corresponds to the maximum emittance ε, i.e., to the fulfilling of the acceptance by ions (Fig. 4). Table 2 presents beam parameters in the collider energy range of 1÷4.5 GeV/n. The transverse emittances and momentum spread of the beam were calculated for the equality of times of IBS heating over all the three degrees of freedom. The table shows betatron frequency shifts corresponding to the stability criterion. These parameters allow to obtain the nominal luminosity L=10^{27} cm^{-2}s^{-1} at E_i=3÷4.5 GeV/n.

Table 2: General parameters of the ring.

Parameter	Value		
Ring perimeter, [m]	503.04		
Number of bunches	22		
R.m.s. beam length, [m]	0.6		
β-function in IP,[m]	0.6		
Betatron tunes, Q_x/Q_y	9.44/9.44		
Chromaticity, Q'_x/Q'_y	-20/-20		
Ring acceptance, [π·mm·mrad]	40		
Momentum acceptance, $\Delta p/p$	±0.010		
Critical factor, γ_{tr}	7.088		
Energy of $^{197}_{79}Au^{+}$ ions, [GeV/n]	1.0	3.0	4.5
Number of particles per bunch	2.8×10^{8}	2.7×10^{9}	2.9×10^{9}
R.m.s. momentum spread, $\Delta p/p$	0.6×10^{-3}	1.2×10^{-3}	1.6×10^{-3}
R.m.s, emittance, [π·mm·mrad]	1.1/1.1	1.1/1.1	1.1/0.9
Luminosity, [cm^{-2} s^{-1}]	0.8×10^{25}	0.8×10^{27}	10^{27}
Betatron tune shifts, ΔQ	0.05	0.05	0.022
IBS rates, [s]	300	1100	3200

Beam cooling

Applying cooling methods in the collider [5] aims, firstly, to the beam stacking by use of the stacking cooling procedure and, secondly, to keeping the luminosity during the experiment. The beam stacking in the collider is supposed to be implemented in the longitudinal phase space using the barrier voltage technique. This will provide the independent optimization of the beam intensity, number of bunches, control for the emittance, and momentum spread of particles during the formation of the beam. The aim of stacking can be reached using the electron or stochastic cooling system with technically implementable parameters due to the low linear density of particles. A numerical simulation of the beam stacking process with allowance for longitudinal forces of the space charge shows that this scheme yields an efficiency of no less than 90%. Both, electron and stochastic cooling systems must cover the entire energy range of the collider of 1÷4.5 GeV/n and provide the maximum possible luminosity at low energies and a luminosity around 10^{27} cm^{-2} s^{-1} at high energies. During the equilibrium between the IBS and cooling, the luminosity lifetime is limited only by the interaction between ions and residual gas. The mean luminosity is close to the peak value, because the beam lifetime is much longer than the stacking time. At the same time, the cooling times are equal to IBS times for all degrees of freedom. To yield an increase in luminosity in the space charge domination mode at low energies, the cooling time must be much less than the IBS time.

The stochastic cooling (SC) is supposed to be used at energies from 3 to 4.5 GeV/n. At high collider energies, cooling times of the order of 500 s are achievable for the system of

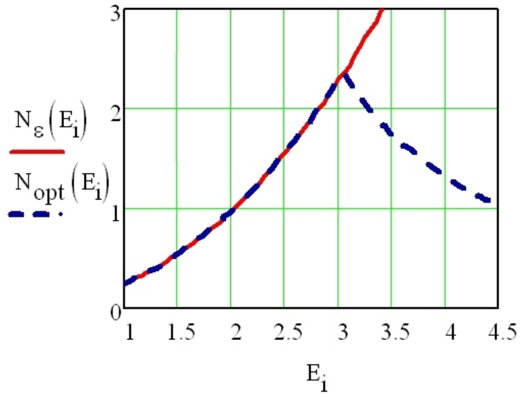

(a)

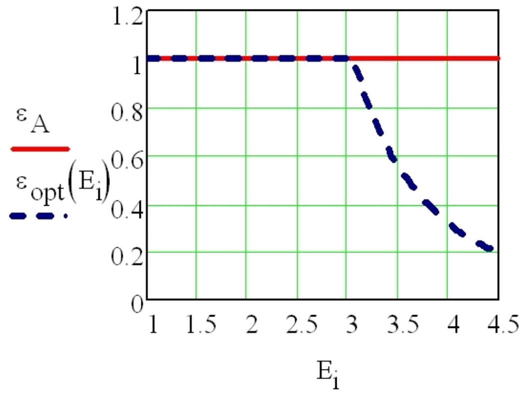

(b)

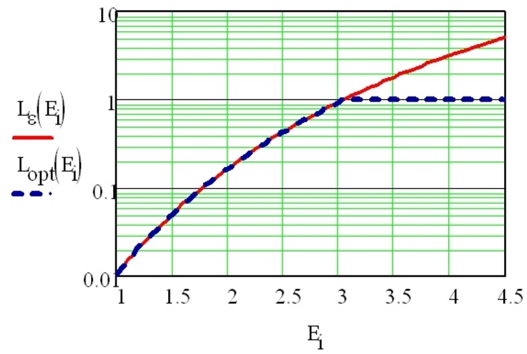

(c)

Figure 4: (a) Number of ions in the beam, (b) beam emittance, and (c) luminosity as functions of the ion energy in two cases: *ring acceptance is completely filled with ions* (solid curves) and *limited luminosity* (dashed curves). The acceptance is 40 π·mm·mrad. The dimensions of the qunatities are as follows:$[N_i]= 10^9$, $[\varepsilon]= \pi$·mm·mrad, $[L]$=10^{27} cm^{-2}s^{-1}.

stochastic cooling with a bandwidth of 2÷3 GHz. The chosen optical structure of the ring allows to find optimal positions for the pickup and kicker of the SC system when the partial slip factor is sufficiently small when passing from the pickup to the kicker. In the chosen Palmer method for the longitudinal cooling, the pickup is positioned in the rotating arc, i.e., in the dispersion region; the kicker is positioned in the long straight section. Using the SC with a band of 3÷6 GHz (or 2÷4 GHz) provides cooling times that are shorter by a factor of two or three as compared to the times of heating due to the IBS. The system of electron cooling is used to completely suppress the beam heating due to the IBS at low energies and to ensure the collider operation in the space charge domination mode. At energies in range from 3 to 4.5 GeV/n, the calculated times of cooling are somewhat shorter than those expected for the IBS and are comparable with times of stochastic cooling. However, at low energies, the cooling times are shorter than IBS times approximately by a factor of 20. For this reason, in the range of 1÷3 GeV/n, the electron cooling system is preferable for collider operation in the space charge domination mode. However, when designing the electron cooling system, it is necessary to take into account the problem of ion recombination.

RF stations

The formation of an ion beam in the Collider is carried out using three different RF systems [5]. The first type is the "barrier" RF voltage station (RF-1), which is used to accumulate and accelerate particles in the energy range from 1 to 4.5 GeV/n. This station creates a sequence of accelerating and decelerating rectangular voltage pulses with an amplitude of up to 5 kV. The RF-2 station of harmonic voltage works at the frequency of the 22^{nd} harmonic of the particle revolution frequency. The maximum voltage amplitude is 25 kV. In each ring of the collider there will be four RF-2 stations, total accelerating voltage is 100 kV. The resonant frequency of the resonator is tuned (depending on the experimental energy of 1÷4.5 GeV/n) within 11÷13 MHz. Stations of the third type RF-3 create a harmonic voltage at the 66^{th} harmonic of the particle revolution frequency in the accelerator with a maximum amplitude of 125 kV. Eight RF-3 stations will stand in each ring, i.e. their total voltage is 1 MV. The resonant frequency of the resonator is tuned (depending on the experimental energy of 1÷4.5 GeV/n) within 34÷39 MHz. Successive particle injection cycles ($^{197}_{79}Au^{+}$) from the Nuclotron are accumulated in the Collider using RF-1. After the accumulation of the required number of particles, the RF-2 system forms 22 bunches. The process is accompanied either by electron or stochastic beam cooling. Beam grouping at the 66^{th} harmonic of the revolution frequency in the presence of an RF-2 with an amplitude of 100 kV with an adiabatic increase in the total voltage of the RF-3 to the maximum value and cooling with a time of 100 s ensures the formation of bunches with r.m.s. length of 0.6 m and a momentum spread as by design.

Optics and beam parameters in the Interaction Region

The collider optics are optimized to obtain the required luminosity with the certain effects which set constraints on the lattice parameters namely the luminosity lifetime limitation by intrabeam scattering in a bunch (IBS), the space charge tune shift, the maximum required RF voltage amplitude and others. Optimized optical functions of the ring are shown in Figure 5 for betatron tunes of Q_x/Q_y=9.44/9.44 and β^*(IP)=0.6 m. Amplitude functions along the beam separation and interaction regions are given in Figure 6.

Beam sizes are rapidly squeezed in interaction drift space according to $\sigma_{x,y}(s) = \sqrt{\varepsilon_{\sigma,x,y}\beta_{x,y}(s)}$, where ε is the beam emittance (Tab. 2), $\beta = \beta^* + s^2/\beta^*$ is the function from the IP to the final focus quadrupole. The 1σ, 3σ beam sizes and 6σ ring acceptance are shown in Figure 7. These values are 0.8 mm, 2.3 mm and 4.6 mm respectively. **From these considerations it seems safe enough for the colliding beams (possible closed orbit distortions, required separation of the beams during accumulation) to have a vacuum pipe diameter of 40 mm in the central part of the MPD.**

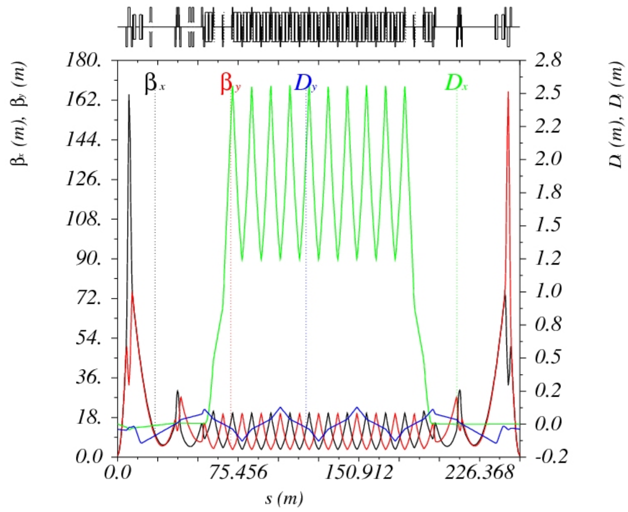

Figure 5: Linear amplitude and dispersion function of the collider (half a ring).

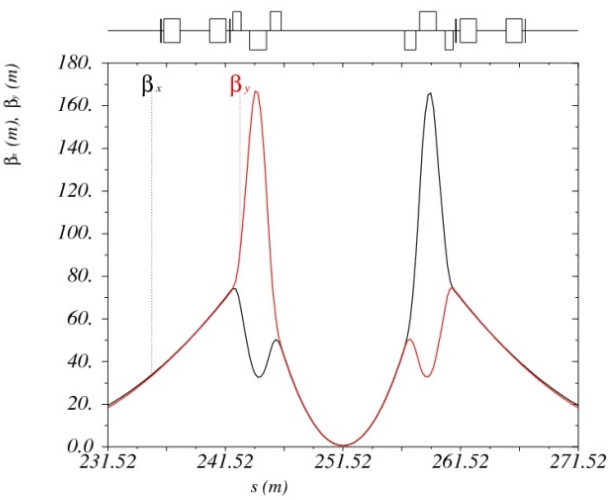

Figure 6: β-functions along the Interaction Region of the collider ring.

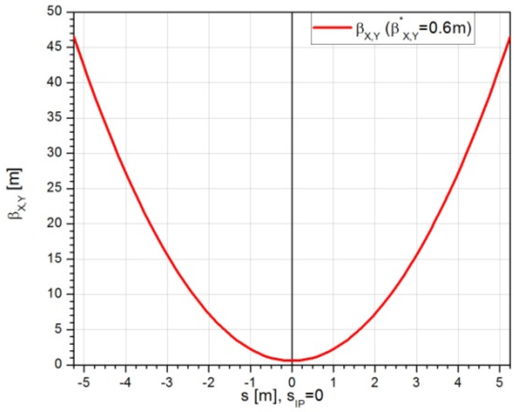

(a)

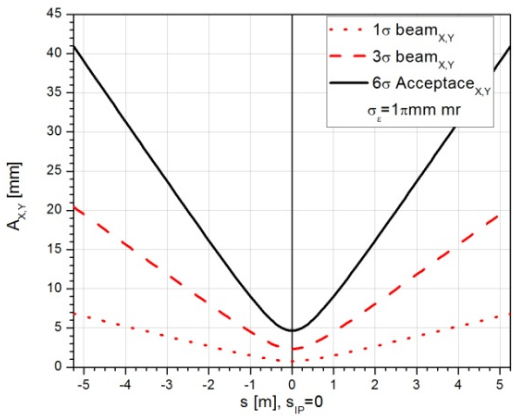

(b)

Figure 7: (a) β-functions and sizes of the colliding beams and (b) ring acceptance at the MPD location.